Прилог 5: Библиографија

Spectrochimica Acta Part A: Molecular and Biomolecular Spectroscopy 355 (2026) 127678

Contents lists available at ScienceDirect

Spectrochimica Acta Part A:
Molecular and Biomolecular Spectroscopy

journal homepage: www.journals.elsevier.com/spectrochimica-acta-part-a-molecular-and-biomolecular-spectroscopy

Temperature-induced spectral anomalies in doxorubicin—A Raman study

Ena Todorović [a,1], Sylwia Orzechowska [b,1], Milan Milovanović [a], Jelena Pešić [c], Malgorzata Baranska [b], Jasmina J. Lazarević [c,*], Nenad Lazarević [c]

[a] Faculty of Physical Chemistry, University of Belgrade, Studentski trg 12–16, PAC 105305, Belgrade, Serbia
[b] Faculty of Chemistry, Jagiellonian University, Gronostajowa 2, 30-387 Krakow, Poland
[c] Center for Solid State Physics and New Materials, Institute of Physics Belgrade, University of Belgrade, Pregrevica 118, 11080 Belgrade, Serbia

HIGHLIGHTS

- Raman spectra of doxorubicin tracked between 100 K and 300 K.
- Temperature changes affect resonance — not phase transformations.
- Theory and experiment agree remarkably well (> 90 % match).

GRAPHICAL ABSTRACT

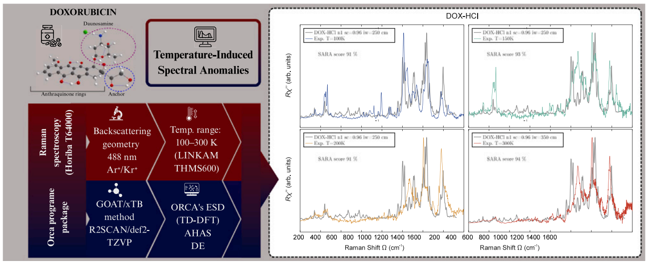

ARTICLE INFO

Keywords:
Doxorubicin
Raman spectroscopy
Resonance Raman
Temperature-dependent Raman
DFT calculations

ABSTRACT

Doxorubicin (DOX) is a widely used chemotherapeutic agent whose spectroscopic behavior can provide insight into its structural dynamics and interactions. Here, we investigate temperature-induced changes in the Raman spectra of DOX between 100 and 300 K, combining experimental measurements with density functional theory (DFT)-based simulations. Temperature-dependent Raman scattering experiments, performed under controlled cryogenic and ambient conditions, revealed pronounced spectral intensity variations accompanied by changes in the luminescence background. Detailed analysis and comparison with simulated resonance Raman spectra showed that these changes originate primarily from temperature-dependent resonance effects. Using the R2SCAN/def2-TZVP level of theory with D3 dispersion corrections, the most stable conformers of DOX, DOX-HCl, and DOX-H^+ were identified, and their resonance Raman spectra were computed. Quantitative comparison using the SARA algorithm yielded 91%–94% agreement between theory and experiment across all temperatures. Increasing temperature is accompanied by a redistribution of relative Raman intensities, with reduced contributions from bands assigned to motions involving hydrogen-bonds and enhanced contributions from ring-dominated modes. This trend is discussed in the context of temperature-dependent resonance conditions.

1. Introduction

Doxorubicin (DOX) (IUPAC: (1S,3S)-3-Glycoloyl-3,5,12-trihydroxy-10-methoxy-6,11-dioxo-1,2,3,4,6,11-hexahydro-1-tetracenyl-3-amino-2,3,6-trideoxy-α-L-lyxo-hexopyranoside), originally approved by the Food and Drug Administration (FDA) in 1974 under the trade name *Adriamycin*, remains one of the most widely used anticancer agents, particularly in the treatment of aggressive malignancies, either as a monotherapy or as part of a treatment protocol, despite its well-known cardiotoxicity [1,2]. As an anthracycline antibiotic, it comprises a tetracyclic aglycone core and a daunosamine sugar moiety. The transition from its parent molecule, red pigment daunorubicin isolated

---

[*] Corresponding author.
E-mail address: jasmina.lazarevic@ipb.ac.rs (J.J. Lazarević).
[1] These authors contributed equally.

https://doi.org/10.1016/j.saa.2026.127678
Received 15 November 2025; Received in revised form 24 February 2026; Accepted 2 March 2026

from *Streptomyces peucetius*, to DOX exemplifies how minor structural modifications, such as the addition of a single hydroxyl group, can significantly enhance therapeutic efficacy, alter tissue distribution, and increase hydrophilicity, thereby affecting both pharmacokinetics and pharmacodynamics. Doxorubicin is considered a gold standard in oncology due to its broad-spectrum activity against solid tumors and leukemias. Its all-encompassing mechanism of action, including DNA intercalation, inhibition of topoisomerase II, and generation of free radicals, underpins its potency [3–5]. Despite its dose-limiting cardiotoxicity, it continues to serve as a basis in chemotherapy protocols and is often employed as a reference compound in the development of novel anticancer therapies [6,7].

Raman spectroscopy plays a vital role in modern pharmaceutical analysis due to its ability to provide rapid, non-destructive, and highly specific molecular information. It is widely used for the identification and quantification of active pharmaceutical ingredients (APIs), monitoring polymorphic forms, identifying structural phase transitions, detecting impurities, and ensuring the homogeneity of formulations. Raman spectroscopy is acknowledged by regulatory agencies such as the U.S. FDA and the European Medicines Agency as part of the Process Analytical Technology (PAT) [8]. For example, it is employed in real-time monitoring of blending and granulation processes to ensure batch-to-batch consistency and compliance with Good Manufacturing Practice [9]. Regulatory guidelines such as the FDA's PAT guidance and International Council for Harmonization of Technical Requirements for Pharmaceuticals in Human Use ICH Q8–Q10 encourage the use of spectroscopic methods like Raman to enhance process understanding and control. Moreover, Raman imaging has been applied for verifying tablet content uniformity and coating thickness in accordance with regulatory expectations for quality assurance. Its compatibility with in-line and on-line systems, minimal sample preparation, and ability to analyze samples through packaging further support its growing adoption in validated pharmaceutical procedures.

The complex interaction between DOX and DNA has been studied using Raman spectroscopy for over four decades, beginning with the pioneering work of Manfait et al. [10,11]. Beyond elucidating DOX–DNA binding, Raman spectroscopy has also been employed to investigate the intracellular distribution of DOX and to monitor changes in cellular spectroscopic signatures at specific time points, such as after 24 h of exposure [12]. Furthermore, Raman spectroscopy has demonstrated the ability to detect DOX and its metabolites at the subcellular level, offering the evaluation of the drug's mechanism of action and cellular responses *in vitro* [13]. The work of Farhane et al. [14] further extended these studies by tracking the temporal evolution of cellular responses, enabling the monitoring of drug activity during both early and late stages of exposure. This highlighted the potential of Raman microspectroscopy not only to follow drug uptake and subcellular effects but also to provide insights into pharmacodynamics and intracellular drug kinetics. In a recent study, Majzner et al. [4] employed tip-enhanced Raman spectroscopy (TERS) to obtain highly localized spectra of DOX–DNA complexes, enabling correlation between drug identification and its precise location on a single DNA strand. TERS revealed new vibrational bands not detectable in earlier SERS studies, highlighting its sensitivity. The high spatial resolution of TERS makes it a powerful tool for investigating site-specific molecular interactions, offering great promise for the qualitative and quantitative assessment of the therapeutic potential of DNA-targeting drugs. Complementing these experimental approaches, Olszowska et al. [15] applied DFT, TD-DFT, and molecular dynamics simulations to model the conformational behavior and spectroscopic properties (IR, UV–Vis, and resonance Raman) of DOX in aqueous solution. Their results indicated that discrepancies with experimental data primarily stemmed from limitations in solvent modeling. This challenge was later addressed by Gómez et al. [16], who employed a hybrid approach to more accurately capture solute–solvent interactions. Moreover, Raman-based method was used to detect and identify erythrocyte-like cells formed during doxorubicin-induced differentiation of leukemic precursors [17]. Using Raman spectroscopy, stimulated Raman scattering microscopy, and a mitochondrial probe, biochemical and metabolic changes such as hemoglobin accumulation, lipid remodeling, and mitochondrial depolarization were tracked. This approach offers a sensitive alternative to conventional staining or flow cytometry for monitoring chemotherapy-induced differentiation.

Despite decades of Raman studies on DOX, the influence of temperature on its resonant vibrational response remains unexplored, leaving a gap in understanding how thermal conditions shape its spectroscopic fingerprint. In this research, we employed temperature-dependent Raman spectroscopy to investigate DOX. Temperature-dependent luminescence was observed, as well as resonant conditions varying with temperature, both of which significantly influence the appearance of the phonon spectrum of DOX. Moreover, theoretical calculations provided a framework to describe these temperature-induced changes in the resonant behavior.

2. Materials and methods

2.1. Material

Doxorubicin hydrochloride (DOX, purity 97.9%) was purchased from Sigma-Aldrich Chemie GmbH—Schnelldorf, Germany. The 5 mg sample of DOX red powder were deposited on the Raman-grade CaF_2 slides.

2.2. Experimental methods

Raman scattering measurements were performed on Horiba-Jobin Yvon T64000 Raman systems in backscattering micro-Raman configuration with 1800/1800/1800 grooves/mm gratings in the subtractive regime. The external and second intermediate slits were set to 100 μm, whereas lateral slits were adjusted to minimize noise. The 488 nm line of a Coherent Ar^+/Kr^+ gas laser was used as an excitation source, focused on the sample through an Olympus 50× objective in a parallel polarization plane. Temperature-dependent measurements were performed using a LINKAM THMS 600 heating/cooling stage with a heating/cooling rate of 5 K/min and a subsequent 25-minute thermalization period. Before starting the cooling procedure, the chamber was purged with argon gas, and a slow argon flow was maintained throughout the experiment to reduce moisture and prevent ice formation. The sample was cooled down to 100 K and gradually heated up to 300 K, with spectral acquisition at 100 K, 150 K, 200 K, and 300 K. The corresponding excitation power at the sample site was 5.60 mW, with an acquisition time of 900 s for ambient temperature measurements, and 1.25 mW with 600 s for the measurements at lower temperatures. All Raman spectra were pre-processed, including background elimination (polynomial fitting, 4th order), corrected by the corresponding Bose factor, and averaged.

2.3. Computational methods

All calculations were conducted for isolated molecules using the ORCA program package [18–21]. Three systems were examined: doxorubicin (DOX), protonated DOX-H^+, and doxorubicin hydrochloride (DOX-HCl), as the most stable conformers. To identify the global minimum on the potential energy surface of these molecules, the Global Optimization Algorithm (GOAT) was employed alongside the xTB method developed by Grimme and colleagues [22,23]. This semi-empirical tight-binding model is designed to provide reasonable structures with high computational efficiency. Given the numerous possible structures leading to the global minimum, all conformations for each molecule and their relative energies were collected.

For the most stable conformers, which have a relative energy of less than 15 kJ/mol compared to the lowest conformer, geometry

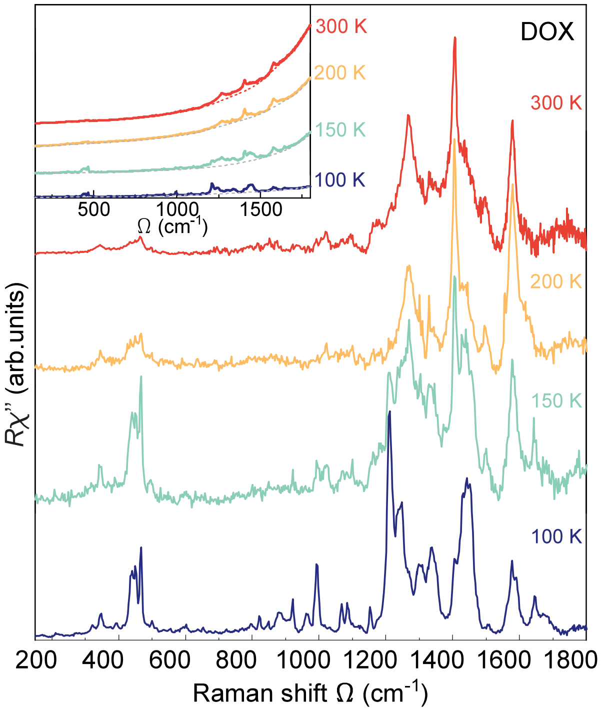

Fig. 1. Temperature-dependent Raman spectra of DOX in the range of 100–300 K. The inset displays the raw spectra, where the contribution of the luminescent tail is clearly visible. This luminescence background is indicated by the gray dashed line.

optimization was carried out using density functional theory (DFT). The optimal geometries were characterized as a minimum by calculations of harmonic vibrational frequency. The R2SCAN functional, [24–26] with D3 dispersion correction [27,28] was utilized with the triple-zeta basis set def2-TZVP [29]. The improved resolution of identity (Split-RI-J) algorithm [30–33] and the auxiliary basis set def2/J [34] were employed for all calculations. Described level of theory is abbreviated as R2SCAN/def2-TZVP.

The experimental laser wavelength of 488 nm (20,492 cm^{-1}) closely matches the excitation energy of the first electronic excited state of DOX [35,36]. Consequently, it is expected that resonance effects play a significant role in a signal intensity. Dynamic properties involving excited states, such as resonant Raman (rR) spectra, were computed in ORCA software using a path integral approach [37,38]. These computations require both ground- and excited-state Hessians. The ground-state Hessian has been obtained for the non-resonant case, by calculation of the derivatives of polarizability with respect to the normal coordinates at the R2SCAN/def2-TZVP level. Different approximations were tested for the excited-state Hessian. The Adiabatic Hessian After Step (AHAS) method combined with Duschinsky rotation effects (DE) [37,39] provided very good agreement with experimental spectra. Although rR spectra could be calculated only at 0 K, spectra at elevated temperatures were simulated by incorporating the effects of spectral line broadening and a scaling factor for anharmonicity [40–42]. Excited states properties were calculated using a time-dependent (TD) DFT method with the R2SCAN functional, D3 corrections and the def2-TZVP basis set. The Python-based SARA (Similarity Assessment of Raman Arrays) [43] program was used to quantitatively compare theoretically predicted and experimental spectra.

3. Results and discussion

Pure DOX powder, widely used in research, requires storage at sub-zero temperatures to ensure chemical stability. Storage at −20 °C is adequate for medium-term use, while −70 °C is recommended for long-term preservation, as it significantly reduces degradation processes such as hydrolysis, oxidation, and moisture absorption [44]. Dividing the material into aliquots and minimizing freeze–thaw cycles further helps maintain its integrity.

Raman spectroscopy plays a crucial role in this study, offering a non-destructive technique to investigate the vibrational properties of DOX without any sample preparation, thereby avoiding artefacts and preserving the intrinsic characteristics essential for practical applications. A key advantage of Raman spectroscopy is its capability for in situ measurements at low temperatures, eliminating the need to warm the sample to room temperature before analysis. Additionally, conducting Raman experiments at low temperatures suppresses anharmonic effects, which at higher temperatures can broaden Raman peaks. Cooling the sample thus enables clearer resolution of individual Raman modes, providing deeper insight into the vibrational structure of DOX.

Fig. 1 presents the temperature-dependent Raman spectra of DOX measured between 100 and 300 K. Notably, the spectrum recorded at 100 K differs significantly from the one obtained at 300 K. The spectra collected at intermediate temperatures display a combination of features observed at these two end temperatures, initially suggesting the possibility of a crossover phase in which intermediate states exhibit mixed-phase characteristics [45].

However, all vibrational modes observed at 100 K remain present at 300 K, exhibiting only gradual softening and peak broadening consistent with expected anharmonic effects and thermal lattice expansion in molecular crystals. No new bands emerge, and none of the existing bands disappear within the investigated temperature range. In contrast to the modest frequency shifts, a pronounced redistribution of Raman spectral weight is observed with increasing temperature. Certain modes decrease in intensity, while others are enhanced in a continuous and mode-selective manner. This intensity evolution is most consistently explained by temperature-dependent modifications of the resonance conditions rather than by a structural phase transition [46]. Importantly, the redistribution of Raman intensities closely follows the progressive evolution of the luminescence background shown in Fig. 1. Since the luminescence originates from electronic excited states, its temperature dependence reflects changes in resonance enhancement, which directly modulate the observed phonon intensities [46].

To further investigate this hypothesis, numerical modeling was performed. Given the very weak interactions between molecules, a single-molecule approach was considered a reasonable and cost-effective approximation in this case. Due to the numerous nuclear degrees of freedom, DOX can exist in several different conformations. To obtain reliable spectra, we determined the most stable conformers. Those conformers of DOX, DOX-HCl, and DOX-H^+ are illustrated in Fig. 2, along with their relative Gibbs free energies compared to the lowest conformer at both $T = 0$ K and $T = 300$ K, calculated using the R2SCAN/def2-TZVP level of theory. The DOX molecule can be divided into three functional domains: the anthraquinone rings (comprising four condensed aromatic rings), the anchor (glycolaldehyde), and the daunosamine region, which contains a sugar amino group. A visual inspection of the structures in Fig. 2 indicates that the anthraquinone rings remain nearly unchanged, while the anchor domain and the daunosamine region exhibit some flexibility.

For pure DOX, the three lowest conformers are labeled d1, d2, and d3. Compared to the d1 structure, the daunosamine region in d2 is rotated relative to the rings, while in d3, the glycolaldehyde segment is altered. The energy differences between the lowest conformer (d1) and the next two (d2 and d3) exceed 11 kJ/mol. Therefore, it is expected that isolated DOX predominantly exists in the d1 form under normal temperature and pressure conditions.

In the case of DOX-HCl, the lowest conformers, labeled n1 and n2, differ only in the position of a chlorine atom. Furthermore, both conformers maintain the same structural features as the d1 conformer. The third DOX-HCl conformer has an energy that is 4.9 kJ/mol higher at

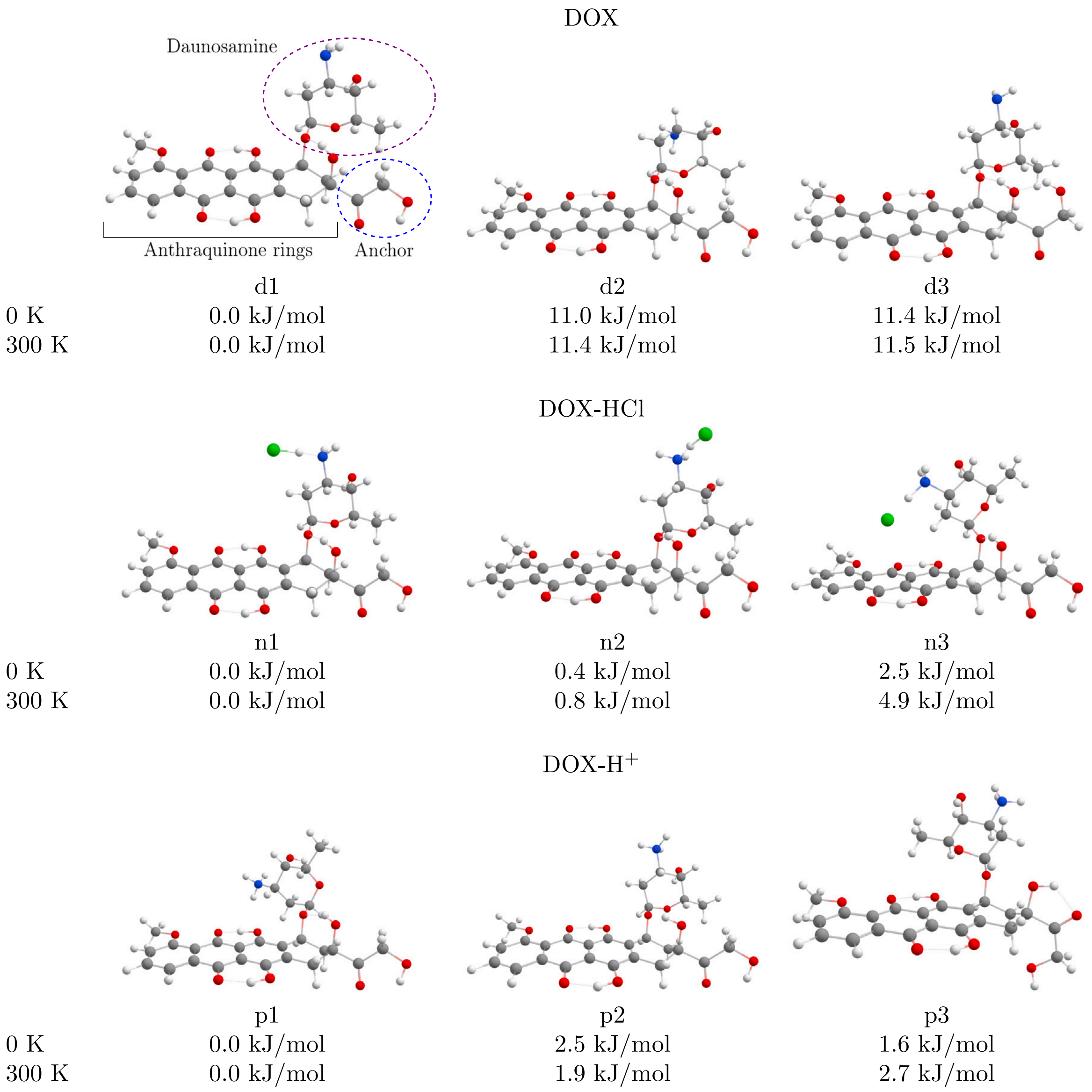

Fig. 2. The most stable conformers of DOX, DOX-HCl and DOX-H$^+$ together with a relative Gibbs free energy compared to the lowest conformer at $T = 0$ K and $T = 300$ K.

$T = 300$ K than n1 and features a rotated daunosamine group in relation to the rings. The most stable protonated DOX-H$^+$ structure (p1) has the daunosamine group rotated compared to the most stable conformers of DOX and DOX-HCl. However, the subsequent p2 conformer, which corresponds to the d1 and n1 structures, is only 1.9 kJ/mol higher in energy than p1 at $T = 300$ K.

When calculating rR spectra the first step is choice of the laser energy to irradiate the sample. It was set to experimental value of 20,492 cm^{-1}, which correspond to 488 nm incident wavelength. Experimental result for the first electronic transition of the DOX molecule is approximately at 480 nm [35,36]. The computations reveal that transition to the first excited states have a charge transfer character, involving π molecular orbitals localized on the anthraquinone moiety [47–49]. Our results for the vertical excited energy at the optimized ground-state geometry were 20,820 cm^{-1} (480 nm) for DOX d1, 20,826 (480 nm) for DOX-HCl n1 and 20,738 (482 nm) for DOX-H$^+$ p2 species. Those were in excellent accordance with the experimental results, suggesting that chosen R2SCAN functional and def2-TZVP basis set yield reliable results for electronic properties of considered system. Thus, calculated vertical excited energy matched the experimental incident wavelength, and no shift was needed.

The stick bands in calculated spectra have been convoluted with a Voigt line shape, with the full width at half maximum (FWHM) set to 10 cm^{-1} . The intensities have been normalized. The homogeneous linewidth was set to 50 cm^{-1}, while the inhomogeneous broadening parameter was varied between 125 cm^{-1} and 500 cm^{-1}. A scaling factor between 0.95 and 0.97 was applied to harmonic vibrational frequencies to account for systematic overestimation inherent to the harmonic approximation in DFT calculations. Such scaling factors are well established in vibrational spectroscopy and typically fall within this range for hybrid and meta-GGA functionals [50]. Inhomogeneous broadening was increased at higher temperatures (from 250 cm^{-1} at 100–200 K to 350 cm^{-1} at 300 K) to reflect enhanced thermal disorder. These empirical adjustments are well established in the simulation of temperature-dependent Raman spectra and are grounded in the physical effects such as enhanced structural disorder, changes in polarizability, and modified hydrogen bonding [51,52]. In our system, the experimentally observed peak broadening at higher temperatures is entirely consistent with these established physical mechanisms, and introducing temperature-dependent line-widths into the simulations reflects these real processes [53]. The theoretically simulated resonance Raman spectra for the most stable conformers of DOX-HCl (n1) were

Table 1
Assignment of vibrational modes of DOX-HCl at T = 100 K. ν and δ belong to the stretching and bending vibration.

Non-resonant Raman		Resonant Raman		Experimental	
Freq. (cm^{-1})	Assignment	Peak pos.	Intensity	Peak pos.	Intensity
338	νNH$_3$, δO–H···O, νO–H···O	340	0.128	348	0.107
434	δO–H···O, νO–H···O, δCH$_2$	440	0.206	441	0.293
449	δO–H···O			450	0.315
462	δO–H···O, δCH$_2$	458	0.122	467	0.397
492	δCH$_2$, δO–H···O, νO–H···O	491	0.069	488	0.051
818	δNH$_3$, δCH$_2$, νCH$_2$, δC–H	816	0.080	821	0.077
850	δCH$_2$	844	0.075	849	0.055
882	δCH$_2$, δCH$_3$, δNH$_3$, δC–H, δO–H δO–H···O	873	0.059	880	0.094
935	νN–H···Cl, δC–H			921	0.150
970	νNH$_3$, δO–H···O, δCH$_2$	970	0.061	992	0.302
1066	νO–H···O, δO–H···O, δCH$_2$, δC–H	1071	0.149	1068	0.128
1073	νNH$_3$, δCH$_2$, δC–H, δO–H			1084	0.136
1163	νNH$_3$, δCH$_2$, δO–H, δC–H	1157	0.211	1154	0.124
1188	δCH$_2$, δC–H	1179	0.174	1188	0.114
1201	δCH$_2$	1202	0.708	1212	1.000
1219	δCH$_2$, δO–H···O, δC–H	1220	0.653	1238	0.564
1249	νC–H, δC–H	1241	0.209	1248	0.595
1272	νO–H···O, δO–H···O, δCH$_2$, δC–H	1267	0.283	1269	0.287
		1286	0.208	1293	0.287
1300	δCH$_2$, δNH$_3$	1300	0.405	1299	0.320
1304	δCH$_2$, νO–H···O, δO–H···O, δNH$_3$, δC–H	1308	0.531	1304	0.314
1313	δCH$_2$, δO–H···O, δC–H	1316	0.534	1309	0.316
1324	δC–H	1333	0.226	1325	0.305
1340	δO–H···O, δC–H	1345	0.338	1338	0.395
1361	δCH$_2$, νC–C (aro), δO–H···O, δC–H	1355	0.271	1369	0.102
1405	δCH$_2$, δCH$_3$, δC–H	1405	0.637	1406	0.342
1422	δCH$_2$, δCH$_3$, δO–H···O	1423	0.894	1432	0.633
1435	δCH$_3$	1436	1.000	1442	0.698
		1464	0.417	1452	0.671
1569	δO–H···O, ring	1574	0.337	1578	0.319
1574	δO–H···O, ring	1584	0.301	1590	0.243
1599	δO–H···O, ring	1596	0.615	1608	0.070
1669	νC=O, δCH$_2$, δO–H	1628	0.178	1646	0.158

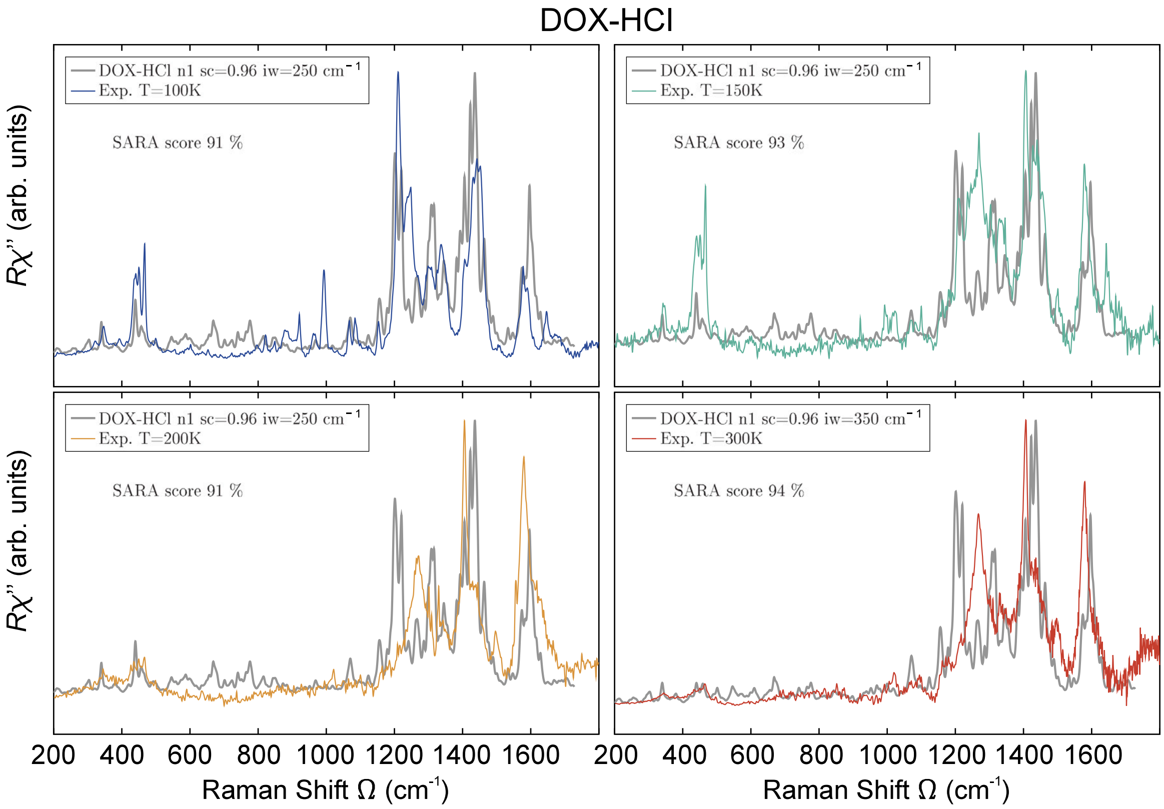

Fig. 3. Calculated spectra for the most stable conformers of DOX-HCl (n1) compared to the experimental spectra at T = 100 K, 150 K, 200 K, and 300 K. sc = scaling factor, iw = inhomogeneous broadening parameter.

compared to the experimental spectra of doxorubicin at temperatures of 100 K, 150 K, 200 K, and 300 K, as presented in Fig. 3. The non-resonant Raman (Figure S1) and rR spectra for other conformers of DOX-HCl, as well as for DOX and DOX-H$^+$ (Figure S2), can be found in the Supplementary Information (SI).

Since resonance conditions exist in the experimental data, the rR predictions demonstrated a better correlation with the experimental resonant spectra than the non-resonant predictions in all cases. Generally, anharmonic effects are expected to be more pronounced at higher temperatures. However, within this temperature range, a scaling factor of 0.96 provided the best alignment between the theoretical and experimental spectra. Additionally, the inhomogeneous broadening parameter (iw) was set to a higher value at elevated temperature. A value of 250 cm^{-1} was applied for 100 K, 150 K, and 200 K, while a value of 350 cm^{-1} was used for 300 K.

The SARA correlation score, which reflects the overall match between theoretical and experimental spectra, is presented for each temperature in Fig. 3. The calculated scores ranged from 91% to 94%, indicating a very good agreement between the theoretical and experimental spectra across all temperatures. It is important to note that the software is designed to penalize mismatches in vibrational frequency more significantly than those in peak intensity.

It is worth bearing in mind that all simulations were performed on isolated molecules, whereas the experimental spectra correspond to solid-state DOX-HCl. In molecular crystals, Raman active modes, particularly those associated with hydrogen bonding networks and low-frequency collective vibrations, are strongly modulated by intermolecular interactions and crystal packing effects, none of which are captured in single molecule simulations. Solid state Raman studies have demonstrated that collective lattice vibrations and hydrogen bond dependent modes show substantial shifts and intensity variations arising from intermolecular forces, highlighting the limitations of isolated-molecule models in reproducing quantitative spectral intensities [54]. Additionally, temperature-dependent Raman analyses reveal that increasing temperature induces structural fluctuations, changes in polarizability, and local disorder, which collectively lead to band broadening and reduced intensities, effects that are fully consistent with the experimental trends observed for DOX-HCl [55]. These temperature-induced modifications of the solid-state structure further amplify deviations from theoretical spectra, particularly in spectral regions where vibrational modes are sensitive to hydrogen bonding. Thus, although isolated-molecule DFT remains a valuable tool for mode assignment, the observed intensity reductions and band broadenings can be attributed to well documented solid-state and temperature-dependent phenomena, providing a coherent explanation for the differences between calculated and experimental spectra. However, the high SARA correlation scores (91–94%) across all temperatures suggest that the isolated-molecule model captures the essential vibrational behavior and the dominant resonance enhancement patterns. Similar isolated-molecule DFT approaches have been successfully employed to interpret solid-state Raman spectra of pharmaceutical compounds [15,56–58]. The remaining discrepancies observed in the 1200 cm^{-1} region may therefore reflect temperature-dependent packing effects not captured in the present molecular model. The SARA scores for various combinations of parameters can be found in Table S1 in the Supplementary Information (SI).

The most pronounced temperature-dependent changes appear as a redistribution of relative Raman intensities. Bands that are assigned (based on the non-resonant calculations) to motions involving hydrogen-bonds show reduced relative intensity with increasing temperature, whereas several ring-dominated modes increase in relative intensity. We interpret these trends as consistent with temperature-dependent changes in resonance enhancement and linewidth broadening, and we note that Raman intensity changes do not provide a direct quantitative measure of hydrogen-bond strength or vibrational delocalization [59].

The method described for calculating rR spectra does not provide a straightforward assignment of the peaks; however, this can be achieved using non-resonant Raman results. Specifically, experimental spectra taken at lower temperatures, where resonance effects are minimized, were effectively predicted using a non-resonant approach. This prediction is supported by a SARA correlation score of 82%, as illustrated in Figure S1 in the SI. These findings help in assigning the key vibrational modes and provide a reference for comparing them with resonant spectra at elevated temperatures.

Table 1 shows the assignment of vibrational modes for the lowest-energy isomer of DOX-HCl. A comparison of theoretically predicted and experimentally measured peak positions and intensities at 100 K is included in the same table. These results provide insights into the resonance effects influencing specific vibrational modes. Notably, a decrease in intensity is evident at around 450 cm^{-1}, as well as at 1250 cm^{-1} and 1490 cm^{-1}, with increasing temperature. Conversely, intensity increases are observed at 1450 cm^{-1} and 1610 cm^{-1}.

4. Conclusion

In conclusion, this study integrates experimental and theoretical investigations to unravel the temperature-dependent vibrational properties of DOX. The structures of the most stable conformers of DOX, DOX-HCl, and DOX-H$^+$ were determined, and their resonance Raman spectra were simulated using the R2SCAN functional with the def2-TZVP basis set, achieving excellent agreement with experimental data. Analysis of the temperature-dependent spectra revealed that while initial observations suggested a possible crossover phase, the spectral changes are predominantly driven by temperature-dependent resonance effects rather than structural phase transitions. Specifically, increasing temperature is accompanied by reduced relative intensities of bands assigned to motions involving hydrogen-bonds and enhanced relative intensities of ring-dominated modes, together with peak broadening. These observations are consistent with temperature-dependent resonance conditions and changes in local environment. Additionally, reductions in certain band intensities are attributed to increased structural disorder, resulting in peak broadening. Numerical modeling, justified by the weak intermolecular interactions in these systems, supports these interpretations. Overall, the theoretical approaches employed provide reliable predictions of Raman spectra and offer valuable insights into the complex vibrational behavior of DOX under varying thermal conditions.

Declaration of competing interest

The authors declare the following financial interests/personal relationships which may be considered as potential competing interests: M.B. serves as Editor-in-Chief at Spectrochimica Acta Part A. Given their role as Editor-in-Chief, Malgorzata Baranska had no involvement in the peer-review of this article and has no access to information regarding its peer-review. Full responsibility for the editorial process for this article was delegated to another journal editor. Other authors declare that they have no known competing financial interests or personal relationships that could have appeared to influence the work reported in this paper.

Acknowledgments

We acknowledge funding provided by the Institute of Physics Belgrade, through the Grant by the Ministry of Science, Technological Development, and Innovation of the Republic of Serbia, as well as additional funding from the same Ministry (contract No. 451-03-34/2026-03/200146). S.O. expresses gratitude to Polish National Agency for Academic Exchange (NAWA) for the financial support in the realization of the project (grant No. BWS/BIL/2022/1/00121) within the bilateral researcher exchange program.

Appendix A. Supplementary data

Supplementary material related to this article can be found online at https://doi.org/10.1016/j.saa.2026.127678.

Data availability

Data will be made available on request.

References

[1] K.B. Wallace, Doxorubicin-induced cardiac mitochondrionopathy, Pharmacol. Toxicol. 93 (3) (2003) 105–115.

[2] C. Carvalho, R.X. Santos, S. Cardoso, S. Correia, P.J. Oliveira, M.S. Santos, P.I. Moreira, Doxorubicin: the good, the bad and the ugly effect, Curr. Med. Chem. 16 (25) (2009) 3267–3285.

[3] A. Congras, N. Caillet, N. Torossian, C. Quelen, C. Daugrois, P. Brousset, L. Lamant, F. Meggetto, C. Hoareau-Aveilla, Doxorubicin-induced loss of dna topoisomerase ii and dnmt1-dependent suppression of mir-125b induces chemoresistance in alk-positive cells, Oncotarget 9 (18) (2018) 14539.

[4] K. Majzner, T. Deckert-Gaudig, M. Baranska, V. Deckert, Dox-dna interactions on the nanoscale: in situ studies using tip-enhanced raman scattering, Anal. Chem. 96 (22) (2024) 8905–8913.

[5] M. Kciuk, A. Gielecińska, S. Mujwar, D. Kołat, Ż. Kałuzińska-Kołat, I. Celik, R. Kontek, Doxorubicin—an agent with multiple mechanisms of anticancer activity, Cells 12 (4) (2023) 659.

[6] S. Ilyas, Y.H. Midoen, P. Santoso, A novel therapeutic approach to doxorubicin-induced cardiotoxicity, with a particular emphasis on the potential cardioprotective properties of vitis gracilis wall, J. Pharm. Pharmacogn. Res. 13 (1) (2025) 254–263.

[7] K. Ito-Hagiwara, J. Hagiwara, Y. Endo, L.B. Becker, K. Hayashida, Cardioprotective strategies against doxorubicin-induced cardiotoxicity: A review from standard therapies to emerging mitochondrial transplantation, Biomed. Pharmacother. 189 (2025) 118315.

[8] K.A. Esmonde-White, M. Cuellar, C. Uerpmann, B. Lenain, I.R. Lewis, Raman spectroscopy as a process analytical technology for pharmaceutical manufacturing and bioprocessing, Anal. Bioanal. Chem. 409 (2017) 637–649.

[9] T. De Beer, C. Bodson, B. Dejaegher, B. Walczak, P. Vercruysse, A. Burggraeve, A. Lemos, L. Delattre, J. Remon Y. Vander Heyden, W. Baeyens, Raman spectroscopy as a pat tool for the in-line monitoring and understanding of a powder blending process, J. Pharm. Biomed. Anal. 48 (3) (2008) 772–779.

[10] F. Yang, S.S. Teves, C.J. Kemp, S. Henikoff, Doxorubicin, dna torsion, and chromatin dynamics, Biochim. Biophys. Acta (BBA)-Reviews Cancer 1845 (1) (2014) 84–89.

[11] M. Manfait, A.J. Alix, P. Jeannesson, J.-C. Jardillier, T. Theophanides, Interaction of adriamycin with dna as studied by resonance raman spectroscopy, Nucleic Acids Res. 10 (12) (1982) 3803–3816.

[12] Z. Farhane, F. Bonnier, A. Casey, H.J. Byrne, Raman micro spectroscopy for in vitro drug screening: subcellular localisation and interactions of doxorubicin, Analyst 140 (12) (2015) 4212–4223, http://dx.doi.org/10.1039/C5AN00256G.

[13] Z. Farhane, F. Bonnier, M.A. Maher, J. Bryant, A. Casey, H.J. Byrne, Differentiating responses of lung cancer cell lines to doxorubicin exposure: in vitro raman micro spectroscopy, oxidative stress and bcl 2 protein expression, J. Biophotonics 10 (1) (2017) 151–165, http://dx.doi.org/10.1002/jbio.201600019.

[14] Z. Farhane, F. Bonnier, H.J. Byrne, Monitoring doxorubicin cellular uptake and trafficking using in vitro raman microspectroscopy: short and long time exposure effects on lung cancer cell lines, Anal. Bioanal. Chem. 409 (5) (2017) 1333–1346, http://dx.doi.org/10.1007/s00216-016-0065-0.

[15] M. Olszówka, R. Russo, G. Mancini, C. Cappelli, A computational approach to the resonance raman spectrum of doxorubicin in aqueous solution, Theor. Chem. Accounts 135 (2) (2016) 27.

[16] S. Gómez, P. Lafiosca, F. Egidi, T. Giovannini, C. Cappelli, Uv-resonance raman spectra of systems in complex environments: A multiscale modeling applied to doxorubicin intercalated into dna, J. Chem. Inf. Model. 63 (4) (2023) 1208–1217.

[17] A. Adamczyk, W. Tipping, O. Mazuryk, D. Graham, M. Baranska, K. Majzner, Sensitive detection and identification method of erythrocyte-like cells upon doxorubicin induced differentiation with vibrational techniques, Anal. Chem. 97 (31) (2025) 16966–16974.

[18] F. Neese, Software update: the orca program system, version 5.0, WIRES Comput. Molec. Sci. 12 (1) (2022) e1606, http://dx.doi.org/10.1002/wcms.1606.

[19] F. Neese, The orca program system, WIRES Comput. Molec. Sci. 2 (1) (2012) 73–78, http://dx.doi.org/10.1002/wcms.81.

[20] F. Neese, Software update: the orca program system, version 4.0, WIRES Comput. Molec. Sci. 8 (1) (2018) 1–6, http://dx.doi.org/10.1002/wcms.1327.

[21] F. Neese, F. Wennmohs, U. Becker, C. Riplinger, The orca quantum chemistry program package, J. Chem. Phys. 152 (2020) L224108, http://dx.doi.org/10.1063/5.0004608.

[22] C. Bannwarth, S. Ehlert, S. Grimme, Gfn2-xtb—an accurate and broadly parametrized self-consistent tight-binding quantum chemical method with multipole electrostatics and density-dependent dispersion contributions, J. Chem. Theory Comput. 15 (3) (2019) 1652–1671, http://dx.doi.org/10.1021/acs.jctc.8b01176.

[23] C. Bannwarth, E. Caldeweyher, S. Ehlert, A. Hansen, P. Pracht, J. Seibert, S. Spicher, S. Grimme, Extended tight-binding quantum chemistry methods, WIRES Comput. Molec. Sci. 11 (2) (2020) e1493, http://dx.doi.org/10.1002/wcms.1493.

[24] J.W. Furness, A.D. Kaplan, J. Ning, J.P. Perdew, J. Sun, Accurate and numerically efficient r 2 SCAN meta-generalized gradient approximation, J. Phys. Chem. Lett. 11 (19) (2020) 8208–8215, http://dx.doi.org/10.1021/acs.jpclett.0c02405, https://pubs.acs.org/doi/10.1021/acs.jpclett.0c02405.

[25] J.W. Furness, A.D. Kaplan, J. Ning, J.P. Perdew, J. Sun, Correction to "accurate and numerically efficient r 2 SCAN meta-generalized gradient approximation", J. Phys. Chem. Lett. 11 (21) (2020) http://dx.doi.org/10.1021/acs.jpclett.0c03077, 9248–9248. https://pubs.acs.org/doi/10.1021/acs.jpclett.0c03077.

[26] S. Lehtola, C. Steigemann, M. Oliveira, M. Marques, Recent developments in libxc - a comprehensive library of functionals for density functional theory, SoftwareX 7 (2018) 1–5, http://dx.doi.org/10.1016/j.softx.2017.11.002.

[27] S. Grimme, J. Antony, S. Ehrlich, H. Krieg, A consistent and accurate ab initio parametrization of density functional dispersion correction (dft-d) for the 94 elements h–pu, J. Chem. Phys. 132 (2010) 154104, http://dx.doi.org/10.1063/1.3382344.

[28] S. Grimme, S. Ehrlich, L. Goerigk, Effect of the damping function in dispersion corrected density functional theory, J. Comput. Chem. 32 (7) (2011) 1456–1465, http://dx.doi.org/10.1002/jcc.21759.

[29] F. Weigend, R. Ahlrichs, Balanced basis sets of split valence, triple zeta valence and quadruple zeta valence quality for h to rn: Design and assessment of accuracy, Phys. Chem. Chem. Phys. 7 (2005) 3297–3305, http://dx.doi.org/10.1039/B508541A.

[30] F. Neese, G. Olbrich, Efficient use of the resolution of the identity approximation in time-dependent density functional calculations with hybrid density functionals, Chem. Phys. Lett. 362 (2002) 170–178, http://dx.doi.org/10.1016/S0009-2614(02)01053-9.

[31] F. Neese, An improvement of the resolution of the identity approximation for the formation of the coulomb matrix, J. Comput. Chem. 24 (14) (2003) 1740–1747, http://dx.doi.org/10.1002/jcc.10318.

[32] D. Bykov, T. Petrenko, R. Izsák, S. Kossmann, U. Becker, E. Valeev, F. Neese, Efficient implementation of the analytic second derivatives of hartree-fock and hybrid dft energies: a detailed analysis of different approximations, Mol. Phys. 113 (2015) 1961–1977, http://dx.doi.org/10.1080/00268976.2015.1025114.

[33] F. Neese, The shark integral generation and digestion system, J. Comput. Chem. (2022) 1–16, http://dx.doi.org/10.1002/jcc.26942.

[34] F. Weigend, Accurate coulomb-fitting basis sets for h to rn, Phys. Chem. Chem. Phys. 8 (2006) 1057–1065, http://dx.doi.org/10.1039/B515623H.

[35] X. Yang, X. Zhang, Z. Liu, Y. Ma, Y. Huang, Y. Chen, High-efficiency loading and controlled release of doxorubicin hydrochloride on graphene oxide, J. Phys. Chem. C 112 (45) (2008) 17554–17558.

[36] C.-J. Lee, J.-S. Kang, M.-S. Kim, K.-P. Lee, M.-S. Lee, The study of doxorubicin and its complex with dna by sers and uv-resonance raman spectroscopy, Bull. Korean Chem. Soc. 25 (8) (2004) 1211–1216.

[37] B. de Souza, F. Neese, R. Izsak, On the theoretical prediction of fluorescence rates from first principles using the path integral approach, J. Chem. Phys. 148 (3) (2018) 034104, http://dx.doi.org/10.1063/1.5010895, http://aip.scitation.org/doi/abs/10.1063/1.5010895. (Accessed 31 January 2018).

[38] B. De Souza, G. Farias, F. Neese, R. Izsák, Efficient simulation of overtones and combination bands in resonant raman spectra, J. Chem. Phys. 151 (14) (2019) 144114, http://dx.doi.org/10.1063/1.5119471.

[39] F. Duschinsky, On the interpretation of electronic spectra of polyatomic molecules. I, Acta Physicochim. URSS 7 (1937) 551.

[40] T. Petrenko, F. Neese, Efficient and automatic calculation of optical band shapes and resonance raman spectra for larger molecules within the independent mode displaced harmonic oscillator model, J. Chem. Phys. 137 (2012) 234107, http://dx.doi.org/10.1063/1.4767536.

[41] T. Petrenko, F. Neese, A general efficient quantum chemical method for predicting absorption bandshapes, resonance raman spectra and excitation profiles for larger molecules, J. Chem. Phys. 127 (2007) 164319, http://dx.doi.org/10.1063/1.2785013.

[42] T. Petrenko, O. Krylova, F. Neese, M. Sokolowski, Optical absorption and emission properties of rubrene: Insight by a combined experimental and theoretical study, New J. Phys. 11 (2009) 015001, http://dx.doi.org/10.1088/1367-2630/11/1/015001.

[43] J.M. McCreery, Towards routine organic structure determination using raman microscopy, J. Raman Spectrosc. 55 (4) (2024) 1234–1245, http://dx.doi.org/10.1002/jrs.12345.

[44] C. Bing, P. Patel, R.M. Staruch, S. Shaikh, J. Nofiele, M. Wodzak Staruch, D. Szczepanski, N.S. Williams, T. Laetsch, R. Chopra, Longer heating duration increases localized doxorubicin deposition and therapeutic index in vx2 tumors using mr-hifu mild hyperthermia and thermosensitive liposomal doxorubicin, Int. J. Hyperth. 36 (1) (2019) 195–202.

[45] S. Djurdjić Mijin, A. Baum, J. Bekaert, A. Šolajić, J. Pešić, Y. Liu, G. He, M. Milošević, C. Petrovic, Z. Popović, et al., Probing charge density wave phases and the mott transition in 1 t-tas 2 by inelastic light scattering, Phys. Rev. B 103 (24) (2021) 245133.

[46] A. Baum, Y. Li, M. Tomić, N. Lazarević, D. Jost, F. Löffler, B. Muschler, T. Böhm, J.-H. Chu, I. Fisher, et al., Interplay of lattice, electronic, and spin degrees of freedom in detwinned bafe 2 as 2: A raman scattering study, Phys. Rev. B 98 (7) (2018) 075113.

[47] M. Jia, X. Song, Q. Zhang, D. Yang, A theoretical investigation about the excited state dynamical mechanism for doxorubicin sensor, J. Cluster Sci. 29 (4) (2018) 673–678, http://dx.doi.org/10.1007/s10876-018-1388-0, http://link.springer.com/10.1007/s10876-018-1388-0.

[48] F. Egidi, G. Lo Gerfo, M. Macchiagodena, C. Cappelli, On the nature of charge-transfer excitations for molecules in aqueous solution: a polarizable QM/MM study, Theor. Chem. Accounts 137 (6) (2018) http://dx.doi.org/10.1007/s00214-018-2259-3.

[49] E. Florêncio E. Silva, E.S. Machado, I.B. Vasconcelos, S.A. Junior, J.D. L Dutra, R.O. Freire, N.B. da Costa, Are the absorption spectra of doxorubicin properly described by considering different tautomers? J. Chem. Inf. Model. 60 (2) (2020) 513–521, http://dx.doi.org/10.1021/acs.jcim.9b00785, http://www.ncbi.nlm.nih.gov/pubmed/31833765.

[50] A.P. Scott, L. Radom, Harmonic vibrational frequencies: an evaluation of hartree-fock, Møller- plesset, quadratic configuration interaction, density functional theory, and semiempirical scale factors, J. Phys. Chem. 100 (41) (1996) 16502–16513.

[51] T. Wang, Y. Jiang, H. Feng, L. Liu, Q. Deng, D. Liu, C. Wang, Recent advances in raman spectroscopy for resolving material surfaces/interfaces, Catalysts 15 (12) (2025) 1131.

[52] T. Petrenko, F. Neese, Analysis and prediction of absorption band shapes, fluorescence band shapes, resonance raman intensities, and excitation profiles using the time-dependent theory of electronic spectroscopy, J. Chem. Phys. 127 (16) (2007).

[53] G. Das, A. Nicastri, M.L. Coluccio, F. Gentile, P. Candeloro, G. Cojoc, C. Liberale, F. De Angelis, E. Di Fabrizio, Ft-ir, raman, rrs measurements and dft calculation for doxorubicin, Microsc. Res. Tech. 73 (10) (2010) 991–995.

[54] M.P. Davis, T.M. Korter, Evaluating hydrogen bonding in organic cocrystals using low-frequency raman vibrational spectroscopy and quantum mechanical simulations, Cryst. Growth Des. 22 (3) (2022) 1922–1932.

[55] G. Batignani, E. Mai, M. Martinati, M.M. Neethish, S. Mukamel, T. Scopigno, Temperature dependence of coherent versus spontaneous raman scattering, Phys. Rev. Lett. 133 (20) (2024) 206902.

[56] M.A. Palafox, V. Rastogi, S. Singh, Ft-ir and ft-raman spectra of 5-chlorocytosine: solid state simulation and tautomerism. effect of the chlorine substitution in the watson-crick base pair 5-chlorodeoxycytidine-deoxyguanosine, Spectrochim. Acta Part A: Mol. Biomol. Spectrosc. 188 (2018) 418–435.

[57] A.A. Omran, W.M. Zoghaib, H.A. Gomaa, T.A. Mohamed, et al., Raman, atrir and nmr spectra, conformational stability, vibrational assignments, normal coordinates analysis and dft calculations of hydrochlorothiazide drug, J. Mol. Struct. 1310 (2024) 138314.

[58] L.P. Canul-Solís, M.d.C. Rodríguez-Aranda, E. Rivera-Pérez, A. Ortiz-Dosal, E. Guevara, E.O. Martínez-Ruiz, L.C. Ortiz-Dosal, A. Reyes-Reyes, E.S. Kolosovas-Machuca, Asymmetric dimethylarginine vibrational spectroscopy spectra and density functional theory model, Sensors 25 (22) (2025) 6818.

[59] N. Lazarević, A. Baum, A. Milosavljević, L. Peis, R. Stumberger, J. Bekaert, A. Šolajić, J. PeŠić, Aifeng Wang, M. Šćepanović, A. M. Milinda Abeykoon, M. V. MiloŠević, C. Petrovic, Z. V. Popović, R. Hackl, Evolution of lattice, spin, and charge properties across the phase diagram of $\mathrm{FeSe}_{1-x}\mathrm{S}_x$, Phys. Rev. B 106 (2022) 094510, http://dx.doi.org/10.1103/PhysRevB.106.094510, https://link.aps.org/doi/10.1103/PhysRevB.106.094510.

Surfaces and Interfaces 73 (2025) 107570

Contents lists available at ScienceDirect

Surfaces and Interfaces

journal homepage: www.sciencedirect.com/journal/surfaces-and-interfaces

Synergistic enhancement of solar photocatalysis in ALD-grown TiO_2-Cu composite films

Ivana Jelovica Badovinac [a,b], Ivna Kavre Piltaver [a,b], Lucija Črep [a], Daria Jardas Babić [a,b], Iva Šarić Janković [a,b], Karlo Veličan [a], Krešimir Salamon [c], Martina Kocijan [a], Matejka Podlogar [d], Nik Gračanin [d], Jasmina Lazarević [e], Mato Knez [a,f,g], Robert Peter [*,a,b]

[a] University of Rijeka, Faculty of Physics, Radmile Matejčić 2, 51000 Rijeka, Croatia
[b] University of Rijeka, Center for Micro- and Nanosciences and Technologies, Radmile Matejčić 2, 51000 Rijeka, Croatia
[c] Ruđer Bošković Institute, Bijenicka Cesta 54, 10000 Zagreb, Croatia
[d] Jožef Stefan Institute, Jamova 39, 1000 Ljubljana, Slovenia
[e] Center for Solid State Physics and New Materials, Institute of Physics Belgrade, University of Belgrade, Pregrevica 118, 11080 Belgrade, Serbia
[f] CIC nanoGUNE, Tolosa Hiribidea, 76, 20018 Donostia- San Sebastián, Gipuzkoa, Spain
[g] Ikerbasque, Basque Foundation for Science, Plaza Euskadi 3, Bilbao E-48009, Spain

ARTICLE INFO

Keywords:
Atomic layer deposition
Titanium dioxide
Thin films
TiO_2-Cu composites
Photocatalysis

ABSTRACT

This study explores the photocatalytic performance of TiO_2 thin films incorporating copper nanoparticles (Cu NPs) under simulated solar irradiation. Cu NPs were integrated *in-situ* into the TiO_2 matrix during film growth by atomic layer deposition (ALD). Structural analysis using X-ray diffraction, X-ray photoelectron spectroscopy, and Raman spectroscopy confirmed the preservation of the anatase TiO_2 phase within the TiO_2-Cu composites, with increasing Cu content leading to a proportional increase in metallic Cu presence. Scanning and transmission electron microscopy revealed that Cu NP size and distribution are tunable by adjusting the number of Cu-ALD cycles. UV–vis measurements showed enhanced visible light absorption by the TiO_2-Cu composite films, attributed to the localized surface plasmon resonance of Cu NPs. Samples with higher photocatalytic activity also showed increased photoconductivity, suggesting that direct electron transfer from the Cu NPs to TiO_2 significantly boosts the photocatalytic efficiency under simulated sunlight irradiation.

1. Introduction

Due to its exceptional combination of low toxicity, robust chemical and photostability, environmental benignity, earth abundance and economic viability, titanium dioxide (TiO_2) stands out as a highly promising photocatalytic material [1]. Its favorable bang edge positions, specifically its conduction band (CB) and valence band (VB), facilitate efficient charge separation and transfer of photogenerated electrons and holes, driving both chemical reduction and oxidation reactions. Consequently, TiO_2 exhibits high photocatalytic activity [1,2]. This property supports its diverse applications, including water and air purification [3,4], photocatalytic water splitting for hydrogen generation [5], CO_2 reduction [6], and self-cleaning surfaces [7]. While TiO_2 exhibits promising photocatalytic properties, its widespread commercial application in solar-driven photocatalytic applications is constrained by two major obstacles. First, its wide band gap (of about 3.2 eV) restricts light absorption to the UV region, which constitutes only about 5 % of the total solar spectrum [2,5]. Second, rapid recombination of photogenerated charge carriers, a common issue in semiconductors, reduces the lifetime of excited electrons and holes [1,5].

To enhance the photocatalytic activity of TiO_2, diverse structural and chemical modifications have been explored, including transition metal and nonmetal doping, dye photosensitization, and heterojunction formation with suitable low bandgap semiconductors [1,2,5]. Over the past fifteen years, the fabrication of TiO_2-metal nanocomposites has emerged as a promising strategy, involving the deposition or incorporation of metallic nanoparticles (NPs) onto or within the TiO_2 matrix [8,9]. These structures offer significant benefits for photocatalytic applications. Firstly, the electrical contact between TiO_2 and metal NPs forms a Schottky junction at the TiO_2-metal interface. The resulting built-in

---

[*] Corresponding author at: University of Rijeka, Faculty of Physics, Radmile Matejčić 2, 51000 Rijeka, Croatia.
E-mail address: rpeter@uniri.hr (R. Peter).

https://doi.org/10.1016/j.surfin.2025.107570
Received 21 May 2025; Received in revised form 29 July 2025; Accepted 29 August 2025

electric field facilitates the separation of photogenerated electron-hole pairs that form in the vicinity of the TiO_2-metal interface, thereby mitigating the charge carrier recombination [9,10].

Furthermore, incorporating metal NPs into TiO_2 can significantly modify its optical properties. Incident electromagnetic (EM) radiation with wavelengths exceeding the NP's dimensions induces localized surface plasmon resonance (LSPR), a collective oscillation of free electrons within the metal NPs. This LSPR amplifies the near-surface light intensity and enhances TiO_2's optical absorption at resonant frequencies, where the NP's intrinsic plasmonic frequency matches that of the incident light. Consequently, LSPR can increase the production of photogenerated charge carriers. Additionally, when the overlap occurs between LSP spectral resonances and the optical absorption of TiO_2, the intensified EM radiation generates more electron-hole pairs. Moreover, plasmon decay can produce so-called "hot electrons" wherein energy transfer from the plasmons to metal CB electrons allows their injection into the TiO_2 CB, provided their energy exceeds the Schottky barrier [8,10]. Thus, LSPR enhances the TiO_2 photocatalytic activity by increasing the charge carrier generation. By selecting appropriate metal NPs (type, size, shape) and surrounding media, the LSPR frequency can be tuned to extend TiO_2's charge carrier generation into the visible or even near-infrared regions [8–10].

Gold (Au) and silver (Ag) NPs are widely used plasmonic enhancers for TiO_2 photocatalysis due to their strong LSPR excitations in the near UV and visible range, coupled with high chemical stability [8,9]. However, their high cost and limited availability hinder large-scale production. Consequently, research has shifted towards more abundant alternatives, including Al [11,12], Ni [13], Cu [14,15], or Bi [16]. Copper, with its high electrical conductivity, low cost, environmental compatibility, and biocompatibility, is an excellent alternative to noble metals [17]. Similar to Au and Ag, Cu nanostructures exhibit plasmonic behavior and strong LSPR in the visible region [18]. Indeed, TiO_2-Cu composites have demonstrated significant enhancements in TiO_2's photocatalytic performance across various applications. For example, surface decoration of TiO_2 NPs or porous structures with Cu nanoparticles improves CO_2 reduction [17,19,20], photocatalytic water-splitting for hydrogen production [21–25] and pollutant degradation [26–29] under simulated solar or visible radiation. Likewise, Cu NP deposition on TiO_2 nanorods, nanotubes or nanosheets has shown substantial benefits in photocatalytic hydrogen evolution [30–32] or pollutant photodegradation [33–35].

In most of those studies, metal NPs are deposited directly onto TiO_2 surface [36,37]. However, ambient exposure (humidity, air, aqueous solvents) leads to Cu NP oxidation, diminishing their plasmonic and catalytic properties [38,39]. Furthermore, surface-attached NPs are susceptible to corrosion, reshaping and detachment during photocatalysis [40]. Ensuring chemical stability of Cu nanostructures is crucial but can be a major challenge in photocatalytic applications. Strategies to protect Cu include coating of TiO_2-Cu composites with a carbon or polymer layer [41,42] or by encapsulating Cu nanostructures within TiO_2 shells [43,44]. Alternatively, incorporating Cu NPs into the TiO_2 matrix offers protection from ambient conditions and enhances the electrical contact between Cu and TiO_2. Wet-chemical methods, such as combined sol-gel and photodeposition [14] or solvothermal synthesis [45], facilitate Cu NP embedded within porous TiO_2 systems like aerogels or micro/nanoparticle clusters. These TiO_2-Cu composites showed excellent photochemical properties when illuminated with visible light.

Embedding metallic NPs partially or completely within the TiO_2 matrix increases their contact area, enhancing charge transfer between the NPs and TiO_2, thereby boosting the photocatalytic activity [40]. For example, TiO_2 electrodes with embedded Au NPs exhibited significantly better water splitting performance under visible light compared to TiO_2 films with surface-deposited Au NPs [46]. Similarly, TiO_2 nanocolumn arrays filled with Ag NPs showed higher methylene blue degradation efficiency than Ag-coated TiO_2 structures [47].

In most photocatalytic studies, active materials in the form of micro/nanoparticles or powders are generally used, as these materials possess high porosity and specific surface area. However, in practical applications, the photocatalyst must be reusable and easily removable from the environment in which the photocatalytic process takes place, which can be a major difficulty with nanoparticles or powders in liquids or aqueous solutions. On the other hand, photocatalytic thin films or coatings on solid substrates can be a viable alternative to powdered materials as they can be easily removed from dispersions or solutions and are reusable over a longer period of time. In addition, polycrystalline thin films can have a nano-grained structure with high surface roughness and high specific surface area, which can be very favorable for photocatalytic processes [48].

Directly incorporating metallic nanostructures into the TiO_2 matrix during growth poses challenges, as metal atoms often exhibit high diffusivity in oxide matrices and are susceptible to oxidation during the process. Consequently, reports on direct TiO_2-metal thin film composite deposition are scarce. For example, pulsed laser deposition yielded Au-incorporated TiO_2 films with excellent solar-driven photocatalytic activity without post-annealing, but required high deposition temperatures (300 – 700 °C) [49]. Similarly, magnetron sputtering produced Cu NP-containing TiO_2 films demonstrated enhanced methyl orange photodegradation activity under UV light, albeit with poor crystallinity [50].

The present study utilizes atomic layer deposition (ALD) to synthesize polycrystalline TiO_2-Cu composite thin films, by directly incorporating Cu NPs into the TiO_2 matrix during growth without post-treatment. ALD has attracted considerable attention for thin semiconductor film growth for its precise nanometer-scale thickness control and conformality on both flat and porous substrates. Previous work demonstrates ALD's efficacy in structural and chemical modification of photocatalytic metal oxide semiconductors, enabling grain size control in polycrystalline TiO_2 [51], tuning the optical, structural, and electrical properties of TiO_2 thin films by the selection of the appropriate substrate, film thickness and deposition temperature [52], efficient copper doping of ZnO thin films [53], or covering titania nanotubes with thin and conformal TiO_2 coatings [54].

ALD-grown TiO_2-Cu composite films were characterized for surface morphology, elemental composition, crystalline and electronic structure, conductivity, and optical absorption using X-ray diffraction (XRD), X-ray photoelectron spectroscopy (XPS), scanning electron microscopy (SEM), energy dispersive X-ray spectroscopy (EDS), transmission electron microscopy (TEM), UV-vis spectroscopy, and photoconductivity measurements. The photocatalytic performance was assessed by monitoring the degradation of methylene blue (MB) in an aqueous solution under simulated sunlight irradiation.

2. Materials and methods

2.1. ALD synthesis

ALD syntheses were carried out in a Beneq TFS 200 system at a deposition temperature of 250 °C on Si(100), quartz(100) or amorphous glass substrates. High-purity nitrogen (purity 6.0) was used as both carrier and purging gas. Prior to the deposition, the substrates were ultrasonically cleaned in acetone, Milli-q water and isopropanol and dried with N_2 gas. Pure TiO_2 samples were grown with 1500 ALD cycles, where titanium tetrachloride ($TiCl_4$, 99.9 %, Sigma-Aldrich) and deionized water (H_2O) were used as titanium- and oxygen-containing precursors, respectively. In one ALD cycle, $TiCl_4$ was pulsed in the deposition chamber for 250 ms, followed by a 3 s purging step with N_2, a 180 ms pulse of H_2O and the final 1 s purging step with N_2.

For the growth of TiO_2-Cu composites with varying copper content, copper(II) acetate ($Cu(OAc)_2$) was added to the TiO_2 growth process. The depositions consisted of 15 ALD supercycles, with alternate pulses of $TiCl_4$, $Cu(OAc)_2$ and H_2O. The first step in the supercyle consisted of 100 $TiCl_4/H_2O$ ALD cycles, as described above. In the second step, x ALD cycles of $Cu(OAc)_2$ and water were employed, where one cycle consisted of a 1 s pulse of $Cu(OAc)_2$, followed by 5 s purge with N_2, 1 s pulse of H_2O and a 5 s purge with N_2. For the composite films marked with TiO_2–Cu25, TiO_2–Cu75, and TiO_2–Cu200, the value of x was 25, 75, and 200, respectively. During the deposition, $Cu(OAc)_2$ was heated at 190 °C in a hot source to provide sufficient vapor pressure and carried into the reaction chamber with N_2. The thickness of all ALD-grown films was within the range of 75 - 90 nm, as established from SEM cross-sectional measurements.

2.2. Material characterization

The crystal structure of the samples was characterized by grazing incidence X-ray diffraction (GIXRD) technique with a *PANalytical X'Pert Pro* diffractometer, using the Cu K_α line of 0.154 nm as the incident X-ray radiation. During the measurements, the angle of incidence was maintained at 1°.

The photoemission spectra were recorded with a SPECS XPS spectrometer, equipped with a monochromatized X-ray source of energy 1486.74 eV (Al K_α line) and a hemispherical Phoibos MCD 100 electron energy analyzer. For spectra around the Cu 2p core levels, the pass energy was set to 50 eV, while for the measurements around Ti 2p and O 1s core levels it was set to 10 eV. In addition, the Auger Cu LMM and valence band spectra were measured with the pass energy of 25 eV. The spectra were calibrated by setting the C 1s peak to a binding energy (BE) of 284.5 eV. Cu 2p, Ti 2p and O 1s experimental curves were fitted with the product of Gaussian and Lorentzian functions after Shirley background subtraction, using the commercial UNIFIT software.

The surface morphology was analyzed using a JEOL JSM-7800F field emission SEM instrument. The micrographs were recorded by collecting the secondary electrons at a working distance of 3 mm and backscattered electrons at a working distance of 4 mm, with the electron beam acceleration voltage of 10 kV. Cross-sectional SEM images were recorded by detecting backscattered electrons applying the same acceleration voltage. Energy dispersive X-ray spectrometer (EDS) (X-Max 80, Oxford Instruments, UK), integrated in the SEM, was used to obtain elemental maps.

The analysis of the cross-sectioned TiO_2-Cu films was performed using a conventional transmission electron microscope (TEM; JEM 2100, Jeol Ltd.) and a scanning transmission electron microscope (STEM; Talos, Thermo Fisher Scientific) for elemental mapping, both operated at 200 kV. A thin, electron-transparent lamella was prepared using a focused ion beam (FIB-SEM; Helios NanoLab 600i dual beam system, Thermo Fisher Scientific). For this purpose, a slice was cut from the middle of the film and thinned to reveal the cross-sectional composition within the layer.

Raman spectra were recorded under ambient conditions in a backscattering configuration using a Jobin Yvon T64000 spectrometer. An Ar^+/Kr^+ ion laser, operating at a wavelength of 514.5 nm, was used as excitation source. The optical absorption was measured on the films deposited on quartz substrates, using the Perkin Elmer Lambda 950 UV-Vis-NIR spectrophotometer equipped with a 150 mm integrating sphere. The relative percentage of absorbed light was determined from the transmittance and reflectance data as $A = 1 - T - R$.

Photoconductivity was measured on pure TiO_2 and TiO_2-Cu composite films deposited on glass substrates, cut to dimensions of 8 mm × 15 mm. Electrical contacts were made with silver paint on the opposite sides of the samples. During the measurements, a constant voltage of 10 V was maintained with Keithley 2401 Source Measure Unit, while the photocurrent (measured using the same instrument with the current range of 1 pA - 5 A) was excited with a solar simulating lamp (OSRAM Vitalux lamp, 300 W).

2.3. Photocatalytic activity measurements

The photocatalytic activity of the ALD-grown thin films was determined by monitoring the temporal decomposition of methylene blue (MB) in an aqueous solution under simulated sunlight irradiation at room temperature. Rectangular samples (1 cm × 3 cm) were immersed in an open beaker filled with 15 mL of 1.35×10^{-5} M aqueous MB solution. First, the photocatalyst and MB solution were kept under constant stirring in ambient conditions for 1 h in the dark, until the adsorption–desorption equilibrium on the photocatalyst surface was achieved. Second, the beaker containing the sample and the MB solution was irradiated with an OSRAM Vitalux lamp (300 W) under continuous stirring. The optical absorption of the MB solution was measured in intervals of 60 min with a UV–vis spectrophotometer (Thermo Scientific, Evolution 201). The change in concentration of MB was calculated from the relative intensity change of the characteristic MB absorption line at 664 nm. Additional measurements of photocatalytic activity were performed by observing the decomposition of caffeine over time in an aqueous solution (with a molar concentration of 1.29×10^{-5} M). All other experimental conditions were the same as in the case of MB, while the change in caffeine concentration was calculated from the intensity change of the characteristic caffeine absorption line at 272 nm.

3. Results and discussion

3.1. Structure and chemical composition

The crystallinity of ALD-grown TiO_2 films depends strongly on the process temperature [51,55]. As the crystalline state also influences the photocatalytic activity, we analyzed our samples by XRD (Fig. 1). The pure TiO_2 sample exhibits a typical anatase structure with characteristic reflections from the (101), (004), (200), (211) and (204) crystallographic planes (JCPDS 88–1175 card). In the TiO_2-Cu25 sample (lowest Cu content), strong anatase TiO_2 peaks are preserved, with a small (111)-Cu reflection appearing at 2θ=43.3° (JCPDS 003–1018). A substrate peak at 56.1° (marked with an asterisk) is also observed. The TiO_2-Cu75 sample shows increased (111)-Cu intensity and a new (200)-Cu diffraction peak at 50.5°, indicating higher metallic Cu content than in the TiO_2-Cu25 sample. Compared to pure TiO_2, TiO_2-Cu25 maintains similar anatase TiO_2 peak intensities, suggesting a well-preserved TiO_2 crystal structure. However, TiO_2-Cu75 shows slightly reduced TiO_2 peak intensities, indicating potential crystallinity loss or lower anatase TiO_2 proportion. The TiO_2-Cu200 sample displays further increased Cu peak intensities and decreased TiO_2 peaks. An additional peak at 28.7° (marked with a circle) is observed, likely attributable to $Cu(OAc)_2$ vaporization residues, as it only appears with Cu prolonged precursor pulsing.

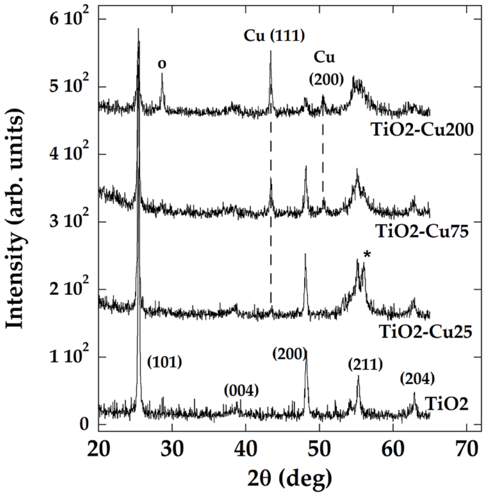

Fig. 1. XRD patterns of a pure TiO_2 and TiO_2-Cu composite films with varied Cu content.

XRD analysis indicates a progressive substitution of the TiO_2 phase by the metallic Cu with increasing Cu content in the TiO_2-Cu composite films. Notably, no copper oxide diffraction lines are seen. Furthermore, the TiO_2-related peaks in the TiO_2-Cu samples remain unshifted compared to pure TiO_2, suggesting Cu atoms are present solely in metallic form, not as substitutional defects in the TiO_2 matrix.

XPS measurements were conducted to determine the Cu chemical state (Fig. 2a). All TiO_2-Cu composite films exhibit similar Cu 2p photoemission spectra with sharp, well-resolved peaks at binding energies of 933.2 eV (Cu $2p_{3/2}$) and 953.2 eV (Cu $2p_{1/2}$), consistent with metallic copper [56,57]. Again, no satellite lines characteristic for cupric oxide (CuO) are observed [56,57]. The Cu $2p_{3/2}$ experimental spectra for all TiO_2-Cu composite films can be fitted with the symmetric Gaussian-Lorentzian curves with the similar full width at half maximum (FWHM) of (2.3 ± 0.1) eV (see Fig. S1 in the Supporting material). As seen from Fig. 2a, the Cu $2p_{3/2}$ and Cu $2p_{1/2}$ peak intensities increase with the number of $Cu(OAc)_2$ ALD cycles, indicating enhanced metallic Cu content.

Since metallic Cu (oxidation state Cu^0) and cuprous oxide Cu_2O (oxidation state Cu^+) have similar Cu 2p photoemission lines, both in terms of energy position and shape, Auger Cu LMM spectra are sometimes used to distinguish between metallic Cu and Cu_2O [57]. However, as seen from Fig. S2 in the Supporting material, the overlap between the Ti 2s photoemission line and the Cu LMM Auger peak makes such an analysis difficult in the case of our TiO_2-Cu composites. For the samples with the lower Cu content (TiO_2-Cu25 and TiO_2-Cu75), the Ti 2s peak shows a clear broadening towards the higher BE side, but the peak at about 568 eV, which is characteristic of metallic Cu [57], is only clearly visible for the sample with the highest Cu content (TiO_2-Cu200). On the other hand, the presence of Cu_2O should be accompanied by the appearance of a peak at about 570 eV [57], which is clearly absent in our TiO_2-Cu composite films. Hence, our XPS measurements presented in Fig. 2 and Figs. S1 and S2 are in good agreement with the XRD analysis from Fig. 1, indicating the presence of Cu in the metallic form, but the absence of features related to copper oxides.

In addition, the Ti 2p photoemission spectra of the TiO_2-Cu composite films show a great similarity with the spectrum measured on pure TiO_2 (Fig. S3). All Ti 2p spectra consist of a symmetric doublet peak with a separation between the Ti $2p_{3/2}$ and Ti $2p_{1/2}$ components of about 5.7 eV, which is characteristic of TiO_2 [51,55]. In addition, the FWHM of the Ti $2p_{3/2}$ component has a value of (1.10 ± 0.05) in all samples, indicating that no additional Ti-related bonds are formed in the TiO_2-Cu samples. The O 1s photoemission peaks also show no major difference between pure TiO_2 and TiO_2-Cu films and reveal only a slight increase in O-related defects in the Cu-impregnated samples (see Fig. S4 in the Supporting Material). XPS survey spectra and relative elemental composition of ALD-grown samples (calculated from XPS survey spectra) are presented in Fig. S5 and Table S1, respectively.

Valence band (VB) XPS spectra provide further information about the chemical composition of our ALD-grown films (Fig. 2b). The pure TiO_2 sample exhibits anatase type of TiO_2, with characteristic peaks A and B at BEs around 7.0 eV and 4.5 eV, respectively. Peak A corresponds to the Ti 3d/O 2p σ-bonding states, and the less intense peak B to O 2p π-anti-bonding states [58,59]. The TiO_2-Cu25 VB spectrum closely resembles pure TiO_2, with a small shoulder peak C at around 2.5 eV. The intensity of this new peak increases in the TiO_2-Cu75 spectrum. The energy position of peak C aligns with the most intense metallic Cu VB peak, which originates from Cu 3d orbitals [60]. While TiO_2 VB peaks A and B dominate the TiO_2-Cu25 and TiO_2-Cu75 spectra, peak C (metallic Cu) is most prominent in the VB spectrum of the TiO_2-Cu200 film. This is in excellent agreement with the XRD results, indicating high metallic Cu content and TiO_2 loss in TiO_2-Cu200.

XRD and XPS confirm the polycrystalline nature of the ALD-grown TiO_2-Cu composites, consisting of anatase TiO_2 and metallic Cu phases. SEM and TEM were employed to investigate the surface morphology and bulk structure of the TiO_2-Cu films (Fig. 3). The pure TiO_2 film exhibited a flat surface with ~100 nm plate-shaped crystallites, consistent with previous studies under similar ALD conditions [51,55]. However, Cu incorporation significantly altered the surface morphology. The surface of the TiO_2-Cu25 sample became rougher with the apperance of small grains, which increased in size and surface concentration in TiO_2-Cu75 (top row of Fig. 3). Tilted SEM images by 10° (insets in Fig.3) further confirm the roughness increase with the Cu content.

Backscattered electrons (BSE) SEM images (see Fig. S6 in the Supporting material) show bright spots on TiO_2-Cu samples, but not on pure TiO_2. Given the BSE signal dependance on the atomic number, these spots, indicative of elements with higher atomic numbers, were attributed to metallic Cu structures, corroborated by XPS and XRD. EDS maps (see Fig. S7 in the Supporting material) confirm Cu presence in the grain-like structures in the composite films.

High-magnification SEM images (bottom row of Fig. 3) show that the TiO_2 crystallite sizes in TiO_2-Cu25 and TiO_2-Cu75 were similar to pure TiO_2. Furthermore, in addition to the larger grains, smaller nanometer-sized grains were also embedded in these films. TiO_2-Cu75 showed a higher, more uniform grain distribution compared to the sporadic

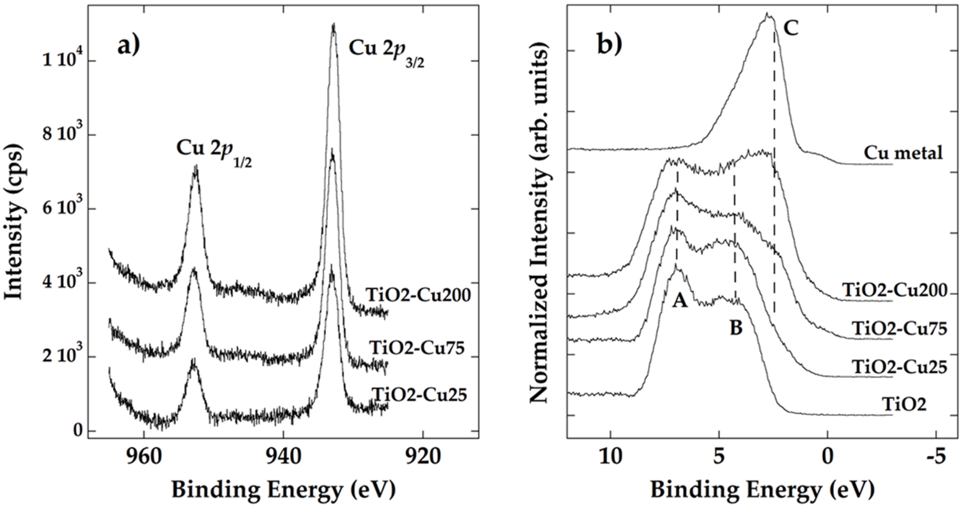

Fig. 2. (a) Cu 2p core-level photoemission spectra of TiO_2 films with incorporated Cu. (b) Valence band photoemission spectra of pure TiO_2 and TiO_2-Cu composite films. For the reference Cu metal spectrum a metallic copper foil was measured after cleaning by in-situ Ar^+ ion bombardment.

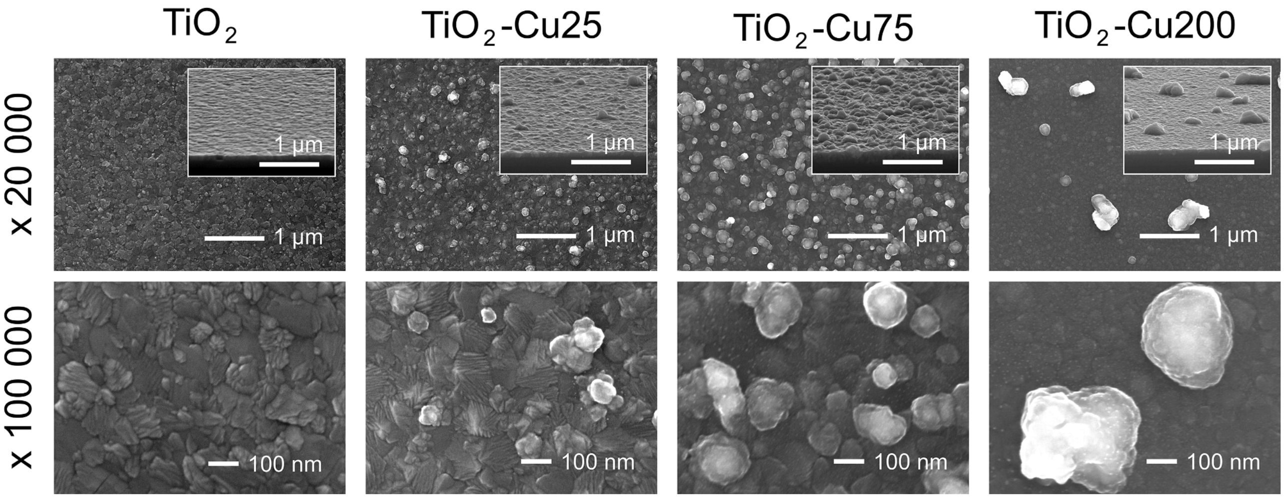

Fig. 3. SEM micrographs (secondary electrons) of pure TiO_2 and TiO_2-Cu composite film surfaces at two different magnifications. Insets: 10° tilted images, 10 mm working distance, 10 kV acceleration voltage.

distribution in the TiO_2-Cu25 sample. For TiO_2-Cu200, Cu structure sizes increased, while the size of TiO_2 crystallites decreased, consistent with our XRD and XPS findings of high metallic Cu content and deteriorated TiO_2 crystallinity.

Cross-sectional backscattered electron SEM measurements (Fig. 4) revealed the bulk composition of the ALD-grown films. Pure TiO_2 exhibited a homogeneous structure throughout its thickness (Fig. 4a). However, the TiO_2-Cu samples contained metallic Cu particles with their size and quantity increasing with the Cu content (Fig. 4b-d). TiO_2-Cu25 shows a single Cu NP (∼ tens of nanometers) embedded in the film (Fig. 4b), while TiO_2-Cu75 shows multiple NPs embedded in the TiO_2 matrix (Fig. 4c). The images confirm that surface protrusions in Fig. 3 originate from embedded Cu particles in the TiO_2 matrix. As can be seen from Figs. 4 and S6, CuNPs in the TiO_2-Cu75 sample are larger and are spatially closer together than in the TiO_2-Cu25 film. In addition, the BSE-SEM images in Fig. S6 show that the Cu NPs in the TiO_2-Cu25 and TiO_2-Cu75 films are uniformly distributed, while the TiO_2-Cu200 sample exhibits a rather uneven distribution of Cu NPs, with a wide range of sizes from 50 nm to 300 nm or more. The size distribution of the Cu particles (determined from the BSE-SEM images) is shown in Fig. S8 in the Supporting material. The TiO_2-Cu25 film has Cu NPs with a size of up to 80 nm and an average size of about 50 nm, while the Cu NPs in the TiO_2-Cu75 sample can reach a size of up to 150 nm and have an average size of 78.5 nm. On the other hand, most of the Cu particles in the TiO_2-Cu200 sample have a size of around 50 – 80 nm, but the film also contains some large Cu particles with a diameter of 300 nm or more.

TEM cross-sectional images (Fig. 5) provide additional insights into the bulk composition of TiO_2-Cu25. Fig. 5a shows two embedded Cu particles. A high-resolution TEM image (Fig. 5b) taken from the left particle in Fig. 5a, along with STEM HAADF and EDS maps (Fig. S9), confirms presence of copper within the TiO_2 matrix, as the Ti and O signals are attenuated in the region where copper is located. The film primarily consists of randomly orientated TiO_2 anatase grains, some of which are elongated, especially in Cu-free regions. In Cu-rich areas, TiO_2 grains are smaller and more uniform, with some terminating at Cu inclusions and others growing from or around them. The high-resolution image (Fig. 5b) reveals smaller TiO_2 grains growing alongside copper, with corresponding lattice spacings: specifically, the (100) plane of anatase TiO_2 and the (110) plane of metallic Cu. The Cu inclusion is polycrystalline, composed of randomly oriented but smaller Cu crystals. Thus, SEM and TEM confirm the presence of Cu nanoparticles in the composite films, with particle size increasing as the Cu content increases.

3.2. Raman analysis and optical absorption

Raman measurements (Fig. 6) complement our XPS, XRD and microscopy analysis. Pure TiO_2 exhibits the characteristic anatase *Eg* mode at 141.6 cm^{-1} [61]. Further peaks at higher energies correspond to other anatase phonon modes and overtone modes from the substrate. With Cu incorporation, the anatase structure persists (consistent with XRD, Fig. 1), but the *Eg* mode broadens (inset in Fig. 6), indicating reduced quasiparticle lifetime due to grain boundary scattering [61]. A discontinuity in the *Eg* modeś energy between TiO_2-Cu25 and TiO_2-Cu75 suggests larger sized and larger amounts of Cu NPs in the latter, inducing greater strain and structural distortion of TiO_2 in the vicinity of the Cu NPs, as confirmed by TEM.

UV-vis absorption spectra (Fig. 7) show that CuNPs incorporation into the TiO_2 matrices significantly alters the optical properties of the films. The pure TiO_2 absorbs negligibly in the visible range with an absorption edge at ∼360 nm, in good agreement with the literature [51]. In contrast, the TiO_2-Cu25 sample shows strong visible and UV absorption, featuring a sharp peak at around 400 nm. Based on our SEM and TEM analysis, we attributed this peak to the LSPR effect in the Cu NPs embedded into the TiO_2 film. Namely, the intensity and the position of the LSPR peaks of metallic NPs strongly depend on the size, shape and spacing of the metal nanoparticles as well as on the concentration of conduction electrons in the metal and the intrinsic dielectric properties

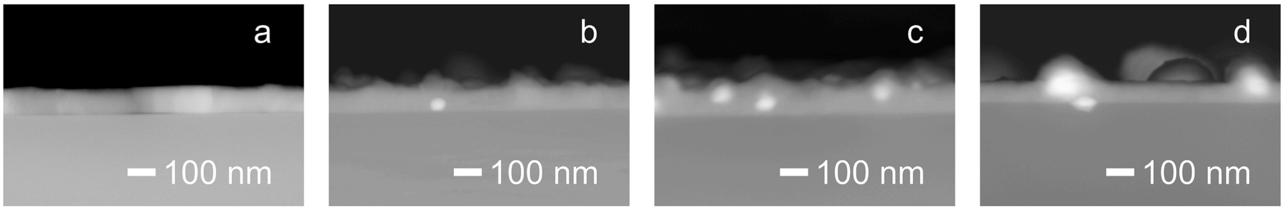

Fig. 4. Cross-sectional backscattered electron SEM micrographs: (a) pure TiO_2 film, (b) TiO_2-Cu25, (c) TiO_2-Cu75. (d) TiO_2-Cu200.

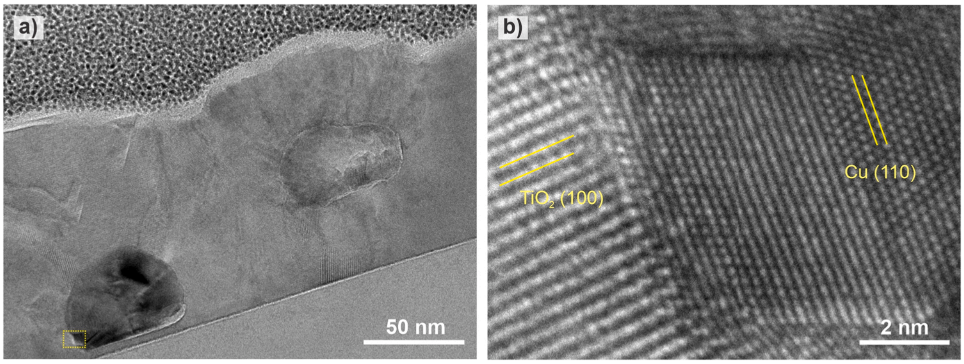

Fig. 5. a) Low-magnification cross-sectional TEM image of two Cu NPs embedded in TiO_2. b) High-magnification TEM image of the left Cu particle in (a) with plane spacing labelled for anatase TiO_2(100) and Cu(110).

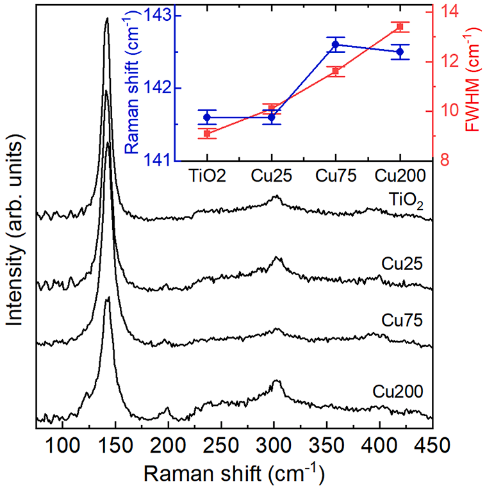

Fig. 6. Raman spectra of pure TiO_2 and TiO_2-Cu composite films. The inset shows the energy position (blue) and linewidth (red) of the anatase *Eg* mode with respect to the Cu content. Due to the clarity of the spectra, the designations for the TiO_2-Cu samples were shortened to Cu25 (TiO_2-Cu25), Cu75 (TiO_2-Cu75) and Cu200 (TiO_2-Cu200).

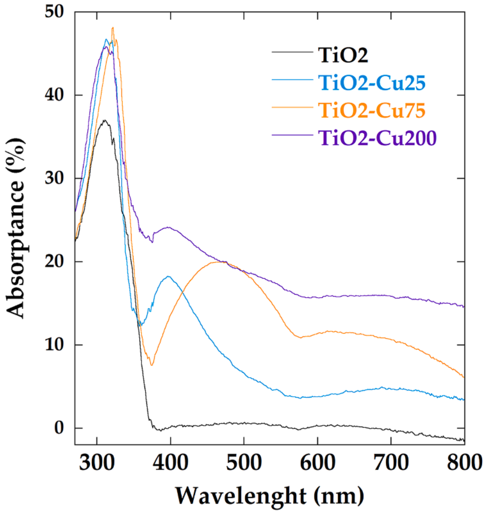

Fig. 7. UV-vis absorption spectra of pure TiO_2 and TiO_2-Cu composite films.

of the NPs and the surrounding medium [62]. Indeed, it has been shown that Cu NPs can exhibit an LSPR peak in a wide range of wavelengths, from the UV [63] to the visible region [14,34,64].

As can be seen in Fig. 7, the LSPR peak in the TiO2-Cu75 sample is broadened and shifted to longer wavelengths (it is centered at around 470 nm) compared to the TiO_2-Cu25 film. The broadening of the LSPR peak can be attributed to the large dispersion of sizes and shapes of Cu particles in the TiO_2-Cu75 sample, as was observed in previous studies on Cu NPs dispersed in mesoporous TiO_2 [14] or composites consisting of TiO_2 nanostructures and Au nanodiscs or NPs [65,66]. On the other hand, the red shift of the LSPR peak is probably related to the occurrence of Cu NPs with larger size in the TiO_2-Cu75 film, as we found in SEM analysis [14,64]. Namely, one of the mechanisms behind this effect is related to the relaxation time of the free electrons in the Cu NPs, which increases with increasing particle size, leading to an increase in the LSPR wavelength [18]. In addition, both the TiO_2-Cu25 and TiO_2-Cu75 samples show a broad absorption at around 700 nm, which can be ascribed to the inter-particle coupling between the Cu NPs [49,67]. This peak is more pronounced in the TiO_2-Cu75 film than in the TiO_2-Cu25 sample due to the smaller gaps between the NPs in TiO_2-Cu75, as observed from our SEM measurements. The LSPR peaks in our TiO_2-Cu composites are in the range of 400-500 nm, which agrees well with the results obtained for Cu NPs with a size of a few tens of nanometers prepared by an electrochemical method on glass substrates [68] or deposited on TiO_2 nanorods by a solvothermal technique [34]. In addition, similar wavelengths for LSP resonances were found for Ag NPs, with the sizes of ~30-100 nm embedded in TiO_2 layer [69]. On the other hand, the LSPR effects are not clearly observed in the sample with the highest Cu content, which is probably due to an abrupt increase in Cu size beyond a few hundred nanometers and possibly impurities present in this film.

The TiO_2 optical band gaps for our ALD-grown samples were determined using the Tauc plot method [70]. The results are shown in Fig. S10 in the Supporting material. Pure TiO_2 has an optical band gap (E_g) of 3.31 eV, which is close in value with the previous studies on TiO_2 anatase thin films [51,52,70]. The film with the lowest Cu content (TiO_2-Cu25) shows a similar band gap value as the pristine sample. However, the band gap decreases significantly for the TiO_2-Cu75 (E_g =3.19 eV) and TiO_2-Cu200 (E_g =3.05 eV) samples, which is most likely due to the overlap of the absorption of TiO_2 and the LSPR peaks of Cu.

Our SEM and TEM measurements show that metallic Cu is present in the ALD-grown composite films in the form of NPs that are well dispersed in the TiO_2 matrix. The source of copper in our syntheses was $Cu(OAc)_2$ which was heated at 190 °C under vacuum conditions, and the evaporation products were transferred into the deposition chamber (heated to 250 °C) with N_2 carrier gas. The formation of metallic Cu in ALD deposition using $Cu(OAc)_2$ and H_2O as precursors seems somewhat counterintuitive, as in most cases reducing co-reactants are needed in addition to the source of metal atoms to deposit pure metals. The previous studies show that the thermal characteristics of $Cu(OAc)_2$ can be quite complex. At annealing temperatures above 150 °C under oxygen-free conditions, the Cu^{2+} ions in $Cu(OAc)_2$ are reduced to lower oxidation states and the various cluster molecules in the gas phase can be formed [71]. When $Cu(OAc)_2$ is heated to below 200 °C, copper(I) acetate (CuOAc) gas was found to be the main product of $Cu(OAc)_2$ evaporation, which was used for the ALD synthesis of Cu_2O thin films [72]. However, in the same study, it was found that the metallic Cu films were formed for the deposition temperatures above 240 °C when Cu $(OAc)_2$ and H_2O were used as precursors, which was ascribed to the thermal decomposition of CuOAc.

On the other hand, $Cu(OAc)_2$ annealed at 150 °C was successfully employed to prepare Cu metal clusters, which were used as a catalyst for the chemical vapor deposition of graphene layers on quartz substrates [73,74]. In addition, our recent work on thin ZnO-Cu films has shown that metallic Cu can be generated during the prolonged evaporation of $Cu(OAc)_2$ at a temperature of 180 °C [52]. In this study, we used a low number of ALD cycles (25-200) for the pulses of $Cu(OAc)_2$ precursor between TiO_2 deposition, which cannot lead to the layer-by-layer growth of Cu structures with sizes up to 100 nm or more, since the growth rate for the ALD depositions with $Cu(OAc)_2$ is about 0.12 Å per cycle [72]. Therefore, based on the previous studies, we argue that Cu clusters and NPs were formed either directly during thermal evaporation of $Cu(OAc)_2$ and deposited on the substrate during ALD growth of TiO_2, or by thermal decomposition of CuOAc in the deposition chamber. As the experimental data show, the employed deposition conditions led to the growth of TiO_2-Cu composites with Cu NPs incorporated into anatase TiO_2 matrices.

3.3. *Photocatalytic activity*

Fig. 8a shows the photocatalytic degradation of MB (determined by measuring the change in intensity of the characteristic MB absorption peak at 664 nm) under simulated solar irradiation for pure TiO_2 and TiO_2-Cu composites. Pure TiO_2 degraded about 75 % of MB in 7 hours (Fig. 8a), driven by UV absorption as TiO_2 didn't absorb in the visible region (see Fig. 7). TiO_2-Cu25 had the highest photocatalytic efficiency, degrading ~95 % of MB. The efficiency decreased with increasing Cu content, however, TiO_2-Cu75 still outperformed pure TiO_2 with 88 % of MB degradation. TiO_2-Cu200 showed the lowest activity of all ALD-grown samples. Photocatalytic measurements performed using only the aqueous MB solution without ALD-grown films (referred to as "blank" in Fig. 8a) show that about 20 % of the MB is degraded even without photocatalyst, indicating that some degree of photolysis or self-sensitization of the MB dye [75] occurs under illumination with the 300 W solar simulating lamp.

While first-order kinetics often describe TiO_2-based photodegradation of azo dyes [26,27,33–35,51], our data are poorly fitted with a single rate constant (see Fig. S11). Instead, a two phase model, each with first-order kinetics and distinct rate constants, better describes our results (Fig. 8b). This figure shows $ln\ (C_t / C_0)$ vs. time, divided into two linear regions, representing two degradation phases of MB. The MB concentration change is described by:

$$C_t = C_0 e^{-k_1 t}, \text{ for } t < \tau,$$

$$C_t = C_\tau e^{-k_2 (t-\tau)}, \text{ for } t > \tau,$$

where τ is duration of the first phase (3 hours), C_τ is the concentration of the MB solution at τ, and k_1 and k_2 are the rate constants for the first and second phases, respectively. The rate constants (see Fig. S12) were derived from the linear fits of the $\ln (C_t / C_0)$ versus time plots: $k_1 = 0.15h^{-1}$ and $k_2 = 0.24h^{-1}$ (TiO_2), $k_1 = 0.28h^{-1}$ and $k_2 = 0.53h^{-1}$ (TiO_2-Cu25), $k_1 = 0.24h^{-1}$ and $k_2 = 0.33h^{-1}$ (TiO_2-Cu75), $k_1 = 0.09h^{-1}$ and $k_2 = 0.12h^{-1}$ (TiO_2-Cu200). For all but TiO_2-Cu200, k_2 is significantly larger than k_1, indicating faster degradation in the second phase. TiO_2-Cu200 exhibited similar k_1 and k_2 values, reflecting its lower photocatalytic efficiency.

The occurrence of two different phases in the photodegradation of Rhodamine-B was observed on Ag NP-decorated TiO_2 [76]. This could be due to: 1) dye concentration effects, where higher initial concentrations slow down the photodegradation process [77,78]. This is explained by the increased competitive surface adsorption of dye molecules leading to a reduced formation of hydroxyl radicals [78]. Indeed, we observe a 40-60 % MB reduction with TiO_2, TiO_2-Cu25 and TiO_2-Cu75 in the first 3 hours of the photocatalytic process. Hence, the concentration of MB is significantly reduced in the second stage of the photodegradation, which leads to higher rate constants; 2) MB degradation occurring in multiple steps, with intermediates influencing the two phases of the photodegradation. The MB decomposition pathway involves initial conversion of MB to intermediates, followed by secondary degradation into smaller compounds, and finally, degradation of colored intermediates [79]. As shown in Fig. S13, a blue shift in the MB absorption peak (664 nm to 635 nm) occurs, indicating the formation of by-products such as Azure A, Azure B, Azure C and Thionine via demethylation [80]. The shift is more pronounced in the second phase, especially for TiO_2-Cu25, suggesting that both reduced dye concentration and by-product formation contribute to a faster second-phase photodegradation.

In addition to monitoring the degradation of MB through

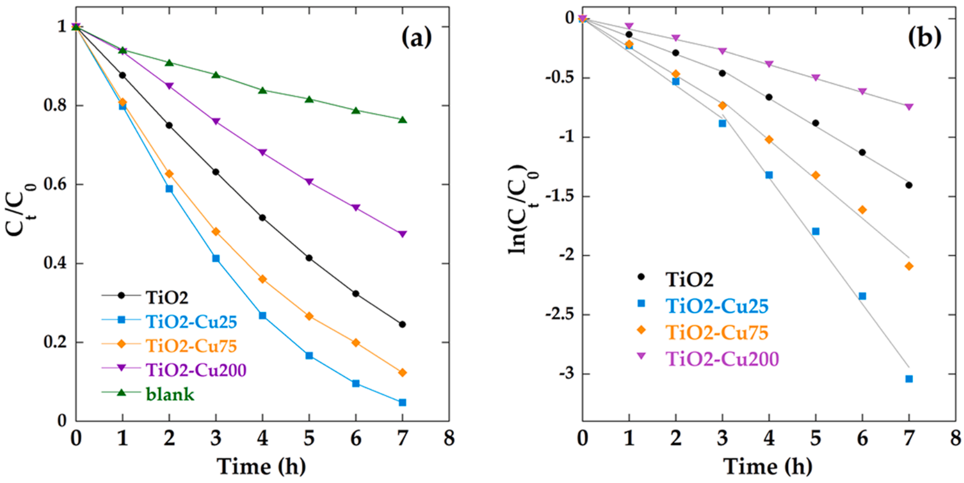

Fig. 8. a) Photocatalytic degradation of MB in aqueous solution under simulated solar irradiation for pure TiO_2 and TiO_2-Cu composite films. Solid lines are drawn as a guide for the eye. b) Plot of $\ln (C_t / C_0)$ as function of the irradiation time. Solid lines are linear fits of the data for two degradation phases of MB: $0 < t < 3h$ and $3h < t < 7h$.

decolorization, measured by observing the change in intensity of the characteristic MB absorption peak at 664 nm (Fig. 8 and Fig. S13), we also monitored the mineralization of MB under simulated sunlight by observing the decrease in intensity of the absorption peak at 292 nm. The results for the TiO_2-Cu25 film can be seen in Fig. S14 in the Supporting Material. As shown in Figs. S13 and S14, the characteristic peaks of MB appear at 246 nm, 292 nm and 664 nm, which correspond to the chromophore, N,S-substituted heterocyclic structure, benzene ring and dimethylamino group, respectively [81]. The intensity of all absorption peaks of MB is significantly reduced after 7 hours of exposure to simulated sunlight, indicating that almost complete mineralization and decolorization of MB is achieved.

In order to test the reusability and stability of the TiO_2-Cu25 sample, the photocatalytic degradation of MB was carried out three times under the same conditions (Fig. 9). The second and third run of the photocatalytic test showed very similar results to the first measurement, with MB degradation of about 93 % after 7 hours of simulated solar illumination, confirming the long-term stability and the possibility of multiple use for photocatalytic applications of our TiO_2-Cu composite films.

To further investigate the photocatalytic activity of our ALD-grown films, we performed measurements of the photocatalytic degradation of caffeine in an aqueous solution. In contrast to the dyes, the photocatalytic degradation of caffeine should not be influenced by dye-sensitizing effects. This can be seen from Fig. S15 in the Supporting material, as the “blank” measurement (i.e. the photocatalytic measurement carried out using only the aqueous caffeine solution without the photocatalyst) showed that the caffeine concentration only decreases insignificantly (~3 %) after 7 hours of exposure to the simulated solar light. On the other hand, as seen from Fig. S15, our ALD-grown films (TiO_2 and TiO_2-Cu25) are also very effective in caffeine degradation, and both films show a slightly increased photocatalytic rate constants compared to the second phase in the degradation of MB ($k(TiO_2)= 0.29$ h^{-1} and $k(TiO_2\text{-Cu25})= 0.56$ h^{-1}). Although the photocatalytic degradation of MB and caffeine has different kinetics (in contrast to MB, the degradation of caffeine can be well described by only one phase of degradation following the first-order kinetics), these results show that our ALD-grown films have high photocatalytic efficiency under simulated solar irradiation.

TiO_2 films with lower Cu NP concentrations exhibit a 1.5-fold (TiO_2-Cu75) and 2-fold (TiO_2-Cu25) enhanced photocatalytic activity compared to pure TiO_2. While direct comparisons with literature are challenging due to varying experimental setups (e.g. different light sources, type and concentrations of azo dyes or toxins, lateral dimensions of the photocatalyst, etc.), our ALD-grown TiO_2-Cu hybrids exhibit excellent performance. Compared to magnetron sputtered TiO_2-Cu films (1.5-fold increase in methyl orange degradation [50]), mesoporous TiO_2 with Cu NPs (rate constants of 0.26-0.63 h^{-1} for ciprofloxacin hydrochloride degradation [27]), and Cu-decorated TiO_2 nanotube arrays (70 % MB degradation in 4 h [34]), our TiO_2-Cu samples showed comparable or superior photocatalytic activity. Notably, our TiO_2-Cu NP composite films even outperform some TiO_2 composites with noble metals, such as PLD-grown TiO_2-Au (20 % MB degradation in 250 min [48]), Ag-decorated porous TiO_2 (60 % amoxicillin and 2, 4-diclorophenol degradation in 5 h [82]), and spin-coated TiO_2-Ag (rate constant ~0.4 h^{-1} for Rhodamine B [83]). These results highlight the potential of our ALD-grown TiO_2-Cu hybrids as a viable alternative to noble metal containing TiO_2 photocatalysts.

In most cases studied in the literature, photocatalytic TiO_2-Cu systems are in the form of CuNPs deposited on the surface of TiO_2NPs or powders [21–25]. Although such materials usually exhibit high photocatalytic activity due to their large surface area, the removal of the powders or NPs from the solutions or the aquatic environment generally poses a major problem for their practical application. Another approach often involves the surface decoration of TiO_2 nanostructures, such as nanotubes [30,34] or nanorods [28,33] with Cu NPs. However, the metallic Cu on the surface of the material can be susceptible to oxidation, which is why in many studies copper oxides, CuO and Cu_2O, are found to be present together with the metallic Cu in the synthesized photocatalysts [21–24,28,34] Also, the additional oxidation of Cu in the solutions or in the aquatic environment where the photocatalytic process takes place can lead to the poor reusability of the photocatalysts containing surface copper species. Although our ALD-grown TiO_2-Cu composite films cannot exhibit such high photocatalytic rates as the highly porous photocatalysts in the form of NPs or nanostructures, we have shown that the direct incorporation of Cu NPs into the TiO_2 matrix leads to the preservation of the Cu metal phase in the synthesized material (we recall that XRD, XPS and TEM analyses only show the presence of metallic Cu in our samples). Moreover, the robust nature of the photocatalyst in the form of thin film allows its reusability in the photocatalytic process (as demonstrated by the repeated measurements of the photocatalytic activity of the TiO_2-Cu25 sample presented in Fig. 9) as well as its easy use in aqueous solutions.

In addition to TiO_2-metal composite systems (used in this study in the form of TiO_2-Cu composite films), another widely used method to improve the photocatalytic properties of TiO_2 is the formation of semiconductor heterostructures consisting of TiO_2 and a semiconductor with a smaller bandgap. In this way, type I or II heterojunctions can be formed, which can enhance the optical absorption of pure TiO_2, improve

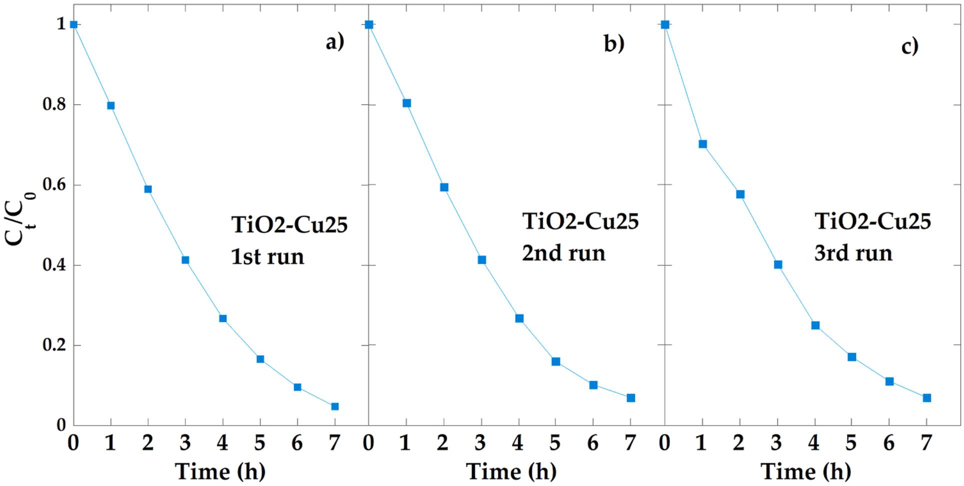

Fig. 9. Reusability test for the TiO_2-Cu25 film performed with three consecutive cycles of photocatalytic degradation of MB in aqueous solution under simulated solar light.

the photogeneration of electrons and holes and/or lead to a more efficient separation of charge carriers in the photocatalyst. Hence, numerous examples of TiO_2-based photocatalysts in various forms and synthesized by different techniques can be found in the literature, and each form of TiO_2 photocatalyst and each growth method has some advantages over the other types of materials or deposition methods. In this work, we opted for the photocatalyst in the form of thin TiO_2-metal (Cu) composite films. In addition to the well-known advantages of the ALD technique: high uniformity and conformality of the deposited material with a well-controlled thickness, this method allowed us to deposit Cu-NP NPs into the TiO_2 matrix during the growth of the material without additional post-deposition treatments. As the experimental results show, this led to the formation of TiO_2-Cu composites with a preserved metallic Cu phase after synthesis, which exhibited a twofold increase in sunlight-induced photocatalytic activity compared to pure TiO_2 material.

3.4. Photocurrent measurements and mechanism of charge transfer in TiO_2-Cu composites

To explain the activity of our samples, we recall that XRD and XPS showed significantly reduced anatase TiO_2 phase in TiO_2-Cu200 sample and high metallic Cu and Cu impurity content, explaining its lower photocatalytic activity compared to pure TiO_2. Conversely, anatase TiO_2 phase is well preserved in TiO_2-Cu25 and TiO_2-Cu75 films, while, at same time, these samples can absorb visible light due to the presence of Cu NPs, which enhances their photocatalytic activity in comparison to pristine film. Despite stronger absorption in the visible region and lower TiO_2 optical band gap, TiO_2-Cu75's activity is lower than TiO_2-Cu25's. On the other hand, our chemical and structural analyses show no major differences between these samples. XPS analysis around O 1s core levels (see Fig. S4) imply a slightly higher content of surface O-related defects (OH groups or vacancies) in TiO_2-Cu75 film, which could influence its photocatalytic properties, while, according to XRD measurements, intensities of TiO_2-related peaks in TiO_2-Cu75 are slightly reduced than in TiO_2-Cu25, indicating potential crystallinity loss, that would reduce its photocatalytic efficiency.

To further investigate the behavior of our ALD-grown films under simulated sunlight, we analyzed the temporal variations of the photocurrents measured on TiO_2-Cu samples during three on-off irradiation cycles (Fig. 10). Photocurrent measurements exhibit a sharp current increase under simulated sunlight irradiation for TiO_2-Cu25 and TiO_2-Cu75, but not for pure TiO_2 (with its current below the detection limit, Fig. S16). Notably, TiO_2-Cu25's photocurrent is an order of magnitude higher than TiO_2-Cu75's, consistent with our photocatalytic results.

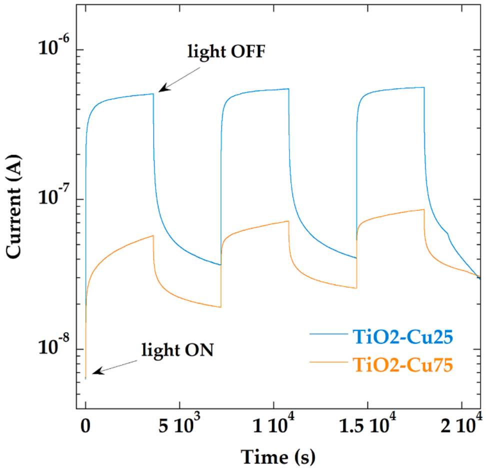

Fig. 10. Temporal variation of photocurrents on TiO_2-Cu25 and TiO_2-Cu75 samples during three on-off light-irradiation cycles using simulating solar lamp.

Fitting the transient photocurrent curves in Fig. 10 (for the second on-off cycle) with second-order exponential equations (see Fig. S17 and Tables S2 and S3) [84,85] yielded steady-state currents: 5.1 10^{-7} A (light) and 3.9 10^{-8} A (dark) for TiO_2-Cu25, and 7.8 10^{-8} A (light) and 2.5 10^{-8} A (dark) for TiO_2-Cu75. The relaxation time constants of 50-3000 s suggest slow charge carrier dynamics, consistent with prior reports on Au NP decorated TiO_2 nanosheets [86].

The higher photocurrent in TiO_2-Cu25 implies more photogenerated electrons, originating from Cu NPs (since pure TiO_2 showed no photocurrent). This suggests that “hot electron” transfer occurs from plasmon-excited Cu NPs to the CB of TiO_2, which, in turn, leads to the higher concentration of charge carriers in TiO_2 available for the photocatalytic degradation processes. As shown in previous studies regarding TiO_2 nanostructures impregnated with different metal NPs such as Pt, Au or Ag [87–90], the height of the Schottky barrier (Φ_{SB}) at the metal/TiO_2 interface is a crucial factor with lower Schottky barriers facilitating higher electron transfer rates. Experimental studies show that the Schottky barrier is generally reduced at the nanoscale metal-semiconductor junction, i.e. the height of the Schottky barrier decreases with the size of the metal-semiconductor interface [44,91]. This means that for composites consisting of metal NPs embedded in the semiconductor matrix, the smaller NPs should produce lower Schottky barriers. For example, the Schottky barrier height was found to increase linearly with the diameter of the metal NPs in Au-decorated TiO_2 nanotubes [92] and MoO_3 thin films coated with Au NPs [93]. The origin of this variation of the Schottky barrier with NP size is generally explained in terms of the increased probability of electron tunneling due to the smaller dimensions of the metal-semiconductor contact [91] or the increased local electric field as the nanoscale metal-semiconductor interface affects the potential distribution at the metal-semiconductor contact [91,92].

Therefore, in our study, the larger average size of Cu NPs in TiO_2-Cu75 (around 80 nm) compared to TiO_2-Cu25 (where Cu NPs exhibit the size of about 50 nm), as observed by electron microscopy, should result in a higher Schottky barrier at the Cu/TiO_2 interface, hindering the charge transfer between Cu metal nanoparticles and TiO_2 photocatalyst (see Fig. 11). Indeed, XPS measurements around VB states of our ALD-grown samples (presented in Fig. 2) show that the energy of TiO_2 VB maximum, with respect to the Fermi energy level, changes from 2.19 eV in pure TiO_2 to 1.78 eV and 1.45 eV in TiO_2-Cu25 and TiO_2-Cu75 samples, respectively (see Fig. S18 in the Supporting material). The observed shift toward lower binding energies in the position of TiO_2 VB maximum is related to the charge transfer and formation of Schottky barrier at the junction between TiO_2 and Cu particles [87,88,94]. Based on our XPS analysis, the height of the Schottky barrier (Φ_{SB}) is equal to 0.41 eV for TiO_2-Cu25 film, while the value of the Schottky barrier increases to 0.57 eV in TiO_2-Cu75 sample [87,88]. The study on the TiO_2 nanotubes decorated with Au has determined the values for Φ_{SB} in the interval of (0.52 – 0.81) eV for the Au NPs with the sizes in the range of (20-80) nm [92], while the Au NPs with a diameter of about 10 nm on TiO_2 nanocrystals have produced the Schottky barrier of 0.43 eV [89]. On the other hand, Au and Pt NPs with diameters below 10 nm impregnated on the surfaces of TiO_2 nanostructures resulted in the Schottky barriers in the range of (0.15-0.5) eV [87,88]. These results show a slightly higher value for Φ_{SB} in the case of Au- or Pt-TiO_2 systems with the metal NPs of smaller or about the same diameter as Cu NPs in our TiO_2-Cu composite films. This is probably the result of the higher value of the metal work function (Φ_M) for Au and Pt compared to Cu, since according to the Mott-Schottky model, the height of the Schottky barrier should be proportional to the factor ($\Phi_M - \chi$), where $\chi$is the electron affinity of TiO_2 [87]. Therefore, our results show that in addition to more expensive noble metals such as Au or Pt, copper (a more abundant and less expensive material) can also be used to efficiently adjust the height of the Schottky barrier between metal NP and TiO_2.

Hence, for our ALD-grown TiO_2-Cu samples, the “hot electrons” in TiO_2-Cu75 sample have to overcome the larger barrier at the Cu/TiO_2

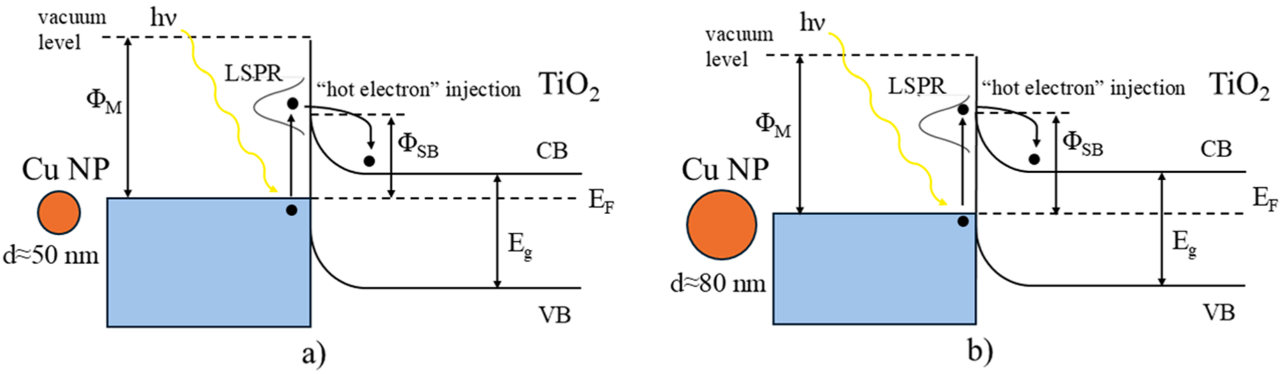

Fig. 11. Schematic diagram of energy band structure at the TiO_2/Cu NP interface and "hot electron" transfer from Cu NP to TiO_2 for two sizes of Cu NPs.

interface compared to TiO_2-Cu25 film, which leads to the lower injection of electrons in TiO_2 photocatalyst (as observed from our photocurrent measurements), and, in turn, lower photocatalytic activity in comparison to TiO_2-Cu25 film.

4. Conclusion

We investigated the structural, chemical, optical and photocatalytic properties of ALD-grown TiO_2 thin films with embedded Cu NPs. The size and amount of Cu NPs were controlled by the number of $Cu(OAc)_2$ ALD precursor pulses. XRD, XPS and Raman confirmed anatase TiO_2 in all samples with metallic Cu in the composites. Increasing the Cu content gradually replaced the TiO_2 phase with metallic Cu.

SEM and TEM revealed varying Cu NPs sizes and concentrations within the TiO_2 matrices. TiO_2-Cu25 exhibited Cu NPs of tens of nanometers, while TiO_2-Cu75's NPs averaged ~80 nm. The Cu particles in the film with the highest Cu content (TiO_2-Cu200) were larger than 200 nm and degraded the crystallinity of TiO_2. All TiO_2-Cu composite films showed strong visible light absorption, with TiO_2-Cu25 and TiO_2-Cu75 exhibiting LSPR peaks.

Photodegradation of MB under simulated sunlight showed 2-fold (TiO_2-Cu25) and 1.5-fold (TiO_2-Cu75) increase in photocatalytic activity over pure TiO_2. TiO_2-Cu200 showed the weakest photocatalytic activity due to the high Cu content and low TiO_2 crystallinity. Conductivity measurements under simulated sunlight showed an order of magnitude higher photocurrent in TiO_2-Cu25 than TiO_2-Cu75. while pure TiO_2 showed no measurable photocurrent. Thus, enhanced photocatalysis in TiO_2-Cu25 and TiO_2-Cu75 can be attributed to an increased electron transfer from the Cu NPs to TiO_2. The smaller Cu NPs in TiO_2-Cu25 result in a lower Schottky barrier at the Cu/TiO_2 interface, leading to more efficient electron transfer and higher photocatalytic activity.

CRediT authorship contribution statement

Ivana Jelovica Badovinac: Writing – review & editing, Writing – original draft, Visualization, Investigation, Formal analysis, Data curation. **Ivna Kavre Piltaver:** Writing – review & editing, Resources, Data curation. **Lucija Črep:** Writing – review & editing, Formal analysis, Data curation. **Daria Jardas Babić:** Writing – review & editing, Formal analysis, Data curation. **Iva Šarić Janković:** Writing – review & editing, Formal analysis, Data curation. **Karlo Veličan:** Writing – review & editing, Formal analysis, Data curation. **Krešimir Salamon:** Writing – review & editing, Formal analysis. **Martina Kocijan:** Writing – review & editing, Formal analysis, Data curation. **Matejka Podlogar:** Writing – review & editing, Formal analysis, Data curation. **Nik Gračanin:** Formal analysis, Data curation. **Jasmina Lazarević:** Writing – review & editing, Formal analysis, Data curation. **Mato Knez:** Writing – review & editing, Resources, Methodology. **Robert Peter:** Writing – review & editing, Writing – original draft, Resources, Methodology, Investigation, Formal analysis, Data curation, Conceptualization.

Declaration of competing interest

The authors declare that they have no known competing financial interests or personal relationships that could have appeared to influence the work reported in this paper.

Acknowledgements

The study has been funded by the project NPOO.C3.2.R2-I1.06.0083 supported by the European Union NextGenerationEU and projects under numbers 23-190 and 23-4 supported by the University of Rijeka. The financial support of the Slovenian Research and Innovation Agency is gratefully acknowledged (Project No. L2-1830, Bilateral project No. BI-HR/20-21-003 and Program No. P2-0084). We acknowledge the access to research equipment via ARIS Program No. P1-0417 and Center for electron microscopy and microanalysis (CEMM) at IJS. We would like to thank Nenad Lazarević and Ana Milosavljević for their help with Raman measurements.

Supplementary materials

Supplementary material associated with this article can be found, in the online version, at doi:10.1016/j.surfin.2025.107570.

Data availability

Data will be made available on request.

References

[1] Q. Guo, C. Zhou, Z. Ma, X. Yang, Fundamentals of TiO2 photocatalysis: concepts, mechanisms, and challenges, Adv. Mater. 31 (2019) 1901997, https://doi.org/10.1002/adma.201901997.
[2] C. Karthikeyan, P. Arunachalam, K. Ramachandran, A.M. Al-Mayouf, S. Karuppuchamy, Recent advances in semiconductor metal oxides with enhanced methods for solar photocatalytic applications, J. Alloys Compd. 828 (2020) 154281, https://doi.org/10.1016/j.jallcom.2020.154281.
[3] F. Tanos, A. Razzouk, G. Lesage, M. Cretin, M. Bechelany, A comprehensive review on modification of titanium dioxide-based catalysts in advanced oxidation processes for water treatment, ChemSusChem 17 (2024) e202301139, https://doi.org/10.1002/cssc.202301139.
[4] S. Sharma, R. Kumar, P. Raizada, T. Ahamad, S.M. Alshehri, V.-H. Nguyen, S. Thakur, C.C. Nguyen, S.Y. Kim, Q. Van Le. P. Singh, An overview on recent progress in photocatalytic air purification: Metal-based and metal-free photocatalysis, Environ. Res. 214 (2022) 113995, https://doi.org/10.1016/j.envres.2022.113995.
[5] C. Ros, T. Andreu, J.R. Morante, Photoelectrochemical water splitting: a road from stable metal oxides to protected thin film solar cells, J. Mater. Chem. A 8 (2020) 10625, https://doi.org/10.1039/D0TA02755C.
[6] Z. Yuan, X. Zhu, X. Gao, C. An, Z. Wang, C. Zuo, D.D. Dionysiou, H. He, Z. Jiang, Enhancing photocatalytic CO2 reduction with TiO2-based materials: Strategies, mechanisms, challenges, and perspectives, Environ. Sci. Ecotechnol. 20 (2024) 100368, https://doi.org/10.1016/j.ese.2023.100368.

[7] A. Seifi, D. Salari, A. Khataee, B. Çosut, L.C. Arslan, A. Niaei, Enhanced photocatalytic activity of highly transparent superhydrophilic doped TiO2 thin films for improving the self-cleaning property of solar panel covers, Ceram. Int. 49 (2023) 1678–1689, https://doi.org/10.1016/j.ceramint.2022.09.130.

[8] A. Kumar, P. Choudhary, A. Kumar, P.H.C. Camargo, V. Krishnan, Recent advances in plasmonic photocatalysis based on TiO2 and noble metal nanoparticles for energy conversion, environmental remediation, and organic synthesis, Small 18 (2022) 2101638, https://doi.org/10.1002/smll.202101638.

[9] L. Gomathi Devi, R. Kavitha, A review on plasmonic metal–TiO2 composite for generation, trapping, storing and dynamic vectorial transfer of photogenerated electrons across the Schottky junction in a photocatalytic system, Appl. Surf. Sci. 360 (2016) 601–622, https://doi.org/10.1016/j.apsusc.2015.11.016.

[10] X. Zhang, Y.L. Chen, R.-S. Liu, D.P. Tsai, Plasmonic photocatalysis, Rep. Prog. Phys. 76 (2013) 046401, https://doi.org/10.1088/0034-4885/76/4/046401.

[11] J. Liu, M. Xu, T. Zhang, X. Chu, K. Shi, J. Li, Al/TiO2 composite as a photocatalyst for the degradation of organic pollutants, Environ. Sci. Pollut. Res. 30 (2023) 9738–9748, https://doi.org/10.1007/s11356-022-22861-9.

[12] A. Bayles, S. Tian, J. Zhou, L. Yuan, Y. Yuan, C.R. Jacobson, C. Farr, M. Zhang, D. F. Swearer, D. Solti, M. Lou, H.O. Everitt, P. Nordlander, N.J. Halas, Al@TiO2 core−shell nanoparticles for plasmonic photocatalysis, ACS Nano 16 (2022) 5839–5850, https://doi.org/10.1021/acsnano.1c10995.

[13] S. He, J. Huang, J.L. Goodsell, A. Angerhofer, W.D. Wei, Plasmonic nickel–TiO2 heterostructures for visible-light-driven photochemical reactions, Angew. Chem. 58 (2019) 1–5, https://doi.org/10.1002/anie.201901987.

[14] P.A. DeSario, J.J. Pietron, T H Brintlinger, M. McEntee, J.F. Parker, O. Baturina, R. M. Stroud, D.R. Rolison, Oxidation-stable plasmonic copper nanoparticles in photocatalytic TiO2 nanoarchitectures, Nanoscale 9 (2017) 11720–11729, https://doi.org/10.1039/C7NR04805J.

[15] F. Yu, L. Chen, X. Li, X. Shen, H. Zhao, C. Duan, Q. Chen, Cu nanocluster-loaded TiO2 nanosheets for highly efficient generation of CO-free hydrogen by selective photocatalytic dehydrogenation of methanol to formaldehyde, ACS Appl. Mater. Interfaces 13 (2021) 18619–18626, https://doi.org/10.1021/acsami.0c20116.

[16] Z. Zhao, W. Zhang, X. Lv, Y. Sun, F. Dong, Y. Zhang, Noble metal-free Bi nanoparticles supported on TiO2 with plasmon-enhanced visible light photocatalytic air purification, Environ. Sci.: Nano 3 (2016) 1306–1317, https://doi.org/10.1039/C6EN00341A.

[17] T. Zhang, J. Low, Xi. Huang, J.F. AI-Sharab, J. Yu, T. Asefa, Copper-decorated microsized nanoporous TiO2 for CO2 reduction by H2O, ChemCatChem 9 (2017) 3054–3062, https://doi.org/10.1002/cctc.201700512.

[18] L. Wang, M.H. Kafshgari, M. Meunier, Optical properties and applications of plasmonic-metal nanoparticles, Adv. Funct. Mater. 30 (2020) 2005400.

[19] J. Xiong, M. Zhang, M. Lu, K. Zhao, C. Han, G. Cheng, Z. Wen, Achieving simultaneous Cu particles anchoring in meso-porous TiO 2 nanofabrication for enhancing photo-catalytic CO2 reduction through rapid charge separation, Chin. Chem. Lett. 33 (2022) 1313–1316, https://doi.org/10.1016/j.cclet.2021.07.052.

[20] E. Liu, L. Qi, J. Bian, Y. Chen, X. Hub, J. Fan, H. Liu, C. Zhu, Q. Wang, A facile strategy to fabricate plasmonic Cu modified TiO2 nano-flower films for photocatalytic reduction of CO2 to methanol, Mater. Res. Bull. 68 (2015) 203–209, https://doi.org/10.1016/j.materresbull.2015.03.064.

[21] G. Cheng, M. Zhang, C. Han, Y. Liang, K. Zhao, Achieving solar-to-hydrogen evolution promotion using TiO2 nanoparticles and an unanchored Cu co-catalyst, Mater. Res. Bull. 129 (2020) 110891, https://doi.org/10.1016/j.materresbull.2020.110891.

[22] F. Platero, A. Caballero, G. Colon, Tuning the co-catalyst loading for the optimization of thermo-photocatalytic hydrogen production over Cu/TiO$_2$, Appl. Catal. A: Gen. 643 (2022) 118804, https://doi.org/10.1016/j.apcata.2022.118804.

[23] J. Nie, A.O.T. Patrocinio, S. Hamid, F. Sieland, J. Sann, S. Xia, D.W. Bahnemann, J. Schneider, New insights into the plasmonic enhancement for photocatalytic H2 production by Cu–TiO2 upon visible light illumination, Phys. Chem. Chem. Phys. 20 (2018) 5264–5273, https://doi.org/10.1039/C7CP07762A.

[24] L. Diaz, V.D. Rodríguez, M. González-Rodríguez, E. Rodríguez-Castellón, M. Algarra, P. Núñez, E. Morettie, M/TiO2 (M = Fe, Co, Ni, Cu, Zn) catalysts for photocatalytic hydrogen production under UV and visible light irradiation, Inorg. Chem. Front. 8 (2021) 3491–3500, https://doi.org/10.1039/D0QI01311K.

[25] H. Tian, X.L. Zhang, J. Scott, C. Ng, R. Amal, TiO2-supported copper nanoparticles prepared via ion exchange for photocatalytic hydrogen production, J. Mater. Chem. A 2 (2014) 6432–6438, https://doi.org/10.1039/C3TA15254E.

[26] R. Kaur, B. Pal, Cu nanostructures of various shapes and sizes as superior catalysts for nitroaromatic reduction and co-catalyst for Cu-TiO2 photocatalysis, Appl. Catal. A: Gen. 491 (2015) 28–36, https://doi.org/10.1016/j.apcata.2014.10.035.

[27] Y. Gan, M. Zhang, J. Xiong, J. Zhu, W. Li, C. Zhang, G. Cheng, Impact of Cu particles on adsorption and photocatalytic capability of mesoporous Cu@TiO2 hybrid towards ciprofloxacin antibiotic removal, J. Taiwan Inst. Chem. Eng. 96 (2019) 229–242, https://doi.org/10.1016/j.jtice.2018.11.015.

[28] L.-F. Chiang, R.-an Doong, Cu–TiO2 nanorods with enhanced ultraviolet- and visible-light photoactivity for bisphenol A degradation, J. Hazard. Mater. 277 (2014) 84–92, https://doi.org/10.1016/j.jhazmat.2014.01.047.

[29] N. Rojas, G. Hincapie-Trivino, M. Velasquez, Photocatalytic oxidation of glycerol using x/TiO2 (with x= Cu, Ag, and Cu-Ag) to dihydroxyacetone and other value-added products, Mol. Catal. 566 (2024) 114390, https://doi.org/10.1016/j.mcat.2024.114390.

[30] S. Zhang, B. Peng, S. Yang, H. Wang, H. Yu, Y. Fang, F. Peng, Non-noble metal copper nanoparticles-decorated TiO2 nanotube arrays with plasmon-enhanced photocatalytic hydrogen evolution under visible light, Int. J. Hydrogen Energy 40 (2015) 303–310, https://doi.org/10.1016/j.ijhydene.2014.10.122.

[31] S. Hejazi, S. Mohajernia, Y. Wu, P. Andryskova, G. Zoppellaro, I. Hwang, O. Tomanec, R. Zboril, P. Schmuki, Intrinsic Cu nanoparticle decoration of TiO2 nanotubes: A platform for efficient noble metal free photocatalytic H2 production, Electrochem. Commun. 98 (2019) 82–86, https://doi.org/10.1016/j.elecom.2018.11.020.

[32] J. Zhu, J. Xiong, G. Cheng, W. Li, S. Dou, Promoting solar-to-hydrogen evolution on Schottky interface with mesoporous TiO2-Cu hybrid nanostructures, J. Colloid Interface Sci. 545 (2019) 116–127, https://doi.org/10.1016/j.jcis.2019.03.007.

[33] H. Guan, X. Zhou, W. Wen, B. Jin, J. Li, S. Zhang, Efficient and Robust Cu/TiO2 Nanorod Photocatalysts for Simultaneous Removal of Cr(VI) and Methylene Blue under Solar Light, J. Chin. Chem. Soc. 65 (2018) 706–713, https://doi.org/10.1002/jccs.201700337.

[34] J. Dong, J. Ye, D. Ariyanti, Y. Wang, S. Wei, W. Gao, Enhancing photocatalytic activities of titanium dioxide via well-dispersed copper nanoparticles, Chemosphere 204 (2018) 193–201, https://doi.org/10.1016/j.chemosphere.2018.04.012.

[35] S. Zhai, X. Yang, M. Tang, W. Gu, F. Teng, Facile synthesis of Cu quantum dots-TiO2 nanosheets Schottky junction and improved photocatalytic degradation activity, ChemistrySelect 5 (2020) 5693–5700, https://doi.org/10.1002/slct.202000377.

[36] M. Scarisoreanu, A.G. Iliea, E. Goncearenco, A.M. Banici, I.P. Morjana, E. Dutu, E. Tanasa, I. Fort, M. Stan, C.N. Mihailescu, C. Fleaca, Ag, Au and Pt decorated TiO2 biocompatible nanospheres for UV & vis photocatalytic water treatment, Appl. Surf. Sci. 509 (2020) 145217, https://doi.org/10.1016/j.apsusc.2019.145217.

[37] T. Fazliev, D. Polskikh, D. Selishchev, Photocatalytic production of H2O2 over rutile TiO2 supported with Pd nanoparticles, Appl. Surf. Sci. 686 (2025) 162124, https://doi.org/10.1016/j.apsusc.2019.145217.

[38] T. Montini, V. Gombac, L. Sordelli, J.J. Delgado, X. Chen, G. Adami, P. Fornasiero, Nanostructured Cu/TiO2 photocatalysts for H2 production from ethanol and glycerol aqueous solutions, ChemCatChem 3 (2011) 574–577, https://doi.org/10.1002/cctc.201000289.

[39] J.M. Kum, Y.J. Park, H.J. Kim, S.O. Cho, Plasmon-enhanced photocatalytic hydrogen production over visible-light responsive Cu/TiO2, Nanotechnology 26 (2015) 125402, https://doi.org/10.1088/0957-4484/26/12/125402.

[40] H. Peeters, M. Keulemans, G. Nuyts, F. Vanmeert, C. Li, M. Minjauw, C. Detavernier, S. Bals, S. Lenaerts, S.W. Verbruggen, Plasmonic gold-embedded TiO2 thin films as photocatalytic self-cleaning coatings, Appl. Catal. B: Environ. 267 (2020) 118654, https://doi.org/10.1016/j.apcatb.2020.118654.

[41] S. Chen, X. Li, W. Zhou, S. Zhang, Y. Fang, Carbon-coated Cu-TiO$_2$ nanocomposite with enhanced photostability and photocatalytic activity, Appl. Surf. Sci. 466 (2019) 254–261, https://doi.org/10.1016/j.apsusc.2018.10.036.

[42] T. Yamaguchi, E. Kazuma, N. Sakai, T. Tatsuma, Photoelectrochemical responses from polymer-coated plasmonic copper nanoparticles on TiO$_2$, Chem. Lett. 41 (2012) 1340–1342, https://doi.org/10.1246/cl.2012.1340.

[43] B. Babu, K. Mallikarjuna, C.Venkata Reddy, J. Park, Facile synthesis of Cu@TiO2 core shell nanowires for efficient photocatalysis, Mater. Lett. 176 (2016) 265–269, https://doi.org/10.1016/j.matlet.2016.04.146.

[44] I. Mondal, S. Gonuguntla, U. Pal, Photoinduced fabrication of Cu/TiO$_2$ core−shell heterostructures derived from Cu-MOF for solar hydrogen generation: The size of the Cu nanoparticle matters, J. Phys. Chem. C 123 (2019) 26073–26081, https://doi.org/10.1021/acs.jpcc.9b07171.

[45] W. Hao, L. Zhao, X. Li, L. Qin, S. Han, S.-Z. Kang, Cu nanoclusters incorporated mesoporous TiO2 nanoparticles: An efficient and stable noble metal free photocatalyst for light driven H2 generation, Int. J. Hydrogen Energy 46 (2021) 6461–6473, https://doi.org/10.1016/j.ijhydene.2020.11.146.

[46] Z. Zhan, J. An, H. Zhang, R.V. Hansen, L. Zheng, Three-dimensional plasmonic photoanodes based on Au-embedded TiO2 structures for enhanced visible-light water splitting, ACS Appl. Mater. Interfaces 6 (2014) 1139–1144, https://doi.org/10.1021/am404738a.

[47] J. Xu, Y. Liu, Y. Zhao, Effect of Ag loading position on the photocatalytic performance of TiO2 nanocolumn arrays, Beilstein J. Nanotechnol. 11 (2020) 717–728, https://doi.org/10.3762/bjnano.11.59.

[48] R.S. Pedanekar, S.K. Shaikh, K.Y. Rajpure, Thin film photocatalysis for environmental remediation: a status review, Curr. Appl. Phys. 20 (2020) 931–952, https://doi.org/10.1016/j.cap.2020.04.006.

[49] S. Misra, L. Li, J. Jian, J. Huang, X. Wang, D. Zemlyanov, J. Jang, F.H. Ribeiro, H. Wang, Tailorable Au nanoparticles embedded in epitaxial TiO$_2$ thin films for tunable optical properties, ACS Appl. Mater. Interfaces 10 (2018) 32895–32902, https://doi.org/10.1021/acsami.8b12210.

[50] Z. Zhao, J. Sun, G. Zhang, L. Bai, The study of microstructure, optical and photocatalytic properties of nanoparticles (NPs)-Cu/TiO$_2$ films deposited by magnetron sputtering, J. Alloys Compd. 652 (2015) 307–312, https://doi.org/10.1016/j.jallcom.2015.08.117.

[51] I. Jelovica Badovinac, R. Peter, A. Omerzu, K. Salamon, I. Šarić, A. Samaržija, M. Perčić, I. Kavre Piltaver, G. Ambrožić, M. Petravić, Grain size effect on photocatalytic activity of TiO$_2$ thin films grown by atomic layer deposition, Thin Solid Films 709 (2020) 138215, https://doi.org/10.1016/j.tsf.2020.138215.

[52] A. Jolivet, C. Labbe, C. Frilay, O. Debieu, P. Marie, B. Horcholle, F. Lemarie, X. Portier, C. Grygiel, S. Duprey, W. Jadwisienczak, D. Ingram, M. Upadhyay, A. David, A. Fouchet, U. Lüders, J. Cardin, Structural, optical, and electrical properties of TiO2 thin films deposited by ALD: Impact of the substrate, the deposited thickness and the deposition temperature, Appl. Surf. Sci. 608 (2023) 155214, https://doi.org/10.1016/j.apsusc.2022.155214.

[53] R. Peter, A. Omerzu, I. Kavre Piltaver, R. Speranza, K. Salamon, M. Podlogar, K. Veličan, M. Perčić, M. Petravić, Large enhancement of visible light

photocatalytic efficiency of ZnO films doped in-situ by copper during atomic layer deposition growth, Ceram. Int. 49 (2023) 35229–35238, https://doi.org/10.1016/j.ceramint.2023.08.196.
[54] M. Motola, L.Hromadko R.Zazpe, J. Prikryl, V. Cicmancova, J. Rodriguez-Pereira, H. Sopha, J.M. Macak, Anodic TiO2 nanotube walls reconstructed: Inner wall replaced by ALD TiO2 coating, Appl. Surf. Sci. 549 (2021) 149306, https://doi.org/10.1016/j.apsusc.2021.149306.
[55] I.Kavre Piltaver, R. Peter, I. Šarić, K. Salamon, I.Jelovica Badovinac, K. Koshmak, S. Nannarone, I. Delač Marion, M. Petravić, Controlling the grain size of polycrystalline TiO_2 films grown by atomic layer deposition, Appl. Surf. Sci. 419 (2017) 564–572, https://doi.org/10.1016/j.apsusc.2017.04.146.
[56] M.C. Biesinger, L.W.M. Lau, A.R. Gerson, R.St.C. Smart, Resolving surface chemical states in XPS analysis of first row transition metals, oxides and hydroxides: Sc, Ti, V, Cu and Zn, Appl. Surf. Sci. 257 (2010) 887–898, https://doi.org/10.1016/j.apsusc.2010.07.086.
[57] R. Peter, M. Petravić, Initial stages of oxide formation on copper surfaces during oxygen bombardment at room temperature, J. Phys. Chem. C 125 (2021) 25290–25297, https://doi.org/10.1021/acs.jpcc.1c07615.
[58] Y. Eda, T. Manaka, T. Hanawa, P. Chen, M. Ashida, K. Noda, X-ray photoelectron spectroscopy-based valence band spectra of passive films on titanium, Surf. Interface Anal. 54 (2022) 892–898, https://doi.org/10.1002/sia.7102.
[59] D.A. Zatsepin, D.W. Boukhvalov, N.V. Gavrilov, A.F. Zatsepin, V.Y. Shur, A.A. Esin, S.S. Kim, E.Z. Kurmaev, Soft electronic structure modulation of surface (thin-film) and bulk (ceramics) morphologies of TiO2-host by Pb-implantation: XPS-and-DFT characterization, Appl. Surf. Sci. 400 (2017) 110–117, https://doi.org/10.1016/j.apsusc.2016.12.154.
[60] M. Okada, Y. Tsuda, K. Oka, K. Kojima, W.A. Diño, A. Yoshigoe, H. Kasai, Experimental and theoretical studies on oxidation of Cu-Au alloy surfaces: Effect of bulk Au concentration, Sci. Rep. 6 (2016) 31101, https://doi.org/10.1038/srep31101.
[61] M.J. Šćepanović, M. Grujić-Brojčin, Z.D. Dohčević-Mitrović, Z.V. Popović, Characterization of anatase TiO2 nanopowder by variable-temperature Raman spectroscopy, Sci. Sinter. 41 (2009) 67–73, https://doi.org/10.2298/SOS0901067S.
[62] S. Peiris, J. McMurtrie, H.-Y. Zhu, Metal nanoparticle photocatalysts: emerging processes for green organic synthesis, Catal. Sci. Technol. 6 (2016) 320–338, https://doi.org/10.1039/C5CY02048D.
[63] G. Vijayakumar, H. Kesavan, A. Kannan, D. Arulanandam, J.H. Kim, K.J. Kim, H. J. Song, H.J. Kim, S.K. Rangarajulu, Phytosynthesis of copper nanoparticles using extracts of spices and their antibacterial properties, Processes 9 (2021) 1341, https://doi.org/10.3390/pr9081341.
[64] L. Sang, S. Zhang, Y. Gao, Investigation of plasmonic Cu with controlled diameter over TiO2 photoelectrode for solar-to-hydrogen conversion, Int. J. Hydrogen Energy 44 (2019) 25486–25494, https://doi.org/10.1016/j.ijhydene.2019.08.047.
[65] A. Chang, W.-S. Peng, I.-T. Tsai, L.-F. Chiang, C.-M. Yang, Efficient hydrogen production by selective alcohol photoreforming on plasmonic photocatalyst comprising sandwiched Au nanodisks and TiO2, Appl. Catal. B: Environ. 255 (2019) 117773, https://doi.org/10.1016/j.apcatb.2019.117773.
[66] D. Ding, K. Liu, S. He, C. Gao, Y. Yin, Ligand-exchange assisted formation of Au/TiO2 Schottky contact for visible-light photocatalysis, Nano Lett. 14 (2014) 6731–6736, https://doi.org/10.1021/nl503585m.
[67] M. Ghidelli, L. Mascaretti, B.R. Bricchi, A. Brognara, T.A. Afifi, V. Russo, C. Spartaco Casari, A.L. Bassi, Light management in TiO2 thin films integrated with Au plasmonic nanoparticles, Semicond. Sci. Technol. 35 (2020) 035016, https://doi.org/10.1088/1361-6641/ab6cea.
[68] C.C. Crane, F. Wang, J. Li, J. Tao, Y. Zhu, J. Chen, Synthesis of copper-silica core-shell nanostructures with sharp and stable localized surface plasmon resonance, J. Phys. Chem. C 121 (2017) 5684–5692, https://doi.org/10.1021/acs.jpcc.6b11891.
[69] H. Shi, S. Zhang, X. Zhu, Y. Liu, T. Wang, T. Jiang, G. Zhang, H. Duan, Uniform gold nanoparticles decorated {001}-faceted anatase TiO2 nanosheets for enhanced solar light photocatalytic reactions, ACS Appl. Mater. Interfaces 9 (2017) 36907–36916, https://doi.org/10.1021/acsami.7b12470.
[70] M.S. Mohammed, S.E. Kadhim, Study of the optical and structural properties of copper nanoparticles prepared via the electrochemical technique, J. Opt. (2024), https://doi.org/10.1007/s12596-024-02178-1.
[71] K. Awazu, M. Fujimaki, C. Rockstuhl, J. Tominaga, H. Murakami, Y. Ohki, N. Yoshida, T. Watanabe, A plasmonic photocatalyst consisting of silver nanoparticles embedded in titanium dioxide, J. Am. Chem. Soc. 130 (2008) 1676–1680, https://doi.org/10.1021/ja076503n.
[72] H. Tang, K. Prasad, R. Sanjines, P.E. Schmid, F. Levy, Electrical and optical properties of TiO_2 anatase thin films, J. Appl. Phys. 75 (1994) 2042–2047, https://doi.org/10.1063/1.356306.
[73] D.A. Edwards, R.N. Hayward, Transition metal acetates, Can. J. Chem. 46 (1968) 3443–3446, https://doi.org/10.1139/v68-572.
[74] T. Iivonen, M.J. Heikkila, G. Popov, H.-E. Nieminen, M. Kaipio, M. Kemell, M. Mattinen, K. Meinander, K. Mizohata, J. Raisanen, M. Ritala, M. Leskela, Atomic layer deposition of photoconductive Cu2O thin films, ACS Omega 4 (2019) 11205–11214, https://doi.org/10.1021/acsomega.9b01351.
[75] J. Shan, S. Fang, W. Wang, W. Zhao, R. Zhang, B. Liu, L. Lin, B. Jiang, H. Ci, R. Liu, W. Wang, X. Yang, W. Guo, M.H. Rummeli, W. Guo, J. Sun, Z. Liu, Copper acetate-facilitated transfer-free growth of high-quality graphene for hydrovoltaic generators, Natl. Sci. Rev. 9 (2022) nwab169, https://doi.org/10.1093/nsr/nwab169.
[76] K. Jia, J. Zhang, L. Lin, Z. Li, J. Gao, L. Sun, R. Xue, J. Li, N. Kang, Z. Luo, M. H. Rummeli, H. Peng, Z. Liu, Copper-containing carbon feedstock for growing superclean graphene, J. Am. Chem. Soc. 141 (2019) 7670–7674, https://doi.org/10.1021/jacs.9b02068.
[77] A. Hernández-Gordillo, M. Bizarro, T.A. Gadhi, A. Martínez, A. Tagliaferro, S. E. Rodila, Good practices for reporting the photocatalytic evaluation of a visible-light active semiconductor: Bi_2O_3, a case study, Catal. Sci. Technol. 9 (2019) 1476–1496, https://doi.org/10.1039/C9CY00038K.
[78] K.K. Paul, P.K. Giri, Role of surface plasmons and hot electrons on the multi-step photocatalytic decay by defect enriched Ag@TiO2 nanorods under visible light illumination, J. Phys. Chem. C 121 (2017) 20016–20030, https://doi.org/10.1021/acs.jpcc.7b05328.
[79] R.S. Dariani, A. Esmaeili, A. Mortezaali, S. Dehghanpour, Photocatalytic reaction and degradation of methylene blue on TiO2 nano-sized particles, Optik 127 (2016) 7143–7154, https://doi.org/10.1016/j.ijleo.2016.04.026.
[80] Z.Z. Vasiljevic, M.P. Dojcinovic, J.D. Vujancevic, I. Jankovic-Castvan, M. Ognjanovic, N.B. Tadic, S. Stojadinovic, G.O. Brankovic, M.V. Nikolic, Photocatalytic degradation of methylene blue under natural sunlight using iron titanate nanoparticles prepared by a modified sol–gel method, R. Soc. Open Sci. 7 (2020) 200708, https://doi.org/10.1098/rsos.200708.
[81] S. Mondal, M.E. De Anda Reyes, U. Pal, Plasmon induced enhanced photocatalytic activity of gold loaded hydroxyapatite nanoparticles for methylene blue degradation under visible light, RSC Adv. 7 (2017) 8633–8645, https://doi.org/10.1039/C6RA28640B.
[82] M. Antoniadou, M.K. Arfanis, I. Ibrahim, P. Falaras, Bifunctional g-C3N4/WO3 thin films for photocatalytic water purification, Water 11 (2019) 2439, https://doi.org/10.3390/w11122439.
[83] J. Jiang, N. Xie, Y. Jiang, J. Han, G. Feng, Z. Shic, C. He, Rapid photodegradation of methylene blue by laser-induced plasma, RSC Adv 12 (2022) 21056, https://doi.org/10.1039/d2ra03633a.
[84] K.H. Leong, B.L. Gan, S. Ibrahim, P. Saravanan, Synthesis of surface plasmon resonance (SPR) triggered Ag/TiO2 photocatalyst for degradation of endocrine disturbing compounds, Appl. Surf. Sci. 319 (2014) 128–135, https://doi.org/10.1016/j.apsusc.2014.06.153.
[85] A. Subrahmanyam, K.P. Biju, P. Rajesh, K.J. Kumar, M.R. Kiran, Surface modification of sol gel TiO2 surface with sputtered metallic silver for Sun light photocatalytic activity: Initial studies, Sol. Energy Mater. Sol. Cells 101 (2012) 241–248, https://doi.org/10.1016/j.solmat.2012.01.023.
[86] S. Zhou, H. Zhang, X. Peng, H. Liu, H. Li, Y. Xiong, W. Li, P.-A. Yang, L. Ye, C. Kong, Fully transparent and high-performance ε-Ga2O3 photodetector arrays for solar-blind imaging and deep-ultraviolet communication, Adv. Photonics Res. 3 (2022) 2200192, https://doi.org/10.1002/adpr.202200192.
[87] D. Guo, Y. Su, H. Shi, P. Li, N. Zhao, J. Ye, A.Liu S.Wang, Z. Chen, C. Li, W. Tang, Self-powered ultraviolet photodetector with superhigh photoresponsivity (3.05 A/W) based on the GaN/Sn:Ga2O3 pn junction, ACS Nano 12 (2018) 12827–12835, https://doi.org/10.1021/acsnano.8b07997.
[88] J. Long, H. Chang, Q. Gu, J. Xu, L. Fan, S. Wang, Y. Zhou, W. Wei, L. Huang, X. Wang, P. Liu, W. Huang, Gold-plasmon enhanced solar-to-hydrogen conversion on the {001} facets of anatase TiO2 nanosheets, Energy Environ. Sci. 7 (2014) 973–977, https://doi.org/10.1039/C3EE43289K.
[89] G. Žerjav, J. Zavašnik, J. Kovač, A. Pintar, The influence of Schottky barrier height onto visible-light triggered photocatalytic activity of TiO2+Au composites, Appl. Surf. Sci. 543 (2021) 148799, https://doi.org/10.1016/j.apsusc.2020.148799.
[90] G. Žerjav, Z. Say, J. Zavašnik, M. Finšgar, C. Langhammer, A. Pintar, Photo, thermal and photothermal activity of TiO2 supported Pt catalysts for plasmon-driven environmental applications, J. Environ. Chem. Eng. 11 (2023) 110209, https://doi.org/10.1016/j.jece.2023.110209.
[91] A. Wang, S. Wu, J. Dong, R. Wang, J. Wang, J. Zhang, S. Zhong, S. Bai, Interfacial facet engineering on the Schottky barrier between plasmonic Au and TiO2 in boosting the photocatalytic CO2 reduction under ultraviolet and visible light irradiation, Chem. Eng. J. 404 (2021) 127145, https://doi.org/10.1016/j.cej.2020.127145.
[92] W. Zhang, X. Li, S. Liu, J. Qiu, J. An, J. Yao, S. Zuo, B. Zhang, H. Xia, C. Li, Photocatalytic oxidation of 5-hydroxymethylfurfural over interfacial-enhanced Ag/TiO2 under visible light irradiation, ChemSusChem 15 (2022) e202102158, https://doi.org/10.1002/cssc.202102158.
[93] L. Amirav, M. Wächtler, Nano Schottky?, Nano Lett. 22 (2022) 9783–9785, https://doi.org/10.1021/acs.nanolett.2c04150.
[94] S.Y. Moon, H.C. Song, E.H. Gwag, I.I. Nedrygailov, C. Lee, J.J. Kim, W.H. Doh, J. Y. Park, Plasmonic hot carrier-driven oxygen evolution reaction on Au nanoparticles/TiO2 nanotube arrays, Nanoscale 10 (2018) 22180, https://doi.org/10.1039/C8NR05144E.

Microchemical Journal 213 (2025) 113533

Contents lists available at ScienceDirect

Microchemical Journal

journal homepage: www.elsevier.com/locate/microc

Temperature-induced phase transitions in atorvastatin calcium trihydrate revealed by low-energy Raman analysis

J.J. Lazarević [a],*, S. Uskoković-Marković [b], J. Mitrić [a], N. Lazarević [a]

[a] Center for Solid State Physics and New Materials, Institute of Physics Belgrade, University of Belgrade, Pregrevica 118, Belgrade, 11080, Serbia
[b] Faculty of Pharmacy, University of Belgrade, Vojvode Stepe 450, Belgrade, 11221, Serbia

ARTICLE INFO

Keywords:
Raman spectroscopy
Low-energy region
Phase transitions
Atorvastatin calcium trihydrate

ABSTRACT

We present a comprehensive inelastic light scattering study of atorvastatin calcium trihydrate Form I across a broad temperature range (100 K to 460 K), with a focus on the low-energy spectral region, providing key insights into the crystal structure for the first time. The Raman spectra revealed significant temperature-dependent changes, particularly at 420 K, where external vibrations at approximately 34 cm^{-1}, 44 cm^{-1}, and 140 cm^{-1} disappeared, indicating a structural phase transition. Strong fluctuations near this temperature led to notable broadening in the linewidths of the 645 cm^{-1} and 1650 cm^{-1} modes. Additionally, a new mode around 75 cm^{-1} appeared at the phase transition, suggesting the presence of structural order in the anhydrous phase before reaching the isotropic melt.

1. Introduction

The majority of a potential drug candidates do not accomplish to become a drug product due to challenges related to stability, solubility, and interactions with other drugs. These issues often stem from the diverse physicochemical, mechanical, and biopharmaceutical properties exhibited by active pharmaceutical ingredients (APIs) and excipients in various solid-state forms, such as crystalline (including polymorphs, hydrates, solvates, salts, and cocrystals), and amorphous forms. These can influence the safety, quality, and efficacy of the drug. Many of the APIs form multiple hydrates. Crystal hydrates form when water molecules associate with solids and incorporate into a crystal lattice, leading to distinct physicochemical and mechanical properties compared to the anhydrous form. Dehydration commonly takes place during manufacturing, either by disrupting the original crystal lattice and forming a new one for the anhydrous form, or by preserving the existing structure. As bioavailability and ensuing biological activity depend on the exact solid state form, identifying the crystalline phase of the API in solid dosage forms is considered essential in the manufacturing process and regulatory affairs [1].

Statins are among the most commonly prescribed medications globally. They have a significant role in preventing and managing cardiovascular diseases in individuals with a high risk of cardiovascular events by lowering cholesterol levels, stabilizing plaques, reducing inflammation, improving endothelial function, and exerting antithrombotic effects [2–4]. In the Biopharmaceutical Classification System, statins fall under class II, indicating that they have poor solubility but can effectively permeate biological membranes. Their bioavailability varies significantly due to the effects of first-pass metabolism.

Atorvastatin calcium trihydrate (ACT), chemical name (βR, δR)-2-(4-fluorophenyl)–β, δ-dihydroxy-5-(1-methyl-ethyl)-3-phenyl-4-[(phenylamino)carbonyl]-1H-pyrrole-1-heptanoic acid, is a synthetic lipid-lowering agent that competitively inhibits hepatic hydroxymethyl-glutaryl coenzyme A (HMG-CoA) reductase. This enzyme catalyzes the conversion of HMG-CoA to mevalonate, a critical step in cholesterol synthesis. Originally marketed by Pfizer in Form I, it is considered as the best seller drug of all time, even after its patent loss in 2011. By increasing the number of low density lipoprotein (LDL) receptors on hepatic cell surfaces, atorvastatin enhances the uptake and breakdown of LDL, consequently reducing LDL production and the number of LDL particles. This mechanism leads to lowered plasma LDL-cholesterol, lipoprotein levels, and triglycerides. On the other hand, it increases serum levels of high density lipoprotein (HDL), so-called “good” cholesterol [5]. Similar to other statins, atorvastatin may exhibit direct antineoplastic effect by potentially stopping cell progression in the G1 phase of the cell cycle. Furthermore, atorvastatin may sensitize tumor cells to cytostatic drugs [6–8]. Additionally, a significant number of clinical trials showed a direct anti-inflammatory effects of statins that are not mediated by their antihyperlipidemic activity [9]. It has been shown that they reduce cardiovasculatory-related morbidity and mortality irrespective of the lipid profile and cardiac artery disease [10].

---

* Corresponding author.
E-mail address: jasmina.lazarevic@ipb.ac.rs (J.J. Lazarević).

https://doi.org/10.1016/j.microc.2025.113533
Received 19 October 2024; Received in revised form 5 March 2025; Accepted 31 March 2025

Characterization of ACT crystal forms was performed by X-ray powder diffraction (XRPD) as described in the filed patents that regulate production, while quantification in solid dosage forms depended mostly on high-performance liquid chromatography, spectrophotometric methods, and electrophoresis [11]. Previous researches on atorvastatin were predominantly focused on thermal techniques, such as differential scanning calorimetry, thermogravimetric analysis, and nuclear magnetic resonance [11–16]. Lately, Raman spectroscopy has been applied to determine the APIs both in process samples and final products [17]. Moreover, Raman spectroscopy has the potential to be utilized as process analytical technology for monitoring manufacturing processes [18,19]. Furthermore, progress has been made in applying Raman spectroscopy for the quantitative analysis of ACT [17,20,21]. So far, the ACT solid-state characterization was extensively researched using thermoanalytical techniques and XRPD [11–16]. Raman spectroscopy stands out as a highly specific and selective technique, capable of identifying polymorphs and crystalline states with minimal to no sample preparation. Its short analysis time, ease of use, and versatility make it suitable for application at every stage of the manufacturing process. The Raman spectra of ACT have been previously reported by Christensen et al. [16], Skorda et al. [11], and Oprica et al. [22]; however, the temperature dependence of the low-energy spectral region has not yet been explored. In this study, we present Raman scattering measurements of ACT Form I over the temperature range of 100 K to 460 K, focusing on the low-energy spectra (20 cm^{-1} to 175 cm^{-1}) measured with high spectral resolution. These spectra, which predominantly reflect intermolecular vibrations and crystal structure, show a strong temperature-dependent evolution, directly revealing a structural transition.

2. Experiment

ACT crystallizes in at least 12 different forms [12], with crystalline Form I first identified in a U.S. patent Number 5969156 [23]. To avoid uncontrollable alterations in crystal structure and properties that may occur during sample preparation, all experiments in this study were conducted using powdered samples, as obtained. The ACT Form I reference standard used in this investigation had a purity of 99.27% (Alkaloid DOO, Belgrade, Serbia).

2.1. X – ray powder diffraction analysis of atorvastatin calcium trihydrate

Structural analysis to confirm Form I of powder ACT was performed with XRPD. The XRPD patterns were obtained using CuKα radiation (λ = 1.5418 Å) on a Rigaku Smartlab X-ray diffractometer. The measurements were performed in the 2θ range of 3°–50°, with a step size of 0.02° and a rate of 1.5°/min. The FullProf software package was used to refine the XRPD pattern of the prepared sample by using the whole-pattern decomposition procedure(Le Bail fitting) and calculate unit cell parameters [24].

2.2. μ-Raman spectroscopy

The Raman scattering measurements were performed using a TriVista 557 Raman spectrometer (S&I Spectroscopy and Imaging GmbH, Warstein, Germany), equipped with a Spec-10: 256E N_2 cooled CCD detector and coupled to the OLYMPUS BX51 optical microscope in a backscattering configuration. For this study, the spectrometer was set up in a triple subtractive mode. The system features three stages, each fitted with motorized turret and three gratings, allowing for quick switching between different regimes and grating configurations. The entrance slit and second intermediate slit were set to 100 μm, while the first intermediate slit was set to the value that ensures the full utilization of the CCD chip width. The Coherent Ar^+/Kr^+ laser was used as the excitation source, providing multiple high-quality lines at different wavelengths that could be easily switched to meet experimental needs. The laser lines were cleaned using a Semrock Narrowband Clean-up filters. An Olympus LMPlanFI 50×/0.50 microscope objective was used to focus the incident light onto the sample, with a laser spot diameter of approximately 4 μm. To prevent sample damage and avoid uncontrollable temperature-related effects, the laser power at the sample plane was maintained at low levels, approximately 1 mW. The acquisition time was set to 300 s.

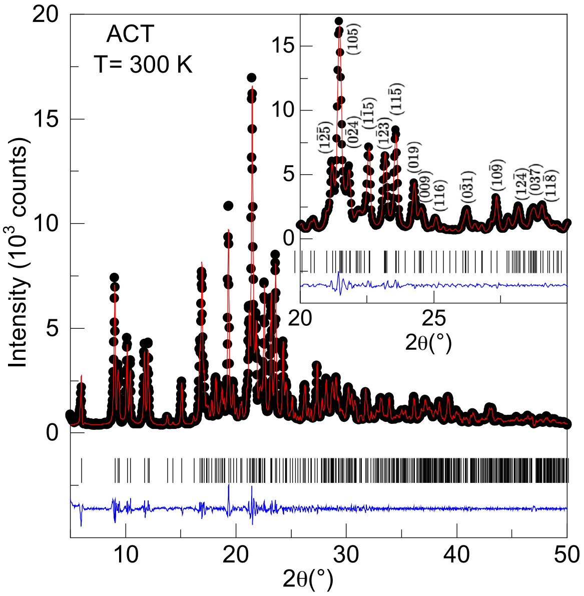

Fig. 1. XRPD pattern of refined ACT structure. Black represent experimental results, red solid lines are results from Le Bail fitting, black lines below XRPD pattern are peak positions, and blue line represents differences between experimental and fitted data.

For low-energy measurements, a 514.5 nm laser line and 1800/1800/2400 grooves/mm gratings were used. For measurements across a wider spectral range, a 647 nm laser line and 300/300/500 grooves/mm gratings were employed. These setups provided spectral resolutions of approximately 2 cm^{-1} and 13 cm^{-1}, respectively. They were optimized to balance laser line suppression, spectral resolution, and spectral range according to the specific experimental requirements.

Temperature-dependent Raman scattering measurements were conducted using a LINKAM THMS 600 heating/cooling stage, with the sample mounted on a custom copper plate. The heating/cooling rate was set to 5 K/min, followed by a 25 min thermalization period after each temperature change. The sample chamber was purged with argon, and continuous low-flow argon purging was maintained throughout the experiment. All the Raman scattering spectra are corrected by the corresponding Bose factor $n(T)$.

3. Results and discussion

As previously mentioned, ACT may exist in several phases. The crystal structure of ACT Form I has been previously solved and refined using synchrotron X-ray powder diffraction data [23], and further optimized using density functional theory techniques [12,14]. Temperature dependent XRPD measurements were reported in Refs. [15,16].

To verify the room temperature crystal structure of the obtained sample prior to the Raman scattering experiments, we performed XRPD analysis. The resulting XRPD pattern corresponding to the refined structure is shown in Fig. 1. The black dots in Fig. 1 represent experimental data, while the red solid line corresponds to the Le Bail fitting results. The black lines below the XRPD pattern indicate peak positions, and the blue line represents the difference between the experimental and fitted results. The XRPD pattern shows an excellent match with previously

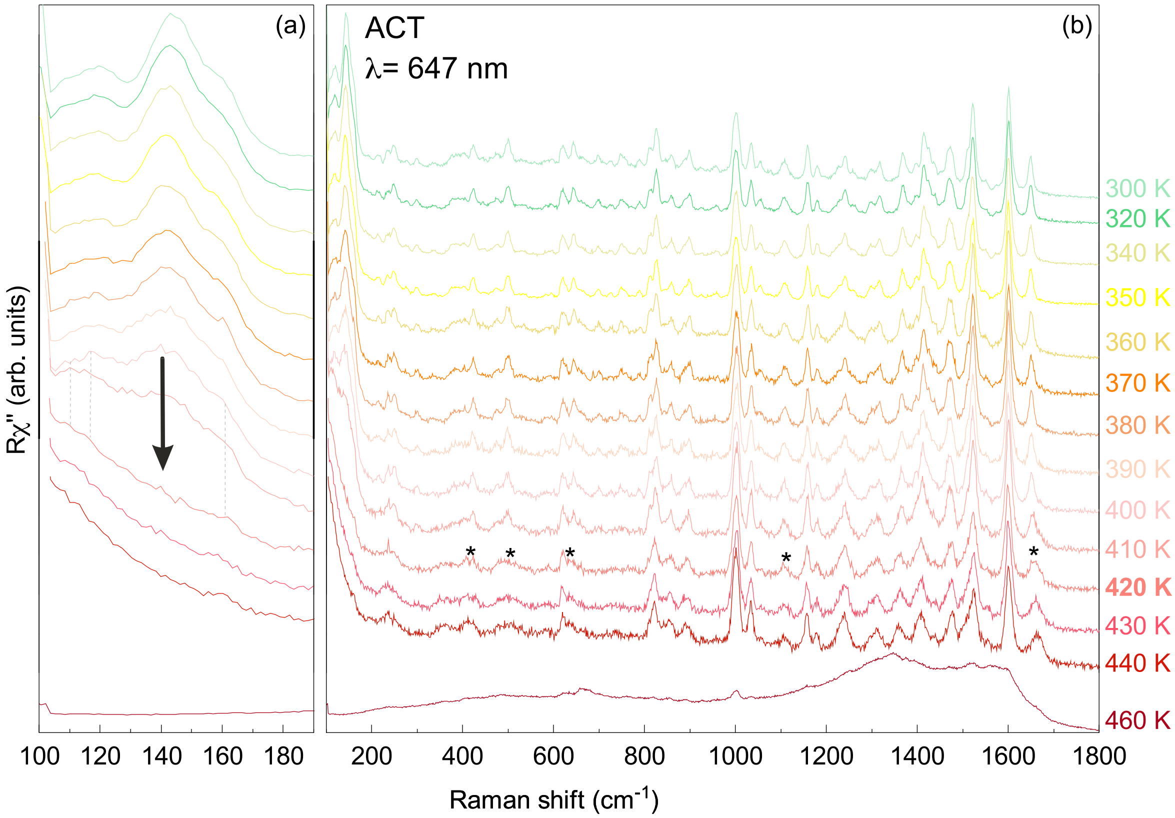

Fig. 2. Temperature dependent Raman spectra of ACT measured with 300/300/500 grooves/mm gratings combination and 647 nm laser line of (a) low and (b) wide energy spectral region. Black arrow indicates the disappearance of the 140 cm^{-1} peak, while dashed lines serve as guides to the eye. Asterisks mark the peaks that show pronounced discontinuities in their temperature evolution.

published data, with all observed peaks closely aligning with those reported in the literature [12,14,23], including synchrotron data [25], confirming that the analyzed sample corresponds to ACT Form I. The obtained results show total number of 1312 reflections. ACT crystallizes in $P1$ crystal group, with cell parameters a = 5.4497(2), b = 9.8976(4), c = 30.2558(2), α = 76.8631(2), β = 99.0525(8), γ = 4105.2850(3). This undoubtedly show that our ACT sample crystallizes in Form I.

To further highlight the key structural features, the top-right corner of Fig. 1 presents a zoomed-in section of the XRD pattern, displaying 2Θ values ranging from 20° to 30°, along with the corresponding Miller indices. This region is crucial for the identification of ACT Form I, and all indexed peaks match synchrotron measurements [23], providing further confirmation of the structure.

Additionally, Form I ACT appears to have smaller particle sizes, a more uniform particle size distribution, and greater stability than previously reported more amorphous products. Moreover, Form I ACT is purer and more stable than other amorphous forms [12]. These results conclusively confirm that our ACT sample crystallizes in Form I.

In molecular crystals, two types of vibrations can generally be distinguished: external vibrations, which occur between molecules, and internal vibrations, which occur within molecules [26]. External vibrations can be further classified based on the type of motion—either as translations, representing the translational movement of molecules, or librations, representing their rotational movement. They are, in particular, strongly linked to the structural properties of molecular compounds, offering valuable insights into structural phase transitions.

Intramolecular vibrations within a molecular crystal, compared to those in an isolated molecule, may show slight shifts in energy and/or changes in linewidth due to perturbations from the relatively weak intermolecular interactions. In the similar manner structural changes can also lead to variations in the energy and/or linewidth of these vibrations. Moreover, when the number of molecules in the primitive unit cell exceeds one, intramolecular vibrations may manifest as multiplets due to symmetry considerations and the typically weak nature of intermolecular interactions [26,27].

The vibrational structure of ACT can be determined by correlating the translational, rotational and vibrational motions of a single molecule to the corresponding site and crystal symmetries [26,27]. Given the very low symmetry of ACT Form I ($P1$), this straightforwardly results in only three librational modes and 474A symmetry internal vibrations that are expected to be observed in the Raman scattering experiment (Γ point distribution). While intramolecular vibrations dominate the Raman spectra of ACT, intermolecular vibrations are expected to be observed in the low-energy spectral region, below 175 cm^{-1}. Moreover, given the low symmetry of ACT ($P1$), no dependence of the Raman spectra on the polarization of the incident and scattered light is anticipated. As a result, a crossed polarization configuration was used in all light scattering experiments presented in this study, and this aspect will not be discussed further.

The ACT Raman spectra, measured in the temperature range from 300 K to 460 K using a 647 nm laser line and 300/300/500 grooves/mm gratings are shown in Fig. 2. It is noticeable that as the temperature increases, Raman modes soften and broaden, driven by thermal expansion and anharmonic effects [28,29]. In general, in the absence of phase transitions (and coupling to other elementary excitations) the temperature evolution of linewidth is fully driven by anharmonic coupling. On the other hand, the change in phonon frequency with temperature is not entirely due to anharmonic coupling, but also thermal expansion. Although thermal expansion itself occurs as a result of anharmonicity, it affects the quasi-harmonic frequencies through the harmonic force constant.

Closer inspection revealed discontinuities at 420 K in the temperature evolution of intensities and/or linewidths for the internal modes

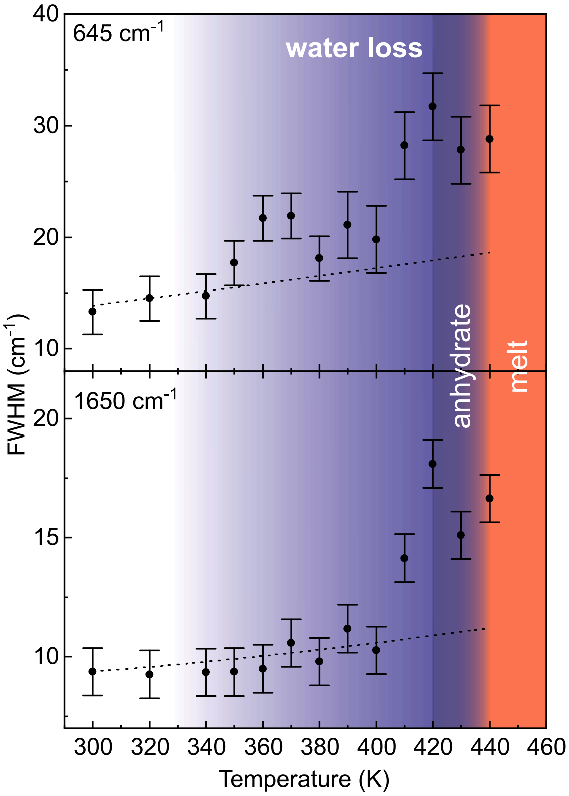

Fig. 3. Linewidth temperature dependence of peak structures at 645 cm^{-1} and 1650 cm^{-1} measured by 647 nm laser line. The values are error-weighted, and the dashed lines represent the anharmonic behavior described by $\Gamma = \Gamma_0 \left(1 + \frac{2\lambda_{ph-ph}}{exp(\frac{\hbar\omega_0}{2k_BT})-1}\right)$, where Γ_0 and ω_0 are the zero-temperature limits and λ_{ph-ph} is the phonon–phonon coupling constant [28].

around 420 cm^{-1}, 505 cm^{-1}, 645 cm^{-1}, 1110 cm^{-1}, and 1650 cm^{-1} (marked by asterisks in Fig. 2). These modes were previously assigned [22] to in-plane OCO rocking + out-of-plane benzene deformation, C–C–C deformation, O–H out-of-plane deformation, CH wagging in the benzene ring + C–N–C stretching in the amide group + C–C–O stretching, and C═O stretching, respectively. Similar discontinuities may also be present for other modes, but due to the overlapping of a larger number of modes, finite spectral resolution, and/or low intensity, they are not easily discernible.

The temperature evolution of the linewidths for the peaks at 645 cm^{-1} and 1650 cm^{-1} is shown in Fig. 3. Above 340 K, the 645 cm^{-1} peak begins to deviate from the expected anharmonic behavior, as illustrated by the dashed lines. As evidenced by TGA and DSC results [15,16], this corresponds to the temperature range where the stepwise loss of H-bonded water molecules occurs (highlighted in the blue shaded area in Fig. 3). It should be noted that the exact temperatures of the dehydration process may vary between techniques due to differences in water vapor pressure around the sample. While no significant deviation is observed below 400 K for the 1650 cm^{-1} peak, both peaks exhibit strong, peak-like deviations in linewidth around 420 K. This is likely a result of strong fluctuations [29] indicating the structural phase transition at this temperature. In general, while selection rules based on symmetry determine whether a phonon mode can couple to structural fluctuations, the coupling strength is reflected in the phonon linewidth, which increases when phonons interact with dynamic structural fluctuations.

More notable changes are observed in the low-energy spectral region (see Fig. 3(a)). While the peak at 140 cm^{-1} completely disappears at 420 K, the peaks at 110 cm^{-1}, 117 cm^{-1}, and 160 cm^{-1}, although broadened, remain observable at higher temperatures. This suggests that the 140 cm^{-1} peak corresponds to external vibration (lattice libration) specific to ACT Form I, as previously discussed. In contrast, the peaks at 110 cm^{-1}, 117 cm^{-1}, and 160 cm^{-1} are internal in nature. To elucidate temperature induced changes in the crystal structure of ACT, we focus on the ultra-low energy region in wide temperature range.

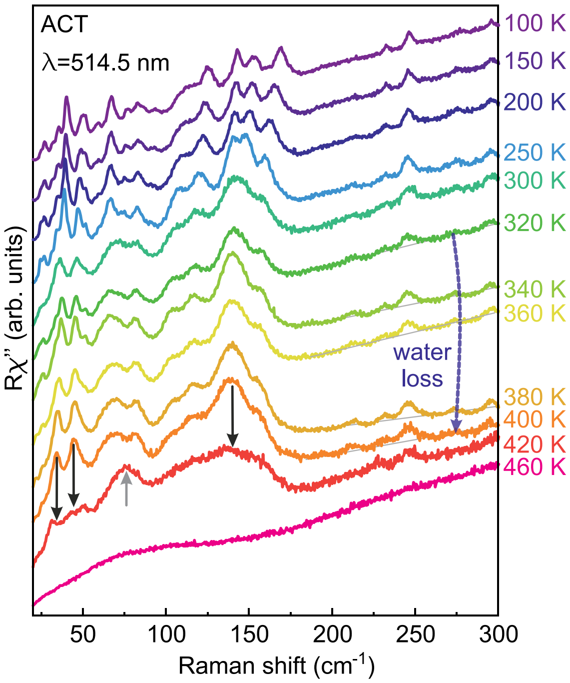

Fig. 4. Temperature dependent low-energy Raman spectra measured by 1800/1800/2400 grooves/mm gratings combination and 514.5 nm laser line ensuring high suppression of the elastically scattered light. Black arrows indicate the disappearing peaks, while the gray arrow marks the peak that appears at 420 K.

The ultra-low energy Raman spectra (20–300 cm^{-1}) of ACT, measured over the temperature range of 100 K to 460 K using 1800/1800/2400 grooves/mm gratings with a 514.5 nm laser line, is presented in Fig. 4. The sample was first cooled from room temperature to 100 K and then gradually heated to 460 K. As expected, a large number of peaks become clearly discernible at 100 K due to anharmonic effects, as previously discussed. Upon heating, changes in the slope of the spectra are observed in the region associated with the stepwise loss of H-bonded water molecules in ACT [13,15,16]. This is not unexpected, as small changes in the electronic structure can cause variations in the spectral slope.

Closer inspection of the temperature evolution reveals the disappearance of peaks at approximately 34 cm^{-1} and 44 cm^{-1}, as indicated by the black arrows in Fig. 4, in addition to the previously observed peak at 140 cm^{-1} shown in Fig. 2. These three peaks correspond to external vibrations, consistent with earlier symmetry considerations. Their disappearance at 420 K indicates a structural phase transition and the breaking of crystal symmetry of Form I, as also suggested by the behavior of the previously analyzed internal vibrational modes. In light of the DSC and TGA results [15,16], this suggests that the Form I crystal structure is preserved until the transition to the anhydrous phase, consistent with second-harmonic generator and XRPD findings [15].

The most striking feature is the appearance of a new mode around 75 cm^{-1}, indicated by a gray arrow in Fig. 4. The emergence of this additional mode in the low-energy region at the phase transition temperature suggests an intermolecular origin for this vibration. This implies the presence of a certain, presumably one-dimensional, order up to 460 K, beyond which the isotropic melt is reached. This interpretation is further supported by the $2\theta{\sim}17°$ observation reported in Ref. [15], where X-ray diffraction reveals a broad, diffuse-like signal above the transformation temperature and just before the onset of the isotropic melt. While Raman spectroscopy can detect this type of order, the structural coherence might only extend across a few unit cells. Employing advanced nanoscale-sensitive characterization techniques, such as total X-ray scattering-based pair distribution function analysis, could enable a more comprehensive characterization of this behavior in future studies.

4. Conclusion

In this study, comprehensive temperature-dependent low-energy Raman analyses of ACT were conducted, revealing complex vibrational and structural changes induced by temperature. The previously reported stepwise loss of hydrogen-bonded water molecules was also detected in the low-energy Raman data. Moreover, the peak-like deviation from anharmonic behavior in the linewidths of the 645 cm^{-1} and 1650 cm^{-1} modes serves as a clear fingerprint of strong structural fluctuations at 420 K. At this temperature, three peaks, identified as external vibrations, characteristic of the Form I crystal structure, disappear, indicating the breaking of symmetry as the system enters the anhydrous phase. The appearance of a new vibrational mode around 75 cm^{-1} at the phase transition temperature indicates the presence of short-range order up to 460 K, beyond which the system transitions into an isotropic melt. This interpretation aligns with previous X-ray diffraction studies [Ref. [15]], where a broad, diffuse-like signal near $2\theta{\sim}17°$ was observed above the transition temperature, just before the isotropic phase fully develops. While Raman spectroscopy can detect such structural order, the coherence may extend only over a few unit cells. Future studies employing nanoscale-sensitive techniques, such as total X-ray scattering-based pair distribution function analysis, could provide a more detailed characterization of these structural fluctuations and their role in phase transitions.

CRediT authorship contribution statement

J.J. Lazarević: Writing – review & editing, Writing – original draft, Methodology, Investigation, Formal analysis, Data curation, Conceptualization. **S. Usković-Marković:** Writing – review & editing, Supervision, Resources, Methodology. **J. Mitrić:** Writing – original draft, Investigation. **N. Lazarević:** Writing – review & editing, Visualization, Supervision, Resources, Methodology, Conceptualization.

Declaration of competing interest

The Authors have no competing interests to declare.

Acknowledgments

The authors acknowledge funding provided by the Institute of Physics Belgrade through the grant by the Ministry of Science, Technological Development and Innovation of the Republic of Serbia. The authors are grateful to Dr. Jelena Pešić and Dr. Emil Božin for fruitful discussions.

Data availability

Data will be made available on request.

References

[1] C.R. Gardner, C.T. Walsh, Ö. Almarsson, Drugs as materials: valuing physical form in drug discovery, Nat. Rev. Drug Discov. 3 (11) (2004) 926–934.

[2] S.P. Adams, M. Tsang, J.M. Wright, Lipid lowering efficacy of atorvastatin, Cochrane Database Syst. Rev. 12 (2012).

[3] B.F. Asztalos, K.V. Horvath, J.R. McNamara, P.S. Roheim, J.J. Rubinstein, E.J. Schaefer, Comparing the effects of five different statins on the hdl subpopulation profiles of coronary heart disease patients, Atherosclerosis 164 (2) (2002) 361–369.

[4] E.J. Schaefer, J.R. McNamara, T. Tayler, J.A. Daly, J.L. Gleason, L.J. Seman, A. Ferrari, J.J. Rubenstein, Comparisons of effects of statins (atorvastatin, fluvastatin, lovastatin, pravastatin, and simvastatin) on fasting and postprandial lipoproteins in patients with coronary heart disease versus control subjects, Am. J. Cardiol. 93 (1) (2004) 31–39.

[5] F.M. Sacks, M.A. Pfeffer, L.A. Moye, J.L. Rouleau, J.D. Rutherford, T.G. Cole, L. Brown, J.W. Warnica, J.M.O. Arnold, C.-C. Wun, et al., The effect of pravastatin on coronary events after myocardial infarction in patients with average cholesterol levels, N. Engl. J. Med. 335 (14) (1996) 1001–1009.

[6] A.K. Altwairgi, Statins are potential anticancerous agents, Oncol. Rep. 33 (3) (2015) 1019–1039.

[7] M. Jakobisiak, J. Golab, Potential antitumor effects of statins, Int. J. Oncol. 23 (4) (2003) 1055–1069.

[8] J. Longo, J.E. van Leeuwen, M. Elbaz, E. Branchard, L.Z. Penn, Statins as anticancer agents in the era of precision medicine, Clin. Cancer Res. 26 (22) (2020) 5791–5800.

[9] G. Weitz-Schmidt, Statins as anti-inflammatory agents, Trends Pharmacol. Sci. 23 (10) (2002) 482–487.

[10] I. Inoue, S.-I. Goto, K. Mizotani, T. Awata, T. Mastunaga, S.-I. Kawai, T. Nakajima, S. Hokari, T. Komoda, S. Katayama, Lipophilic hmg-coa reductase inhibitor has an anti-inflammatory effect: reduction of mrna levels for interleukin-1β, interleukin-6, cyclooxygenase-2, and p22phox by regulation of peroxisome proliferator-activated receptor α (pparα) in primary endothelial cells, Life Sci. 67 (8) (2000) 863–876.

[11] D. Skorda, C.G. Kontoyannis, Identification and quantitative determination of atorvastatin calcium polymorph in tablets using ft-raman spectroscopy, Talanta 74 (4) (2008) 1066–1070.

[12] R.L. Hodge, J.A. Kaduk, A.M. Gindhart, T.N. Blanton, Crystal structure of atorvastatin calcium trihydrate form i (lipitor®), (c33h34fn2o5) 2ca (h2o) 3, Powder Diffr. 35 (2) (2020) 136–143.

[13] K.A. Salazar-Barrantes, J.R. Vega-Baudrit, M. Navarro-Hoyos, A.M. Araya-Sibaja, Thermoanalytical techniques applied to the solid-state characterization of atorvastatin calcium trihydrate form I, Chem. Thermodyn. Therm. Anal. 14 (2024) 100130.

[14] G. Shete, V. Puri, L. Kumar, A.K. Bansal, Solid state characterization of commercial crystalline and amorphous atorvastatin calcium samples, AAPS PharmSciTech 11 (2) (2010) 598–609.

[15] C. Tizaoui, H. Galai, M. Barrio, S. Clevers, N. Couvrat, V. Dupray, G. Coquerel, J.-L. Tamarit, I.B. Rietveld, Does the trihydrate of atorvastatin calcium possess a melting point? Eur. J. Pharm. Sci. 148 (2020) 105334.

[16] N.P.A. Christensen, B. Van Eerdenbrugh, K. Kwok, L.S. Taylor, A.D. Bond, T. Rades, J. Rantanen, C. Cornett, Rapid insight into heating-induced phase transformations in the solid state of the calcium salt of atorvastatin using multivariate data analysis, Pharm. Res. 30 (2013) 826–835.

[17] Y.-I. Lim, J. Han, Y.-A. Woo, J. Kim, M.J. Kang, Rapid quantitation of atorvastatin in process pharmaceutical powder sample using raman spectroscopy and evaluation of parameters related to accuracy of analysis, Spectrochim. Acta Part A: Mol. Biomol. Spectrosc. 200 (2018) 26–32.

[18] T. De Beer, C. Bodson, B. Dejaegher, B. Walczak, P. Vercruysse, A. Burggraeve, A. Lemos, L. Delattre, Y. Vander Heyden, J.P. Remon, et al., Raman spectroscopy as a process analytical technology (pat) tool for the in-line monitoring and understanding of a powder blending process, J. Pharm. Biomed. Anal. 48 (3) (2008) 772–779.

[19] T. De Beer, A. Burggraeve, M. Fonteyne, L. Saerens, J. Remon, C. Vervaet, Near infrared and raman spectroscopy for the in-process monitoring of pharmaceutical production processes, Int. J. Pharm. 417 (1) (2011) 32–47, advanced characterization techniques..

[20] S. Mazurek, R. Szostak, Quantification of atorvastatin calcium in tablets by ft-raman spectroscopy, J. Pharm. Biomed. Anal. 49 (1) (2009) 168–172.

[21] T. Fukami, T. Koide, H. Hisada, M. Inoue, Y. Yamamoto, T. Suzuki, K. Tomono, Pharmaceutical evaluation of atorvastatin calcium tablets available on the internet: A preliminary investigation of substandard medicines in japan, J. Drug Deliv. Sci. Technol. 31 (2016) 35–40.

[22] M. Oprica, M. Iota, M. Daescu, S.N. Fejer, C. Negrila, M. Baibarac, Spectroscopic studies on photodegradation of atorvastatin calcium, Sci. Rep. 11 (1) (2021) 15338.

[23] C. Briggs, R. Jennings, R. Wade, K. Harasawa, S. Ichikawa, S. Minohara K. Nakagawa, U.S. Patent, Vol. 5, 1999, 959156.

[24] A. Le Bail, H. Duroy, J. Fourquet, Ab-initio structure determination of lisbwo6 by x-ray powder diffraction, Mater. Res. Bull. 23 (3) (1988) 447–452, http://dx.doi.org/10.1016/0025-5408(88)90019-0, URL https://www.sciencedirect.com/science/article/pii/0025540888900190.

[25] S.G. Antonio, F.R. Benini, F.F. Ferreira, P.C.P. Rosa, C. de Oliveira Paiva-Santos, Synchrotron x-ray powder diffraction data of atorvastatin, Powder Diffr. 23 (4) (2008) 350–355, http://dx.doi.org/10.1154/1.2996511.

[26] W.G. Fateley, Infrared and Raman selection rules for molecular and lattice vibrations: the correlation method, 1972.

[27] J. Lazarević, S. Uskoković-Marković, M. Jelikić-Stankov, M. Radonjić, D. Tanasković, N. Lazarević, Z. Popović, Intermolecular and low-frequency intramolecular raman scattering study of racemic ibuprofen, Spectrochim. Acta Part A: Mol. Biomol. Spectrosc. 126 (2014) 301–305.

[28] A. Baum, A. Milosavljević, N. Lazarević, M. Radonjić, B. Nikolić, M. Mitschek, Z.I. Maranloo, M. Šćepanović, M. Grujić-Brojčin, N. Stojilović, et al., Phonon anomalies in fes, Phys. Rev. B 97 (5) (2018) 054306.

[29] N. Lazarević, R. Hackl, Fluctuations and pairing in fe-based superconductors: Light scattering experiments, J. Phys.: Condens. Matter. 32 (41) (2020) 413001.

2D Materials

TOPICAL REVIEW • OPEN ACCESS

2D materials: advances in regenerative medicine and human health sensing

To cite this article: Jasmina Lazarević and Bojana Višić 2025 *2D Mater.* **12** 042001

IOP Publishing 2D Mater. 12 (2025) 042001 https://doi.org/10.1088/2053-1583/adf5d4

2D Materials

OPEN ACCESS

RECEIVED
3 April 2025

REVISED
19 June 2025

ACCEPTED FOR PUBLICATION
30 July 2025

PUBLISHED
12 August 2025

TOPICAL REVIEW

2D materials: advances in regenerative medicine and human health sensing

Jasmina Lazarević[1] **and Bojana Višić**[1,2,*]

[1] Center for Solid State Physics and New Materials, Institute of Physics Belgrade, University of Belgrade, Pregrevica 118, Belgrade 11080, Serbia
[2] Department of Condensed Matter Physics, Jozef Stefan Institute, Jamova cesta 39, Ljubljana 1000, Slovenia
[*] Author to whom any correspondence should be addressed.

E-mail: bojana.visic@ijs.si

Keywords: 2D materials, humidity sensing, wearable sensors, transition-metal dichalcogenides, biological activity, regenerative medicine

Abstract

The potential of 2D materials goes beyond the use in electronic applications, extending to regenerative medicine and noninvasive sensing. They hold great promise in these fields due to their remarkable properties, such as high surface area, electrical conductivity and modular chemistry. However, they face significant challenges related to biocompatibility, long-term safety, reproducible large-scale production and lack of standardization and clinical protocols, among others. This review presents a comprehensive overview of their application in regenerative medicine and interactions with various biological systems. We comment on the influence of their innate, but tunable properties on biological response. The chemical composition and exfoliation state of these materials also play a critical role in their bioactivity. The high sensitivity of 2D materials to humidity holds a significant promise in sensor development, which is presented here in detail. Combining them with polymer matrices can enhance the flexibility and performance of the sensors, making them suitable for wearable devices and environmental monitoring. However, challenges remain in the search for the best sensing characteristics, which can be addressed through functionalization and combining with alternative materials like metal oxide nanowires. We critically examined the key challenges (biological interactions, exposure risks, environmental changes and scalability), while assessing their potential for sustainable technologies. Despite the advancements, thorough safety assessments are needed before large-scale production and clinical deployment of 2D materials for health sensing applications.

1. Introduction

The vast, diverse and complex field of 2D materials affects nearly every aspect of life, with applications extending far beyond electronics to energy storage, coatings, cosmetics, food industry and biomedicine. Their biological and environmental interactions are of particular significance, as both living organisms and entire ecosystems ultimately become end users, whether through intentional applications or unintended exposure. Factors such as size, shape and surface characteristics of nanomaterials significantly influence the extent of their stability. These transformations can alter their physicochemical properties, which may, in turn, affect their environmental interactions and potentially modify their toxicity.

There is a notable dominance of high-quality research papers on graphene and its derivatives, likely because they were the first and most extensively studied group of 2D materials. However, inorganic layered materials, particularly MoS_2, have attracted increasing research attention into their bioactivity. In chapter 2, we discuss the recent application advances in regenerative medicine, including cardiac, neural and bone tissue regeneration from the perspective of the materials, emphasizing their functional roles while integrating both physical principles and biological relevance. We also comment on related topics such as drug delivery, organoid culture, angiogenesis, adipogenesis and phototherapy. Composite materials were mentioned only where necessary to emphasize the specific functionalities of 2D materials, such as improving mechanical strength, electrical conductivity or biological performance relevant to regenerative applications.

The field of noninvasive sensing has been increasingly popular due to a variety of possibilities for applications, such as e-skin [1], touchless interfaces, skin patches etc. For example, skin patches can be used to monitor different types of vital human health information. Tracking the levels of humidity of human skin in real-time can provide a variety of crucial information about the health status, such as wound healing, metabolic conditions and effectiveness of cosmetic products [2]. The search for a sensor with high sensitivity, wide detection range, quick response and short recovery time is moving into the area of novel 2D materials. One of the major challenges is to achieve high and even sensitivity for the full range of humidity. 2D materials hold a lot of potential, as their high surface-to-volume ratio allows for better sensitivity to humidity changes. In chapter 3, we review the recent progress in the fabrication of humidity sensors based on 2D materials. Their performance for monitoring human breath, touch, or humidity in agriculture is discussed in chapters 4 and 5. In chapter 6, we have critically addressed key challenges of application of 2D materials, including their interactions with biological systems, exposure risks, environmental transformations, and limitations in scalability and stability, while also evaluating their potential in sustainable technologies. Finally, the last chapter focuses on the future perspectives and mitigation strategies necessary to advance these fields further.

2. 2D materials in regenerative medicine

With the world population getting older, modern medicine aims to restore tissues and organs damaged by injuries, illnesses, aging or congenital abnormalities, with stem cells (SCs) playing a key role in regenerative therapies due to their ability to self-renew, differentiate into tissue specific cells, immunomodulation properties and secretion of paracrine factors [3, 4]. Their inherent plasticity enables precise response to external cues and adoption of specific lineages. From a clinical standpoint, while embryonic SCs (ESCs) and induced pluripotent SCs (iPSCs) offer the highest differentiation potential due to their pluripotency, their use presents significant challenges. ESCs raise ethical concerns related to their isolation, while both ESCs and iPSCs carry risks of uncontrolled differentiation, tissue overgrowth and teratoma formation. On the other hand, adult SCs, such as mesenchymal SCs (MSCs), are multipotent and widely studied due to the ease of their isolation and absence of ethical concerns [5]. It is of utmost importance to ensure SCs survival during transplantation and *in vivo* for the success of regenerative medicine approaches. Beyond regenerative medicine, MSCs serve as valuable models in drug development, offering physiologically relevant alternatives to immortalized cell lines and minimizing dependence on animal testing [6]. Given their lifelong presence, ensuring MSCs survival and functionality is crucial for both regenerative and toxicological research [7].

Although at the forefront as a tool for treating currently incurable medical conditions, SCs still need a little encouragement, and this is where 2D materials come into play. Materials reviewed in this paper, as well as their role in the field of regenerative medicine, are summarized in table 1. They offer not only physical scaffolding for transplanted cells but also actively modulate the biological microenvironment to enhance cellular responses. By mimicking key features of the native extracellular matrix (ECM), such as surface topography, stiffness and biochemical cues, 2D materials can significantly improve SC adhesion, proliferation, and lineage-specific differentiation [8, 9]. Their high surface area and tunable surface chemistry facilitate the adsorption and presentation of growth and differentiation factors, making them powerful tools for directing SC fate. The interaction at the cell-material interface, being the initial point of contact, is crucial. Nanoscale surface features of 2D materials promote focal adhesion formation and cytoskeletal reorganization, both of which are essential for mechanotransduction pathways that drive differentiation. Therefore, the integration of 2D materials into regenerative platforms holds great promise for advancing SC-based therapies by providing structural support and biological guidance within the physiologically relevant environments.

2.1. 2D materials in cardiac regeneration and angiogenesis

Regenerative strategies offer the most promising long-term solutions for cardiovascular diseases, which are the leading cause of death globally, according to the World Health Organization. They are utilizing biomaterial-based scaffolds, SCs and growth factors to repair damaged cardiac tissue, although surgical and pharmacological treatments are still the first line methods. The effectiveness of 2D materials in this context depends on their physicochemical properties, such as high electrical conductivity and surface to volume ratio, mechanical strength and flexibility; biocompatibility and immunomodulatory capabilities [8, 9].

According to the literature, graphene and its derivatives, such as graphene oxide (GO) and reduced GO (rGO), are among the most extensively studied

Table 1. The summary of 2D materials discussed in this paper, their key features and the application in regenerative medicine.

2D material	Key characteristics	Role in regenerative medicine
Graphene oxide (GO)	High surface area; oxygenated functional groups; tunable electrical conductivity	Promotes osteogenesis, enhances angiogenesis, supports stem cell proliferation and differentiation in bone tissue scaffolds, neural tissue regeneration
Reduced graphene oxide (rGO)	Conductive; lower oxygen content; excellent mechanical reinforcement	Enhances osteoblast differentiation, mineralization; supports bone formation *in vivo,* scaffold for neural tissue regeneration
MXenes (e.g. $Ti_3C_2T_x$)	Metallic conductivity; hydrophilic; antioxidant (ROS scavenging); electrically conductive	Creates conductive hydrogel scaffolds for cardiac repair, supports tissue adhesion and cardiomyocyte function
Transition metal dichalcogenides (e.g. MoS_2, WS_2)	Semiconducting; photothermal properties; good biocompatibility	Promotes MSC adhesion and osteogenic differentiation; used in skin, bone and nerve regeneration
Hexagonal boron nitride (h-BN)	Chemically inert; high thermal and mechanical stability	Supports both osteogenic and adipogenic differentiation; neural tissue regeneration

materials, with a wide range of applications in modern medicine. These include their use as scaffolds and guidance materials in regenerative medicine, components in biosensors, as neural interface devices and brain implants, some of which have already entered clinical trial phases [10, 11]. They provide an excellent surface for cell attachment and proliferation, particularly for MSCs and cardiomyocytes, as shown in figure 1. The extent to which GO affects SC behavior is highly dependent on several factors, including concentration, exposure time and surface modifications. Studies suggest that altering the physicochemical properties of GO, such as functionalization with biocompatible coatings, could mitigate some of its adverse effects. In addition to the mechanical support that promotes cell differentiation and consequently, tissue regeneration and functional repair, graphene and its derivatives also guide and enhance differentiation of MSCs towards specific cardiac cell types due to their electrical features [12, 13]. Namely, these materials possess extraordinary electrical conductivity across large surface area which facilitates cell-to-cell communication and maturation by the upregulation of key cardiac markers, such as connexin 43 (a gap junction protein crucial for electrical coupling) and cardiac-specific genes, thereby enhancing the differentiation process. Moreover, the surface of GO, rich in oxygen-containing functional groups, promotes strong interactions with ECM proteins, improving SC adhesion, proliferation and survival. These interactions protect MSCs from oxidative stress and enhance their paracrine signaling, contributing to angiogenesis and tissue repair when transplanted to infracted myocardium [14, 15]. Through these mechanisms, graphene-based materials not only guide SCs differentiation, but also ensure better integration and functionality of the newly formed cardiac tissues, offering promising strategies for cardiac tissue engineering and regenerative therapies. The conductivity of graphene closely resembles that of the native myocardium, which allows these scaffolds to effectively transmit electrical signals between cardiomyocytes, promoting synchronized contractions and improved tissue integration. Myogenic scaffolds require higher conductivity and mechanical robustness to facilitate rhythmic, force-generating contractions, whereas neurogenic scaffolds prioritize directional growth, synapse formation, and moderate signal transmission support [13]. Functionalized graphene derivatives (e.g. GO functionalized with peptides or proteins) further improve cell adhesion, viability, and differentiation into cardiac-like cells by mimicking physiological conditions in ECM [16, 17]. It was observed that graphene-coated surfaces promote cardiomyocyte alignment, mimicking the native structure of heart tissue, which is crucial for functional integration. However, recent findings of Heo *et al* [18] indicate that GO may have unintended consequences when interacting with human iPSCs generated from fibroblasts. This raises concerns about its suitability for regenerative medicine applications. One of the most critical observations is that exposure to GO of varying lateral sheet sizes (in average 150 nm, 400 nm and 1 μm) and concentrations appears to interfere with key molecular pathways that sustain pluripotency [18]. Human iPSCs rely on a strictly regulated microenvironment to maintain their undifferentiated state, and any disruption to this balance can lead to premature lineage commitment. In this study, when cultured in cardiomyocyte induction medium, the upregulation of cardiomyocyte marker NKS2.5 was evidenced. This premature differentiation is a significant challenge, as maintaining precise control over SC behavior is

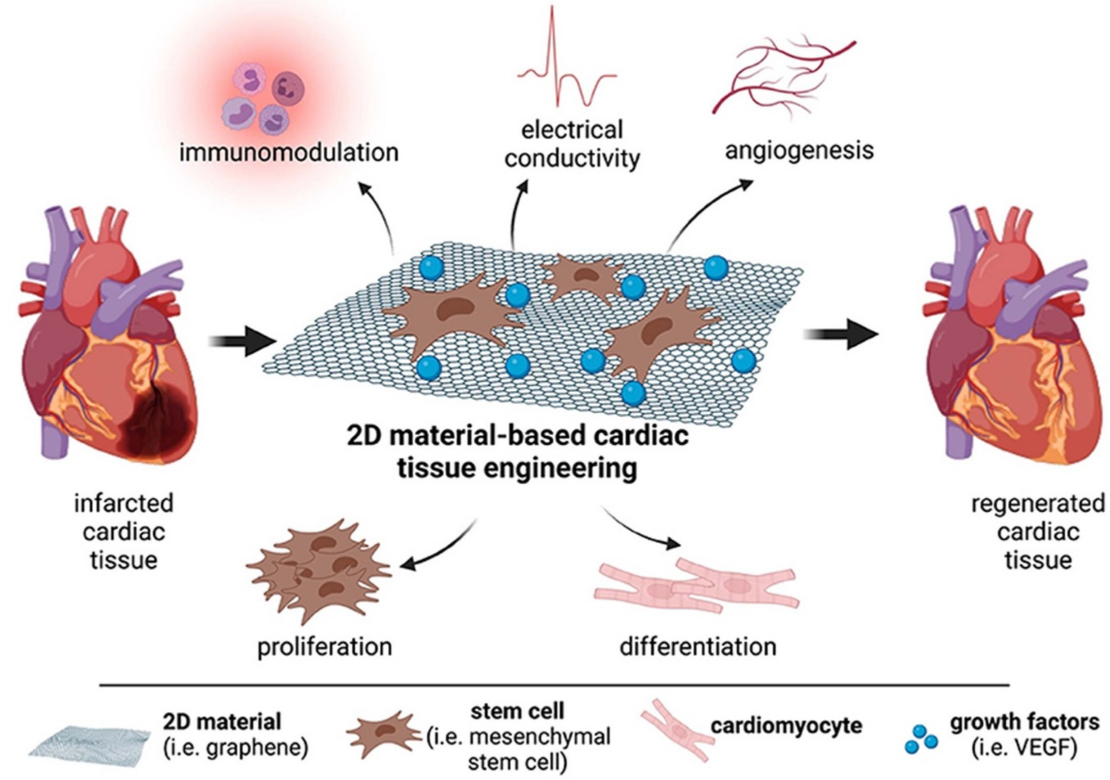

Figure 1. The potential of 2D materials for cardiac repair and regeneration. Graphene or graphene derivatives can act as scaffolds for MSCs and deliver growth factors to the infracted area. Reproduced from [8]. CC BY 4.0.

essential for their successful application in regenerative therapies. When intentional, the ability to interfere with differentiation is valuable, but in this case, the lack of control could undermine the reliability of GO as a biomaterial for SC-based treatments. Additionally, GO increased both reactive oxygen species (ROSs) and caspase-3 activity as a result from cellular uptake initializing apoptotic signal in concentration of 100 μg ml^{-1}. The hiPSCs lost their pluripotency, based on significant loss in pluripotency markers OCT-4 and NANOG regardless the lateral sheet size.

GO-based 3D scaffolds (including pure and functionalized GO) provide structural support that enhances cell proliferation, differentiation and tissue formation, making them particularly valuable in regenerative medicine and organoid development [19, 20]. They offer several advantages over Matrigel, which is derived from mouse tumor ECM and shows batch-to-batch variability, undefined composition and presence of xenogeneic contaminants. GO-based scaffolds have been used in organoid cultures to create disease models that closely resemble *in vivo* conditions and are essential for studying disease mechanisms, testing new drugs and understanding tissue responses to different treatments. In a recent study, 3D liver organoids (LOs) composed of upcyte® human hepatocytes, liver sinusoidal endothelial cells, and mesenchymal stromal cells were repeatedly exposed to GO at concentrations of 2–40 μg ml^{-1}. While the LOs maintained overall viability and structural integrity, they showed a downregulation of CYP3A4 expression, suggesting potential disruption of hepatic metabolic function [21]. These findings point out the value of LOs as physiologically relevant *in vitro* models for evaluating the long-term and cumulative effects of nanomaterials, especially under conditions resembling real-life exposure scenarios. Due to its bio functional properties, GO can also act as a drug delivery system, allowing controlled and targeted drug release in cancer therapy and regenerative applications.

The recent study by Yu *et al* highlights MXene-incorporated hydrogels as a promising platform for functional cardiac regeneration following an ischemic injury [22]. A $Ti_3C_2T_x$ MXene-based hydrogel was developed by incorporating MXene nanosheets into a GelMA–PANI matrix, achieving conductivity of 0.23 S m^{-1} and a compressive modulus of ∼35 kPa, closely mimicking native myocardial tissue. *In vitro*, neonatal rat cardiomyocytes cultured on the hydrogel showed enhanced viability, spreading, and expression of cardiac-specific markers (cTnT, α-actinin, connexin-43), along with synchronous contractions and improved calcium signaling. *In vivo*, MXene hydrogel treatment led to significant functional recovery, with increases in ejection fraction (16.5%) and fractional shortening (12.8%), alongside reduced infarct size, fibrosis, and increased angiogenesis. Immunofluorescence showed better tissue preservation and cellular alignment. The MXene component also provided antioxidative and anti-inflammatory effects by scavenging ROS and reducing TNF-α and IL-6 expression. The hydrogel biodegraded over 4 weeks, aligning with tissue healing.

Enhancing angiogenesis, as focal point in tissue engineering and SC therapy, can improve the success of transplanted tissues and the repair of damaged organs, like the heart after a myocardial infarction. GO and rGO materials significantly influence the angiogenic differentiation of hUC-MSCs [12, 23]. Cells cultured on large GO flakes demonstrated a notable increase in the expression of angiogenic markers such as GATA-2, endoglin and VE-cadherin. The expression levels were up to 3.5 times higher compared to cells grown on standard culture surfaces. Interestingly, the differentiation medium did not enhance this effect further, indicating that the GO-lf surface itself played a critical role in promoting angiogenic differentiation. Additionally, cells cultured on rGO-lr-P60 surfaces (a slightly reduced form of rGO) exhibited significantly elevated expressions of angiogenic markers, particularly GATA-2, which showed a 110-fold increase in expression compared to standard culture surfaces. The promotion of angiogenesis was further supported by functional assays, where hUC-MSCs demonstrated enhanced capillary tube formation on GO and rGO surfaces, indicating improved proangiogenic capabilities.

2.2. 2D materials in bone tissue regeneration

Bone tissue engineering aims to develop materials that surpass traditional bone autografts and allografts and the process must be finely tunable and dynamic as osteogenesis and bone remodeling physiologically are. Materials used must account for age-related changes in bone microstructure and diminished regenerative capacity for elderly patients and, in contrast, pediatric applications require materials with adaptable structural properties or those that facilitate remodeling to support skeletal growth. Additionally, sex-related differences in bone microstructure and size further emphasize the need for personalized approaches. In natural bone, bioelectrical signals such as piezoelectricity, ferroelectricity and pyroelectricity are generated in response to mechanical stress, polarization and temperature variations, respectively. These signals play a crucial role in regulating cellular activities essential for bone healing, remodeling and growth [24, 25]. Piezoelectricity, produced by the deformation of collagen and other structural components, generates localized electrical charges that influence osteoblast function and guide SC differentiation toward bone-forming pathways. Ferroelectricity, which involves reversible spontaneous polarization under an external electric field, provides continuous electroactive signals that support bone matrix mineralization. Arising from temperature-induced potential changes, pyroelectricity introduces additional electrical stimuli that may be particularly relevant during inflammatory responses or thermal fluctuations following injury. These mechanisms form a dynamic bioelectrical environment that is integral to bone regeneration and scaffolds should not only structurally support but also [24] generating bioelectrical stimuli to promote tissue regeneration. Moreover, scaffold materials in bone tissue engineering are designed to gradually degrade and be replaced by newly formed tissue that closely replicates the mechanical properties of native bone. This ensures that the regenerated bone can provide the necessary strength, stability and functionality required for long-term integration within the body. When it comes to osteogenesis, it was demonstrated that graphene can promote the osteogenic differentiation of hMSCs even without a key growth factor in bone formation, BMP-2 [26, 27]. Higher calcification was observed by alizarin red staining in the presence of graphene. Additionally, variations in osteogenesis were noted depending on the presence or absence of both graphene and BMP-2. This effect is attributed to the localized accumulation of osteogenic molecules, such as dexamethasone and β-glycerophosphate, facilitated by non-covalent interactions like π–π stacking with the graphene surface [28]. A single layer GO at low doses increases the roughness and decreases the stiffness of the alginate hydrogels in which single human BMSCs have been encapsulated, as indicated by microfluidics-based approach. This enhances cell viability, proliferation and osteogenic differentiation and thus, offers a promising approach for minimally invasive injectable bone tissue transplants [29]. When Raw264.7 cells were cultured on bioactive glass/GO scaffolds, GO significantly facilitated the polarization of macrophages toward the M2 phenotype, promoting the secretion of osteogenic and angiogenic factors. This, in turn, enhanced the osteogenic differentiation of rat BMSCs and stimulated angiogenesis in endothelial cells [19]. The degradation rate of the scaffold is carefully tuned, combined with biopolymers like collagen and gelatin, to align with the pace of natural bone regeneration, preventing structural deficiencies while promoting seamless tissue remodeling [26, 30, 31]. Furthermore, 3D printed composite materials that include GO and polycaprolactone (PCL) are designed as scaffolds for application in wound healing and tissue engineering, encompassing its mechanical strength with biological functionality. In GO-PCL composite, GO adds strong antibacterial properties, disrupting bacterial membranes

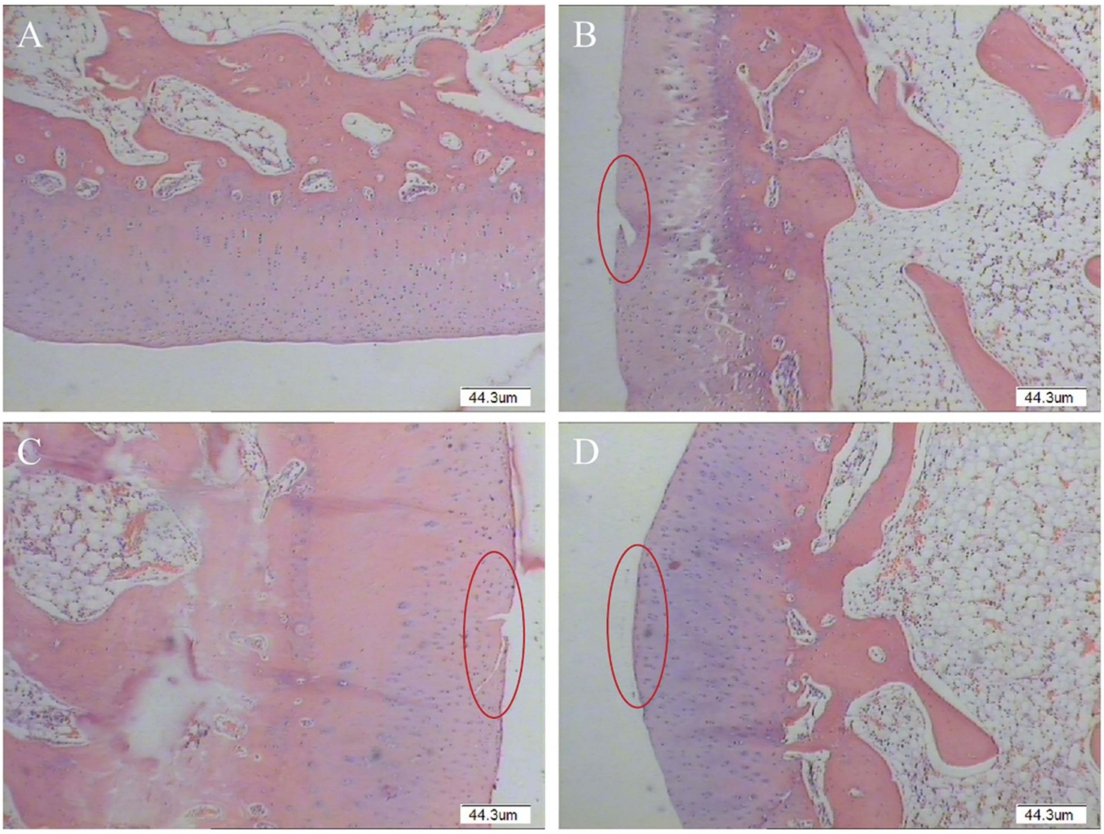

Figure 2. Patho-histological observation results of modified papain release joint injection group. (A) Blank, (B) GO group, (C) UCMSCs group, (D) GO + UCMSCs group. Red circle denotes cartilage erosion area. Reproduced from [33]. CC BY 4.0.

and inducing oxidative stress, minimizing in that way the risk of bacterial infection during the healing process [32]. On the other hand, its low cytotoxicity and high biocompatibility enhance its potential for various applications. Importantly, umbilical cord-derived MSCs (hUC-MSCs) loaded with GO granular lubricant can enhance chondrocyte secretion, lower joint inflammation, improve subchondral bone osteoporosis and support cartilage regeneration in knee osteoarthritis animal models (see figure 2) [33]. GO serves as a multifunctional reinforcing agent that not only strengthens the scaffold mechanically but also amplifies its bioelectrical functionality. When incorporated into polyvinylidene fluoride (PVDF) scaffolds produced by selective laser sintering, GO significantly promotes the transformation of the polymer's α phase to the electroactive β phase [34]. This is achieved through strong hydrogen bonding between the oxygen-containing groups of GO and the fluorine atoms in PVDF, which induces chain alignment favorable to β-phase formation. As a result, the PVDF/0.3GO scaffold demonstrated a marked increase in piezoelectric performance, achieving an output voltage of ∼8.2 V and current of ∼101.6 nA—improvements of 82.2% and 68.2%, respectively, compared to pure PVDF. In addition to enhancing electrical output, GO also reinforced the scaffold mechanically, leading to a 97.9% increase in compressive strength and a 24.5% increase in tensile strength. These improvements are attributed to the strong interfacial interactions between GO and the PVDF matrix. Furthermore, *in vitro* studies confirmed that the enhanced electrical activity positively influenced cell behavior.

Transition metal dichalcogenides (TMDs) offer key advantages over graphene and its derivatives in regenerative medicine, primarily due to their intrinsic semiconducting properties and photothermal/photodynamic capabilities. Unlike graphene, which lacks a bandgap, TMDs enable light-responsive and electrically regulated applications, such as controlled drug release and phototherapy which enhance cell behavior and tissue repair [35]. Their broader chemical diversity, stimuli-responsiveness and ability to support cell differentiation without extensive functionalization make them especially attractive for developing smart, bioactive scaffolds. Molybdenum disulfide (MoS_2) promotes osteogenic differentiation of hMSCs by facilitating the adsorption of differentiation-inducing factors, enhancing cell adhesion and promoting differentiation into osteoblasts by upregulating osteogenic marker genes. This was confirmed through various assays, including optical microscopy and alizarin red S staining, which

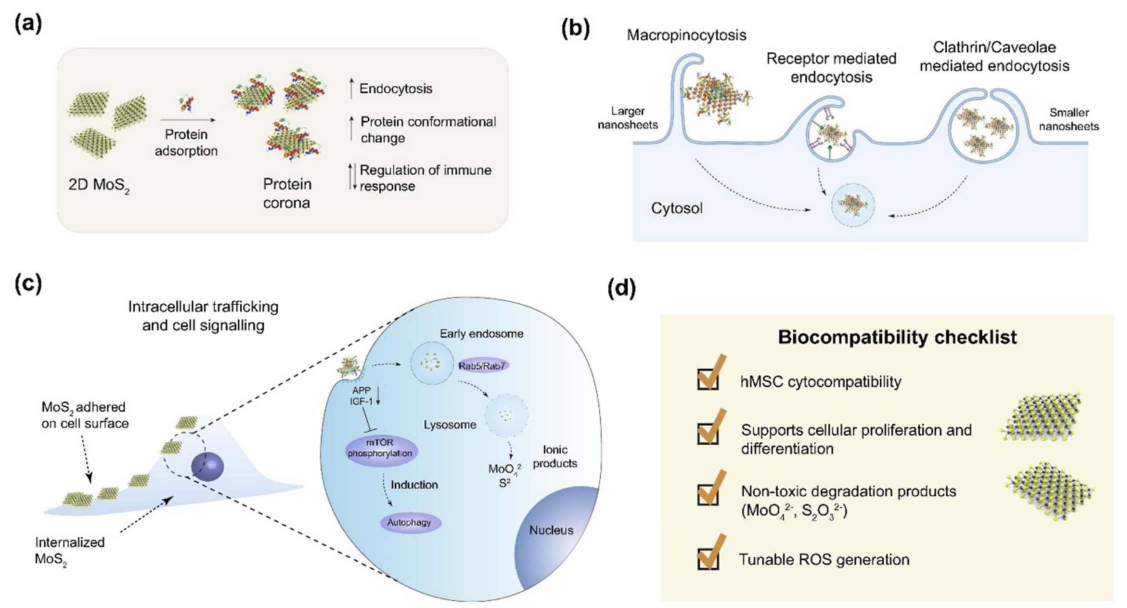

Figure 3. MoS_2-protein interactions, cellular uptake and biocompatibility. (a) Internalization of 2D MoS_2 nanosheets with proteins result in the formation of a protein corona on the surface of the nanosheets, which regulates different cellular processes like nanosheet uptake, protein function and regulation of immune response. (b) Size dependent cellular uptake of 2D MoS_2 nanosheets occurs through micropinocytosis or endocytosis. Presence of corona also facilitates receptor mediated endocytosis. (c) Intracellular trafficking of 2D MoS_2 nanosheets through endo-lysosomal pathway leads to its degradation into ionic products. (d) Biocompatibility checklist of 2D MoS_2 nanosheets. Reprinted from [37], Copyright (2022), with permission from Elsevier.

highlighted significant mineralization, a fingerprint of osteogenic differentiation. Furthermore, gene expression analysis validated the upregulation of key osteogenic marker genes, indicating that MoS_2 effectively supports the osteogenic lineage. Adversely, it has minimal influence on adipogenic differentiation. Due to its photothermal properties, light-mediated modulation of SCs behavior can further influence differentiation outcomes [36]. Similar to MoS_2, tungstensulfide's (WS_2) surface properties enhanced the adhesion of hMSCs and facilitated their differentiation into osteocytes with minimal or no influence over adipogenesis. Both of these materials possess strong in-plane covalent bonds and weak out-of-plane van der Waals interactions, with surface roughness that promotes interactions between cells and surface, tunable for optimization. Moreover, both of these materials show minimal cytotoxicity [27]. In SC research, MoS_2 nanosheets provide biophysical stimuli that enhance adhesion, proliferation and differentiation. Their nanostructured surfaces mimic extracellular matrices, improving cytoskeletal organization and focal adhesion formation, as shown in figure 3 [37]. Biomolecule corona on MoS_2 nanosheets that dictates its biological interaction and compatibility is, unlike in graphene-protein interactions, the consequence of van der Waals energies and electrostatic interactions that regulates the conformation of the adsorbed protein [36]. That initial interaction with proteins allows cellular uptake, intracellular trafficking and immune responses. Cellular uptake of MoS_2 occurs mainly via endocytosis, influenced by factors like nanosheet size, surface chemistry and functionalization. Furthermore, MoS_2 nanoflowers exhibits interactions with immune cells, such as macrophages and dendritic cells, modulating immune responses, leaving the space to be used as drug delivery vehicle for immunomodulation [38]. It can promote pro-inflammatory responses at higher concentrations but also shows potential in immunomodulation strategies. The *in vivo* formation of a biomolecular corona on nanoparticles (NPs) has only recently been recognized as a critical advancement in the field of nanomedicine, facilitating a range of significant biomedical applications, including the modulation of immune responses, targeted delivery through endogenous pathways and the scavenging of disease-associated biomarkers [39].

On the other hand, boron nitride (BN) as a chemically inert, thermally conductive and electrically insulating 2D material with excellent mechanical strength supported both, osteogenic differentiation and adipogenesis, but with significantly higher potential for adipogenesis, which was proved with oil red O staining and significantly elevated expression levels of adipogenic marker genes. This is explained by favoring the adsorption of adipogenic-inducing factors and relatively smoother surface which provides less mechanical stimulation and promotes lower cytoskeletal tension and rounded cell shape characteristic for adipogenesis. Moreover, BN stimulates adipogenesis-related signaling pathways like such as the PPARγ and C/EBPα while providing insufficient mechanical or biochemical stimuli to effectively trigger osteogenic differentiation [40, 41].

2D metal carbides and nitrides (MXenes), known for their exceptional electrical conductivity, play a significant role in promoting the growth and differentiation of electrically active tissues, such as neural and cardiac tissues. Strong interlayer interactions in MXenes yield a stable aqueous colloidal suspension which allows endurance and lower cytotoxicity in biological environment [42]. Through the combined effects, photoactivated MXene promotes bone and soft tissue repair at the same time [43]. The photoactivation of MXene nanosheets ($Ti_3C_2T_x$), which converts light into localized heat, occurs through the absorption of near-infrared (NIR) light (808 nm). This photothermal activation enhances the antibacterial properties of MXene, generating sufficient heat to expose antibacterial effect on pathogenic bacteria, including methicillin-resistant *S. aureus*. The photoactivation also stimulates angiogenesis by upregulating pro-angiogenic factors (such as VEGF) while promoting cell migration and proliferation, accelerating wound healing. Moreover, MXene exposed to NIR light indirectly activates ERK signal pathway in adipose-derived SCs *in vitro*, elevating calcium mineralization by improving the activity of alkaline-phosphatase, driving osteogenic differentiation. Despite their promising potential in healthcare, MXenes face several limitations that must be addressed for successful biological application. Their tendency to oxidize in physiological environments compromises stability and functionality over time. Additionally, concerns regarding cytotoxicity, inconsistent surface terminations and unpredictable interactions with biological media raise challenges in ensuring biocompatibility and safety. The complexity of their synthesis, often involving harsh chemicals, further limits scalability and clinical translation. Therefore, comprehensive *in vivo* studies and standardized protocols are essential to fully realize MXenes' potential in biomedical settings [44]. In addition to their electrical properties, MXenes show remarkable mechanical robustness, making them ideal candidates for reinforcing scaffolds designed for load-bearing tissues, such as bone and cartilage. Their mechanical strength enhances scaffold stability, supports cellular integration and ensures better structural integrity during tissue formation.

2.3. 2D materials in neural tissue regeneration

Neural repair and regeneration are inherently slow and limited processes, particularly within the central nervous system, where neurons have a restricted ability to regenerate after injury. This limited regenerative capacity is due to factors such as inhibitory environments, the formation of scar tissue, and the complex structure of neural networks, which altogether obstruct the restoration of normal neural function [45]. Graphene-based scaffolds have demonstrated promising potential in promoting neuronal regeneration, particularly for repairing peripheral nerve injuries. In an extensive 18 month rat study, these scaffolds exhibited low toxicity, with no significant adverse effects observed in major organs such as the liver, kidneys, heart, lungs or spleen [46, 47]. These scaffolds effectively supported myelination, axonal growth and improved both locomotor and electrophysiological functions. The enhanced expression of myelin basic protein and Tuj1 highlighted the scaffolds' role in facilitating myelin and axonal regeneration. Moreover, they contributed to angiogenesis, a critical process for nutrient supply and tissue repair, by upregulating CD34 and vascular growth factor expression. Notably, graphene-based scaffolds exhibited dual regulation of Schwann cells and astroglia, positively influencing both central and peripheral nervous systems to promote neural repair. Despite these advancements, several challenges hinder clinical translation. The variability in biocompatibility results, stemming from differences in experimental models, presents a significant hurdle. Concerns about the long-term toxicity and limited biodegradability of graphene-based materials, especially at higher concentrations, also require deeper investigation. Additionally, understanding the interactions between graphene-based scaffolds and diverse cell types, alongside their effects on immune responses in large animal models, is crucial to ensure safety and effectiveness before advancing to human clinical trials. The graphene-based neural interface developed by INBRAIN Neuroelectronics represents one of the most advanced and successful examples of translating 2D material technologies from academic research into real-world medical applications [11]. By overcoming key challenges in scalability, industrial fabrication, regulatory approval and interdisciplinary collaboration, INBRAIN not only brought graphene-based devices closer to clinical use but also demonstrated a viable pathway for other emerging nanotechnologies. Their progress, culminating in FDA Breakthrough Device Designation and the launch of first-in-human clinical trials, serves as a model for how strategic partnerships, sustained funding and startup-driven innovation can bridge the critical 'lab-to-fab' gap in advanced medical technologies. Functionalization of 3D nanofibrous scaffolds made of decellularized ECM derived from porcine adipose tissue with polydopamine (PDA)-rGO enhanced its bioactivity and electrical conductivity, both very important for neural tissue engineering. Doping with PDA-rGO significantly boosted the performance of scaffolds towards neuronal differentiation, particularly in the 3D environment, which on its own created biomimetic environment that supported neural SCs adhesion, proliferation, migration and differentiation

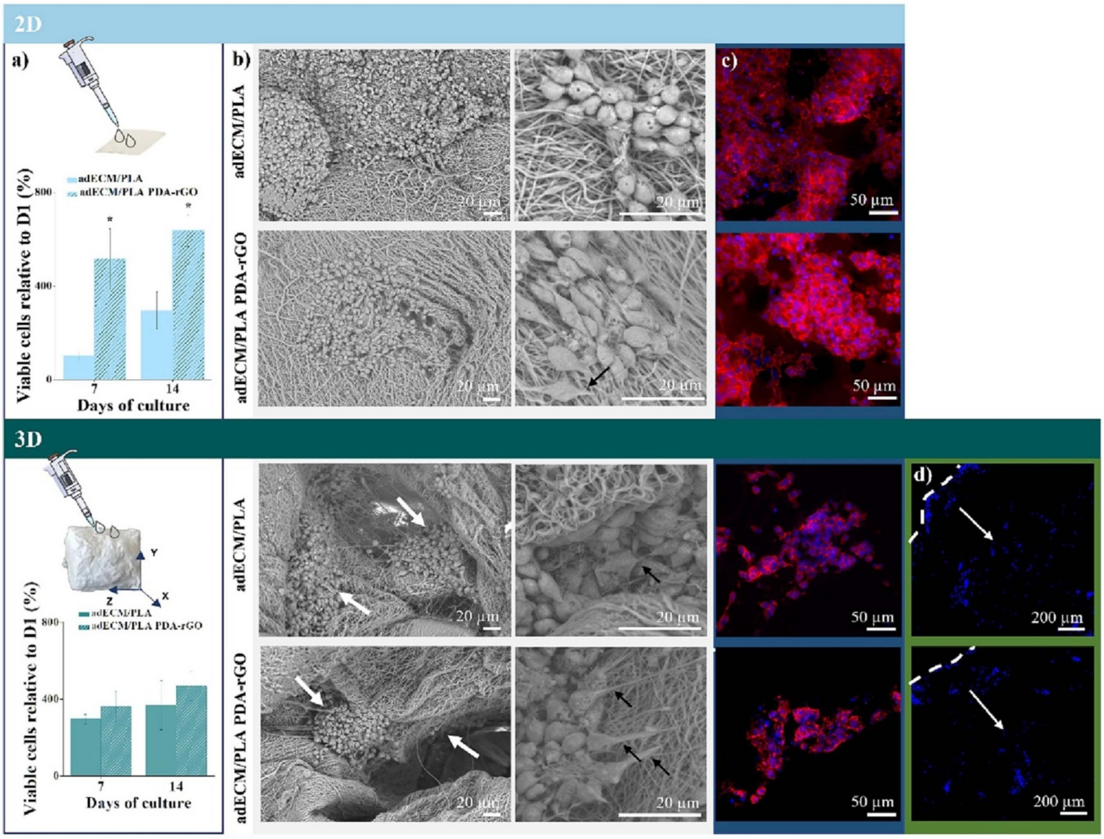

Figure 4. Proliferation and morphology of NSC-seeded bidimensional and three-dimensional platforms: (a) percentage of viable NSCs on the platforms relative to the adhered cells on day 1, after 7 and 14 d of culture and schematic illustrations of the seeding process in each platform; (b) SEM images of the NSCs-seeded platform after 7 d of culture, with white arrows highlighting the cellular clusters and black arrows pointing to the out-growing processes; (c) immunocytochemistry of actin filaments (phalloidin in red) and nuclei (DAPI in blue) of the NSC-seeded platform after 14 d of culture; (d) DAPI staining of the cross-sectioned NSC-seeded 3D platforms, with white arrows showing the cellular migration pathway. Reprinted from [48], Copyright (2023), with permission from Elsevier.

[48]. The scaffold also facilitated spontaneous differentiation, favoring a neuronal over an astrocytic lineage. In more detail, PDA-rGO in 3D platforms significantly enhanced neuronal differentiation, resulting in a 1.26-fold increase in Tuj1 levels and a 1.72-fold increase in MAP2a/b neuronal isoforms (see figure 4). Graphene, GO and rGO nanosheets, thanks to their large surface area, functionalized with molecules that enhance the ability to penetrate blood–brain barrier (BBB), can carry a variety of biomolecules, targeting the specific cell type or area in central nervous system. By serving as efficient drug delivery systems capable of crossing the BBB with ease, these nanosheets offer a promising solution to overcoming the challenges associated with drug delivery to the brain [49, 50]. The functionalization of rGO with polydopamine (PDA) has been shown to significantly influence SCs behavior, particularly by encouraging spontaneous differentiation toward the neuronal lineage [48]. This effect is observed in both 2D and 3D culture platforms, suggesting that PDA-rGO can serve as a powerful biointerface for neural tissue engineering. The gas foaming technique offers a simple yet effective method for generating 3D nanofibrous constructs with tunable physical properties. This approach allows the creation of biomaterial-based microenvironments that closely replicate native extracellular matrices, revealing biomaterial-induced cellular responses that may remain undetected in traditional 2D cultures. By incorporating PDA-rGO into gas-foamed 3D scaffolds, its potential as a neurogenic biomaterial can be assessed, revealing new possibilities for neural tissue engineering and regenerative medicine. The ability to fine-tune material properties using gas foaming further enhances its adaptability for various biomedical applications. Additionally, excellent electrical conductivity attributed to the structure of MoS_2 with unsaturated d-orbitals, and biocompatibility create nurturing microenvironment for neural SCs differentiation, allowing their attachment to porous architecture, efficient charge transport at the cell-membrane interface, proliferation and differentiation into neural cells [51]. This differentiation is marked by the increased expression of key neural markers such as Tuj1, GFAP, and MAP2 over extended culture

periods [52]. The porous nature enables stronger protein absorption, including growth factors like EGF and FGF, which further supports the maintenance of neural SCs stemness and promotes differentiation efficiency over time.

Its structure also provides excellent template for cell elongation, which is a preferred feature in neural tissue regeneration. Moreover, 3D cylindrical scaffolds made of MoS_2-PVDF hybrid films, with randomly assembled MoS_2 nanoflakes, showed potential for nerve regeneration encompassing flexibility, conductivity and compatibility, hence mimicking natural neural structures [51]. Significant regenerative potential through the light responsive properties of 2D materials with the focus on G and derivatives and TMDs lays within their capability to finely modulate cellular response. Excellent conductivity and photothermal capabilities stimulate cell growth, differentiation and tissue regeneration, particularly in neural and muscle tissues by non-genetic optical modulation. NIR light stimulation of MoS_2 nanosheets influenced more genes related to cell migration and wound healing in MSCs than nanosheets itself, as evidenced by transcriptome sequencing [53, 54].

BN nanosheets functionalized polycaprolactone channel scaffold was evaluated for neuronal repair through piezocatalytic stimulation [55]. This 3D scaffold, produced by layer-by-layer droplet spraying method, is highly elastic, hydrophilic and biocompatible [56]. After ultrasonic actuation, the scaffold generates bioelectrical signals that promote the secretion of neurotrophic factors, enhancing Schwann cell viability and modulate ROS levels to maintain metabolic balance. Schwann cell cultured on this scaffold showcased an increased expression of proliferative and neural markers (Ki67, Tuj1 and MBP), alongside reduced oxidative stress and elevated growth factor expression. *In vivo,* improved nerve regeneration, remyelination and functional recovery in a rat sciatic nerve defect model were observed. Higher nerve conduction velocities, enhanced axonal alignment and improved muscle reinnervation compared to control groups were noted as well as promoted angiogenesis and reduced amyotrophy. High biocompatibility of the scaffold played significant role all along.

3. 2D materials as humidity sensors

The increasing interest in wearable devices, namely, flexible and transparent sensors, has expanded the demand for novel materials [57]. Electronic devices that can be attached to the skin and that are able to continuously record vital signs are going to minimize both the size and the cost of healthcare monitoring. These types of devices require developing of a variety of noninvasive sensors for monitoring of human physiological biomarkers. For example, tracking the gas molecules that are transmitted from the body can play an important role in personalized medicine. The main requirements for these functional sensors is to be able to get comfortably attached on human skin and continuously and unobtrusively monitor human activities. Hence, this type needs to be conformable to the skin, and the substrate should not be an irritant. Some of the activities that should be uninterupptedly tracked are vital signs (respiration, pulse, blood pressure) and physiological activities (muscle movements, cognitive states). Furthermore, basic humidity sensors can have wide application in various fields outside of medical uses, such as environmental monitoring, agriculture, industrial production, process control and safety.

Some of the drawbacks of commercially available sensors is that they are mostly made of polymer films or porous ceramics, and are unable to operate at high humidity levels, have slow response time, high levels of hysteresis and a long-term drift. 2D layered materials have been extensively studied and shown great potential as resistive gas sensors due to their excellent electrical, physiochemical, and mechanical properties [58–60]. The need for these types of sensors is becoming highly important as the air pollution, caused by gases such as NO_2, SO_2, CO; VOCs and particulate matter, becomes ubiquitous. In this review, we focus on their emerging potential as humidity, human respiration and touch sensors. We firstly describe various mechanisms for humidity sensing from the aspect of sensor fabrication. In the next step, we assess the performance of different families of 2D materials, with the summary of relevant parameters.

3.1. Humidity sensing mechanisms

Humidity sensors can be fabricated through a variety of methods. While the majority of the commercially available sensors are capacitive-based, devices based on resistor/impedance response are becoming increasingly popular due to easier fabrication. In recent years, new operating mechanisms are emerging based on FET, QCM and fiber-optics. Here, we outline the most prominent sensing mechanisms and their advantages and disadvantages.

3.1.1. Capacitive

Commercially available humidity sensors are mostly based on the capacitive technique, where the dielectric constant of the active layer changes in response to humidity. The standard mechanism consists of parallel plate capacitors, where an intermediate moisture-sensitive dielectric layer is sandwiched between two metal electrodes. As the output, the change in capacitance is recorded, which occurs when the distance between the two electrodes changes (i.e. upon water molecule adsorption). The variations in capacitance also depend on the area of the electrodes and the dielectric constant of the intermediate material. The straightforward assembly of parallel plate capacitors has led researchers to develop capacitive sensors using diverse materials, and to improve their flexibility and sensitivity. Nevertheless, capacitive sensors have several drawbacks, including hysteresis, stability at high temperatures and humidity levels, limited durability against certain organic vapors and their fabrication can be expensive.

The capacitance value is defined as:

$$C = \varepsilon A/d$$

where ε represents the dielectric constant, A the area of the capacitor, and d is the distance between the capacitor plates.

The response of the sensor is defined by the following formula:

$$\text{Response} = \frac{C - C_0}{C_0}\, x\ 100\%$$

where C_0 and C represent the capacitance measured under dry air and measured humidity, respectfully.

Sensitivity of the sensor is calculated using the equation

$$S = \frac{\Delta R}{R\Delta\% RH} X100$$

where S is defined as the percent change in resistance divided by the percent change in relative humidity (RH), RH is defined as the ratio of 'water vapor present in a particular volume and at a particular temperature' to the 'maximum capacity of air to absorb the water molecule at the same volume and temperature'.

The response time is defined as the time required for reaching 90% of the total response value, while the recovery time is defined as the time required to return the response to 10% of the total response value.

The change in RH is detected as the change in voltage, as the conversion circuit (usually, a simple RC circuit) is transforming the change in the capacitance into change in voltage.

Capacitive-based humidity sensors have been reported on GO [61–65] and MoS_2 [66], which will be discussed in more detail in section 3.2. Figure 5 depicts two setups based on GO [61] and GO-PSS film [63].

3.1.2. Resistive

In contrast to capacitors, resistive humidity sensors have a simpler structure and are easier to integrate with CMOS technology. As a result, considerable research is focused on the development of resistive humidity sensors, which are expected to lower the cost per unit and offer improved long-term stability.

The sensing mechanism is based on recording the change in humidity, as the adsorbed water molecules affect the electronic density of states and the carrier concentration of the active material and change its conductivity.

The response is defined as:

$$\text{Response} = \frac{R - R_0}{R_0} x100\%,$$

where R_0 and R represent the resistance measured under dry air and measured humidity, respectfully.

A typical response of this type of setup, prepared on a hybrid composite of rGO and MoS_2 [67], is shown in figure 6.

3.1.3. Impendence

Sensor with impedance output is structurally similar to the resistive sensors, whereby they consist of three parts, a substrate, interdigital electrodes, and the sensing material. The output is highly dependent on the frequency and RH. Sensors show better performance at lower frequencies, as the impedance significantly increases with the decrease in both RH and frequency. In the typical setup, the output current is measured by applying a sinusoidal voltage to the electrodes, and the impedance is calculated as the voltage/current ratio. Some of the reported impedance-based sensors used GO [68], MoS_2 [69, 70], MXene [71], Al_2O_3 NTs [72] as the sensing material, and their performances will be discussed in detail in section 3.2. Two typical setups are depicted in figure 7.

3.1.4. Other sensing mechanisms

Other than the previously explained mechanisms, based on resistive or capacitive effects, new approaches have been proposed. Here, we discuss the most promising ones, which bring forth better integration into electronics, or miniaturize the size of the sensing device.

QCM

Quartz crystal microbalance is a technique capable of detecting mass change as small as the sub-nanogram, making it suitable for vapor phase sensors. A thin slice of quartz crystal is placed in a circuit, and with the applied voltage, alternating compression and stretching vibrations appear [73, 74]. The change in the resonant frequency can be detected, as the adsorbed water molecules change the mass of the crystal. The amount of the adsorbed water and the resonant frequency change are correlated, allowing for the calculation of the humidity level. This type of setup is shown in the left panel of figure 8.

Potentiometric

A self-powered potentiometric mechanism was reported [75]. The sensing mechanism was based on a sandwiched material structure, made of rGO/GO/-foamed metal (such as nickel, zinc, iron and copper), and it modulates the measured potential difference between the two electrodes by humidity

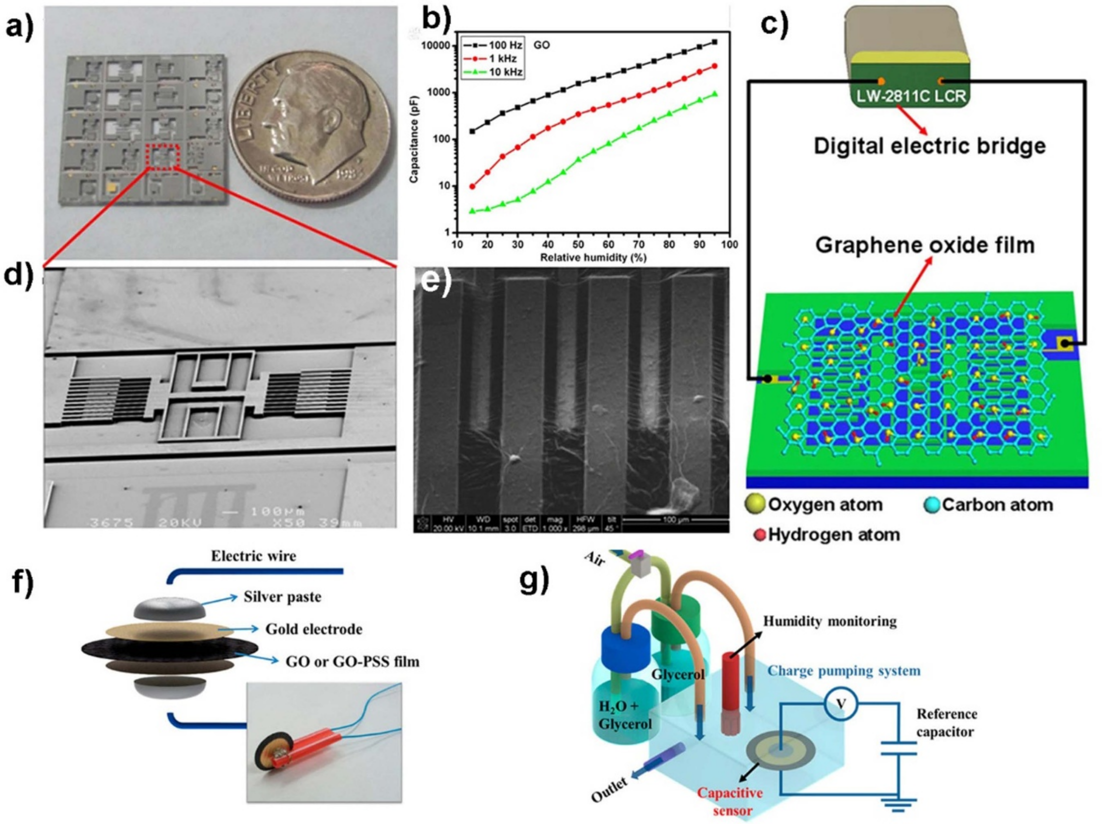

Figure 5. Capacitive-type humidity sensors based on (a)–(e) GO [61] and (f), (g) GO-PSS film [63]. (a) Digital photographs of the device, (b) SEM image of the area set off by a red dashed line, (c) output capacitances of sensors as a function of RH, (d) SEM image of interdigitated electrodes covered with GO films, (e) schematic diagram of the humidity testing system of GO as a humidity sensing material between the two sets of interdigitated electrodes. (a)–(e) Reproduced from [61], with permission from Springer Nature. (f) Sensor based on the GO and GO-PSS dielectric films. An optical image of the fabricated sensor is shown in the inset. (g) Schematic diagram of the RH controlled-environment chamber and charge pumping system. Reprinted with permission from [63]. Copyright (2014) American Chemical Society.

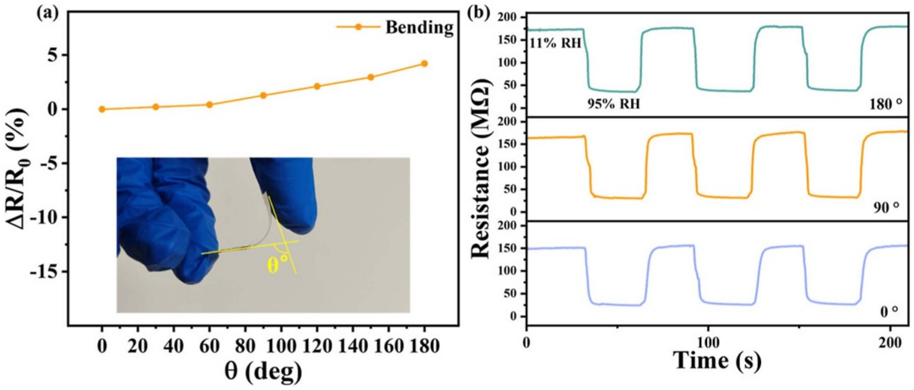

Figure 6. Resistance response of a device based on rGO and MoS_2 as it was gradually bended in the atmospheric environment. (b) Humidity experiments of a device with the relative humidity change between 11% RH and 95% RH as it was bended with different bending angles (0, 90, and 180°). Reprinted with permission from [67]. Copyright (2024) American Chemical Society.

stimulation. While the resistive or capacitive devices are difficult to miniaturize because they require an external power supply, potentiometric humidity-transduction method is able to detect both steady and rapid humidity response of multiple cycles with high response value and short response/recovery time (RRT). The external humidity stimuli can regulate the hydration across GO, as a solid electrolyte, and bring about a change in the output voltage measured between the two electrodes. The sensor showed high stability, high RRT and was able to monitor both the static and dynamic humidity stimulation.

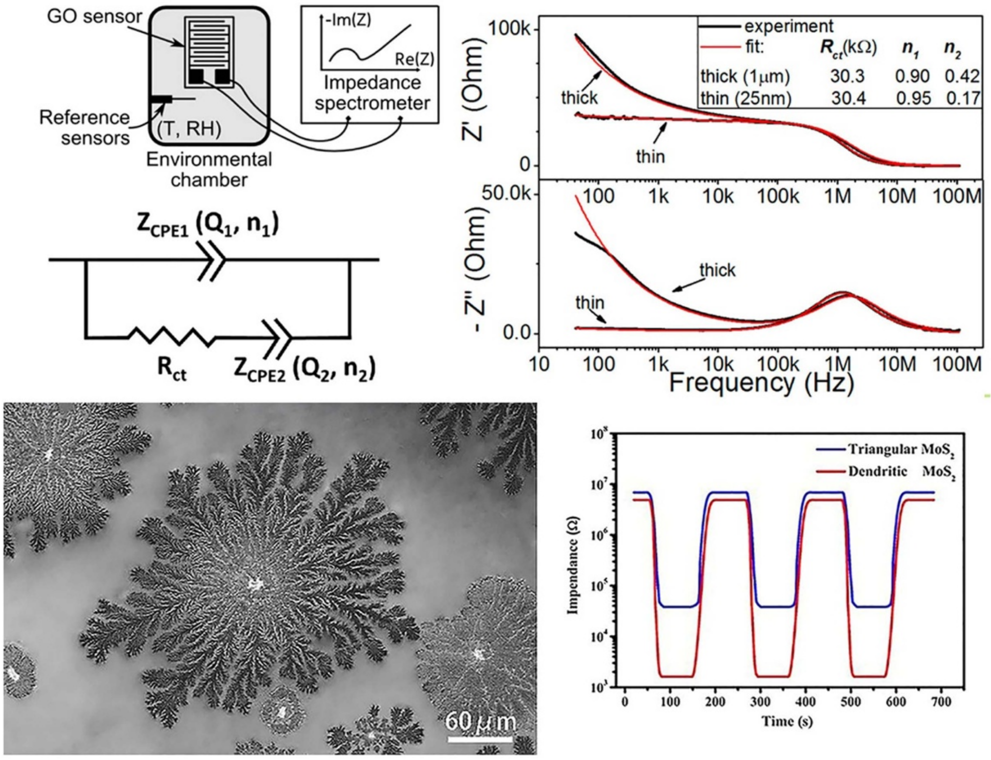

Figure 7. Impendence-based humidity sensors. Top panel: diagram of the experimental setup and fitting of the impedance spectrum, by using the displayed equivalent circuit, for two different GO film thickness values and the conductance response of an ultrathin GO film to RH variation. Reprinted with permission from [68]. Copyright (Year) American Chemical Society. Bottom panel: SEM images of dendritic MoS_2 and impedance vs RH curves of dendritic MoS_2 and triangular MoS_2 at 100 Hz. Reprinted from [70], Copyright (2020), with permission from Elsevier.

Fiber optics

Sensors based on fiber optics are helpful for overcoming the drawbacks of electrical sensors, as they have fast response, high accuracy and long service life. They are easy to fabricate and are compatible with pre-established fiber optic systems. The sensing mechanism is based on the change in the light transmission. Namely, the water molecules adsorbed by the high refractive index (RI) coating result in a difference in the reference optical signal and the detected signal. This change can be used to calculate the humidity. For example, by overlaying WS_2 on side of a polished fiber, a first all-fiber-optics humidity sensor was developed, with rather fast RRT (1 s/5 s) [76]. This setup holds a lot of promise, and by using some other high RI materials, such as MoS_2, or the combination of materials, RRT can potentially be improved.

FET

Field effect transistor-based sensors have a standard setup of a source, drain, gate and channel materials. Channel material is the active sensing material and it bridges the source and the drain. The sensing materials absorbs or releases water, affecting the charge distribution between the layer and the gate. Graphene is not a good candidate for FET-based sensors due to low on/off ratio and zero bandgap, therefore, these types of devices are reported on MoS_2 [69] and metallic nanowires (NWs) [77].

3.2. Sensing performance of 2D materials

Here, we assess the performance of humidity sensors for a variety of 2D materials. The summary of critical parameters, such as type of the device, material, mechanical status (whether it is rigid, flexible or stretchable), the measured humidity range, the RRT and the response/sensitivity of the device are presented in table 2. *NA* stands for parameters which were not reported (and cannot be deduced) in the paper, in the units typical for that specific measurement setup.

3.2.1. Graphene, GO and rGO

Graphene, GO and rGO [61, 62, 64, 68] were all studied as sensing materials, and their performances will be discussed here in detail.

As previously mentioned, single layer graphene has high electrical conductivity ascribed to the p-orbital electrons, which form π-bonds with neighboring atoms. On the other hand, delocalized π-electrons are sensitive to the modifications of their immediate environment, making them suitable for sensing [99]. Nevertheless, humidity sensors based on graphene alone have shown limited range and/or response times [100]. Some of these drawbacks can

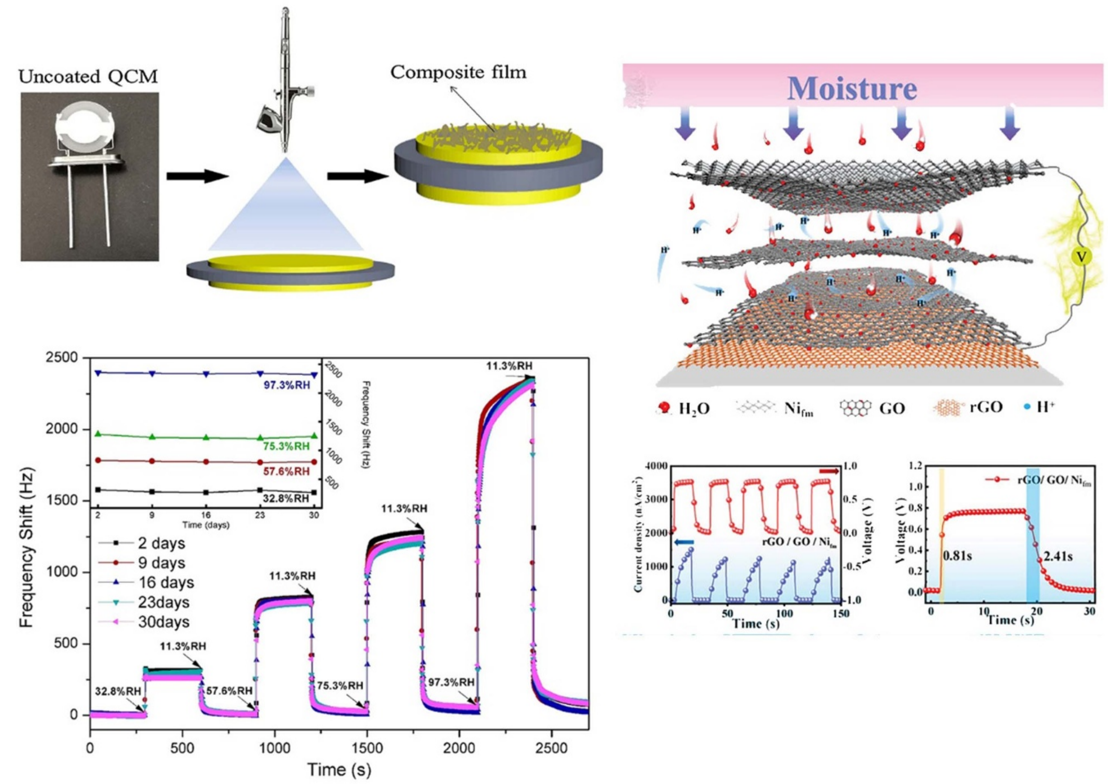

Figure 8. Left panel: QCM-based sensor. Top: fabrication illustration. Reprinted from [73], Copyright (2018), with permission from Elsevier. Bottom: dynamic frequency shift of QCM sensors, inset are response values versus RH. Reprinted from [74], Copyright (2016), with permission from Elsevier. Right panel: potentiometric humidity sensor design: schematic illustration of the humidity response mechanism; response/recovery curve of open circuit voltage (V_{oc}) and short current density (I_{sc}) of rGO/GO/Ni_{fm} sensor and the response/ recovery time of rGO/GO/Nifm sensor. [75] John Wiley & Sons. © 2021 Wiley-VCH GmbH.

be overcome by using CVD graphene. For example, graphene deposited on a SiO_2 layer on a Si wafer, was prepared as a resistive humidity sensor and showed response time comparable to GO [79]. As there has been extensive work done on graphene, we will focus more on GO and rGO.

GO film is a laminated material formed from oxygenated graphene platelets. It is a good candidate for humidity-response platforms, as it is a low-cost, easily synthesized material. It possesses a large specific surface area, which can highly improve the number of exposed atoms at the edges that can act as water molecule absorbers. It also contains diverse oxygen-containing groups on a basal plane, and carboxylic acid groups at the edges, which can increase hydrophilicity [75]. These characteristics allow GO to be utilized as humidity sensing material, as the layered and interlocked structure of GO films effectively undergoes the permeation of water molecules into the film under humid conditions [101]. Nanoscale capillaries between individual GO platelets facilitate low-friction water molecule flow on the surface, making the permeation process both rapid and reversible [102]. As a result, the interlayer distance between GO platelets increases with increasing RH, making it possible to monitor the humidity in the environment.

The sensing mechanism based on resistivity has been developed by measuring the electrical conductance changes in the GO films upon the exposure to a humid environment [103]. Namely, electrical interactions between water molecules and GO platelets cause electrical perturbations in the GO films that can be monitored in real-time. The water molecules that are hydrogen-bonded to the oxygen groups on the GO surface easily lose a degree of rotational freedom because of the strong interactions in the layered and interlocked structure between the platelets. As a result of the confined water intercalation through exposure to humidity, there is an increase in dielectric strength and a decrease in the electrical conductivity of GO films. A capacitive-type humidity sensor was prepared, reporting high sensitivity, explained as a result of violent oxidation and a creation of large density of sulfur vacancies and hydrophilic (carboxyl, hydroxyl) functional groups [61]. Through previously mentioned basal plane and edges of GO, composed of distributed oxygen groups, the hydrophilicity is improved. Another GO humidity sensor was prepared on chemically exfoliated

Table 2. Summary of the device performance based on sensing material, mechanical status, testing RH range, response or sensitivity and response/recovery time. NA stands for non-applicable, i.e. this parameter was not evaluated.

Device	Material	Mechanical status	RH range (%)	Response/sensitivity	Response/recovery time (s)
Capacitor	GO [61]	Rigid	15–95	37 800% at 1 kHz	10.5/41
	GO/PDDA [62]	Flexible	11–97	1552 pF/% RH	108/94
	GO/PSS [63]	Flexible	20–80	NA	60/50
	GO-Au [64]	Rigid	11–97	25 809 pF/% RH	8/12
	GO [65]	Flexible	10–90	3215.25 pF/%RH	15.8/NA
	MoS_2 (liquid exf) [66]	Rigid	11–96	43 684%	30/40
Resistor	rGO [78]	Flexible	10–95	100	50/3
	Graphene [79]	Rigid	1–96	S%: 0.31 ($\Delta R/R$/%RH)	0.6/0.4
	GO [80]	Flexible	30–95	S%: 7.9	100/NA
	rGO/PU [2]	Stretchable	10–70	$\Delta R/R_0$ 4.63 at RH = 35%)	3.5/7
	GO [81]	Rigid	8–95	124%	3/7.7
	r-CMGO [82]	Rigid	0–100	0.33%RH − 1	0.025/0.127
	rGO [83]	Rigid	11–97	NA	15/28
	MoS_2/GO [84]	Rigid	25–85	IH/IB = 1600	43/37
	rGO/MoS_2 [85]	Rigid	5–85	2494.25	6/31
	rGo/MoS_2 /PI [67]	Flexible	11–95	96.7%	0.65 s/14.4
	MoS_2 (nanosheets) [86]	Rigid	10–60	NA	9/17
	MoS_2/Si NW [87]	Rigid	11–95	392%	26/15
	MoS_2/PEO [88]	Flexible	0–80	$\sim 0.7\ \Omega\ ^\circ C^{-1}$	0.6/0.3
	MoS_2 NTs [89]	Rigid	20–85	668	0,5/0,8
	MoS_2@$MoSe_2$ flowers [90]	Rigid	H_2O conc 25–12 000 ppm	NA	30/33
	WS_2 NPs [91]	Rigid	11–97	469%	12/13
	WS_2 nanosheets [92]	Rigid	8–85	IH/IB = 1300 at 85% RH	140/30
	MoS_2 NPs-plasma [93]	Rigid	20–95	NA	0.5/0.8
	SnS_2 nanoflakes [94]	Rigid	11–97	−11 300%	85/6
	SnO_2 film [95]	Flexible	15–70		
	CeO_2 NW [96]	Rigid	15–97	*Rair*/RRH = 6.2	3/3
	ZnO NW [97]	Rigid	17–60	4000 for 50% RH	60/3
	MXene/TPU	Flexible	11–94		12/30
Impendance	GO [68]	Flexible	35–80	NA	0.03/0.09
	MoS_2 dendrites [70]	Rigid	10–95	413 S = Im (11%)/Im (95%)]	17/24
	MoS_2—spiropyran [69]	Rigid	10–75	1.0% · (%) RH − 1	NA
	MXene/GO/COC [71]	Flexible	6–97	182 * 10^6/%RH at 1 Hz	0.8/0.9 s
	TiO_2 NW [98]	Rigid	11–95	3000%	3/7
	Al_2O_3 NT [72]	Rigid	11–95	10 000%	10/20
QCM	GO/PEI [74]	Rigid	11.3–97.3	27.3 Hz/%RH	53/18
	GO/SnO_2/PINI [73]	Rigid	0–97	29.1 Hz/%RH	7/2
Potentiometric	GO [75]	Rigid	20–90	5–20 mV/%RH	0.8/2.4
Fiber optics	WS_2 [76]	Rigid	33–85	0.1213 dB/%RH	1/5
FET	SnO_2 NW [77]	Rigid	NA	NA	120/20

large-area thin films [80]. While easier to scale-up, these films showed a slow response time of 100 s.

In another approach, a GO-based single-layered sensor chip with multiple sensing capabilities was prepared [81]. It showed potential to operate as a microheater, temperature sensor and a flow sensor. This device was fabricated on two sides of the Si wafer. On one side of the chip, a GO-based humidity sensor is fabricated, offering ultrahigh sensitivity of 124/% RH, rapid RRT, and a wide detection range (8%–95% RH). Additionally, the effect of temperature on the humidity sensing properties of GO is demonstrated using the microheater platform. On the other side of the chip, serpentine Pt micropatterns serve as high-performance temperature and flow sensors in cold and heated states, respectively, when connected to the appropriate circuits. Low and high voltages are applied to the Pt microlines for temperature and flow sensing, respectively, generating negligible and significant Joule heating effects. As a result, the Pt micropatterns enable the realization of three distinct functionalities within a single device. The humidity was tested from 8% to 95%, with fast RRT of 3 s/7.7 s. Another technique used to increase the active surface area is to combine GO with metal NPs. For example, Ag NPs were added to GO in different concentrations, in order to improve the humidity sensitivity of capacitive-type sensors [64]. The sensing properties were tested in a 11%–97% RH range at room temperature. The best performance was achieved by the GO/Ag (2 wt%) composite-based sensors. Addition of Ag NPs increases the large specific surface area and hydrophilicity by adding the wrinkles. Beyond 2%, the initial resistance of the composites becomes too small to be dielectric, and the performance of the sensor deteriorates.

Nevertheless, sensors based on natural GO have limited sensitivity at low humidity levels. The material is also electrically insulating, but its conductivity could be partially restored if certain reduction processes are performed to remove oxygen groups. Therefore, rGO can sustain both the conductivity and the chemically active defect sites. One drawback is its relatively low surface area, which significantly hinders the sensing capabilities. Therefore, it is highly desired to prepare rGO as hierarchical nanostructures. Such a sensor was developed, whereby two-beam-laser interference was used to control the content of graphene functional groups [78]. With this approach, conductivity could be partially restored, leading to tuning of RRT due to the interaction between the water molecules and oxygen functional groups.

rGO was also prepared as a humidity sensor via modified Hummers' method, and showed faster RRT (15 s/28 s) than pure GO (18 s/31 s) [83].

Using a simple chemical modification of rGO with hydrophilic moieties can improve the sensing performance significantly. Another drawback of using rGO as a humidity sensor is the hydrophobic nature, as the reduction of GO removes the oxygen-containing functional groups. It was reported that, by using triethylene glycol chains, rGO resistive-based sensor increased the sensitivity by 31%, with ultrafast response (25 ms) and recovery (127 ms) times [82]. By using chemical functionalization of GO with carefully designed molecules allows for achieving optimal performance in humidity sensing while ensuring high selectivity to water molecules. Similar functionalization of GO and other 2D materials with specific receptors for the desired analyte, strategically selected from the well-established library of supramolecular chemistry, will enable the creation of high-performance chemical sensors for a wide range of analytes.

3.2.2. MS_2

In the covalently-bonded S–M–S (M is a transition metal such as Mo, W, Sn), MS_2-layers are bound together by van der Waals interactions. The atoms of each individual layer can be classified into basal plane sites and edge sites. The basal plane is terminated by sulfur atoms with lone-pair electrons and no dangling bonds, making it inactive. In contrast, the edge sites, where either transition metal or sulfur atoms lack coordination bonds, tend to be more active. As the analogue of graphene, semiconducting MS_2 materials, together with lower background carrier densities, are expected to display a comparative or preferable sensing performance. Furthermore, they are suited to be a good sensing platform, as this family of materials has excellent thermal stability, ideal bandgaps, very high mobility and strong electron–hole confinement. One of the first successful humidity sensors based on MoS_2 was reported in 2012, on a two- and five-layer resistor-type device, but this early work shows slow recovery and response times [104].

One of the drawbacks of the devices based on single-layer films is that they suffer from an unstable current response and are not suitable for scale-up [105]. One of the solutions is fabrication of devices based on liquid-phase exfoliated nanosheets [66]. This method of exfoliation increases the molecular adsorption area, due to the presence of dangling bonds at the edge sites and defects and vacancies. The resulting sensor showed RRT of 30/40 s. Moreover, MoS_2-based sensors show lower hysteresis than GO-based sensors, which have strong interaction between GO oxygen functionalities and the physisorbed water molecules [82]. Furthermore, few-layer nanosheets have a superior long-term stability, and they do not need to be functionalized with NPs or polymers to improve the slow recovery. Another resistive device based on a exfoliated thin film of MoS_2 was prepared by drop-casting and tested in the RH range of 0%–60% [86]. This sensor showed fast RRT of 9 s/17 s, surpassing that of bulk MoS_2. This effect can be explained by the increased surface area of the nanosheets after exfoliation, leading to more water molecules absorption sites. When MoS_2 is exfoliated into few-layer nanosheets, it exposes a significant number of low-coordination step edges, kinks, and corner atoms. These exposed edge sites play a crucial role in the material's gas sensing behavior. Another large-area few-layer MoS_2 film heterojunction was prepared with Si NWs array [87]. While the contact area of MoS_2/bulk Si is not large enough to be used as a detector, resulting in poor device performances, using NWs can increase the specific surface area, improving the sensitivity and response speed.

This sensor showed high sensitivity with the RRT of 22 s/12 s.

Although functionalization is not required for improving the stability, this process can be used to introduce other mechanisms, such as light switching. By interfacing them with organic photocromatic molecules such as spiropyran (SP), electronic characteristic of 2D materials can be modulated [69]. SP-functionalized MoS_2 light-switchable bi-functional field-effect transistors were reported [106]. SP exhibits reversible photo-isomerization from neutral (SP) form and a zwitterionic merocynine (MC) form through UV light. Owing to this effect, the functionalization of 2D surfaces with SP molecules represents a useful approach to confer to them a reversible light-controlled wettability. It was demonstrated that decorating mechanically exfoliated MoS_2 with solution-processed SP, functionalized with either ethylene glycol chains (EGO-SP) or alkyl chains (C13-SP), provides an effective approach to modulate the sensitivity of FETs to humidity changes. This is achieved by using a subtle, non-dynamic control over the interaction with environmental water molecules. The light-induced photo-switching triggers a wettability change of the SP/MoS_2 interface, which, in turn, worsens the optoelectronic properties of the MoS_2 semiconductor due to water's known role as an electron trap in MoS_2. The reversible behavior of water adsorption on the MoS_2 surface was evaluated through repeated exposure of the device to humid and dry air. It was observed that the MoS_2 device's initial performance could be partially restored after 1 h of flushing with a gentle stream of N_2 to remove the water.

While the pure MoS_2 humidity sensors suffer from low sensitivity at room temperature, coating them with metal NPs can increase their performance, but it also increases the cost. Combining GO with MoS_2 flakes to prepare a nanocomposite showed significant improvement as a chemoresistive humidity sensor [84, 85]. In the nanocomposite, water molecules attach to defect sites found in both the MoS_2 and GO layers. Additionally, the functional groups on the GO layer facilitate the adsorption of water molecules. Due to the large surface area of both MoS_2 nanoflakes and GO nanosheets, the amount of adsorbed water is significant, which in turn increases the density of charge carriers. The high response of the RGMS humidity sensor was attributed to the p–n heterojunction formed by the p-type rGO and n-type MoS_2 and the effect of the oxygen functional groups remaining on the surface of rGO.

MoS_2 can be prepared in other morphologies in order to increase the surface area. For example, MoS_2 nanoflowers were decorated with Au NPs in order to enhance electrical conductivity of the humidity sensor [107]. The prepared solution was drop casted on an electrode and mounted on a cotton mask so that it sits between the nose and the mouth and detects breathing. The sensor showed promising results with RRT of around 100 s. $MoSe_2$@MoS_2 nanoflowers were synthesized and tested as humidity sensors with a unique 3D interface structure [90]. The direct growth of MoS_2 on $MoSe_2$ nanosheets spontaneously forms a high number of n–n heterojunctions enabling more sensitive adjustment of resistivity by influencing interface electron transfer efficiency. By finding an optimal ratio of these two moieties, a sensor with improved sensitivity and response times with respect to single-phase sensors was achieved. The fastest times were 40 s/33 s for a 50:50 ratio, and the sensitivity increases almost 10 times than that of the single-phase material. Few-layer dendrites of MoS_2 were prepared via CVD method and deposited on Si/SiO_2 substrate. This fractal configuration increases the humidity sensing performance due to the increase in structural complexity and edge active sites [70]. The dendritic MoS_2 has a lower impedance and a higher rate of change for the same response time compared to the triangular MoS_2. The RRTs were 11 s/17 s and 17/24 s, respectively. Under high RH conditions, free water can penetrate the interlayer of dendritic MoS_2 nanomaterials, enhancing the dielectric constant and sensor response. The abundance of edge active sites contributes to its high conductivity and faster charge transfer, significantly improving its humidity sensing properties.

Another approach to modify and improve sensor parameters is by plasma irradiation. MoS_2 NPs were exposed to O_2 plasma, which increased the total pore volume and the specific surface area, while shifting the pore size distribution towards lower values [93]. O_2 plasma can have several effects on 1T/2H NPs. It can create defects in the crystal structure; it can act as the etching medium and remove the excessive sulfur. It is also possible that the heat generated by plasma can change the phase structure, and increase surface roughness due to formation of MoO_3. Response/recovery times for non-treated MoS_2 were 76 s/382 s, while the treated showed an increase in response time and decrease in recovery time. The decrease of the pore size slows down the diffusion of water to the pore surfaces to decrease the response time.

WS_2 was tested as humidity sensors both in the shape of nanosheets and NPs. WS_2 NPs, in the size range of 25–40 nm, were deposited on a quartz wafer [91]. The fast recovery time (13 s) is attributed to the fast desorption process of H_2O molecules from the WS_2 NP, and the slow response (12 s) is due to hydrophilic surface of the NP resulting in slow adsorption of H2O molecules on the surface. 2D-WS_2 nanosheets were prepared via exfoliation and drop-casted on a commercial alumina substrate with Ag electrodes [92]. This resistive sensor showed RRT during a pulse between 8 and 85 RH % of 140 s and 30 s. While the reported times are not fast, the sensor showed high stability, as it had a nearly constant response over many weeks. An all-fiber-optics sensor based on WS_2 showed rather fast RRT (1 s/5 s) [76].

SnS_2 is another layered material, where tin cations (filling the octahedral sites of the alternating layers) and sulfide anions form hexagonal structures, and it is gaining interest due to its stability. SnS_2 nanoflakes, prepared by an economically viable hydrothermal synthesis method, were tested as humidity sensors [94]. This sensor showed promising recovery time of 6 s, with the longer response time of 85 s. The response of the sensor device is most likely constrained by the strong adsorption and desorption of analyte molecules at room temperature. The thermodynamic adsorption of analyte molecules may not be highly favorable during the response time, and during the recovery phase, analyte molecules easily desorb due to their low absorption energy. As a result, the response time is significantly longer than the recovery time.

3.2.3. Flexible sensors

In order to prepare flexible sensors, TMDC materials can be introduced into flexible substrates. Given the need for permeability, biocompatibility, and comfort in wearable devices, a variety of porous materials can be utilized as flexible substrates, with the polymers being the most popular. When the nanomaterials are added to a polymer matrix to prepare a composite, unique mechanical, thermal and spectroscopic properties can be achieved that would be otherwise infeasible with the individual materials. The nanomaterials add to the improvement of the overall strength and stiffness, making them the load-bearing component, while the polymer matrix uniformly transfers the applied force to the nanomaterial, serving as a load distributor. The parameters that determine the performance of such composite are the individual properties of the constituents, their weight ratio, and the geometry and the orientation of the nanomaterial in the composite. They can improve stiffness, toughness, structural and thermal stability and tensile strength. The potential use of silicon-based nanocomposites as flexible and stretchable sensors is opening up the search for the best filler for different applications, such as motion detection, structural health monitoring, artificial electronic skin, nanosensors [108, 109]. As they can have high stretchability and sensitivity, simple manufacturing process and fast response, they can be added to wearable devices or attached directly to the skin. Nanomaterials have been shown to be superior fillers to the conventional metals and semiconductors that are limited due to their poor stretchability, brittleness and dispersion difficulties. Variety of novel nanomaterials, such as NWs [110], graphene [111–113] and metal oxides [108], have been successfully incorporated into elastomers. These fillers can be further modified to enhance their integration with polymeric matrices and substrates and to tailor the sensing efficiency of the overall nanocomposite material.

A humidity sensor prepared from intrinsically stretchable components, instead of a combination of rigid and flexible materials, should be preferred. One of the first transparent and stretchable humidity sensors was reported on a rGO/PU (polyurethane) device [2]. This resistor-based sensor has a faster RRT than previously reported devices based on graphene and GO. It can detect the humidity of the human breath, remains stable up to a strain of 60% and after 10 000 stretching cycles at 40% strain. In other work, GO/PEI (Poly(ethyleneimine)) was sprayed on a QCM for humidity detection. This sensor exhibited high sensitivity, good RRT (53/18 s), negligible hysteresis and good repeatability [74]. QCM method was also used on a GO/SnO_2/PANI nanocomposite [73]. This composite has higher surface area, accessible pore volume and pore size distribution, as well as a smaller water contact angle than the separate GO/PANI and SnO_2/PANI composites. The sensing mechanism was analyzed using the Langmuir adsorption isotherm model. Water molecules are adsorbed on the GO/SnO_2/PANI nanostructure through the hydroxyl, carboxyl and epoxy functional groups attached on the GO nanosheets, the amino groups on PANI nanofibers, as well as surface vacancies and defects on SnO_2 NPs. The water molecules were firstly chemisorbed on the coated film at low RH, followed by physisorption by double hydrogen bonding. At high RH, the first-layer water molecules were physisorbed through the action of double hydrogen bonding. The resulting sensor has a rather short RRT (7 s/2 s), with high stability, making this sensing mechanism promising for future applications.

Using hydrophilic polymer can improve the characteristics of GO-based sensors. PSS (poly (sodium 4-styrenesulfonate)) was added as an intercalant between individual GO platelets to enhance the water permeation characteristics [63]. The capacitive-type humidity sensor fabricated by forming metal electrodes on the film was equipped into the charge pumping system, which can produce voltage outputs as a response to humidity sensing. Compared to the pure GO sensor, GO-PSS films showed a 3 times faster response to humidity and 5 times higher voltage output. In comparison with covalent bonding in GO and RGO, non-covalent methods could offer the π bonding on graphene basal plane while retaining graphene unique electronic properties without necessarily making use of harsh chemicals. One of the approaches to non-covalently functionalize graphene was to coat it with a thin layer of hydrophilic polymer. Trough functionalization with PEI (polyethylenimine), an amine-rich polymer, the electron transfer from amine groups to graphene improved the humidity sensing performance [114]. GO/PDDA multilayer film was fabricated on a polyimide substrate using layer-by-layer self-assembly method and tested as a capacitive humidity sensor [62]. This sensor showed high sensitivity in the 11%–97% range, as well as a fast RRTs.

MoS_2 flake suspended in PEO were prepared as an active layer of a resistive temperature and humidity sensor with RRT of 0.6 s/0.3 s [88]. Furthermore, compared to the bulk MoS_2, MoS_2 NPs are more promising for improving the adsorption performance of water molecules/humidity because they have a high specific surface area, which is beneficial for enhancing the number of water molecules attached on the surface of MoS_2. A fully-flexible humidity sensor was prepared based on a hybrid composite of rGO and MoS_2 with high responsivity and fast response times [67]. rGO was chemically reduced in an environmentally friendly manner, mixed with MoS_2 via ultrasonic dispersion and the resulting GO/MoS_2 dispersion was drop-casted onto a PI substrate with interdigitated electrodes. The resulting flexible humidity sensor demonstrated a responsivity of 96.7% within the RH range of 11% RH–98% RH, along with fast RRT of 0.65 s and 14.4 s, respectively.

3.2.4. MXenes

MXenes, made from thin layers of transition metal carbides, nitrides, or carbonitrides, feature alternating metal and carbon layers. To reduce or control their conductivity for humidity-sensing applications, they can be functionalized or mixed with oxides, polyelectrolytes, and polymers. Sensing mechanism of MXenes is based on the abundance of hydrophilic active sites, such as –OH and –O terminated groups for water adsorption and intercalation [115]. They are great candidates for resistive sensing, as the intercalation of water molecules within the interlayer of MXene leads to an increase of resistance. Nevertheless, the incorporation of MXenes into flexible polymers remains a challenge, as the weak affinity between MXene and polymer fibers because the hydrophilic groups of MXene is incompatible to hydrophobic nature of polymers. It usually results in the exfoliation of sensing materials during the deformation process, restricting the stability of humidity sensors. One approach to solving this issue is coating MXenes with TPU electrospun nanofibers [115]. This sensor showed RRT of 12 s/30 s, respectively, with good stability.

Using GO as the sensing layer and MXenes as the electrodes in a humidity-sensing device offers numerous advantages. While GO exhibits a strong affinity for water molecules, MXenes, known for their excellent electrical conductivity, facilitate reliable measurement of the resistance changes in the GO layer, resulting in a more sensitive humidity sensor [71]. Furthermore, GO's highly interconnected 2D layered structure facilitates rapid diffusion of water molecules, resulting in fast response times. Its compatibility with TMNSs and flexible substrates makes it ideal for the development of flexible humidity sensors, which are well-suited for applications involving bending, molding, and mechanical stress. This type of a capacitive sensor exhibited a large response range of 6%–97%, with ultrahigh RRT of 0.8 s/0.9 s.

3.2.5. Metal oxides

Other promising humidity sensing materials are metal–oxide NWs and nanotubes [72, 77, 96–98]. While the conventional metal oxide-based sensors usually require high annealing temperatures (larger than 200 °C), NTs and NWs have many characteristic optimal for sensing, such as larger surface-to-volume ratio, higher surface activity, and better absorption performance. The tube-like nanostructures offer an increased number of efficient adsorption sites for water vapor, resulting in high surface charge densities that promote physisorption processes, thereby enhancing the sensor's sensitivity at low humidity levels. Amorphous Al_2O_3 NTs impedance-based humidity sensors were prepared, and showed promising RRT of 10 s/20 s [72]. CeO_2 NWs humidity sensors was reported, with the ion-type conductivity as the sensing mechanism [96]. They have a humidity-independent RRT of 3 s/3 s. LiCl-doped TiO_2 nanofibers [98] humidity sensors showed high RRT of 3 s and 7 s, with stability of one month with almost no changes in the impendences. Due to the 1D structure of the fibers, rapid mass transfer of water molecules to and from the interaction region is promoted, while also enhancing the rate at which charge carriers pass the barriers along the wires. Additionally, compared to 2D nanoscale films, the interfacial area between the active sensing region of the nanofibers and the underlying substrate is significantly reduced. These advantages result in a substantial improvement in the sensing signal and stability.

SnO_2 was used as a sensing layer and it was annealed using NIR laser, with low annealing temperature of 41 °C [95]. They were deposited on soft plastic wrap substrates. This ultra flexible SnO_2-based sensor can detect very small incremental changes (0.1%–2.2%) of RH in air, with RRT of 90 s/150 s. A single-NW SnO_2 humidity sensor was prepared as FET and tested as a humidity sensor for RH between 30% and 85% [77]. These NWs possess a large number of oxygen vacancies in the crystal; therefore, the surface is very sensitive to oxygen and water vapor in air. The RRTs were 20 s/60 s, faster than that of flat SnO_2. Additionally, when the sensor was kept in the moisture for about 1 h, the current still recovered to the original value, indicating that the interaction between water vapor and the surface of the NW should be dominated by physisorption, while chemisorption plays a minor role. A single ZnO NWs was deposited between gold electrodes and placed into a chamber with humidified air [97]. These devices shows exponential change in the resistance of more than five orders of magnitude in response to a change of RH from a dry air to 60% RH air at room temperature. This is a result of a subthreshold carrier modulation in the NW core, high surface-to-volume ratio of the NW and complete exposure of the NW surface to air, due to the free standing structure. These sensors demonstrate stable behavior, reproducible switching response, with RRTs of 60 s/3 s time in response to 30% RH pulses between dry air flushes and pronounced sensitivity at elevated temperatures.

4. Human breath and touch monitoring

Respiration is one of the key human vital signs that reflects the state of the respiratory system and overall health. By monitoring respiration, health can be assessed through factors such as respiratory rate, depth, pattern, and oxygen saturation. In healthy adults, the normal respiratory rate typically ranges from 12 to 20 breaths per minute, while children tend to have a slightly higher rate. Abnormal rates can signal health issues such as anxiety, hypoxia, fever and other conditions, whereas slow breathing can be indicative of medication overdose or neurological disorders. The breathing pattern shows the regularity and rhythm of breathing. However, traditional respiratory monitoring methods often cannot provide real-time, synchronized, and comprehensive measurements. Typically, real-time monitoring requires wearing medical respiratory equipment, which can significantly interfere with normal activities. Therefore, the development of flexible respiratory monitoring e-skins is a crucial advancement in healthcare. Those novel respiratory sensors are designed to monitor human breath non-invasively by detecting, measuring and interpreting respiratory data in real-time. Some of the parameters they should track are respiratory rate and volume, and the composition of the exhaled gas. These parameters can be further used to diagnose respiratory disorders, and guide the physical activity after the recovery. For example, such wearable sensors were tested for early diagnosis of Covid-19, through non-invasive monitoring of the respiratory behavior, body temperature and blood oxygen level [116]. Graphene FETs were also able to detect SARS-CoV-2 spike protein [117]. This method of monitoring can be particularly useful for people outside of hospital settings. Specifically, humidity sensors can effectively differentiate the inhalation and exhalation phases, as well as the depth of each respiratory cycle, by detecting changes in RH during the inhale and exhale processes. Therefore, the sensor should be placed near the nostril or mouth, realizing contactless measurement. Additionally, respiratory monitoring based on RH in the airflow is minimally influenced by environmental factors such as temperature, noise, and others, ensuring reliable data. The breathing process consists of two periodic stages: inhaling air that contains O_2 into the lungs and exhaling CO_2 through the nose or mouth. The complete cycle, from inhalation to exhalation, is referred to as a respiration cycle. The airflow can be monitored as exhaled air is warmer, has higher humidity, and contains more water molecules than inhaled air. In addition to breath monitoring, the real-time monitoring of the human skin humidity level via a skin patch can be an important development in prevention of fatal illnesses due to dehydration.

Previously mentioned first transparent and stretchable a rGO/PU sensor was able detect the humidity of the human breath [2]. The device was placed at a distance of 3 cm from the nose, and successfully detected the resistance change between dry air, ambient air and human breath. To test different environments, it was attached to the human finger, providing the feedback on the humidity of the environment, moisture of human skin and dampness of objects. A GO sensor, shown in the top left panel of figure 10, was prepared in an impedance setup and showed ultrafast RRTs of less than 100 ms for thickness of 15 nm, being among the fastest humidity sensors to be reported, comparable to the commercially available optical sensors [68]. It was further tested for speaking, breathing and whistling. The ultrafast performance of these sensors allows the capture of fine features due to moisture modulation during speech. This sensor was also capable of recognizing different whistled tunes, by capturing their distinct patterns characteristic. The patterns were then analyzed using FFT and Principal Components Analysis, resulting in clear clustering for each tune. After training the system with 10 data points per tune, each whistled tune was classified and recognized with an accuracy of approximately 90%, enabling user authentication. A GO/PDDA capacitive sensor was tested for human breath monitoring [62]. The breath response characteristics for a normal adult were measured over 45 s, during which 11 repetitive breathing cycles were observed. The capacitance response showed a sharp increase during exhalation and a drop during inhalation, corresponding to the breathing cycles. Notably, the sensor's response and recovery times were both within 1 s, enabling the capture of fine details related to moisture modulation in human breath. Another GO-based single-layered sensor chip with multiple sensing (figure 9, left panel, middle) was able to monitor human breathing, nose breath and human touch [81]. Because the three different sensors operate independently, as explained in section 3.2.1, they have good sensitivity.

MoS_2 NPs exposed to O_2 plasma were also tested as a human breath sensor and for skin monitoring [93]. The breathing test was conducted with three different conditions, including deep breath, normal

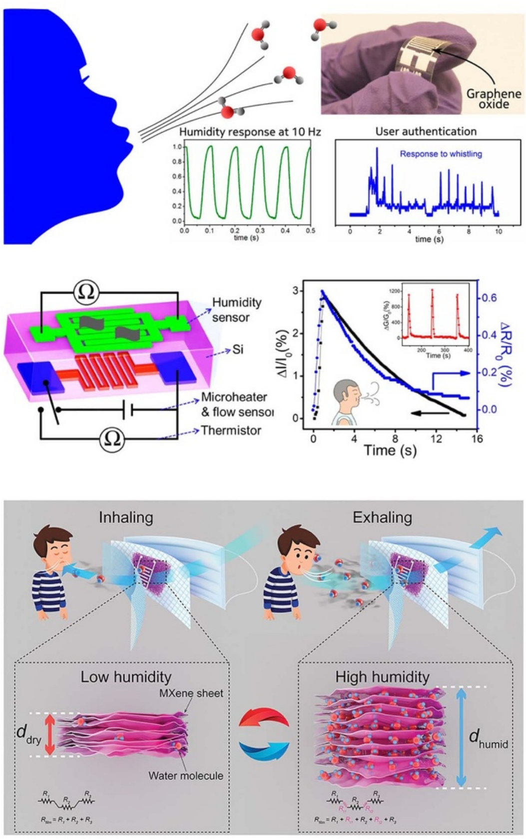

Figure 9. Top: a 15 nm thick GO sensor with the normalized response to a modulated humid airflow at 10 Hz; and a response to ta whistled tune. Reprinted with permission from [68]. Copyright (2013) American Chemical Society. Middle: scheme illustrating the structure of the multifunctional sensor. The GO-based humidity sensor and the microheater/flow/temperature sensor were fabricated on two sides of the Si wafer. Dynamic responses of the flow and temperature sensors to the blow with mouth. Reprinted with permission from [81]. Copyright (2019) American Chemical Society. Bottom: schematic image describing the proposed humidity sensing mechanism of the MXene/TPU sensor. R_1, R_2, and R_3 represent the intrinsic resistance of MXene nanosheets. R_{t1} and R_{t2} represent tunneling resistance at the junctions. R_{flim} represents the total resistance of MXene/TPU composite film. [118] John Wiley & Sons.© 2023 The Authors. Advanced Sensor Research published by Wiley-VCH GmbH.

breath, and fast breath. The breath testing indicated a good response, and the sensor also distinguished wet and dry hands clearly. Inhalation was indicated by the decrease of the resistance, and exhalation by the increase of the resistance.

A sensor based on MXenes with TPU electrospun nanofibers sensors was tested for respiratory monitoring, and embedded into the middle layer of a face mask to avoid the contamination from saliva, as shown in figure 10, left panel, bottom [118]. When a sensing material is added to a flexible and wearable face mask, its resistance has to be stable upon bending. As the MXene nanosheets are abundantly wrapped on the TPU fibers to form a conductive network, the resistance remained stable as the bending angle increased from 0° to 210°, indicating good stability and flexibility. The sensor showed promise for distinguishing different degrees of breathing and accurately monitoring respiratory signals during different physical activities [118]. Another MXenes sensor, combined with GO, successfully detected moisture from human breath and fingertip [71]. MXene/MWCNT-sensing material was drop-coated on pristine fabric and cured by UV light. The electrical circuit was printed by conducting ink and encapsulated by polyimide to avoid short circuiting due to the water vapor. Finally, the whole sensor with the encapsulated circuit was attached inside the mask near the nose as a wearable wireless humidity sensing tag, as shown in figure 9, right panel [119]. The size of the entire tag was 2 cm × 4 cm. The fabric sensor, coupled with a flexible detecting tag, enabled the detection of respiration and the accurate identification of various breathing patterns. It was also able to record respiration signals accurately, even under deformation caused by movement for standing, walking and running. This sensor also provides a practical approach for real-time, wireless respiration monitoring using electronic fabrics.

A flexible humidity sensor, based on SnO_2 thin film, with the food plastic wrap as the substrate material, was integrated into a face mask to detect the breathing pattern [95]. Slow, normal, and fast respiratory patterns were monitored by the real-time current curves, with respiratory rates of 8, 20 and 29 breaths per minute, respectively. Sensor was put inside a glass chamber with a fixed background RH of 70%, 60%, and 50%, and the breath was released 5 cm away from the substrate.

Another fully flexible humidity sensor based on rGO/MoS_2 demonstrated finger proximity detection and non-touch switching [67]. The device was placed at 3 cm away from the human nose. When the breathing rate was 20 breaths per minute (rapid breathing), the device showed a responsivity of 70%. However, at a slower breathing rate of 10 breaths per minute, the responsivity increased to over 90%, demonstrating the good reliability. Water molecules adsorbed and desorbed quickly on the device surface in both rapid and slow breathing modes, resulting in a strong response to human breathing. Additionally, a series of finger proximity detection experiments were conducted in an atmosphere with 46% RH. The results showed that the relative resistance of the device increased gradually from 48.4% to 95.6% as the distance between the finger and the device surface decreased from 2 cm to 0.5 cm. These human respiration and finger proximity measurements demonstrate that the device has potential applications in wearable technology.

A heterojunction made of 3D $MoSe_2@MoS_2$ nanoflowers was positioned at 8 cm from human mouth to monitor respiration, and the finger was positioned

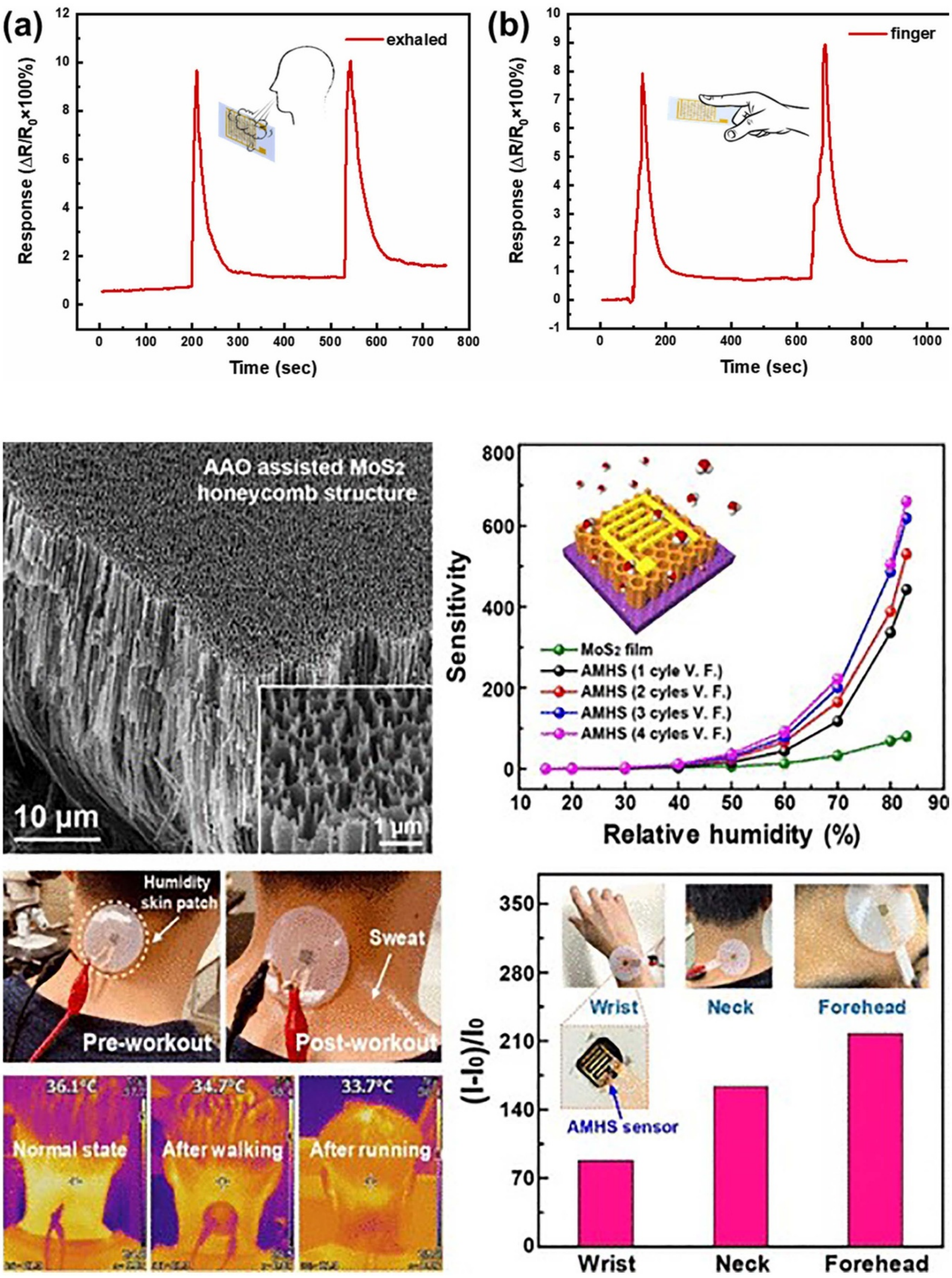

Figure 10. Top panel: (a) the continuous monitoring of the sensor to human deep breath. (b) Repeatability test of the sensor for finger approach distance of 2 cm. Reprinted from [90], Copyright (2024), with permission from Elsevier. Middle panel: FESEM image of the sensor and sensitivity as a function of RH. A bar chart in inset illustrating sensitivity dependence on the RH. Bottom panel: photograph of the attached skin humidity patch on the neck before and after sweating from exercise (top), and the variation in body temperature measured by the IR image camera (bottom). Comparison of the relative current variation in volunteers measured by the skin humidity patch from the neck at different physical conditions. Reprinted with permission from [89]. Copyright (2020) American Chemical Society.

at 2 cm to test for human touch, as shown in the top panel of figure 10 [90]. Both response curves show potential for non-contact detection.

A resistive-type humidity sensor made of a 3D-honeycomb structure based on MoS_2 NTs showed a promising response in humidity in the atmosphere, human breath and human skin in a 20%–85% RH range [89]. As a result, it can be incorporated in multifunctional sensing applications using skin humidity, human respiration pattern and speech recognition using humidity in exhaled air. These open-ended NTs combined in a honeycomb provide a large number of absorption sites for H_2O molecules. The sensor showed ultrafast RRTs of 0.47 s/0.81 s, respectively, much faster than sensors based on 2D MoS_2. In order to test it in human skin conditions, the sensor was tested in the human body temperature range (31 °C–38 °C) at room RH condition. The sensor showed promise for non-contact applications, as the resistance change was almost negligible when it was placed at 3.8 mm above the heater, showing that it is not affected by the human body temperature, as depicted in the bottom panel of figure 10.

While reducing the MoS_2 flake size leads to formation of S-vacancies as active sites for water molecule absorption, a honeycomb structure contains an even larger number of sites. The absorbed molecules can easily diffuse into the NTs through the open pores, while the defect-rich surface with large number of S-vacancies on the open NT edges, together with the cylindrical shape, allows the water molecules to absorb and assemble easily. In addition, it was assembled into a wearable patch, detecting human skin humidity under different physical conditions and regional sweat rate.

5. Humidity sensors in agriculture

5.1. Soil moisture

Another field of use of humidity sensors is agriculture, as the estimation of soil moisture is of critical importance to avoid over-wetting or water deficiency in order to gain maximal crop production. Sensors based on 2D materials can be utilized as the capacitive devices as they can provide a direct relationship of the soil moisture content and dielectric permittivity of the soil [120]. A device prepared based on MoS_2 sheets showed good sensitivity for both black and red soil, it demonstrated stable performance over 6 months and good reproducibility with response time of 35 s [66]. In another study, a variety of 2D materials were tested as low-cost soil moisture capacitive sensors [121]. The best sensitivity (30%) was reported for MoS_2, following by MoO_3 (13%), GO (11%) and V_2O_5 (9%).

5.2. Plant transpiration monitoring

Efforts have been made to monitor the water status of plants using sensors that can be attached to leaves or placed near plants. However, these sensors with rigid designs often face mechanical incompatibility with the soft surfaces of plant leaves. In this regard, recent advancements in flexible electronics have paved the way for the development of leaf-mounted sensors, which can provide real-time and quantitative information about the water status of plants.

A flexible capacitive-type GO-based humidity sensor with low hysteresis, high sensitivity (3215.25 pF/% RH), and long-term stability was prepared in order to be directly attached onto plant leaves for real-time transpiration tracking [65]. The sensor was fabricated by laser-induced graphene (LIG) interdigital electrode on a PI film, as PI serves as both a precursor for producing LIG and a humidity sensing material. To further improve the sensor's performance, GO was incorporated as the humidity sensing material. The prepared sensor offers excellent flexibility, high sensitivity, and long-term stability, enabling multifunctional applications such as non-contact humidity sensing. Moreover, it can be attached to the surface of leaves without causing any visible damage to plants. By recording capacitance signals, real-time and long-term monitoring of plant transpiration is possible. It can be observed that the capacitance increases 1 d after watering, but over time, it significantly decreases, resembling the pristine condition. However, when the plant was watered again, the capacitance increased accordingly. These findings suggest that the humidity level on the plant surface varies depending on the plant's water conditions. Overall, these results demonstrate that the plant's response to drought can be translated into visible electrical signals, highlighting the potential of the fabricated flexible humidity sensor in the field of intelligent agriculture.

6. Human exposure and environmental impact of 2D materials

The relationship between 2D materials and biological systems is bidirectional, involving interactions where both components influence each other and undergo simultaneous changes. Human exposure to 2D materials falls into three categories: occupational, environmental and biomedical, based on three basic modes of the interactions with biological systems: chemical, mechanical and electronic (see figure 11) [122]. Occupational exposure is already occurring among researchers and is expected to become more significant for workers in nano-manufacturing industries as the field expands. In these settings, workers are primarily exposed to materials in their original synthesized form or as intermediates and byproducts during production processes, highlighting the need to study their biological interactions in these states. In contrast, environmental exposure arises from the unintentional release of these materials, which may undergo chemical transformations before reentering human systems through air, food or water. Biomedical exposure happens in a somewhat controlled manner and undergoes rigorous investigation through processes which ensure safety, efficacy and biocompatibility before therapeutic applications or medical device approvals. Moreover, synthesis methods play a significant role. Occupational and industrial handling of 2D materials, especially in dry or

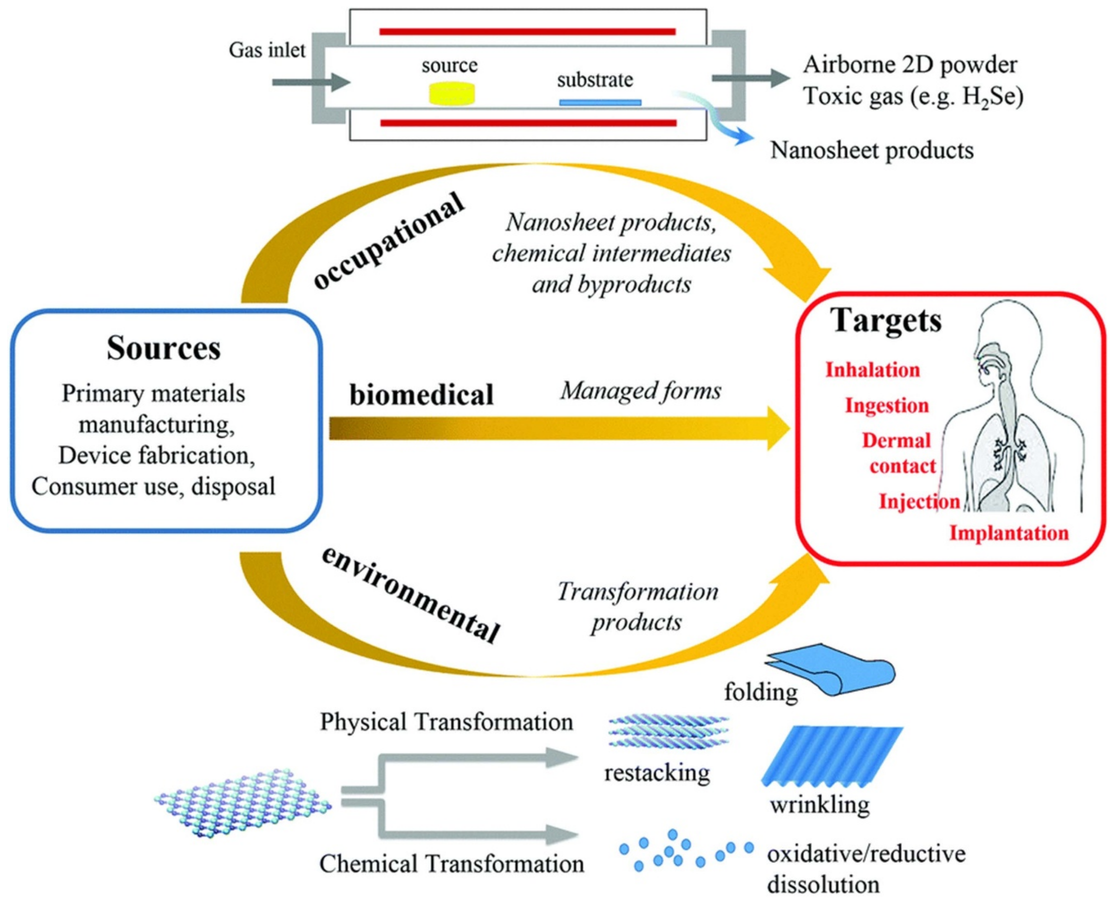

Figure 11. Exposure types and pathways for emerging 2D nanomaterials. Reproduced from [56] with permission from the Royal Society of Chemistry.

powder form, can result in airborne particles that pose inhalation risks and potential deposition into surrounding environment. Aggregation, sedimentation or restacking behaviors of 2D materials in natural systems may further affect their transport and reactivity. However, their widespread adoption is still limited by challenges including large-scale production, long-term durability and economic feasibility. The overall environmental and health risks of engineered nanomaterials are generally low, particularly when strategies like green synthesis and immobilization are applied to reduce exposure [123]. The first in-human study assessing the controlled inhalation of GO on the cardiorespiratory system demonstrated good tolerance without any adverse effects. Blood proteomics revealed minimal changes in plasma protein levels, and only a mild increase in thrombus formation was observed in an *ex vivo* arterial injury model. Overall, short-term exposure to highly purified, ultra-thin GO nanosheets did not result in any significant harm in healthy individuals. These findings support the safe implementation of human exposure studies in clinical settings and provide a foundation for evaluating the biological effects of other two-dimensional nanomaterials [124].

The potential negative impacts of 2D materials remain to be extensively explored, especially as the number of newly synthesized materials continues to grow. Even slight modifications in their composition by, for example, functionalization can significantly alter their physicochemical properties, making the range of possible effects vast and largely unpredictable. The environmental fate of 2D materials is complex due to their diverse chemistries and physical forms. Once released, these materials may undergo chemical (and physical) transformations such as oxidation, sulfidation, aggregation, dissolution, changing chemical state [125, 126] etc, induced by environmental conditions in the presence of atmospheric oxygen, moisture, sunlight and microbial species [127, 128]. Some materials, such as MoS$_2$, although considered to have low toxicity in bulk, in 2D and nanoscale versions can generate ROS and exhibit dose-dependent cytotoxicity. Moreover, TMDs may degrade and release heavy metals or toxic elements like selenium and tellurium, which are known to accumulate and disrupt biological functions. Their persistence, mobility and interaction with environmental components like soil, water and microbial population raise concerns about long-term ecological effects. TMDs have been shown to degrade more rapidly under ambient conditions (exposure to air and moisture) compared to graphene-based materials, primarily due to the presence of defect sites and grain boundaries. For instance, MoS_2 undergoes gradual oxidation in air to form MoO_3, and in aqueous environments it further breaks down into soluble ${MoO_4}^{2-}$ and ${SO_4}^{2-}$ ions (see figure 3(d)) [128, 129]. Members of the 2D material family do not exhibit uniform resistance to oxidation, and their degradation can occur even at physiologically and environmentally relevant concentrations of oxidative compounds, such as H_2O_2, in both single- and multilayer forms, as observed with pristine graphene [130]. TMDs are also susceptible to H_2O_2-induced oxidation. This oxidative degradation can compromise their electrical, mechanical, and chemical properties, ultimately limiting their effectiveness in environmental applications. Mitigation strategies include procedures such as surface passivation, chemical functionalization and development of protective coatings and nanocomposites. Nanocomposites are particularly interesting due to the synergistic properties they offer [131]. Additionally, surface and interfacial behavior of 2D materials may also be altered by the exposure to common airborne contaminants such as hydrocarbons, water vapor and oxygen. Even at trace levels, they can impact the wettability, electrochemical performance and doping, masking the intrinsic properties of the material (i.e. hydrophobicity of graphene is largely due to adsorbed hydrocarbons rather than its true behavior) [132]. Cracking and quenching (corrosion) occur in MoS_2 and WS_2 after they are stored in the presence of water and oxygen for several months. Recently published research on WS_2 nanotubes found that material stored for a long time in protected atmosphere oxidized only marginally, while other, kept under less controllable conditions suffered severe autocatalytic oxidation [133].

Equally important is the role of these materials in environmental remediation, as a result of synergy between 2D materials and electrochemical methods (electrooxidation and electroreduction) [134, 135]. Their high surface area, tunable surface chemistry and exceptional conductivity is what make them highly effective for removing pollutants from air, water and soil. These applications include the adsorption and absorption of heavy metals, drugs, dyes and other potentially toxic compounds. United Nations' sustainable development goal 6 aims to ensure access to clean water and sanitation for all, a challenge that can be significantly addressed through the innovative use of 2D materials. With their exceptional filtration, sensing, and antimicrobial properties, 2D materials can offer solutions for efficient water purification and real-time quality monitoring [136]. Materials like graphene, MXenes, and TMDs are extensively studied for their role in electrochemical sensing, catalytic degradation of pollutants and fabrication of advanced filtration membranes [137–139]. Notably, MXenes, particularly $Ti_3C_2T_x$, have shown excellent performance in adsorbing heavy metals like Pb^{2+}, Cr^{3+}, and Cd^{2+} due to their rich surface functional groups and high charge capacity. GO and its derivatives are widely used as membranes for water purification, thanks to their ultrahigh water permeability and chemical stability [140, 141]. Degradation of organic pollutants is also possible due to photocatalysis [142, 143]. Environmentally, the use of MoS_2 nanofertilizers reduces dependence on synthetic nitrogen inputs, thereby lowering greenhouse gas emissions and minimizing ecological impact [144]. The vision of clean energy generation is becoming increasingly achievable through the advancement of nanomaterial-based engineering approaches.

7. Outlook and future perspectives

The use of 2D materials in regenerative medicine presents immense potential, but it is held back by critical biocompatibility and toxicity challenges. Factors like size, surface charge and functionalization influence their interaction with biological systems, potentially triggering inflammatory responses, immune reactions or long-term toxicity due to accumulation. Additionally, concerns regarding mechanical stability, controlled drug release, large-scale production, regulatory approval and environmental impact necessitate advanced material engineering and thorough safety assessments to ensure their safe and effective clinical translation [31]. The overall biological impact of 2D materials is strongly governed by their chemical composition, surface characteristics and the extent of exfoliation, all of which shape their interactions with cellular systems. In the case of TMDs, both *in vitro* and *in vivo* studies highlight that their elemental composition, particularly the choice of chalcogen (e.g. sulfur, selenium, tellurium), plays a crucial role in cytotoxicity. Telluride and selenide variants generally elicit more pronounced toxic effects than sulfides, likely due to higher chemical reactivity and chalcogen release [145]. The exfoliation state further modulates bioactivity: nanosheets with high degrees of exfoliation expose more reactive surface area and edge sites, often leading to elevated cellular responses such as oxidative stress and inflammation [146, 147]. Conversely, TMDs that are well-characterized and stably dispersed, especially MoS_2, tend to exhibit lower toxicity profiles and greater biocompatibility, stressing the importance of controlled synthesis and processing in developing safe 2D materials for biomedical and environmental applications [148, 149]. Designing synthesis methods that are not only scalable and cost-effective but also environmentally sustainable is essential for transitioning from laboratory research to industrial production. Furthermore, addressing the existing gaps in regulatory strategy and standardization is crucial to support the broader commercialization and clinical integration of nanomaterial-based technologies [150].

The previously discussed challenges in the practical utilization, from laboratory research to clinical application, can largely be described as 'cellular response heterogeneity driven by material tunability'. Overcoming these issues requires not only advancements in synthesis/production, standardization and characterization of these materials, but also hand-in-hand progress in SC biology. Recent insights into SC biology have revealed how mechanical and chemical cues from the microenvironment influence cell fate through mechanotransduction pathways [151]. This mechanotransductive signaling integrates the microenvironment, cell membrane, cytoskeleton and nucleus, ultimately guiding SCs behavior and fate. To bridge the gap between controlled laboratory settings and large-scale production, as well as for translation to clinical studies, the development of robust legal frameworks, standards, and protocols is essential. Additionally, mimicking physiological conditions through mathematical modeling, integrated data analysis, and the design of patient-specific therapies will be beneficial to the successful application of 2D materials in regenerative medicine. It offers cost-effective, ethically clean and fast solution [152].

Overall, graphene-based materials pose both risks and opportunities, with toxicity varying based on their form, properties and exposure route. Inhalation can cause lung inflammation, ingestion may disrupt gut microbiota, dermal contact might lead to irritation, and systemic exposure can result in organ accumulation and inflammation. Despite these concerns, graphene shows promise in biomedical applications such as drug delivery, antimicrobial treatments and cancer therapy [153]. Discrepancies that arise between *in vitro* and *in vivo* conditions during the evaluation of nanomaterials and their biocompatibility are the consequences of inability to replicate the complex biological environment of systemic circulation (in comparison to *in vitro* cell culture media). This mismatch, based on how the biomolecular corona differs *in vivo* and *in vitro*, can lead to biases, stressing the importance of the comprehensive approach, using advanced data analyses and machine learning [154]. While no 2D material is universally superior, GO and rGO dominate in bone, cardiac and neural applications due to their conductivity and compatibility. MXenes contribute in cardiac repair and wound healing because of their antioxidative and electroactive nature. TMDs like MoS_2 and WS_2 show great promise in osteogenesis and neuroregeneration due to their semiconducting and photothermal properties, whereas hBN can be considered beneficial in adipogenesis and neural tissue regeneration, (see table 1). The future of regenerative medicine lies in precisely engineering these materials for specific tissue environments while ensuring long-term safety and performance.

In addition, 2D and related materials have become a fertile ground for preparation of a variety of sensors, with the humidity sensing being among the most promising. These sensors can be used in different scenarios, such as for simple monitoring of the RH of the environment, to the human health and agriculture monitoring. In the field of agriculture, these sensors can be utilized to detect soil moisture, or the transpiration cycles of plants, whereby they are coming to a direct contact with the environment. Furthermore, as they can have high stretchability and sensitivity, simple manufacturing process and fast response, they can be added to wearable devices or attached directly to the skin. This is another incentive for studying their biological activity and toxicity, as these novel devices have to be biocompatible if they are to be in contact with human skin and/or soil. This is especially important as the best sensing materials so far are exfoliated or surface modified with reactive surface area and edge sites, which usually leads to elevated cellular response.

In this review, we discussed different sensing mechanisms, and summarized the performance of different families of materials. While the standard types of sensors, such as capacitive and resistive, are relatively easy to fabricate and test, new methods are needed in order to minimize the size and the cost of the sensor. For example, sensors based on fiber optics can be easily integrated into the pre-established fiber optic systems. While developing new sensing mechanisms can lead to improved general performance of the device, another approach is to prepare a material with the best characteristics for the specific need. One way to enhance the sensitivity and RRTs is to increase the density of active edge sites of nanomaterials. This can be achieved via size control, where reducing the size leads to the increase in the density of edge sites. Another approach is shape control, where nanomaterials with unique structures, such as dendrites, nanotubes, NWs and nanoflowers, intrinsically containing a high number of edge sites, improve sensing performance. While rigid sensors based on GO and rGO showed promising characteristics and high RRTs, similar sensors based on or surface-modified or TMDC nanotubes showed superior response. For example, as summarized in table 2, sensor based on plasma-irradiated MoS_2 NPs has a far better performance than MoS_2 sheets, with sub-second RRTs [93]. The best performance was achieved by rGO functionalized with hydrophilic moieties, with ultrafast RRTs of 25 ms/127 ms [82]. Nevertheless, the stiffness of these materials limits their use for human health sensing.

The increasing need to move away from intrinsically rigid to flexible and wearable sensors requires finding a sensing material that responds well to mechanical deformations through a change in the electrical signal. The best way to achieve flexibility is to combine 2D and TMDC materials with polymer matrices. Some of the most promising candidates are rGO/PU [2], a combined sensing material made of rGO/MoS_2/PI, MXene/GO/COC [71], with the best two reported sensors being MoS_2-based: MoS_2/PEO with RRTs of 0.6 s/0.3 s [88] and MoS_2 NTs/Ecoflex with 0.5 s/0.8 s [89]. Therefore, a good approach to improving the performance of the polymer matrix is to use TMDC nanotubes or NWs. While the CNTs have a good potential, they have a few setbacks as well-they do not disperse well in most organic solvents, resulting in poor homogeneity when mixed with a polymer matrix, so they have to be functionalized in order to enhance the interaction with the solvent. On the other hand, various inorganic TMDC NTs promise a wide spectrum of physical effects beyond the physics of CNTs [155]. They have a high aspect ratio, high specific surface area and excellent mechanical and vibrational/acoustic properties, making them suitable as composite nanofillers as only a small amount can be used for forming a conductive path [156, 157]. The high aspect ratio can also improve the low electrical percolation of the insulating polymer matrix and form an efficient electrical network. Furthermore, MS_2 NTs disperse well in all commonly used solvents, simplifying the composite preparation [158]. As previously mentioned, properly stored WS_2 NTs oxidize only marginally even after more than 20 years [133]. Another family of nanomaterials that shows a great promise as a filler, is the family of metal oxides, as seen in table 2 [159]. Their substoichiometric MO_{3-x} ($0 \leqslant x \leqslant 1$) phases grow in different shapes, such as NWs, flakes, needles and sheets. The optical, electrical and structural properties depend strongly on the degree of the reduction [160]. Together with the already reported sensors on stoichiometric CeO_2 [96], ZnO [97], TiO_2 [98] and SnO_2 NWs [77], W_5O_{14} and $W_{18}O_{49}$, are interesting candidates due to their large aspect ratio, while the presence of photoluminescence and localized surface plasmon resonances can introduce interesting optical effects. Nevertheless, one important aspect that has to be taken into account is the cost, ease of preparation and the field of use of a specific sensor. While some applications require high sensitivity and fast RRT, for some practical uses, such as a quick diagnostic tool outside the hospital setting, the priority should be the cost and the ease of use. For example, 20 breaths per minute is defined as rapid breathing, therefore, a sensor that has a complicated and expensive synthesis method but RRT of microseconds might be superior in performance, but not necessary for practical purposes.

Future health sensing potential of these materials is vast. In addition to devices reviewed here, 2D materials have been slowly incorporated into different types of health sensors. They were reported as respiration sensors for estimation of blood oxygen saturation (SpO_2) [161]. LIG was placed on a PI tape, and this patch-like sensor detected the changes in mechanical deflection (such as chest movement), and measured the respiration rate in real time. Graphene-based biosensors have also been successfully integrated into an automated sensing platform for transporter protein drug delivery, showing to be biocompatible with a picomolar ionic sensitivity [162]. Furthermore, inks made of 2D materials were prepared, compatible with the standard inkjet printing. For example, water-based additive-free ink was prepared from nitrogen-doped carboxylated graphene [163]. This ink was used to fabricate fully inkjet-printed electrodes, which successfully enabled the electrochemical detection of the key neurotransmitter dopamine. The carboxyl groups in NGA ink also enable covalent attachment to biomolecules such as antibodies or aptamers, making it possible to create fully inkjet-printed biosensors.

Overall, 2D and related TMDC materials possess a variety of properties desirable for fabrication of sensors for human health monitoring. Nevertheless, their biological impact has to be thoroughly studied before they can be mass-produced.

Data availability statement

All data that support the findings of this study are included within the article (and any supplementary files).

Acknowledgments

We acknowledge funding provided by the Center for Solid State Physics and New Materials, Institute of Physics Belgrade, through the Grant by the Ministry of Education, Science, and Technological Development of the Republic of Serbia and Center for Solid State Physics and New Materials. BV acknowledges financial support from the Slovenian Research Agency through contract P1-0099. BV acknowledges funding from the European Union's Horizon Europe research and innovation programme under Grant Agreement No. 101185375. This research was also supported by the Science Fund of the Republic of Serbia, 10925, Dynamics of CDW transition in strained quasi-1D systems—DYNAMIQS.

ORCID iDs

Jasmina Lazarević 0000-0001-8980-1688
Bojana Višić 0000-0002-2065-0727

References

[1] Sun X, Guo X, Gao J, Wu J, Huang F, Zhang J-H, Huang F, Lu X, Shi Y and Pan L 2024 E-skin and its advanced applications in ubiquitous health monitoring *Biomedicines* **12** 2307

[2] Trung T Q, Duy L T, Ramasundaram S and Lee N-E 2017 Transparent, stretchable, and rapid-response humidity sensor for body-attachable wearable electronics *Nano Res.* **10** 2021–33

[3] McKinley K L, Longaker M T and Naik S 2023 Emerging frontiers in regenerative medicine *Science* **380** 796–8

[4] Shafiq M, Ali O, Han S-B and Kim D-H 2021 Mechanobiological strategies to enhance stem cell functionality for regenerative medicine and tissue engineering *Front. Cell Dev. Biol.* **9** 747398

[5] Pittenger M F, Discher D E, Péault B M, Phinney D G, Hare J M and Caplan A I 2019 Mesenchymal stem cell perspective: cell biology to clinical progress *npj Regen. Med.* **4** 22

[6] English K P, Mahon B J and Wood K 2014 Mesenchymal stromal cells; role in tissue repair, drug discovery and immune modulation *Concurr. Drug Deliv.* **11** 561–71

[7] Zakrzewski W, Dobrzyński M, Szymonowicz M and Rybak Z 2019 Stem cells: past, present, and future *Stem Cell Res. Ther.* **10** 68

[8] Gokce C, Gurcan C, Delogu L G and Yilmazer A 2022 2D materials for cardiac tissue repair and regeneration *Front. Cardiovasc. Med.* **9** 802551

[9] Qasim M, Chae D S and Lee N Y 2020 Bioengineering strategies for bone and cartilage tissue regeneration using growth factors and stem cells *J. Biomed. Mater. Res. A* **108** 394–411

[10] Hasnain A and Tarasov A 2023 Graphene-based electronic biosensors for disease diagnostics *Graphene Field-Effect Transistors: Advanced Bioelectronic Devices for Sensing Applications ed* O Azzaroni W Knoll (Wiley) pp 71–101

[11] Kostarelos K, Aguilar C and Garrido J A 2024 Clinical translation of graphene-based medical technology *Nat. Rev. Electr. Eng.* **1** 75–76

[12] Sekuła-Stryjewska M, Noga S, Dźwigońska M, Adamczyk E, Karnas E, Jagiełło J, Szkaradek A, Chytrosz P, Boruczkowski D and Madeja Z 2021 Graphene-based materials enhance cardiomyogenic and angiogenic differentiation capacity of human mesenchymal stem cells *in vitro*–focus on cardiac tissue regeneration *Mater. Sci. Eng. C* **119** 111614

[13] Jalilinejad N *et al* 2023 Electrically conductive carbon-based (bio)-nanomaterials for cardiac tissue engineering *Bioeng. Transl. Med.* **8** e10347

[14] Cahill T J, Choudhury R P and Riley P R 2017 Heart regeneration and repair after myocardial infarction: translational opportunities for novel therapeutics *Nat. Rev. Drug Discovery* **16** 699–717

[15] Hu X, Yu S P, Fraser J L, Lu Z, Ogle M E, Wang J-A and Wei L 2008 Transplantation of hypoxia-preconditioned mesenchymal stem cells improves infarcted heart function via enhanced survival of implanted cells and angiogenesis *J. Thoracic Cardiovasc. Surg.* **135** 799–808

[16] Lee W C, Lim C H Y, Shi H, Tang L A, Wang Y, Lim C T and Loh K P 2011 Origin of enhanced stem cell growth and differentiation on graphene and graphene oxide *ACS Nano* **5** 7334–41

[17] Ikram R, Shamsuddin S A A, Mohamed Jan B, Abdul Qadir M, Kenanakis G, Stylianakis M M and Anastasiadis S H 2022 Impact of graphene derivatives as artificial extracellular matrices on mesenchymal stem cells *Molecules* **27** 379

[18] Heo J, Choi J, Kim J Y, Jeong H, Choi D, Han U, Park J H, Park H H and Hong J 2021 2D graphene oxide particles induce unwanted loss in pluripotency and trigger early differentiation in human pluripotent stem cells *J. Hazard. Mater.* **414** 125472

[19] Qi X, Liu Y, Yin X, Zhao R, Zhang W, Cao J, Wang W and Jia W 2023 Surface-based modified 3D-printed BG/GO scaffolds promote bone defect repair through bone immunomodulation *Composites B* **257** 110673

[20] Sulaksono H L S, Annisa A, Ruslami R, Mufeeduzzaman M, Panatarani C, Hermawan W, Ekawardhani S and Joni I M 2024 Recent advances in graphene oxide-based on organoid culture as disease model and cell behavior–a systematic literature review *Int. J. Nanomed.* **19** 6201–28

[21] Romaldini A, Spanò R, Veronesi M, Grimaldi B, Bandiera T and Sabella S 2024 Human multi-lineage liver organoid model reveals impairment of CYP3A4 expression upon repeated exposure to graphene oxide *Cells* **13** 1542

[22] Yu S, Wang L, Chen M, Chen Y and Peng Z 2025 MXene-incorporated conductive hydrogel simulating myocardial microenvironment for cardiac repair and functional recovery *Biomacromolecules* **26** 2378–89

[23] Edrisi F, Baheiraei N, Razavi M, Roshanbinfar K, Imani R and Jalilinejad N 2023 Potential of graphene-based nanomaterials for cardiac tissue engineering *J. Mater. Chem. B* **11** 7280–99

[24] Zaszczyńska A, Zabielski K, Gradys A, Kowalczyk T and Sajkiewicz P 2024 Piezoelectric scaffolds as smart materials for bone tissue engineering *Polymers* **16** 2797

[25] Collins M N, Ren G, Young K, Pina S, Reis R L and Oliveira J M 2021 Scaffold fabrication technologies and structure/function properties in bone tissue engineering *Adv. Funct. Mater.* **31** 2010609

[26] Koons G L, Diba M and Mikos A G 2020 Materials design for bone-tissue engineering *Nat. Rev. Mater.* **5** 584–603

[27] Kang E-S, Kim D-S, Suhito I R, Lee W, Song I and Kim T-H 2018 Two-dimensional material-based bionano platforms to control mesenchymal stem cell differentiation *Biomater. Res.* **22** 10

[28] Yadav S, Singh Raman A P, Meena H, Goswami A G, Bhawna, Kumar V, Jain P, Kumar G, Sagar M and Rana D K 2022 An update on graphene oxide: applications and toxicity *ACS Omega* **7** 35387–445

[29] Soleymani H, Moghaddam M M, Naderi-Manesh H and Taheri R A 2024 Single-layer graphene oxide nanosheets induce proliferation and Osteogenesis of single-cell hBMSCs encapsulated in Alginate Microgels *Sci. Rep.* **14** 25272

[30] Nayak T R, Andersen H, Makam V S, Khaw C, Bae S, Xu X, Ee P-L R, Ahn J-H, Hong B H and Pastorin G 2011 Graphene for controlled and accelerated osteogenic differentiation of human mesenchymal stem cells *ACS Nano* **5** 4670–8

[31] Ma X, Luan Z and Li J 2023 Inorganic nanoparticles-based systems in biomedical applications of stem cells: opportunities and challenges *Int. J. Nanomed.* **18** 143–82

[32] Saikia N 2024 Inorganic-based nanoparticles and biomaterials as biocompatible scaffolds for regenerative medicine and tissue engineering: current advances and trends of development *Inorganics* **12** 292

[33] Liu A, Chen J, Zhang J, Zhang C, Zhou Q, Niu P and Yuan Y 2022 Intra-articular injection of umbilical cord mesenchymal stem cells loaded with graphene oxide granular lubrication ameliorates inflammatory responses and osteoporosis of the subchondral bone in rabbits of modified papain-induced osteoarthritis *Front. Endocrinol.* **12** 822294

[34] Shuai C, Zeng Z, Yang Y, Qi F, Peng S, Yang W, He C, Wang G and Qian G 2020 Graphene oxide assists polyvinylidene fluoride scaffold to reconstruct electrical microenvironment of bone tissue *Mater. Des.* **190** 108564

[35] Zhou X, Sun H and Bai X 2020 Two-dimensional transition metal dichalcogenides: synthesis, biomedical applications and biosafety evaluation *Front. Bioeng. Biotechnol.* **8** 236

[36] Carrow J K, Singh K A, Jaiswal M K, Ramirez A, Lokhande G, Yeh A T, Sarkar T R, Singh I and Gaharwar A K 2020 Photothermal modulation of human stem cells using light-responsive 2D nanomaterials *Proc. Natl Acad. Sci.* **117** 13329–38

[37] Roy S, Deo K A, Singh K A, Lee H P, Jaiswal A and Gaharwar A K 2022 Nano-bio interactions of 2D molybdenum disulfide *Adv. Drug Deliv. Rev.* **187** 114361

[38] Sun G, Yang S, Cai H, Shu Y, Han Q, Wang B, Li Z, Zhou L, Gao Q and Yin Z 2019 Molybdenum disulfide nanoflowers mediated anti-inflammation macrophage modulation for spinal cord injury treatment *J. Colloid Interface Sci.* **549** 50–62

[39] Hadjidemetriou M, Mahmoudi M and Kostarelos K 2024 *In vivo* biomolecule corona and the transformation of a foe into an ally for nanomedicine *Nat. Rev. Mater.* **9** 219–22

[40] Murali A, Lokhande G, Deo K A, Brokesh A and Gaharwar A K 2021 Emerging 2D nanomaterials for biomedical applications *Mater. Today* **50** 276–302

[41] Suhito I R, Han Y, Kim D-S, Son H and Kim T-H 2017 Effects of two-dimensional materials on human mesenchymal stem cell behaviors *Biochem. Biophys. Res. Commun.* **493** 578–84

[42] Natu V, Sokol M, Verger L and Barsoum M W 2018 Effect of edge charges on stability and aggregation of $Ti_3C_2T_z$ MXene colloidal suspensions *J. Phys. Chem. C* **122** 27745–53

[43] Qu X, Guo Y, Xie C, Li S, Liu Z and Lei B 2023 Photoactivated MXene nanosheets for integrated bone–soft tissue therapy: effect and potential mechanism *ACS Nano* **17** 7229–40

[44] Babar Z U D, Iannotti V, Rosati G, Zaheer A, Velotta R, Della Ventura B, Álvarez-Diduk R and Merkoçi A 2025 MXenes in healthcare: synthesis, fundamentals and applications *Chem. Soc. Rev.* **54** 3387–440

[45] Li K, Ji Q, Liang H, Hua Z, Hang X, Zeng L and Han H 2023 Biomedical application of 2D nanomaterials in neuroscience *J. Nanobiotechnol.* **21** 181

[46] Qian Y, Wang X, Song J, Chen W, Chen S, Jin Y, Ouyang Y, Yuan W-E and Fan C 2021 Preclinical assessment on neuronal regeneration in the injury-related microenvironment of graphene-based scaffolds *npj Regen. Med.* **6** 31

[47] Qian Y, Zhao X, Han Q, Chen W, Li H and Yuan W 2018 An integrated multi-layer 3D-fabrication of PDA/RGD coated graphene loaded PCL nanoscaffold for peripheral nerve restoration *Nat. Commun.* **9** 323

[48] da Silva D M, Barroca N, Pinto S C, Semitela Â, de Sousa B M, Martins P A, Nero L, Madarieta I, García-Urkia N and Fernández-San-Argimiro F-J 2023 Decellularized extracellular matrix-based 3D nanofibrous scaffolds functionalized with polydopamine-reduced graphene oxide for neural tissue engineering *Chem. Eng. J.* **472** 144980

[49] Fabbro A, Scaini D, León V, Vázquez E, Cellot G, Privitera G, Lombardi L, Torrisi F, Tomarchio F and Bonaccorso F 2016 Graphene-based interfaces do not alter target nerve cells *ACS Nano* **10** 615–23

[50] Bramini M, Alberini G, Colombo E, Chiacchiaretta M, DiFrancesco M L, Maya-Vetencourt J F, Maragliano L, Benfenati F and Cesca F 2018 Interfacing graphene-based materials with neural cells *Front. Syst. Neurosci.* **12** 358913

[51] Wang Z and Mi B 2017 Environmental applications of 2D molybdenum disulfide (MoS_2) nanosheets *Environ. Sci. Technol.* **51** 8229–44

[52] Zhao C, Deng W and Gage F H 2008 Mechanisms and functional implications of adult neurogenesis *Cell* **132** 645–60

[53] Lee H P and Gaharwar A K 2020 Light-responsive inorganic biomaterials for biomedical applications *Adv. Sci.* **7** 2000863

[54] Wan X, Liu Z and Li L 2021 Manipulation of stem cells fates: the master and multifaceted roles of biophysical cues of biomaterials *Adv. Funct. Mater.* **31** 2010626

[55] Qian Y, Xu Y, Yan Z, Jin Y, Chen X, Yuan W-E and Fan C 2021 Boron nitride nanosheets functionalized channel scaffold favors microenvironment rebalance cocktail therapy for piezocatalytic neuronal repair *Nano Energy* **83** 105779

[56] Merlo A, Mokkapati V, Pandit S and Mijakovic I 2018 Boron nitride nanomaterials: biocompatibility and bio-applications *Biomater. Sci.* **6** 2298–311

[57] Silvestri A, Wetzl C, Alegret N, Cardo L, Hou H-L, Criado A and Prato M 2022 The era of nano-bionic: 2D materials for wearable and implantable body sensors *Adv. Drug Deliv. Rev.* **186** 114315

[58] Ansari H R, Mirzaei A, Shokrollahi H, Kumar R, Kim J-Y, Kim H W, Kumar M and Kim S S 2023 Flexible/wearable resistive gas sensors based on 2D materials *J. Mater. Chem. C* **11** 6528–49

[59] Anwer A H, Saadaoui M, Mohamed A T, Ahmad N and Benamor A 2024 State-of-the-Art advances and challenges in wearable gas sensors for emerging applications: innovations and future prospects *Chem. Eng. J.* **502** 157899

[60] Pawar K K, Kumar A, Mirzaei A, Kumar M, Kim H W and Kim S S 2024 2D nanomaterials for realization of flexible and wearable gas sensors: a review *Chemosphere* **352** 141234

[61] Bi H, Yin K, Xie X, Ji J, Wan S, Sun L, Terrones M and Dresselhaus M S 2013 Ultrahigh humidity sensitivity of graphene oxide *Sci. Rep.* **3** 2714

[62] Zhang D, Tong J, Xia B and Xue Q 2014 Ultrahigh performance humidity sensor based on layer-by-layer self-assembly of graphene oxide/polyelectrolyte nanocomposite film *Sens. Actuators B* **203** 263–70

[63] Yu H-W, Kim H K, Kim T, Bae K M, Seo S M, Kim J-M, Kang T J and Kim Y H 2014 Self-powered humidity sensor based on graphene oxide composite film intercalated by poly (sodium 4-styrenesulfonate) *ACS Appl. Mater. Interfaces* **6** 8320–6

[64] Li N, Chen X, Chen X, Ding X and Zhao X 2017 Ultrahigh humidity sensitivity of graphene oxide combined with Ag nanoparticles *RSC Adv.* **7** 45988–96

[65] Lan L, Le X, Dong H, Xie J, Ying Y and Ping J 2020 One-step and large-scale fabrication of flexible and wearable humidity sensor based on laser-induced graphene for real-time tracking of plant transpiration at bio-interface *Biosens. Bioelectron.* **165** 112360

[66] Siddiqui M S, Mandal A, Kalita H and Aslam M 2022 Highly sensitive few-layer MoS_2 nanosheets as a stable soil moisture and humidity sensor *Sens. Actuators B* **365** 131930

[67] Ke N, Si F, Ma H, Gao Q, Ge G, Liu W, Ding J, Zhang W and Fan X 2024 Fully flexible humidity sensor with fast response and high responsivity based on rGO/MoS_2 for human respiration monitoring and nontouch switches *ACS Appl. Mater. Interfaces* **17** 2317–26

[68] Borini S, White R, Wei D, Astley M, Haque S, Spigone E, Harris N, Kivioja J and Ryhänen T 2013 Ultrafast graphene oxide humidity sensors *ACS Nano* **7** 11166–73

[69] Tamayo A, Danowski W, Han B, Jeong Y and Samorì P 2024 Light-modulated humidity sensing in spiropyran functionalized MoS_2 transistors *Small* 2404633

[70] Ren J, Guo B, Feng Y and Yu K 2020 Few-layer MoS_2 dendrites as a highly active humidity sensor *Physica E* **116** 113782

[71] Waheed W, Anwer S, Khan M U, Sajjad M and Alazzam A 2024 2D $Ti_3C_2T_x$-MXene nanosheets and graphene oxide based highly sensitive humidity sensor for wearable and flexible electronics *Chem. Eng. J.* **480** 147981

[72] Cheng B, Tian B, Xie C, Xiao Y and Lei S 2011 Highly sensitive humidity sensor based on amorphous Al_2O_3 nanotubes *J. Mater. Chem.* **21** 1907–12

[73] Zhang D, Wang D, Zong X, Dong G and Zhang Y 2018 High-performance QCM humidity sensor based on graphene oxide/tin oxide/polyaniline ternary nanocomposite prepared by *in-situ* oxidative polymerization method *Sens. Actuators B* **262** 531–41

[74] Yuan Z, Tai H, Ye Z, Liu C, Xie G, Du X and Jiang Y 2016 Novel highly sensitive QCM humidity sensor with low hysteresis based on graphene oxide (GO)/poly (ethyleneimine) layered film *Sens. Actuators B* **234** 145–54

[75] Lei D, Zhang Q, Liu N, Su T, Wang L, Ren Z, Zhang Z, Su J and Gao Y 2022 Self-powered graphene oxide humidity sensor based on potentiometric humidity transduction mechanism *Adv. Funct. Mater.* **32** 2107330

[76] Luo Y, Chen C, Xia K, Peng S, Guan H, Tang J, Lu H, Yu J, Zhang J and Xiao Y 2016 Tungsten disulfide (WS_2) based all-fiber-optic humidity sensor *Opt. Express* **24** 8956–66

[77] Kuang Q, Lao C, Wang Z L, Xie Z and Zheng L 2007 High-sensitivity humidity sensor based on a single SnO_2 nanowire *J. Am. Chem. Soc.* **129** 6070–1

[78] Guo L *et al* 2012 Two-beam-laser interference mediated reduction, patterning and nanostructuring of graphene oxide for the production of a flexible humidity sensing device *Carbon* **50** 1667–73

[79] Smith A D, Elgammal K, Niklaus F, Delin A, Fischer A C, Vaziri S, Forsberg F, Råsander M, Hugosson H and Bergqvist L 2015 Resistive graphene humidity sensors with rapid and direct electrical readout *Nanoscale* **7** 19099–109

[80] Naik G and Krishnaswamy S 2015 Room-temperature humidity sensing using graphene oxide thin films *Graphene* **5** 1–13

[81] Wu J, Wu Z, Ding H, Wei Y, Yang X, Li Z, Yang B-R, Liu C, Qiu L and Wang X 2019 Multifunctional and high-sensitive sensor capable of detecting humidity, temperature, and flow stimuli using an integrated microheater *ACS Appl. Mater. Interfaces* **11** 43383–92

[82] Anichini C, Aliprandi A, Gali S M, Liscio F, Morandi V, Minoia A, Beljonne D, Ciesielski A and Samorì P 2020 Ultrafast and highly sensitive chemically functionalized graphene oxide-based humidity sensors: harnessing device performances via the supramolecular approach *ACS Appl. Mater. Interfaces* **12** 44017–25

[83] Tripathi S, Gangwar N, Gangwar C and Shukla R 2025 Enhanced humidity sensing using graphene oxide and reduced graphene oxide synthesized via modified Hummers' method *Sens. Imaging* **26** 20

[84] Burman D, Ghosh R, Santra S and Guha P K 2016 Highly proton conducting MoS_2/graphene oxide nanocomposite based chemoresistive humidity sensor *RSC Adv.* **6** 57424–33

[85] Park S Y, Kim Y H, Lee S Y, Sohn W, Lee J E, Shim Y-S, Kwon K C, Choi K S, Yoo H J and Suh J M 2018 Highly selective and sensitive chemoresistive humidity sensors based on rGO/MoS_2 van der Waals composites *J. Mater. Chem. A* **6** 5016–24

[86] Zhang S-L, Choi H-H, Yue H-Y and Yang W-C 2014 Controlled exfoliation of molybdenum disulfide for developing thin film humidity sensor *Curr. Appl Phys.* **14** 264–8

[87] Lou Z, Wu D, Bu K, Xu T, Shi Z, Xu J, Tian Y and Li X 2017 Dual-mode high-sensitivity humidity sensor based on MoS_2/Si nanowires array heterojunction *J. Alloys Compd.* **726** 632–7

[88] Yousaf H Z, Kim S W, Hassan G, Karimov K, Choi K H and Sajid M 2020 Highly sensitive wide range linear integrated temperature compensated humidity sensors fabricated using electrohydrodynamic printing and electrospray deposition *Sens. Actuators B* **308** 127680

[89] Mondal S, Kim S J and Choi C-G 2020 Honeycomb-like MoS_2 nanotube array-based wearable sensors for noninvasive detection of human skin moisture *ACS Appl. Mater. Interfaces* **12** 17029–38

[90] Guo W, He Z, Li J, Yao L, Qiao Y, Wang F, Wang Y and Wang F 2024 3D $MoSe_2$@ MoS_2 heterojunction for humidity sensors to improve sensing performance *J. Alloys Compd.* **983** 173833

[91] Pawbake A S, Waykar R G, Late D J and Jadkar S R 2016 Highly transparent wafer-scale synthesis of crystalline WS_2 nanoparticle thin film for photodetector and humidity-sensing applications *ACS Appl. Mater. Interfaces* **8** 3359–65

[92] Leonardi S, Wlodarski W, Li Y, Donato N, Sofer Z, Pumera M and Neri G 2018 A highly sensitive room temperature humidity sensor based on 2D-WS2 nanosheets *FlatChem* **9** 21–26

[93] Taufik A, Asakura Y, Hasegawa T, Kato H, Kakihana M, Hirata S, Inada M and Yin S 2020 Surface engineering of 1T/2H-MoS_2 nanoparticles by O_2 plasma irradiation as a potential humidity sensor for breathing and skin monitoring applications *ACS Appl. Nano Mater.* **3** 7835–46

[94] Bharatula L D, Erande M B, Mulla I S, Rout C S and Late D J 2016 SnS_2 nanoflakes for efficient humidity and alcohol sensing at room temperature *RSC Adv.* **6** 105421–7

[95] Deb M, Chen M-Y, Chang P-Y, Li P-H, Chan M-J, Tian Y-C, Yeh P-H, Soppera O and Zan H-W 2023 SnO_2-based ultra-flexible humidity/respiratory sensor for analysis of human breath *Biosensors* **13** 81

[96] Fu X, Wang C, Yu H, Wang Y and Wang T 2007 Fast humidity sensors based on CeO_2 nanowires *Nanotechnology* **18** 145503

[97] Kiasari N M, Soltanian S, Gholamkhass B and Servati P 2012 Room temperature ultra-sensitive resistive humidity sensor based on single zinc oxide nanowire *Sens. Actuators A* **182** 101–5

[98] Li Z, Zhang H, Zheng W, Wang W, Huang H, Wang C, MacDiarmid A G and Wei Y 2008 Highly sensitive and stable humidity nanosensors based on LiCl doped TiO_2 electrospun nanofibers *J. Am. Chem. Soc.* **130** 5036–7

[99] Fowler J D, Allen M J, Tung V C, Yang Y, Kaner R B and Weiller B H 2009 Practical chemical sensors from chemically derived graphene *ACS Nano* **3** 301–6

[100] Ma H, Ding J, Zhang Z, Gao Q, Liu Q, Wang G, Zhang W and Fan X 2024 Recent advances in graphene-based humidity sensors with the focus of structural design: a review *IEEE Sens. J.* **24** 20289–311

[101] Buchsteiner A, Lerf A and Pieper J 2006 Water dynamics in graphite oxide investigated with neutron scattering *J. Phys. Chem. A* **110** 22328–38

[102] Nair R, Wu H, Jayaram P N, Grigorieva I V and Geim A 2012 Unimpeded permeation of water through helium-leak–tight graphene-based membranes *Science* **335** 442–4

[103] Wang D-W, Du A, Taran E, Lu G Q M and Gentle I R 2012 A water-dielectric capacitor using hydrated graphene oxide film *J. Mater. Chem.* **22** 21085–91

[104] Late D J *et al* 2013 Sensing behavior of atomically thin-layered MoS_2 transistors *ACS nano* **7** 4879–91

[105] Li H, Yin Z, He Q, Li H, Huang X, Lu G, Fam D W H, Tok A I Y, Zhang Q and Zhang H 2012 Fabrication of single-and multilayer MoS_2 film-based field-effect transistors for sensing NO at room temperature *Small* **8** 63–67

[106] Gobbi M *et al* 2018 Collective molecular switching in hybrid superlattices for light-modulated two-dimensional electronics *Nat. Commun.* **9** 2661

[107] Pujari S *et al* 2024 Au–MoS_2 nanoflowers sensors on interdigitated electrode for monitoring human respiration *Nano Express* (https://doi.org/10.1088/2632-959X/ad6c67)

[108] Wang B, Thukral A, Xie Z, Liu L, Zhang X, Huang W, Yu X, Yu C, Marks T J and Facchetti A 2020 Flexible and stretchable metal oxide nanofiber networks for multimodal and monolithically integrated wearable electronics *Nat. Commun.* **11** 2405

[109] Baloda S, Gupta N and Singh S 2022 A flexible pressure sensor based on multiwalled carbon nanotubes/polydimethylosiloxane composite for wearable

electronic-skin application *IEEE Trans. Electron. Devices* **69** 7011–8

[110] Panth M, Cook B, Alamri M, Ewing D, Wilson A and Wu J Z 2020 Flexible zinc oxide nanowire array/graphene nanohybrid for high-sensitivity strain detection *ACS Omega* **5** 27359–67

[111] Baloda S, Ansari Z A, Singh S and Gupta N 2020 Development and analysis of graphene nanoplatelets (GNPs)-based flexible strain sensor for health monitoring applications *IEEE Sens. J.* **20** 13302–9

[112] Irani F S, Shafaghi A H, Tasdelen M C, Delipinar T, Kaya C E, Yapici G G and Yapici M K 2022 Graphene as a piezoresistive material in strain sensing applications *Micromachines* **13** 119

[113] Xu W, Yang T, Qin F, Gong D, Du Y and Dai G 2019 A sprayed graphene pattern-based flexible strain sensor with high sensitivity and fast response *Sensors* **19** 1077

[114] Ben Aziza Z, Zhang K, Baillargeat D and Zhang Q 2015 Enhancement of humidity sensitivity of graphene through functionalization with polyethylenimine *Appl. Phys. Lett.* **107** 134102

[115] Célérier S *et al* 2018 Hydration of $Ti_3C_2T_x$ MXene: an interstratification process with major implications on physical properties *Chem. Mater.* **31** 454–61

[116] Mirjalali S, Peng S, Fang Z, Wang C H and Wu S 2022 Wearable sensors for remote health monitoring: potential applications for early diagnosis of Covid-19 *Adv. Mater. Technol.* **7** 2100545

[117] Silvestri A *et al* 2023 Ultrasensitive detection of SARS-CoV-2 spike protein by graphene field-effect transistors *Nanoscale* **15** 1076–85

[118] Liu T, Qu D, Guo L, Zhou G, Zhang G, Du T and Wu W 2024 MXene/TPU composite film for humidity sensing and human respiration monitoring *Adv. Sens. Res.* **3** 2300014

[119] Xing H, Li X, Lu Y, Wu Y, He Y, Chen Q, Liu Q and Han R P 2022 MXene/MWCNT electronic fabric with enhanced mechanical robustness on humidity sensing for real-time respiration monitoring *Sens. Actuators B* **361** 131704

[120] SU S L, Singh D N and Baghini M S 2014 A critical review of soil moisture measurement *Measurement* **54** 92–105

[121] Surya S G, Yuvaraja S, Varrla E, Baghini M S, Palaparthy V S and Salama K N 2020 An in-field integrated capacitive sensor for rapid detection and quantification of soil moisture *Sens. Actuators B* **321** 128542

[122] Wang Z, Zhu W, Qiu Y, Yi X, von Dem Bussche A, Kane A, Gao H, Koski K and Hurt R 2016 Biological and environmental interactions of emerging two-dimensional nanomaterials *Chem. Soc. Rev.* **45** 1750–80

[123] Huang X, Auffan M, Eckelman M J, Elimelech M, Kim J-H, Rose J, Zuo K, Li Q and Alvarez P J 2024 Trends, risks and opportunities in environmental nanotechnology *Nat. Rev. Earth Environ.* **5** 572–87

[124] Andrews J P *et al* 2024 First-in-human controlled inhalation of thin graphene oxide nanosheets to study acute cardiorespiratory responses *Nat. Nanotechnol.* **19** 705–14

[125] Garner K L and Keller A A 2014 Emerging patterns for engineered nanomaterials in the environment: a review of fate and toxicity studies *J. Nanopart. Res.* **16** 1–28

[126] Fojtů M, Teo W Z and Pumera M 2017 Environmental impact and potential health risks of 2D nanomaterials *Environ. Sci. Nano* **4** 1617–33

[127] Lin H *et al* 2024 Environmental and health impacts of graphene and other two-dimensional materials: a graphene flagship perspective *ACS Nano* **18** 6038–94

[128] Vranic S, Kurapati R, Kostarelos K and Bianco A 2025 Biological and environmental degradation of two-dimensional materials *Nat. Rev. Chem.* **9** 1–12

[129] Gao J, Li B, Tan J, Chow P, Lu T-M and Koratkar N 2016 Aging of transition metal dichalcogenide monolayers *ACS Nano* **10** 2628–35

[130] Yoo M J and Park H B 2019 Effect of hydrogen peroxide on properties of graphene oxide in Hummers method *Carbon* **141** 515–22

[131] Najmi P, Keshmiri N, Ramezanzadeh M, Ramezanzadeh B and Arjmand M 2023 Epoxy nanocomposites holding molybdenum disulfide decorated with covalent organic framework: all-in-one coatings featuring thermal, UV-shielding, and mechanical properties *Composites B* **260** 110785

[132] Dong W, Dai Z, Liu L and Zhang Z 2024 Toward clean 2D materials and devices: recent progress in transfer and cleaning methods *Adv. Mater.* **36** 2303014

[133] Rosentsveig R, Feldman Y, Kundrat V, Pinkas I, Zak A and Tenne R 2025 Long-term aging of multiwall nanotubes and fullerene-like nanoparticles of WS_2 *J. Solid State Chem.* **346** 125259

[134] Raza S, Hayat A, Bashir T, Chen C, Shen L, Orooji Y and Lin H 2024 Electrochemistry of 2D-materials for the remediation of environmental pollutants and alternative energy storage/conversion materials and devices, a comprehensive review *Sustain. Mater. Technol.* **40** e00963

[135] Yang J *et al* 2022 Oxidations of two-dimensional semiconductors: fundamentals and applications *Chin. Chem. Lett.* **33** 177–85

[136] Arora N K and Mishra I 2022 Sustainable development goal 6: global water security *Environ. Sustain.* **5** 271–5

[137] Garg A, Basu S, Shetti N P and Reddy K R 2021 2D materials and its heterostructured photocatalysts: synthesis, properties, functionalization and applications in environmental remediation *J. Environ. Chem. Eng.* **9** 106408

[138] Zhang C, Ma Y, Zhang X, Abdolhosseinzadeh S, Sheng H, Lan W, Pakdel A, Heier J and Nüesch F 2020 Two-dimensional transition metal carbides and nitrides (MXenes): synthesis, properties, and electrochemical energy storage applications *Energy Environ. Mater.* **3** 29–55

[139] Ikram M, Khan M, Raza A, Imran M, Ul-Hamid A and Ali S 2020 Outstanding performance of silver-decorated MoS_2 nanopetals used as nanocatalyst for synthetic dye degradation *Physica E* **124** 114246

[140] Velusamy S, Roy A, Sundaram S and Kumar Mallick T 2021 A review on heavy metal ions and containing dyes removal through graphene oxide-based adsorption strategies for textile wastewater treatment *Chem. Rec.* **21** 1570–610

[141] Ranjan P *et al* 2024 2D materials for potable water application: basic nanoarchitectonics and recent progresses *Small* **20** 2407160

[142] Junaidi N F D, Othman N H, Fuzil N S, Shayuti M S M, Alias N H, Shahruddin M Z, Marpani F, Lau W J, Ismail A F and Aba N D 2021 Recent development of graphene oxide-based membranes for oil–water separation: a review *Sep. Purif. Technol.* **258** 118000

[143] Perveen H and Zahoor I 2024 Two dimensional materials for wastewater treatment *Int. J. Chem. Biochem. Sci.* **25** 164–77

[144] Li M *et al* 2023 Molybdenum nanofertilizer boosts biological nitrogen fixation and yield of soybean through delaying nodule senescence and nutrition enhancement *ACS Nano* **17** 14761–74

[145] Teo W Z, Chng E L K, Sofer Z and Pumera M 2014 Cytotoxicity of exfoliated transition-metal dichalcogenides (MoS_2, WS_2, and WSe_2) is lower than that of graphene and its analogues *Chemistry A* **20** 9627–32

[146] Latiff N M, Sofer Z, Fisher A C and Pumera M 2017 Cytotoxicity of exfoliated layered vanadium dichalcogenides *Chemistry* **23** 684–90

[147] Chng E L K, Sofer Z and Pumera M 2014 MoS_2 exhibits stronger toxicity with increased exfoliation *Nanoscale* **6** 14412–8

[148] Guiney L M, Wang X, Xia T, Nel A E and Hersam M C 2018 Assessing and mitigating the hazard potential of two-dimensional materials *ACS Nano* **12** 6360–77

[149] Wang X, Mansukhani N D, Guiney L M, Ji Z, Chang C H, Wang M, Liao Y P, Song T B, Sun B and Li R 2015 Differences in the toxicological potential of 2D versus

aggregated molybdenum disulfide in the lung *Small* **11** 5079–87

[150] Baig N, Kammakakam I and Falath W 2021 Nanomaterials: a review of synthesis methods, properties, recent progress, and challenges *Mater. Adv.* **2** 1821–71

[151] Ferrai C and Schulte C 2024 Mechanotransduction in stem cells *Eur. J. Cell Biol.* **103** 151417

[152] Lu B *et al* 2024 When machine learning meets 2D materials: a review *Adv. Sci.* **11** 2305277

[153] Volkov Y, McIntyre J and Prina-Mello A 2017 Graphene toxicity as a double-edged sword of risks and exploitable opportunities: a critical analysis of the most recent trends and developments *2D Mater.* **4** 022001

[154] Castagnola V, Tomati V, Boselli L, Braccia C, Decherchi S, Pompa P P, Pedemonte N, Benfenati F and Armirotti A 2024 Sources of biases in the *in vitro* testing of nanomaterials: the role of the biomolecular corona *Nanoscale Horiz.* **9** 799–816

[155] Višić B, Panchakarla L S and Tenne R 2017 Inorganic nanotubes and fullerene-like nanoparticles at the crossroads between solid-state chemistry and nanotechnology *J. Am. Chem. Soc.* **139** 12865–78

[156] Evarestov R, Kovalenko A, Bandura A, Domnin A and Lukyanov S 2018 Comparison of vibrational and thermodynamic properties of MoS_2 and WS_2 nanotubes: first principles study *Mater. Res. Express* **5** 115028

[157] Sedova A, Višić B, Vega-Mayoral V, Vella D, Gadermaier C, Dodiuk H, Kenig S, Tenne R, Gvishi R and Bar G 2020 Silica aerogels as hosting matrices for WS_2 nanotubes and their optical characterization *J. Mater. Sci.* **55** 1–12

[158] Yadgarov L *et al* 2018 Strong light–matter interaction in tungsten disulfide nanotubes *Phys. Chem. Chem. Phys.* **20** 20812–20

[159] Pirker L and Višić B 2022 Recent progress in the synthesis and potential applications of two-dimensional tungsten (Sub) oxides *Isr. J. Chem.* **62** e202100074

[160] Višić B, Pirker L, Opačić M, Milosavljević A, Lazarević N, Majaron B and Remškar M 2022 Influence of crystal structure and oxygen vacancies on optical properties of nanostructured multi-stoichiometric tungsten suboxides *Nanotechnology* **33** 275705

[161] Madevska Bogdanova A, Koteska B, Vićentić T, Ilić S D, Tomić M, Spasenović M and Michel C 2024 Blood oxygen saturation estimation with laser-induced graphene respiration sensor *J. Sens.* **2024** 4696031

[162] Meincke M *et al* 2025 Integration of highly sensitive large-area graphene-based biosensors in an automated sensing platform *Measurement* **240** 115592

[163] Nalepa M-A, Panáček D, Dědek I, Jakubec P, Kupka V, Hrubý V, Petr M and Otyepka M 2024 Graphene derivative-based ink advances inkjet printing technology for fabrication of electrochemical sensors and biosensors *Biosens. Bioelectron.* **256** 116277

International Journal of
Molecular Sciences

Article

A Single-Cell Raman Spectroscopy Analysis of Bone Marrow Mesenchymal Stem/Stromal Cells to Identify Inter-Individual Diversity

Tamara Kukolj [1,*,†], Jasmina Lazarević [2,†], Ana Borojević [3], Uroš Ralević [2], Dragana Vujić [3,4], Aleksandra Jauković [1], Nenad Lazarević [2] and Diana Bugarski [1]

[1] Group for Hematology and Stem Cells, Institute for Medical Research, National Institute of Republic of Serbia, University of Belgrade, 11129 Belgrade, Serbia; aleksandra@imi.bg.ac.rs (A.J.); dianab@imi.bg.ac.rs (D.B.)
[2] Center for Solid State Physics and New Materials, Institute of Physics Belgrade, University of Belgrade, Pregrevica 118, 11080 Belgrade, Serbia; jasminal@ipb.ac.rs (J.L.); uros.ralevic@ipb.ac.rs (U.R.); nenad.lazarevic@ipb.ac.rs (N.L.)
[3] Mother and Child Health Care Institute of Serbia "Dr Vukan Čupić", 11000 Belgrade, Serbia; ana.stojanovic.89@gmail.com (A.B.); vujicdbg@gmail.com (D.V.)
[4] School of Medicine, University of Belgrade, 11000 Belgrade, Serbia
* Correspondence: tamara.kukolj@imi.bg.ac.rs; Tel.: +381-11-2685-788
† These authors contributed equally to this work.

Abstract: The heterogeneity of stem cells represents the main challenge in regenerative medicine development. This issue is particularly pronounced when it comes to the use of primary mesenchymal stem/stromal cells (MSCs) due to a lack of identification markers. Considering the need for additional approaches in MSCs characterization, we applied Raman spectroscopy to investigate inter-individual differences between bone marrow MSCs (BM-MSCs). Based on standard biological tests, BM-MSCs of analyzed donors fulfill all conditions for their characterization, while no donor-related specifics were observed in terms of BM-MSCs morphology, phenotype, multilineage differentiation potential, colony-forming capacity, expression of pluripotency-associated markers or proliferative capacity. However, examination of BM-MSCs at a single-cell level by Raman spectroscopy revealed that despite similar biochemical background, fine differences in the Raman spectra of BM-MSCs of each donor can be detected. After extensive principal component analysis (PCA) of Raman spectra, our study revealed the possibility of this method to diversify BM-MSCs populations, whereby the grouping of cell populations was most prominent when cell populations were analyzed in pairs. These results indicate that Raman spectroscopy, as a label-free assay, could have a huge potential in understanding stem cell heterogeneity and sorting cell populations with a similar biochemical background that can be significant for the development of personalized therapy approaches.

Keywords: human bone marrow mesenchymal stem/stromal cells (BM-MSCs); Raman spectroscopy; single cell; inter-individual heterogeneity

check for updates

Citation: Kukolj, T.; Lazarević, J.; Borojević, A.; Ralević, U.; Vujić, D.; Jauković, A.; Lazarević, N.; Bugarski, D. A Single-Cell Raman Spectroscopy Analysis of Bone Marrow Mesenchymal Stem/Stromal Cells to Identify Inter-Individual Diversity. *Int. J. Mol. Sci.* **2022**, *23*, 4915. https://doi.org/10.3390/ijms23094915

Academic Editor: Sébastien Bonhommeau

Received: 30 March 2022
Accepted: 25 April 2022
Published: 28 April 2022

1. Introduction

In the field of regenerative medicine, mesenchymal stem/stromal cells (MSCs) are reported to be the most frequently investigated stem cells (SCs) in clinical trials [1]. This type of SCs is capable of self-renewing and differentiating toward mature cells [2–4], whereby their potential therapeutic application is also based on their abilities to produce a wide variety of bioactive factors that support tissue remodeling and exhibit immunoregulatory features as well [5–7]. MSCs are a particularly convenient type of SCs for therapeutic use, since they can be isolated from almost all adult and postnatal tissues obtained after regular medical procedures. Along with minimal invasiveness and accessibility, MSCs are easy to expand, thus providing sufficient yield for use in potential therapy treatments [4,8,9]. However, the main challenge for their wide therapeutic usage is the heterogeneity of biological properties between different MSCs populations [10], as there is no specific cellular marker to identify MSCs [11–13]. Following isolation, MSCs identification is based on minimal requirements evinced under in vitro conditions. These criteria include the fibroblast-like shape of cells adherent to the plastic surface, a phenotype that considers the expression of mesenchymal markers (CD44, CD73, CD90, CD105, etc.), with the lack of hematopoietic markers (CD34, CD45, CD14, etc.) and differentiation potential toward at least three lineages (osteogenic, chondrogenic or adipogenic) [14,15]. However, despite the morphological, phenotypical and functional similarities between MSCs populations, specific intrinsic properties related to the MSCs tissue source have been documented [16–19]. Moreover, other factors such as culture conditions, donor specificity or age can also have a significant influence on the variability of results related to the MSCs population description [10,20]. All these factors significantly disable the standardization of conditions necessary to establish therapeutic procedures. Therefore, in the field of MSCs research and MSCs-based therapy, the key issue today is still the precise characterization of MSCs that evidently requires the use of more sensitive tests.

In order to fully describe a certain population of cells, the most advanced technologies with the competence to provide data on each analyzed cell (i.e., single cell analysis) are needed. However, most of the cell and molecular biology techniques are very demanding in terms of sample preparation and duration of the process, with cell destruction or perturbation as a common consequence [21–23]. In basic research, there is a strong benefit to utilizing technologies that would allow simple, fast, reproducible, non-destructive and information-rich characterization of each cell within the MSCs population.

Raman spectroscopy of a single cell provides a one-of-a-kind vibrational spectrum in which macromolecules of large light scattering cross-section (e.g., proteins, nucleic acids, carbohydrates and lipids) and their interactions are present as characteristic vibrational modes, as a unique imprint of the analyzed sample. Having in mind the advantages of Raman spectroscopy, it is indicative that it can be a method of choice for the analysis of MSCs properties at a single-cell level. It should also be highlighted that a large number of data on the biochemical composition at the level of a single cell in a short time interval can be analyzed [24,25], thus providing a prompt and unambiguous interpretation of cell populations compositions which is not possible by applying currently available bioassays.

Although Raman spectroscopy has been applied in stem cell analysis [26–31], the subject of these research studies was mostly related to the examination of SCs differentiation processes [29,32–39]. In this study, we showed the potential of Raman spectroscopy to assess the heterogeneity of undifferentiated MSCs through the diversification of bone marrow MSCs (BM-MSCs) populations from different individuals. BM-MSCs from five healthy pediatric donors were isolated and characterized according to the minimal criteria for their characterization set by the International Society for Stem Cells (ISCT). Standard biological tests did not reveal donor-dependent variations of MSC features (adherence, phenotype, clonogenicity, and multilineage differentiation potential). In addition, no differences were detected in terms of their proliferative capacity and expression of pluripotency-associated markers. Raman spectroscopy analysis of BM-MSCs at the single-cell level revealed a similar biochemical background of the tested samples. However, after extensive principal component analysis (PCA), a clustering of MSCs populations was observed, particularly when the samples were analyzed in pairs.

2. Results

2.1. Comparison of Bone Marrow Mesenchymal Stem/Stromal Cell Features Isolated from Five Pediatric Donors

Following the isolation and in vitro expansion of BM-MSCs of each donor, we were guided by the minimal criteria for MSCs identification set by the International Society for Cellular Therapies (ISCT) [14] to confirm the BM-MSC identity of isolated cells. For that purpose, we analyzed the morphology of adherent cells, their immunophenotype and differentiation potential comparing in parallel these features between different donors. At the fifth passage, as well as during long-term cultivation, isolated adherent BM-MSCs derived from all five donors retained a fibroblast-like morphology with a similar cytoskeleton organization of F-actin (Figure 1A). Further on, flow cytometry analysis showed that BM-MSCs exhibited typical immunophenotype since the surface antigens related to the MSCs were highly expressed, while the rate of hematopoietic stem cell markers expression was low as determined by flow cytometry (Figure 1B). Namely, the expression of MSCs-positive markers between donors ranged from 97.89% to 99% for CD29, from 84.6% to 98.05% for CD73, from 78.5% to 97.78% for CD90, and from 96.1% to 98.13% for CD105. A slightly lower expression of CD73 and CD90 markers was observed for BM-MSCs of D5, indicating the inter-individual heterogeneity of BM-MSCs populations. On the other side, less than 2.3% of BM-MSCs expressed CD45, while in less than 1.73% of cells, HLA-DR expression was detectable. Based on these results, no significant difference in immunophenotype at the fifth passage between the BM-MSCs of pediatric donors was detected.

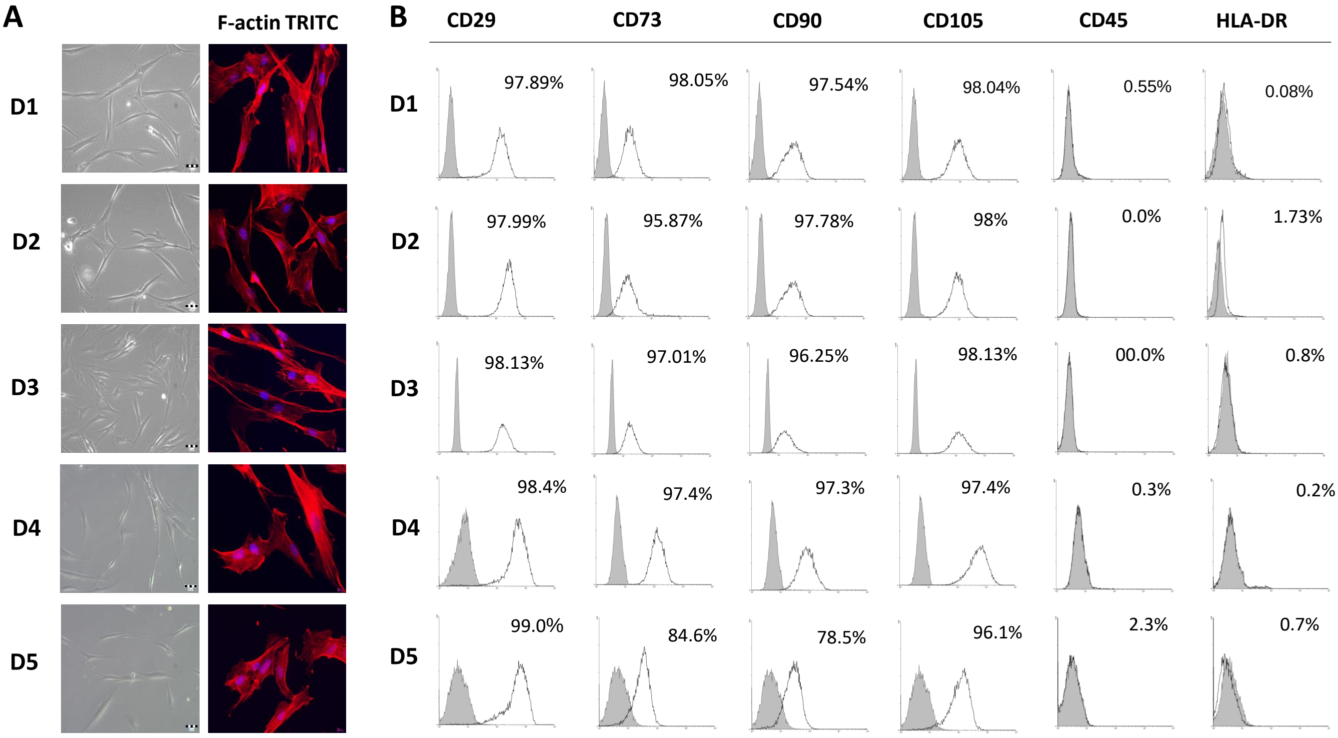

Figure 1. Morphology and immunophenotype of BM-MSCs derived from pediatric donors. (**A**) Adherent BM-MSCs from five donors (D1–D5) with fibroblast-like shape grown in GM under standard conditions for 3 days (scale bars: 50 µM); Florescent images of TRITC-conjugated phalloidin labeled F-actin (red) merged with DAPI (4′,6-diamidino-2-phenylindole) nuclear staining (blue) (scale bars: 20 µM). (**B**) Immunophenotypic characteristics of BM-MSCs estimated by follow cytometry. Representative histograms for each donor presenting percentages of cells positive (empty peaks) for mesenchymal markers (CD29, CD73, CD90, CD105) and hematopoietic markers (CD45, HLA-DR) in comparison to isotype control (shaded peaks).

Regarding the functional analysis related to the potential of MSCs to differentiate toward more mature cells, we examined the ability of isolated BM-MSCs to differentiate toward osteogenic, chondrogenic and adipogenic lineages, to further define the identity features of MSCs. As shown in Figure 2, the obtained results demonstrate that the BM-MSCs of each donor possess tri-lineage differentiation capacity, while no spontaneous differentiation was observed. Namely, the activity of the ALP enzyme was significantly increased in BM-MSC cultivated in the osteogenic medium in comparison to the control cells. In accordance with early osteogenesis increase, BM-MSCs achieved complete osteoblast differentiation through matrix mineralization production, as determined by Alizarin red staining. Thus, the osteogenic differentiation of BM-MSCs of all five donors was confirmed, with no significant differences observed among donors. Similarly, BM-MSCs of each donor were able to differentiate into chondrocytes under chondrogenic inductive conditions, since the significant increase in cartilage-related proteoglycans was observed by Safranin O staining in comparison to the control cells. Along with osteogenesis and chondrogenesis, the BM-MSCs of each donor showed a similar ability to differentiate into adipocytes after cultivation in an adipogenic medium. In these cells, the significant formation of intracellular lipid droplets was evidenced via Oil Red O staining, which was not observed in the control group.

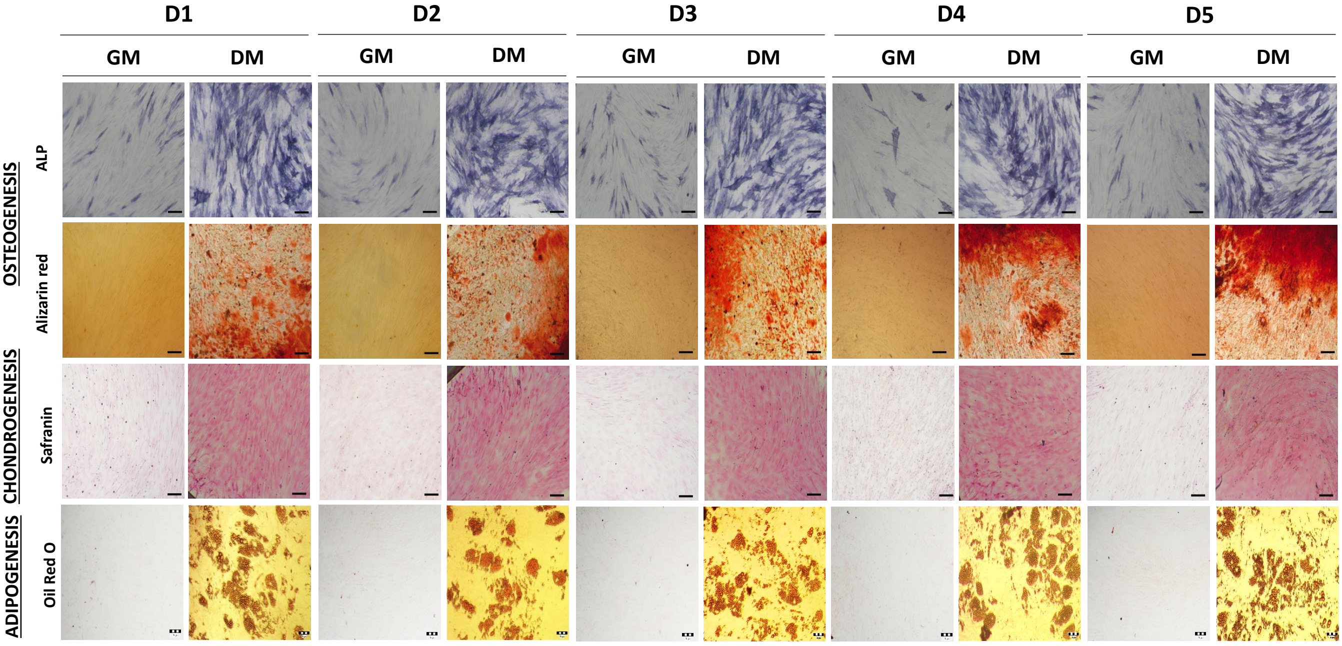

Figure 2. Multilineage differentiation potential of BM-MSCs. Representative images of cells cultivated in GM or differentiation medium (DM) are shown. Osteogenic differentiation detected after 7 days of cultivation by staining for alkaline phosphatase (ALP) activity, and after 21 days for calcium depositions by Alizarin red staining (Scale bar: 50 µM). Chondrogenic differentiation detected with Safranin O staining of proteoglycans after 21 days cultivation (scale bar: 50 µM). Adipogenic differentiation determined based on the presence of intracellular lipid droplets by Oil Red O staining after 21 days (scale bar: 20 µM).

Overall, these data confirm that the BM-MSCs of each pediatric donor exhibit characteristics related to mesenchymal stem cells, while no significant differences between donors were detected.

2.2. *Self-Renewal of BM-MSCs and Expression of Markers Associated with Pluripotency*

Further on, we evaluated the self-renewal potential of BM-MSCs by using Colony Forming Unit–Fibroblast (CFU-F) assay. Results shown in Figure 3A demonstrate that the BM-MSCs of each donor have comparable clonogenic potential, since the average efficiency for each donor was approximately 3%. It can also be noticed that the morphology of CFU-F was heterogenic but similar amongst donors.

Along with clonogenic capacity, we examined the expression of markers associated with pluripotency via immunofluorescent labeling. The results presented in Figure 3B revealed the constitutive expression of pluripotency-related markers including OCT4A, SOX2 and NANOG in the BM-MSCs of each donor observed both in cytoplasmic and in the nuclear region. However, slight differences between donors were noticed. As for OCT4A, a more dominant expression was detected in the nuclear/perinuclear region of cells derived from donors D3, D4, and D5, while weaker cytoplasmatic expression was observed for the BM-MSCs of donors D1 and D2. The expression of SOX2 was highest in the nuclear/perinuclear region of D3 and D5, whereas D1, D2, and D4 exhibited a lower expression of this transcription factor, which was localized mainly in the perinuclear and cytoplasmic compartment. Considering NANOG expression, some differences in protein localization were detected among donors, since nuclear localization was determined in D4 and perinuclear/cytoplasmic in donors D1, D2, D3, and D5.

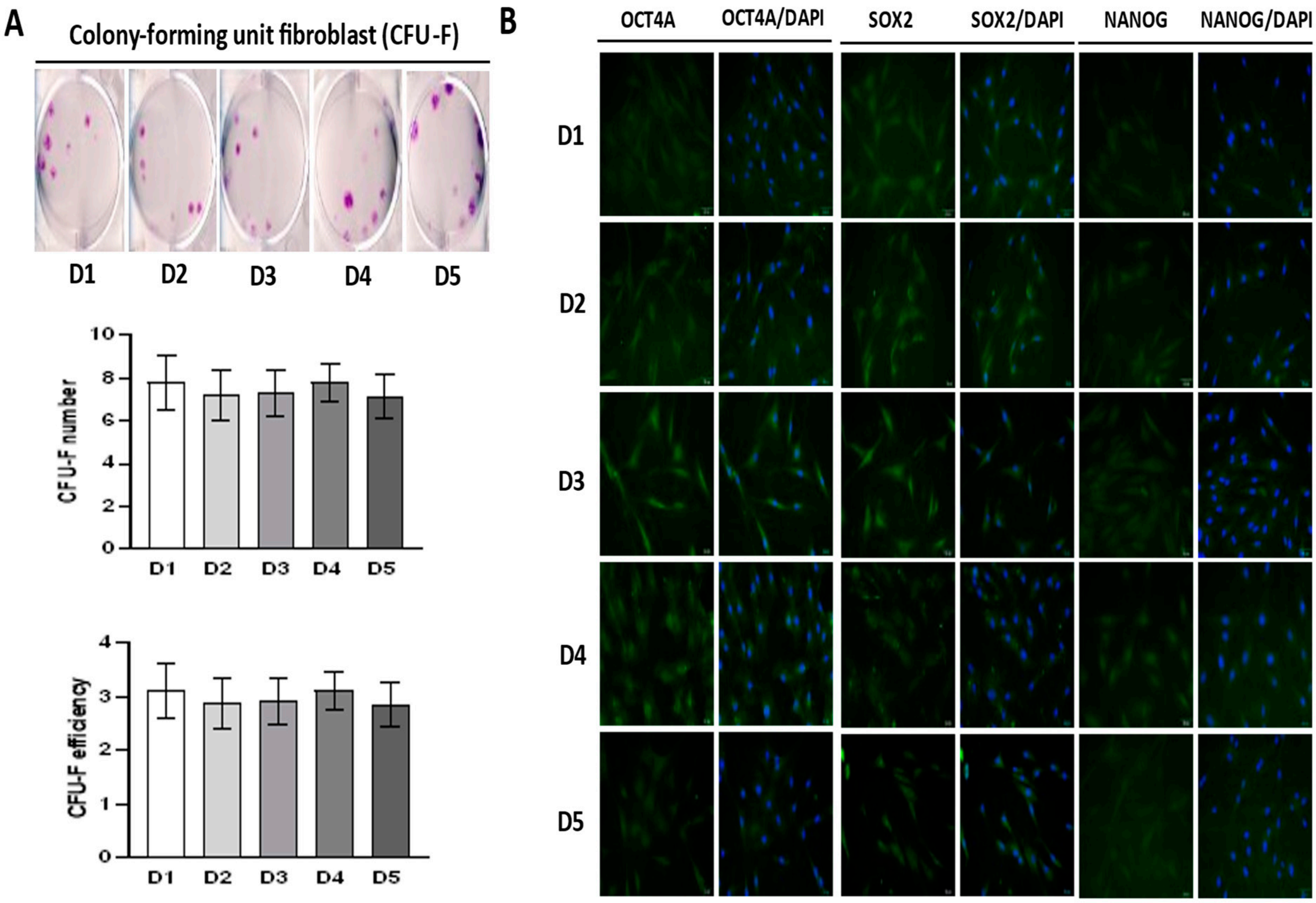

Figure 3. Clonogenic capacity and expression of pluripotency-associated markers in BM-MSCs. (**A**). Representative images of colony-forming unit–fibroblast (CFU-F) stained by crystal violet are shown. CFU-F number and efficiency (number of colonies relative to number of seeded cells) of BM-MSCs are presented as mean ± SEM of three independent experiments. (**B**) Expression of pluripotency-associated transcription factors (OCT4, SOX-2 and NANOG) determined by indirect immunofluorescence labeling with FITC-conjugated corresponding secondary antibodies. Cell nuclei were stained with DAPI (4′,6-diamidino-2-phenylindole). Representative images are shown (scale bars: 50 µm).

2.3. Growth Characteristics of BM-MSCs

A comparison of BM-MSC viability performed by MTT test revealed equivalent metabolic activity between donors following 24 h (Figure 4A). With a slight increase, this trend was retained after 48 h as well (Figure 4A). In accordance with this result, analysis of the population doubling time (PDT) demonstrated that the BM-MSCs of each donor possess a uniform growth rate (Figure 4B). The active proliferative abilities of all donors were further confirmed by investigation of cellular senescence via the determination of β-galactosidase expression that showed a very low number of β-gal-positive cells among all donors (Figure 4C), which is in agreement with MTT and PDT data. These results were also supported on a molecular level by the evidence of strong constitutive expression of the intracellular proliferation marker Ki67 (Figure 4D).

Interestingly, the highest expression of Ki67 was detected for D5, whereby cellular localization varied between donors. BM-MSCs of D1, D2, and D3 expressed Ki67 in the cytoplasm and nucleus, while the Ki67 expression of D4 and D5 was predominantly cytoplasmatic (Figure 4D). Analysis of p53 protein, as a regulator of cell proliferation and senescence, revealed similar basal expression in BM-MSCs with differences in its localization. p53 was detected in the cytoplasm and nucleus in D1, D2 and D3 BM-MSCs, while in donors D4 and D5, p53 was detected only within the nucleus contrary to the Ki67 localization pattern (Figure 4D).

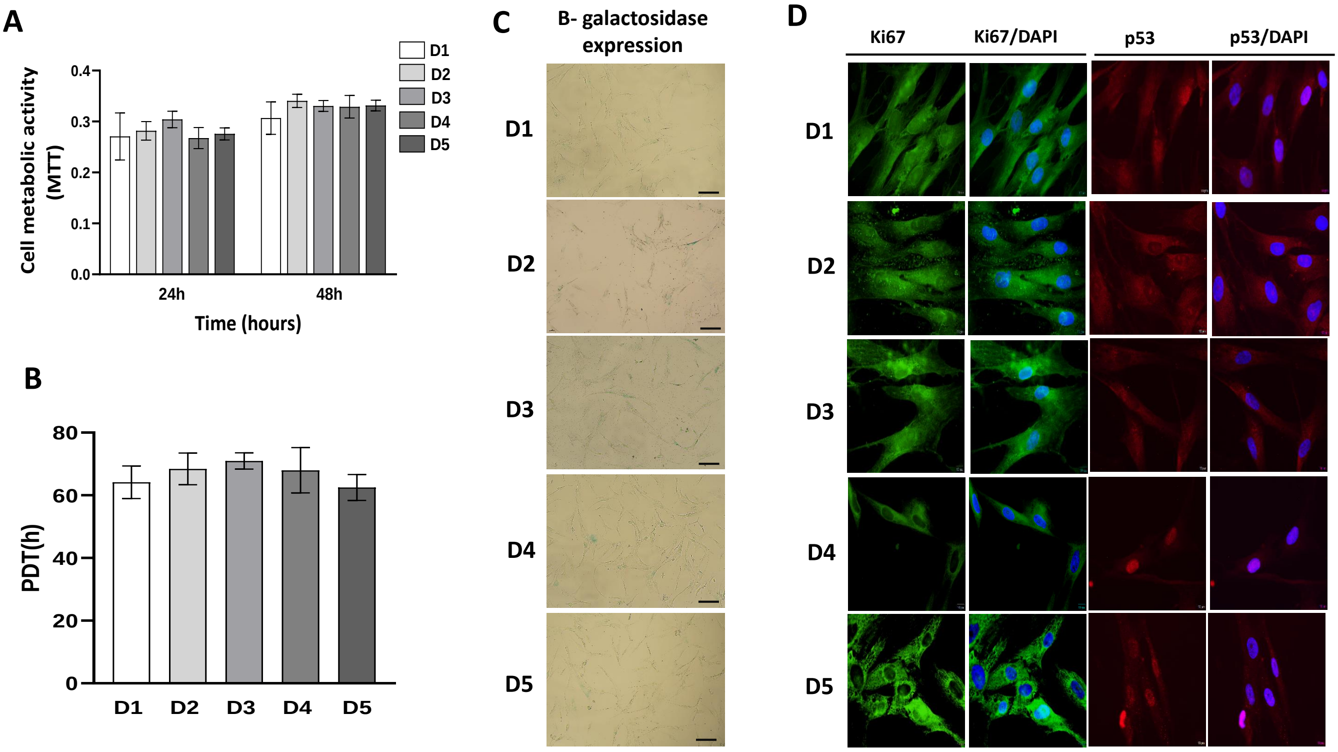

Figure 4. Growth characteristics of BM-MSCs. (**A**) Metabolic activity of cells isolated from 5 donors during 24 h and 48 h estimated by MTT test. (**B**) Population doubling time (PDT) of BM-MSCs. Cells were cultivated in standard conditions, passaged at 90% confluency, and enumerated at each passage (up to 6th passage). For PDTs calculation, the formula described in Material and Methods was applied. Results on the graph are presented as ± SEM of independent experiments. (**C**) Representative images of BM-MSCs stained for β-galactosidase expression after one day of cultivation under standard conditions (scale bar: 50 μM). (**D**) Expression of proliferation-associated marker Ki67 and p53 detected by indirect immunofluorescence labeling with corresponding FITC-conjugated or AlexaFlour555-conjugated secondary antibodies. Cell nuclei were stained with DAPI (4′,6-diamidino-2-phenylindole). Representative images are shown (scale bars: 10 μm).

2.4. Raman Spectra Analyses

The Raman spectra of human cells, depending on their origin, nature or physiological state, have numerous mutual features whose Raman shifts are used as spectral markers. Cells under observation, as primary MSCs cultures, naturally, present a heterogeneous entity highly susceptible to modifications of the intrinsic chemical structure, and consequently, spectral features, by standard culture conditions, among others. As the analyzed cells were fixed to provide a less variable system, it was ensured that physiological processes within the cells were interrupted at the same (desired) stage. In addition, to keep the system out of the additional extrinsic influence, the investigated cells were of the same 5th passage.

The main contribution to BM-MSCs Raman spectra comes from nucleic acids (singled out purine and/or pyrimidine bases and DNA/RNA backbone structure), proteins (individual amino acids, amide groups of proteins' secondary structure and various vibrations within C-C or C-N bonding), and lipids (vibrations within the hydrocarbon chain), as shown in Table 1 [27,36,40–44].

Table 1. Vibrations in BM-MSCs and their energies noticed in obtained Raman spectra. Adapted from [27,36,40–44].

Energy (cm^{-1})	Biomolecule Assignment
940	Skeletal modes in polysaccharides
957	O-P-O symmetric stretch in adenosine-monophosphate
1003	Symmetric ring breathing mode in phenylalanine (Phe)
1010	Ring breathing in benzene ring of tryptophan (Trp)
1033	C-H in plane bend (Phe)
1050	C-O and C-N stretch in proteins
1080	O-P-O symmetric stretch
1100	PO_2^- symmetric stretching in RNA and phosphatidylinositol
1123	Cytochrome C; C-C asymmetric stretch in fatty acids
1155	C-C and C-N stretch in proteins
1165	C-O stretch, C-OH bending, C=C stretch in lipids, C-C stretch in proteins
1173	G-ring stretch, C-C-H bending in phenol ring (DNA)
1206	C-C stretch in phenol ring of tyrosine (Tyr)
1245	NH_2 bending in Amide III_β
1266	Amide III_α
1310	C-H deformation (saturated. lipids)
1335	DNA purine bases (CH_3CH_2 wagging mode of polynucleotide chain)
1450	CH_2 scissoring in lipids
1554	Amide II
1604	Phe, Tyr
1655	Amide I_α
1669	Amide I_β

The averaged Raman spectra of BM-MSCs for each donor are presented in Figure 5A, while PCA score plots (PC1–PC2 and PC1–PC3) are shown in Figure 5B, confirming the similar biochemical background of analyzed samples. Regarding the significant similarity of all Raman spectra (Figure 5), to obtain a comprehensive insight into the biomolecular content of cells originating from different donors, the averaged Raman spectra, as well as statistical analysis, are analyzed and presented in pairs (Figures 6 and 7).

Figure 6A shows the Raman spectra of cell populations from D1 (red) and D2 (blue) and their ratio. By direct spectral reading, which on some occasions may be a formidable task due to various overlapping contributions, a phenylalanine mode at 1003 cm^{-1} is of significantly higher intensity in the D1 spectrum. However, the mode assigned to RNA at 1100 cm^{-1} is of higher intensity in the D2 spectrum and broader, implying higher content of nucleic acids or their enhanced activity. A biochemical discrepancy between D1 and D2 is confirmed statistically when the PCA score plot is considered, which is the one that represents PC1–PC3. The distinct grouping of red and blue dots per mutual spectral features is observed, indicating that the cells from one population have different biomolecular imprint than cells from another.

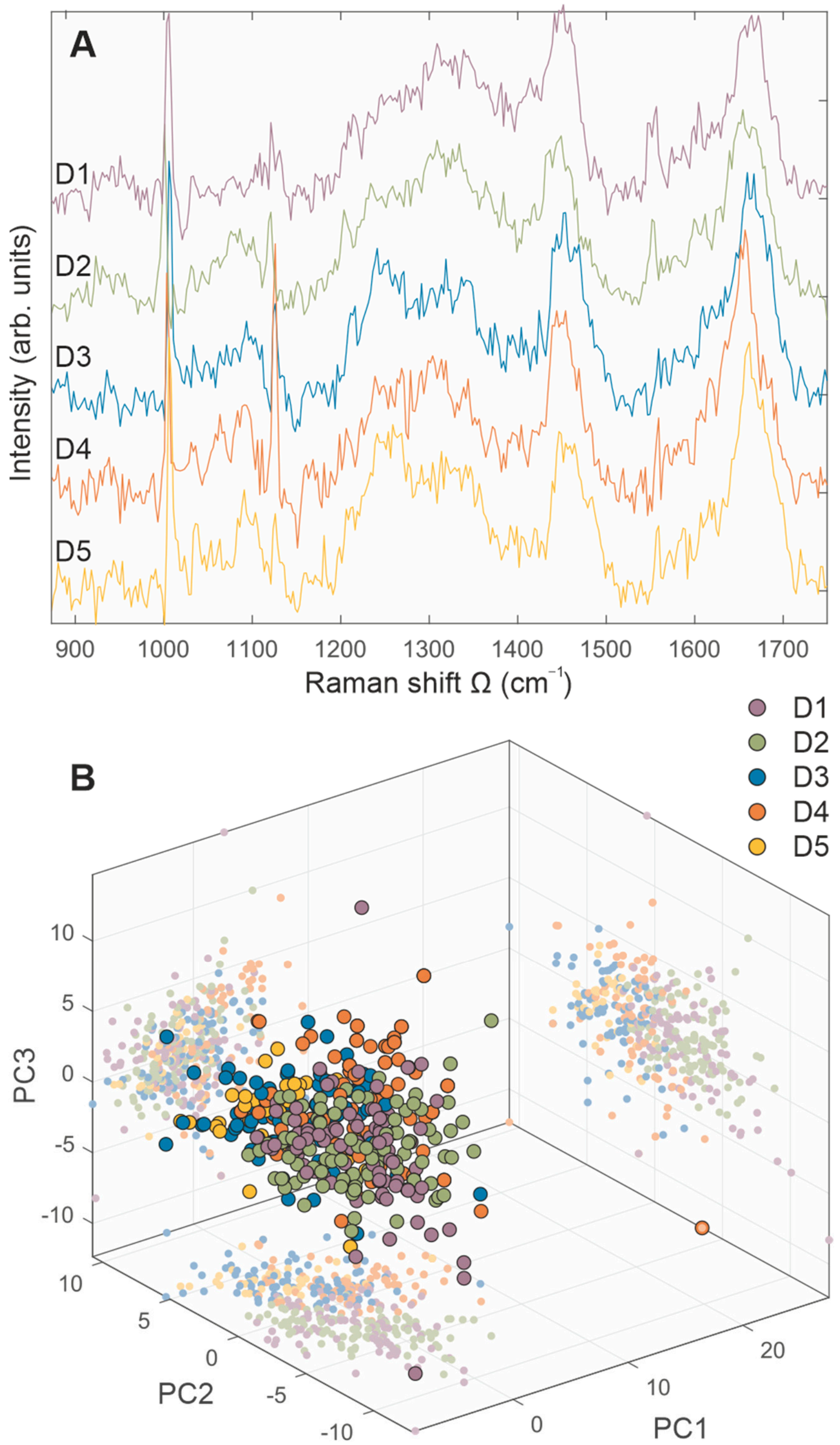

Figure 5. Comparative representation of BM-MSCs Raman spectra, derived from five donors. BM-MSCs were seeded on rounded CaF2 slides (Raman grade quality) and cultivated under standard conditions during 24 h. Before Raman scattering experiments, cells were washed with saline buffer and fixed with methanol for 10 min at the room temperature. On average, 50 to 100 cells per each cell population were analyzed. (**A**) Averaged Raman spectra of BM-MSCs for each donor are presented with purple (D1), green (D2), blue (D3), orange (D4), and yellow (D5) lines. (**B**) 3D PCA score plots (PC1–PC2 and PC1–PC3) are presented with purple (D1), green (D2), blue (D3), orange (D4), and yellow (D5) dots.

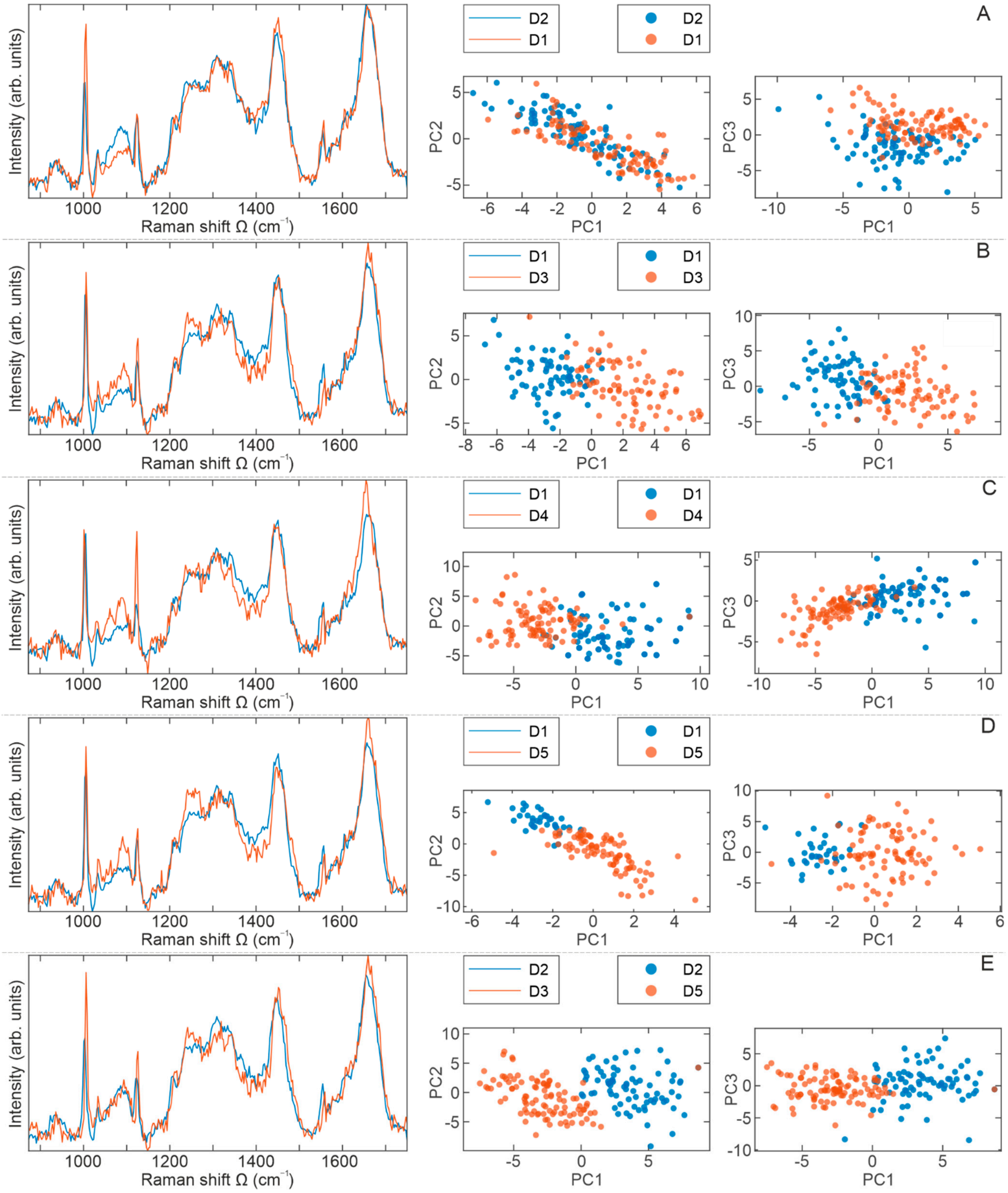

Figure 6. Comparative representation of BM-MSCs Raman spectra presented in pairs. BM-MSCs were seeded on rounded CaF2 slides (Raman grade quality) and cultivated under standard conditions during 24 h. Before Raman scattering experiments, cells were washed with saline buffer and fixed with methanol for 10 min at the room temperature. On average, 50 to 100 cells per each cell population were analyzed. A comparative display of the averaged Raman spectra (red and blue lines) per cell populations: (**A**) D1–D2, (**B**) D1–D3, (**C**) D1–D4, (**D**) D1–D5, and (**E**) D2–D3. Principal component analysis (PCA) score plots are represented with red and blue dots.

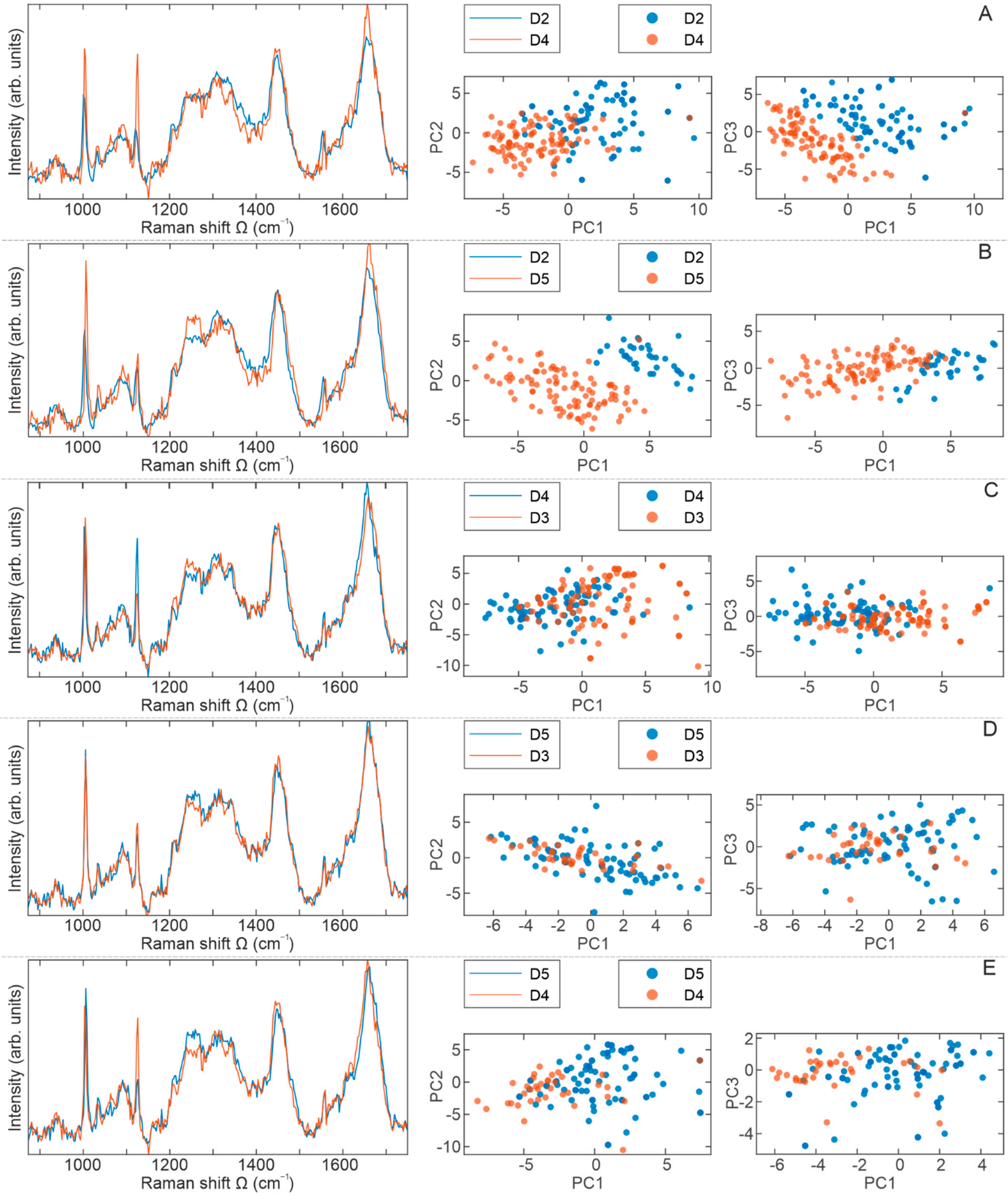

Figure 7. Comparative representation of BM-MSCs Raman spectra presented in pairs. BM-MSCs were seeded on rounded CaF2 slides (Raman grade quality) and cultivated under standard conditions for 24 h. Prior Raman scattering experiments cells were washed with saline buffer and fixed with methanol for 10 min at the room temperature. On average, 50 to 100 cells per each cell population were analyzed. A comparative display of the averaged Raman spectra (red and blue lines) per cell populations: (**A**) D2–D4, (**B**) D2–D5, (**C**) D3–D4, (**D**) D3–D5, and (**E**) D4–D5. PCA score plots are represented with red and blue dots.

The averaged Raman spectra of cell populations D1 (blue) and D3 (red) are presented in Figure 6B. Clearly noticeable are modes of higher intensities in the D3 spectrum: at 1100 cm^{-1} (assigned to RNA), 1124 cm^{-1} (cytochrome c), and at about 1250 cm^{-1} (protein content in the Amide III_β form). Statistically, both PCA score plots (PC1–PC2 and PC1–PC3) show distinct clustering of Raman spectra of BM-MSCs from donors D1 and D3 based on their intrinsic biomolecular contents, confirming the D1–D3 biochemical variability.

A comparison of an averaged Raman spectra of cells from D1 and D4 is shown in Figure 6C. Evidently, a higher intensity of Raman modes at about 1050 cm^{-1}, 1080 cm^{-1}, 1100 cm^{-1}, 1127 cm^{-1} and 1660 cm^{-1} is observed in D4 Raman spectrum. Biomolecular interpretation of this assignment indicates a higher content of proteins, DNA, and RNA respectively, as well as cytochrome c and proteins in their secondary structure. Furthermore, somewhat more dominant is a Raman mode at 1604 cm^{-1}, which is assigned to amino acids Phe and Tyr. Both PCA score plots designate clear and unequivocal grouping of Raman spectra per mutual spectral features, i.e., a biomolecular fingerprint.

Figure 6D presents BM-MSCs' averaged Raman spectra of cell populations D1 and D5, where the D5 (red) spectrum shows few Raman modes of higher intensity: at 1080 cm^{-1}, 1250 cm^{-1}, and 1660 cm^{-1} indicating more nucleic acids and proteins in Amide III form. To some extent, the lipid mode at about 1450 cm^{-1} is broader and of higher intensity in the D1 (blue) spectrum, pointing to the higher lipid content in these cells. Clearly, the PCA score plots show disjunction between these two cell populations, indicating the biochemical discrepancy between D1 and D5.

From the spectra in Figure 6E, it is obvious that the D3 (red) spectrum shows a higher content of amino acids (proteins), cytochrome c, and proteins in Amide III and Amide I form (see Table 1). The Raman peak at about 1310 cm^{-1} shows a greater content of saturated lipids in the D2 (blue) spectrum. Based on the PCA score plots shown in Figure 6, the maximum separation is noticed for D2–D3 cell populations (Figure 6E), while the minimal clustering was observed for D1–D2 cell populations (Figure 6A).

When analyzing the averaged Raman spectra displayed in Figure 7, the results are mostly in a good accordance with those presented in Figure 6, meaning that all changes come from differences in intensities, with no new modes detected in the spectra.

Figure 7A shows the averaged Raman spectra of cell populations D2 (blue) and D4 (red). Of significantly higher intensities are modes at 1003 cm^{-1} (Phe) and 1127 cm^{-1} (cytochrome c), and slightly more intensive is a peak at 1660 cm^{-1} (secondary structure of proteins) in the D4 spectrum. Some discrepancies come from a region around 1335 cm^{-1}, which was assigned to the polynucleotide chain in the D2 spectrum. Although both score plots show distinct grouping, it is more prominent from the score plot PC1–PC3. Nevertheless, the biochemical discrepancy between D2 and D4 cell populations is clearly observed.

A comparison of the averaged Raman spectra of cells from the D2 (blue) and D5 (red) population is presented in Figure 7B. According to the assignation presented in Table 1, cells from the D5 population have higher protein content in both Amide III and Amide I form, as well as free amino acids. A striking clustering of Raman spectra per cell population is obvious from both PCA score plots, confirming the biochemical distinction between D2 and D5.

From Figure 7C, where the averaged spectra of BM-MSCs from D3 and D4 cell populations are displayed, the dominant impression is a higher content of cytochrome c (Raman mode at 1127 cm^{-1}) in the D4 spectrum. Statistically, these two groups show the minimum degree of separation, which is also demonstrated for the spectra of D3 and D5 cell populations presented in Figure 7D.

Finally, Figure 7E shows the last compared pair, the Raman spectra of BM-MSCs from cell populations D4 and D5, giving the conclusion of higher content of cytochrome c in the D4 population, while Amide III_β content is higher in the D5 population. The separation read from PCA score plots is slightly better than in the previous two groups and more clearly indicates the biochemical discrepancy between D4 and D5.

3. Discussion

The goal of this study was to analyze and compare the main functional features of BM-MSCs derived from five pediatric donors. We evaluated their basal stemness-related properties including morphology, phenotype, multilineage differentiation potential, colony-forming capacity, expression of pluripotency-associated markers and proliferation capacity. In parallel with the use of standard biological methods, single BM-MSCs were examined by Raman spectroscopy in order to identify donor-specific differences at the biochemical level with the aim to test whether this method could be used as an additional technique to characterize MSCs at the single-cell level.

Raman spectroscopy has been utilized to study various physiological and pathological conditions with the purpose of disease diagnosis, surgical guidance, and therapeutic or metabolic monitoring [45,46]. In the field of regenerative medicine and stem cell research, the application of Raman spectroscopy is rapidly increasing [24], whereby it can be noticed that stem cell differentiation at a single cell and tissue level was mostly investigated [37,38]. Regarding the use of Raman spectroscopy for distinguishing cell populations, several studies addressed this issue from different viewpoints. The results of [47] showed that this technique can precisely identify and evaluate prostatic adenocarcinoma (CaP) in vitro, based on different degrees of biological aggressiveness between CaP cell lines. Likewise, the distinction and identification of cells from different tissues and species (MDCK, CHO, and NIH 3T3 cells) as well as cells from a single species (NIH 3T3 and Clone 15 cells) were shown in the study of [48], indicating that the slight changes in cell phenotype can be determined based on Raman spectra and used to identify cell type. In addition, confocal Raman micro-spectroscopy was successfully used to delineate immortalized human cell lines derived from lung cancer (A549) and fibroblasts (MRC5) as well as three primary human bronchial epithelial cell (HBEC) lines [49]. Moreover, by using the Fourier Transform Infrared (FTIR) technique together with Raman spectroscopy, a clear distinction between undifferentiated BM-MSCs, their myogenic and osteogenic progeny, and de-differentiated smooth muscle cells were observed based on spectral differences [29] as well as between human ESCs and human MSCs [50]. Raman spectroscopy was shown to be a suitable tool for distinguishing human BM-MSCs and fibroblasts, thus enabling the rapid detection of fibroblastic contaminations in BM-MSC cultures [51]. Recent data also show that MSCs originating from different dental tissues such as apical papilla (SCAP), the dental follicle (DFSC), and pulp (DPSC) can be grouped based on Raman spectra that reveals a subtle distinction between these cells [52]. However, to our best knowledge, no data were published related to the inter-donor variability of MSCs. So, this is the first study that attempted to employ Raman spectroscopy to compare the spectral pattern of undifferentiated BM-MSCs deriving from healthy pediatric donors and to use these data for distinguishing cell populations.

In line with that goal, our first step was to isolate and characterize BM-MSCs by using standard biological tests following the minimal criteria for MSCs identification set by ISCT that include morphologic properties, immunophenotype and multilineage differentiation potential [14]. Our results revealed that plastic-adherent cells derived from the bone marrow of five pediatric donors retain adherence and typical fibroblast-like morphology cells during prolonged cultivation in standard conditions, while no donor-to-donor differences in cells sizes or shape were noticed, as observed under phase contrast microscope. Thus, these findings are in accordance with the first criteria as well as with previous studies related to the BM-MSCs morphology of adults [53–57]. The elongated spindle shape morphology of isolated BM-MSCs of each donor was further confirmed by cytoskeleton visualization. Immunofluorescent staining of the filamentous form of actin (F-actin), a critical structure of the cytoskeleton, revealed a strong expression of branched, multiple-directed F-actin stress bundles distributed through the whole cell, as it has been shown for MSCs derived from human placenta grown in standard adherent conditions [58]. Next, by using flow cytometry, we detected a high expression of surface molecules related to MSCs origin including CD29, CD73, CD90, and CD105, along with the low expression of leukocyte markers CD45 and HLA-DR amongst all donors. A high expression of CD73, CD90 and CD105 markers was previously reported for BM-MSCs derived from adults [53–57,59], along with a high expression of CD29 observed in [56,59]. In parallel, the low percentage of CD45 and HLA-DR positive cells demonstrated in our study is in line with the results of [54,55,59], confirming that the immunophenotype of BM-MSCs of pediatric donors and adults is similar [60] and comparable with MSCs deriving from other tissue sources [59,61,62]. As the third ISCT requirement for MSCs identification, we examined the multilineage differentiation capacity of isolated cells. Indeed, the BM-MSCs of each pediatric donor were able to differentiate toward osteogenic, chondrogenic and adipogenic lineage, which is in agreement with previous research related to the BM-MSCs of adults [53–56,63], while no spontaneous differentiation in standard media was noticed, as reported in [60,64,65]. Overall, our results confirmed that adherent cells isolated from the bone marrow of all five pediatric donors meet the ISCT criteria for MSCs identification, whereby no significant differences were determined in this study.

Further on, we examined the clonogenic potential of BM-MSCs of each donor as a part of the self-renewal capacity analysis. Our results showed that isolated cells form a typical but heterogenic morphology of CFU-F colonies, while their number was uniform among donors (around 3%). Although clonogenic efficiency may vary depending on the cultivation conditions [55,66] and particularly passage [67,68], our results are comparable with the published data. Namely, approximately 5% of BM-MSCs colonies were formed at the fourth passage in the study of [67], 8% in [68]. Likewise, [69] reported that at the P3-6, around 5% colonies were formed, as well as in [55] for the BM-MSCs of P6 cultivated in the serum-containing in-house medium, which all points to the clonogenic potential of BM-MSCs derived from pediatric donors being similar to the BM-MSCs of adults.

As stem cells, MSCs are characterized by self-renewal ability, which encompasses the division ability with stemness maintaining [3,70]. At the molecular level, the regulation of stemness is mostly mediated via pluripotency-associated transcription factors, such as OCT4, SOX2 and NANOG, as described for embryonic stem cells [71]. Thus, it is assumed that these factors play a similar role also in adult stem cells. However, the molecular basis of MSCs stemness is still poorly understood. Nevertheless, previous studies have shown that MSCs derived from adult tissues do express pluripotency-associated markers [72–77] and that stemness-related processes may be associated with the activity of these markers in MSCs [78–83]. Our results are in line with these data and demonstrate that BM-MSCs derived from pediatric donors constitutively express markers associated with pluripotency (OCT4, NANOG and SOX2), while interestingly, we observed slight differences in the expression of these markers that may potentially indicate the existence of donor-dependent variation of self-renewal.

In the next part of describing BM-MSCs populations, we compared their proliferative capacity. Our study revealed a similar metabolic activity of BM-MSCs derived from different donors that increased during the time, as determined by the MTT test. Equal viability was accompanied by a uniform proliferation rate. Namely, all investigated cell types maintained their growth rate during prolonged in vitro culture, whereby the time needed for population doubling ranged between 60 and 70 h among donors during passaging (up to the 6th passage). Thus, these data agree with PDT observed in studies [55,56,84]. Active proliferative capacity was also supported based on β-galactosidase activity, as the low number of senescent cells has been observed in the fifth passage of BM-MSCs of each donor, which is also in accordance with previously published data [85]. These results are additionally confirmed at a molecular level. At first, we showed the basal expression of proliferation marker Ki67, by using immunofluorescence that also revealed slight differences in Ki67 localization between donors. Namely, donors D1, D2 and D3 expressed Ki67 in the nucleus and cytoplasm, while D4 and D5 showed a more dominant cytoplasmatic localization of this marker. Our previous study showed that under basal conditions, Ki67 expression in dental stem cells is predominantly in cell cytoplasm [78], while both cytoplasmic and nuclear Ki67 localization was detected in ASCs [86]. Although

Ki67 has been traditionally considered a cell proliferation marker due to its presence in the nucleus during all active phases of the cell cycle (G1, S, G2 and M), the role of Ki67 has been particularly well described for cancer cells [84,87]. However, recent findings indicate that Ki-67 should not be considered only as a marker of cell proliferation [88,89]. Since differences in the extranuclear pathway of Ki-67 regulation in non-cancer and cancer cells have been identified [90], additional studies will potentially provide answers related to the biological role of nuclear and cytoplasmic Ki67 in adult stem cells.

Along with Ki67 expression, we investigated the expression of p53, which has been widely implicated in cellular senescence and aging [91,92], MSCs differentiation, bone homeostasis [93] as well as other MSCs functions [94]. Our results confirmed the basal expression of p53 in BM-MSCs of pediatric donors and interestingly revealed cellular localization differences. Namely, p53 was localized in the nucleus of donors D4 and D5, while donors D1, D2 and D3 expressed p53 predominantly in the cytoplasm. The regulation of p53 cellular localization is conditioned by many signaling factors that affect its nuclear transport, subnuclear localization, and cytoplasmatic sequestration [95–97]. As for stem cells, there are indications that p53 is localized predominantly in the cytoplasm in proliferating embryonic stem cells, while upon DNA damage, the nuclear accumulation of p53 is induced, leading to the transcriptional activation of genes involved in cell cycle arrest [98]. The study of [96] showed that BM-MSCs from systemic lupus erythematosus patients exhibit characteristics of senescence, whereby p53 and p21 were mainly localized in the nuclei of these cells. The higher nuclear localization of p53 was also detected in MSCs derived from the periosteum of old patients [99], indicating potential age-related p53 localization. However, there are still open questions that are related to the p53 functions in different cells and tissues within the human body or how p53 activity is modulated in humans depending on sex, age or metabolic state [100]. Although cellular localization is changeable, further studies are needed to address p53 location in MSCs and its potential correlation with Ki67 expression/localization pattern.

Altogether, these data show that no significant differences between BM-MSCs of examined donors can be observed based on ISCT criteria and the use of standard biological methods for testing clonogenic and proliferative capacity. Nevertheless, variations between BM-MSCs of different donors at the molecular and biochemical level certainly exist [10]. Therefore, we further examined the biochemical composition of these cells at the individual level by using Raman spectroscopy. As expected, our results of BM-MSCs Raman spectra revealed that the dominant contribution to BM-MSCs Raman spectra is related to the nucleic acids (singled out purine and/or pyrimidine bases and DNA/RNA backbone structure), proteins (individual amino acids, amide groups of proteins' secondary structure and various vibrations within C-C or C-N bonding), and lipids (vibrations within the hydrocarbon chain), as described previously [27,36,41,101–104]. A comparison of BM-MSCs spectra did not reveal new vibrational bands; however, changes related to existing bands' intensities are detected. Despite Raman spectra similarities, following their comprehensive direct and statistical analyses, subtle distinctions between the averaged Raman spectra of BM-MSCs of each donor were detected, providing an important indication that this method can be used to clearly distinguish cell populations with a similar biochemical background. Namely, based on PCA score plots, the disjunctions between BM-MSCs populations were observed, whereby clustering between cell populations was most conspicuous when analyzed in pairs. Interestingly, maximum separation was noticed between D2 and D3 BM-MSCs, while the minimum separations were detected between D3 and D4 as well as D3 and D5 BM-MSCs (Figures 6 and 7). Certainly, further biochemical and Raman studies of MSCs populations is needed to understand the specific reasons for the level of variations in donor-specific separations. This issue will be the subject of our future research in order to provide biological validation of Raman spectra analysis. Nevertheless, in the following text, we discuss possible explanations for the obtained differences in the Raman spectra of different BM-MSCs donors.

Regarding the nucleic acid content, our results revealed differences in RNA and DNA content between BM-MSCs, whereby a higher level of RNA was detected in D2, D3, D4 and D5 in comparison to D1, while D4 and D5 donors had a higher content of DNA when compared to D1. Although we did not detect donor-related differences in metabolic activities of BM-MSCs based on MTT, we may only speculate that variations in RNA content detected by Raman spectroscopy are captured due to differences in RNA synthesis, i.e., metabolic activity [105] that cannot be detected by the MTT test. Differences in the DNA level detected by Raman spectroscopy may reflect a different stage of the cell cycle [36,106] or proliferation rate [107]; however, we did not observe differences in BM-MSCs proliferation rate between donors based on population doubling time. Still, during the cell cycle, the DNA level varies [107], so we may assume that detected differences in DNA come from variations in the cell cycle captured at a specific moment. On the other hand, a decrease in spectral features of RNA and DNA has been documented in differentiated murine embryonic cells that can be interpreted by the fact that differentiated cells are more in the G1 phase of the cell cycle and consequently exhibit reduced proliferative capacity [36]. Along with DNA decrease during differentiation, it has been reported that RNA levels also diminish during this process [36]. Indeed, MSCs populations are heterogenic in terms of proliferation dynamics that results in a population of cells that consist of mitotically active (dividing) and mitotically inactive (non-dividing) cells encompassing quiescent cells, differentiated cells and senescent cells [108,109]. Therefore, it should not be neglected that variations in DNA/RNA content determined by Raman spectroscopy may also reflect the heterogeneity of cell population related to the differentiation stage.

Along with changes in nucleic acid content, our results also revealed variations in proteins (1003, 1030, 1250, 1660, 1669 cm^{-1}) and lipids bands (1310 and 1440 cm^{-1}) that can also be implicated in the metabolic activity of the cells [110] or may indicate the existence of spontaneous differentiation, as it has been demonstrated for human pluripotent stem cells [34,110]. As for MSCs, considerable lipid content was detected in dental MSCs (peaks at 1440 and 1650 cm^{-1}) [52]. Although it is not fully clarified, lipid content may be associated with the stemness level, as the study [50] showed by using FTIR spectroscopy that divergence between hESC and hMSCs comes from the increased presence of lipids in the cytoplasm of hESC, while their level progressively decreases during differentiation [50]. Similar findings were observed in the study of [111], showing that mouse embryonic stem cells exhibited a higher intensity of fatty acids (1260 cm^{-1} and 1650 cm^{-1}) and lower amounts of unsaturated lipids (1445 cm^{-1}) than their neural progenitors and reprogrammed counterparts. Interestingly, based on immunofluorescence staining, no differences in the expression of pluripotency markers (Nanog, Oct4 and Sox2) were detected between embryonic and reprogrammed cells; however, Raman spectroscopy revealed significant spectral differences in unsaturated lipids. Since it has been reported that the fatty acid synthesis is important for the cellular stemness regulation [112], additional studies need to be carried out to reveal a correlation between lipids bands and fatty acid synthesis and to address whether this can be a significant spectral marker associated with stemness.

Another interesting finding of our study is related to the variations of band intensities for cytochrome c (1127 cm^{-1}) between BM-MSCs populations. Cytochrome c is a small, multi-functional protein with a significant role in the electron transport, and it is a part of the pathway for ATP synthesis necessary in the energy-production process. Under physiological conditions, it is located in the inner mitochondrial membrane, but upon proapoptotic signal, it is released to the cytoplasm [113–116]. The role of cytochrome c in apoptosis is well established [117,118], and few Raman studies addressed the correlation between cytochrome c and programmed cell death. As for HeLa cells, [119] reported that changes in cytochrome c distribution can be distinguished as a release of cytochrome c from mitochondria, while mitochondrial membrane potential confirmed that the observed cytochrome c release was associated with apoptosis. Likewise, confocal Raman microscopy has been successfully used to detect the apoptosis of the MCF-7 cell line mediated by cytochrome c release from mitochondria [120]. On the other hand, a comparison of cytochrome c signals within the Raman spectra of human ESC and human iPSCs did not reveal differences between these cell lines, whereby equivalent cytochrome c levels correlated with the level of mitochondria detected by MitoTracker staining [107]. Interestingly, it has been demonstrated that after the differentiation of a mouse neuroblastoma cell-line Neuro2a (N2a) toward neurons and differentiation of the 3T3L1 cell-line into adipocytes, Raman spectroscopy detected an increased amount of cytochrome c in the cytosol in both cell lines [121], indicating that cytochrome c detection also may be dependent on differentiation status. Therefore, due to multiple cellular functions, a cautious interpretation of the cytochrome c signal in the Raman spectra of BM-MSCs is needed. Our biological analysis, along with the detection of other spectral markers (primarily proteins), indicates that these cell populations are viable, so we may assume that the detection of a cytochrome c signal in Raman spectra can be a result of the metabolic variations or even differentiation heterogeneity. Nevertheless, a deeper investigation of cytochrome c localization along with mitochondrial characterization is necessary to determine the biological basis of detected cytochrome c in Raman spectra.

4. Materials and Methods

4.1. Collection, Isolation, Expansion, and Cultivation of MSCs

Bone marrow samples (2 mL) from five healthy donors (age range 2–12 years) (Table 2) were aspirated from iliac bone during the collection of bone marrow for allogenic transplantation at the Mother and Child Health Care Institute of Serbia. For each sample, informed consent was assigned, and all samples were collected in accordance with the ethical standards of the local ethical committee and the Declaration of Helsinki.

Table 2. The main characteristics of BM-MSCs donors enrolled in the study.

Donor	Sex	Blood Type	Karyotype	Age
D1	male	AB+	46, XY, 20	8 years and 10 months
D2	female	B+	46, XX, 20	12 years and 3 months
D3	female	O+	46, XX, 20	2 years and 5 months
D4	male	AB+	46, XY, 20	12 years and 4 months
D5	female	O+	46, XX, 20	12 years and 2 months

Lymphocyte separation media Lymphocyte Separation Medium 1077 (Capricorn-Scientific, Ebsdorfergrund, Germany) and density gradient centrifugation were used to obtain mononuclear fraction (MNCs) of bone marrow. MNCs were resuspended in growth medium (GM) composed of MEM Alpha Modification medium supplemented with nucleosides (Capricorn-Scientific), 10% Fetal Bovine Serum, certified, United States (FBS, Gibco, Thermo Fisher Scientific, Waltham, MA, USA), 1% Penicillin/Streptomycin (P/S, Gibco, Thermo Fisher Scientific) and 1% L-glutamine (Capricorn-Scientific) and cultured in plastic tissue culture flasks (Greiner Bio-One, Monroe, NC, USA) in GM at 37 °C in a humidified atmosphere containing 5% CO_2 (standard conditions). The GM was replaced twice a week, and non-adherent cells were disposed of. After reaching 80–90% of confluence, adherent BM-MSCs were passaged using 0.25% Trypsin/EDTA solution (Capricorn-Scientific) and replated at concentration of 1×10^4 cells/cm^2. Cell number was evaluated by Trypan blue solution (Invitrogen, Carlsbad, CA, USA). The morphology of adherent cells was visualized by using the light microscope (Olympus, Tokyo, Japan). All further experiments were performed using BM-MSCs from the 5th passage.

4.2. Immunophenotyping

The detection of BM-MSCs phenotype was determined following the cultivation of cells in GM at standard conditions. Upon reaching confluence, cells were detached using Accutase solution (Biowest, Nuaillé, France), and for each cell-surface marker analysis,

2×10^5 BM-MSCs were separated and washed in cold 0.5% BSA/PBS. Then, cells were labeled with fluorescein isothiocyanate (FITC)- or phycoerythrin (PE)-conjugated monoclonal antibodies against human antigens CD29, CD73, CD90, CD45 (all from R&D Systems, Minneapolis, MN, USA), CD105 and HLA-DR (both form Invitrogen, Carlsbad, CA, USA) during 30 min in the dark at +4 °C. For determination of the level of non-specific binding, corresponding FITC- and PE-conjugated isotype control antibodies (R&D Systems) were used. Flow cytometry was conducted using a Cytomics FC 500 (Beckman Coulter, Brea, CA, USA) cytometer, while data were analyzed using WinMDI 2.9 software (J. Trotter, The Scripps Research Institute, La Jolla, CA, USA).

4.3. Multipotent Differentiation

To determine the multilineage differentiation potential, BM-MSCs were plated in a 96-well plate (5×10^3 cells/well) in GM and incubated under standard conditions. GM was changed every 2–3 days until cells reached subconfluence when the GM was replaced with specific differentiation medium (DM), while cells cultivated in GM served as control.

For osteogenic differentiation medium, GM was supplemented with 200 μM ascorbic acid-2-phosphate (Sigma-Aldrich, St. Louis, MO, USA), 10 mM β-glycerophosphate (AppliChem, Darmstadt, Germany) and 10 nM dexamethasone (Sigma-Aldrich). After 7 days of cultivation, the early stage of osteogenic differentiation was analyzed via assessment of alkaline phosphatase (ALP) activity stained with 5-bromo-4-chloro-3-indolyl phosphate/nitro blue tetrazolium, BCIP/ NBT substrate (Sigma-Aldrich) in alkaline phosphatase buffer (0.1 M Tris, 100 mM NaCl, 5 mM MgCl2, pH 9.5). Late osteogenic differentiation was confirmed upon visualization of calcified deposits and extracellular matrix mineralization by using 2% Alizarin red dye (Merck Chemicals, Darmstadt, Germany) after three weeks of cultivation.

To determine the chondrogenic differentiation capacity of BM-MSCs, chondrogenic medium containing GM with 200 mM ascorbic acid-2-phosphate (Sigma-Aldrich), 10 nM dexamethasone (AppliChem, Darmstadt, Germany) and 5 ng/mL transforming growth factor (TGF-β) (R&D Systems) was used. Chondrogenic differentiation was estimated via proteoglycans staining with Safranin O (Merck Chemicals, Darmstadt, Germany) following the three weeks of treatment.

For adipogenic differentiation induction, BM-MSCs were cultivated in an adipogenic differentiation medium that contained GM enriched with 1 mM dexamethasone (Sigma-Aldrich), 10 μg/mL insulin (Sigma-Aldrich) and 100 μg/mL isobutyl methylxanthine (IBMX, Sigma-Aldrich). After four weeks, the formation of intracellular lipid droplets was confirmed by staining with Oil Red O (Merck Chemicals, Darmstadt, Germany).

Following the incubation period and staining assays, differentiated cells and control groups were analyzed by using the light microscope (Olympus, Tokyo, Japan).

4.4. CFU-F (Colony-Forming Units-Fibroblastic) Assay

To detect the clonogenicity of BM-MSCs, a colony-forming unit–fibroblastic (CFU-F) test was applied. BM-MSCs were plated in a 6-well plate (triplicate) at a seeding density of 250 cells per well. Following the 14 days of culturing in GM at standard conditions, cells were washed two times with PBS and fixed using ice-cold methanol for 5 min at room temperature. After fixation, cells were stained with 0.3% crystal violet (Carlo Erba reagents S.A.S., Emmendingen, Germany) for 15 min, when the cells were washed using distilled water. The number of colonies was determined by a light microscope (Olympus, Tokyo, Japan). Only colonies that were larger than 2 mm in diameter and consisted of more than 50 cells were counted. The ratio of the number of colonies to the number of cells plated was denoted as colony- forming efficiency.

4.5. Cellular Proliferation, Viability and Senescence

The population doubling time (PDT) of BM-MSCs was estimated through passaging. Cells were seeded in flasks at a concentration of $1 \times 10^4/\text{cm}^2$ and grown in GM under standard conditions until reaching confluency. Further on, BM-MSCs were detached, and cell number was determined by Trypan blue dye. Subsequently, cells were reseeded at the initial density. This process was repeated at every passage, up to passage 6. For calculation of the PDT, the following formula was used: PDT = (T − T0) lg2/(lgNt − lgN0), where T0 corresponds to the starting time of cell culture, T corresponds to the ending time of cell culture, N0 corresponds to the cell number at the start of culture, and Nt corresponds to the cell number at the end of culture.

To assess the viability of BM-MSCs, the metabolic activity of these cells was analyzed. Cells were seeded in 96-well-plates (5×10^3/well) and cultivated under standard conditions for 24 h and 48 h. Then, 3-(4,5-dimethylthiazol-2-yl) 2,5-diphenyltetrazolium bromide (MTT) solution (5 mg/mL) (Sigma-Aldrich) was added to each well, and incubation was continued for the next 2 h. Formed formazan crystals were dissolved with isopropanol, and the optical density was measured at 540 nm by the automatic reader for microplates (Labsystems Multiskan PLUS, Nelsirrki, Finland).

For BM-MSCs, the senescence activity of the β-galactosidase enzyme was analyzed. Cells were seeded in 96-well plates (2×10^3 cells/well) and cultivated in GM under standard conditions for 24 h. Next, cells were washed with PBS, fixed, and stained using Senescence Cells Histochemical Kit according to the manufacturer's instructions (Sigma Aldrich). Samples were visualized by a light microscope (Olympus).

4.6. Immunofluorescence

To perform immunofluorescent labeling, BM-MSCs were seeded in 24-well plates, over rounded glass coverslips (3×10^3 cells/well) in GM and grown under standard conditions for 24 h to ensure adhesion of the cell. Samples were then washed with PBS twice and fixed in 4% formaldehyde. Subsequently, cells were permeabilized with 0.1% Triton X − 100 in PBS for 10 min, blocked with 1% BSA/PBS (30 min at room temperature) and incubated with primary antibodies: rabbit anti-Ki67 (Abcam, Cambridge, UK), rabbit anti-Oct-4, mouse anti-NANOG, mouse anti-SOX-2 (all from Cell Signaling Technology, Danvers, MA, USA) and mouse anti-p53 (Santa Cruz Biotechnologies, Dallas, TX, USA). Following 2 h of incubation at room temperature, samples were washed with PBS and treated with corresponding FITC-coupled secondary antibodies (Sigma-Aldrich) or Alexa Fluor 555-coupled anti-mouse antibody (Cell Signaling Technology) and 1 ng/mL of nuclear dye DAPI (Sigma-Aldrich) for 2 h. An epi-fluorescent microscope (Olympus, Tokyo, Japan) was used for the examination of mounted cell samples.

4.7. Sample Preparation for Raman Experiment

For the purpose of Raman spectroscopy, BM-MSCs were seeded on rounded CaF_2 slides (Raman grade quality, Crystran, Dorset, UK) in a 24-well plate (5×10^3 cells per slide) and cultivated in GM under standard cultivation conditions for 24 h. After the adhesion, BM-MSCs were washed with saline buffer and fixed with methanol for 10 min at room temperature. Chemical fixation allows samples to be collected at a particular moment, preserving biomolecular distribution within cells and making analysis possible to repeat. Just before Raman spectroscopy was performed, samples were washed with distilled water.

4.8. μ-Raman Spectroscopy

In this research, standard μ-Raman spectroscopy was used. Raman scattering experiments were performed on a TriVista 557 Raman system (Teledyne Princeton Instruments, Trenton, NJ, USA) in backscattering configuration. A coherent Ar^+/Kr^+ ion gas laser of 514.5 nm was used as an excitation source. The focusing on the sample was achieved by using a ×50 Olympus microscope objective, $NA = 0.50$. The laser spot diameter in our experimental configuration was ≈20 μm. Sample damage by overheating was prevented by keeping low levels of the laser power at the sample plain, ≈5 mW. It was determined that under these conditions, no laser-induced effects were observed, and the spectra were fully reproducible for the particular cell site. The acquisition time per spectrum was 300 s.

On average, 50 to 100 cells per each cell population (D1–D5) were analyzed. Since cells are heterogeneous dynamical systems, typically for spectral acquisition, several positions are randomly selected per cell to consider a complex chemical and morphological inner structure, which might induce slight variations in Raman spectra, especially in intensities of some Raman bands. To obtain a representative spectrum per each cell, these spectra are averaged. Here, we opted for the alternative approach. By increasing the size of the randomly positioned laser spot (at the expense of the probing acquisition time), a more significant portion of the sample was probed, thus capturing more of its internal inhomogeneity.

4.9. Data Processing and Analysis

The statistical interpretation of the results was completed by using the principal component analysis (PCA) method [36,40,41]. This method is used to reduce the large dimensionality of the Raman dataset in which every wavenumber represents a variable and the light intensity measured at that wavenumber represents a data point. The dimensionality reduction is completed by projecting the data points onto a new set of linearly uncorrelated variables, which are called principal components [42,43]. The PCA method used in this work is based on the singular value decomposition algorithm adopted from the GNU Octave standard library.

The Raman dataset, consisting of spectra collected within one or more donors, was preprocessed before it was forwarded to the PCA algorithm. The preprocessing procedure includes the following steps:

(i) Removal of the irregular spectra from the datasets;
(ii) Removal of the background noise from every spectrum in the data set;
(iii) Spectra normalization.

An irregular spectrum does not have Raman modes characteristic to donor cells. An example would be a spectrum exhibiting high luminescence, which masks the relevant Raman modes or a spectrum without any Raman modes. These types of spectra are omitted from the analysis, since they do not carry any relevant information and are known for introducing unwanted outlier data points when passed through the PCA.

The background removal is completed by subtracting a fourth-degree polynomial function from the measured spectra. The polynomial is tailored to fit the background of every individual spectrum from the dataset.

After the background has been removed, every spectrum from the dataset is normalized to the value of the integral intensity calculated within the considered spectral region.

4.10. Statistical Analysis

All biological assays were repeated at least three times, and the results are presented as mean ± SEM. Differences between groups were tested for statistical significance by Student's two-tailed t-test with p values less than 0.05 considered significant. Data analysis and graphical representations were performed by using GraphPad Prism 7 Software, Inc., San Diego, CA, USA.

5. Conclusions

Overall, the results of this study bring new evidence regarding the use of Raman spectroscopy in the field of MSCs exploration at the level of a single cell. Namely, by using standard biological assays analysis of BM-MSCs isolated from five healthy pediatric donors, no significant differences in terms of their MSCs properties, including morphology, phenotype, multilineage differentiation potential, colony-forming capacity, expression of pluripotency-associated markers or proliferative capacity were observed. On the other hand, Raman analysis revealed biochemical variations between these populations, whereby only changes related to peaks intensities were determined. Despite Raman spectra similarities, following the comprehensive analysis, subtle distinctions between averaged Raman spectra of BM-MSCs of each donor were detected, providing an important indication that this method can be used to clearly distinguish cell populations with a similar biochemical background. Particularly, based on PCA score plots, disjunctions between BM-MSCs populations were observed, whereby clustering between cell populations were most conspicuous when cell populations was analyzed in pairs. Although further studies are needed to elucidate the precise biological validation of Raman results, this study provides an important basis for revealing inter-individual variability between primary MSCs populations at the single-cell level by using this non-invasive, label-free, optical technique.

Author Contributions: Conceptualization, T.K. and J.L.; Methodology, T.K., A.B., J.L. and U.R.; Validation, A.J., D.V., N.L. and D.B.; Investigation, A.B., T.K., J.L. and U.R.; Data curation, T.K., J.L. and U.R. Writing—original draft preparation, T.K., J.L. and A.B.; Review and editing, A.J., N.L., D.V. and D.B.; Supervision, A.J., D.V., N.L. and D.B.; Funding acquisition, N.L. and D.B. All authors have read and agreed to the published version of the manuscript.

Funding: This work was funded by the Ministry of Education, Science, and Technological Development of the Republic of Serbia (contract number 451-03-68/2022-14/200015) and the Institute of Physics Belgrade, through a grant from the Ministry of Education, Science, and Technological Development of the Republic of Serbia. This research is also conducted within the national program “Start up for science” 2019/2020 realized by the Center for Leadership Development and the Philip Morris Company in Serbia.

Institutional Review Board Statement: This study was conducted in accordance with the Declaration of Helsinki and approved by the Ethics Committee of the Mother and Child Health Care Institute of Serbia “Dr. Vukan Čupić” (8/20, 29 June 2018).

Informed Consent Statement: Informed consent was obtained from all subjects involved in the study.

Data Availability Statement: The data presented in this study are available from the corresponding author upon reasonable request.

Acknowledgments: The authors are grateful to Slavko Mojsilović, Group for Hematology and Stem Cells, Institute for Medical Research, National Institute of Republic of Serbia, University of Belgrade, for flow cytometry analysis. In addition, we are thankful to Željko Zečević, Marija Simić, and Borko Gobeljić for tissue collection.

Conflicts of Interest: The authors declare no conflict of interest.

References

1. Teixeira, F.G.; Salgado, A.J. Mesenchymal Stem Cells Secretome: Current Trends and Future Challenges. *Neural Regen. Res.* **2020**, *15*, 75–77. [CrossRef]
2. Zakrzewski, W.; Dobrzyński, M.; Szymonowicz, M.; Rybak, Z. Stem Cells: Past, Present, and Future. *Stem Cell Res. Ther.* **2019**, *10*, 68. [CrossRef]
3. Nava, M.M.; Raimondi, M.T.; Pietrabissa, R. Controlling Self-Renewal and Differentiation of Stem Cells via Mechanical Cues. *J. Biomed. Biotechnol.* **2012**, *2012*, 797410. [CrossRef]
4. Wei, X.; Yang, X.; Han, Z.; Qu, F.; Shao, L.; Shi, Y. Mesenchymal Stem Cells: A New Trend for Cell Therapy. *Acta Pharmacol. Sin.* **2013**, *34*, 747–754. [CrossRef]
5. Caplan, A.I. Mesenchymal Stem Cells: Time to Change the Name! *Stem Cells Transl. Med.* **2017**, *6*, 1445–1451. [CrossRef]
6. Harrell, C.R.; Fellabaum, C.; Jovicic, N.; Djonov, V.; Arsenijevic, N.; Volarevic, V. Molecular Mechanisms Responsible for Therapeutic Potential of Mesenchymal Stem Cell-Derived Secretome. *Cells* **2019**, *8*, 467. [CrossRef]
7. Pittenger, M.F.; Discher, D.E.; Péault, B.M.; Phinney, D.G.; Hare, J.M.; Caplan, A.I. Mesenchymal Stem Cell Perspective: Cell Biology to Clinical Progress. *NPJ Regen. Med.* **2019**, *4*, 22. [CrossRef]
8. Musiał-Wysocka, A.; Kot, M.; Majka, M. The Pros and Cons of Mesenchymal Stem Cell-Based Therapies. *Cell Transpl.* **2019**, *28*, 801–812. [CrossRef]
9. Yin, P.T.; Han, E.; Lee, K.-B. Engineering Stem Cells for Biomedical Applications. *Adv. Health. Mater.* **2016**, *5*, 10–55. [CrossRef]
10. Wilson, A.; Hodgson-Garms, M.; Frith, J.E.; Genever, P. Multiplicity of Mesenchymal Stromal Cells: Finding the Right Route to Therapy. *Front. Immunol.* **2019**, *10*, 1112. [CrossRef]
11. Lv, F.-J.; Tuan, R.S.; Cheung, K.M.C.; Leung, V.Y.L. Concise Review: The Surface Markers and Identity of Human Mesenchymal Stem Cells. *Stem Cells* **2014**, *32*, 1408–1419. [CrossRef]
12. Mo, M.; Wang, S.; Zhou, Y.; Li, H.; Wu, Y. Mesenchymal Stem Cell Subpopulations: Phenotype, Property and Therapeutic Potential. *Cell. Mol. Life Sci.* **2016**, *73*, 3311–3321. [CrossRef]
13. Phinney, D.G. Functional Heterogeneity of Mesenchymal Stem Cells: Implications for Cell Therapy. *J. Cell. Biochem.* **2012**, *113*, 2806–2812. [CrossRef]

14. Dominici, M.; Le Blanc, K.; Mueller, I.; Slaper-Cortenbach, I.; Marini, F.; Krause, D.; Deans, R.; Keating, A.; Prockop, D.; Horwitz, E. Minimal Criteria for Defining Multipotent Mesenchymal Stromal Cells. The International Society for Cellular Therapy Position Statement. *Cytotherapy* **2006**, *8*, 315–317. [CrossRef]
15. Ullah, I.; Subbarao, R.B.; Rho, G.J. Human Mesenchymal Stem Cells—Current Trends and Future Prospective. *Biosci. Rep.* **2015**, *35*, e00191. [CrossRef]
16. Chen, J.-Y.; Mou, X.-Z.; Du, X.-C.; Xiang, C. Comparative Analysis of Biological Characteristics of Adult Mesenchymal Stem Cells with Different Tissue Origins. *Asian Pac. J. Trop. Med.* **2015**, *8*, 739–746. [CrossRef]
17. Guan, Y.-T.; Xie, Y.; Li, D.-S.; Zhu, Y.-Y.; Zhang, X.-L.; Feng, Y.-L.; Chen, Y.-P.; Xu, L.-J.; Liao, P.-F.; Wang, G. Comparison of Biological Characteristics of Mesenchymal Stem Cells Derived from the Human Umbilical Cord and Decidua Parietalis. *Mol. Med. Rep.* **2019**, *20*, 633–639. [CrossRef]
18. Sangeetha, K.N.; Vennila, R.; Secunda, R.; Sakthivel, S.; Pathak, S.; Jeswanth, S.; Surendran, R. Functional Variations between Mesenchymal Stem Cells of Different Tissue Origins: A Comparative Gene Expression Profiling. *Biotechnol. Lett.* **2020**, *42*, 1287–1304. [CrossRef]
19. Xu, L.; Liu, Y.; Sun, Y.; Wang, B.; Xiong, Y.; Lin, W.; Wei, Q.; Wang, H.; He, W.; Wang, B.; et al. Tissue Source Determines the Differentiation Potentials of Mesenchymal Stem Cells: A Comparative Study of Human Mesenchymal Stem Cells from Bone Marrow and Adipose Tissue. *Stem Cell Res. Ther.* **2017**, *8*, 275. [CrossRef]
20. Costa, L.A.; Eiro, N.; Fraile, M.; Gonzalez, L.O.; Saá, J.; Garcia-Portabella, P.; Vega, B.; Schneider, J.; Vizoso, F.J. Functional Heterogeneity of Mesenchymal Stem Cells from Natural Niches to Culture Conditions: Implications for Further Clinical Uses. *Cell. Mol. Life Sci.* **2021**, *78*, 447–467. [CrossRef]
21. Lähnemann, D.; Köster, J.; Szczurek, E.; McCarthy, D.J.; Hicks, S.C.; Robinson, M.D.; Vallejos, C.A.; Campbell, K.R.; Beerenwinkel, N.; Mahfouz, A.; et al. Eleven Grand Challenges in Single-Cell Data Science. *Genome Biol.* **2020**, *21*, 31. [CrossRef]
22. Yuan, G.-C.; Cai, L.; Elowitz, M.; Enver, T.; Fan, G.; Guo, G.; Irizarry, R.; Kharchenko, P.; Kim, J.; Orkin, S.; et al. Challenges and Emerging Directions in Single-Cell Analysis. *Genome Biol.* **2017**, *18*, 84. [CrossRef]
23. Zheng, G.; Xie, Z.-Y.; Wang, P.; Wu, Y.-F.; Shen, H.-Y. Recent Advances of Single-Cell RNA Sequencing Technology in Mesenchymal Stem Cell Research. *World J. Stem Cells* **2020**, *12*, 438–447. [CrossRef]
24. Ember, K.J.I.; Hoeve, M.A.; McAughtrie, S.L.; Bergholt, M.S.; Dwyer, B.J.; Stevens, M.M.; Faulds, K.; Forbes, S.J.; Campbell, C.J. Raman Spectroscopy and Regenerative Medicine: A Review. *NPJ Regen. Med.* **2017**, *2*, 12. [CrossRef]
25. García-Timermans, C.; Props, R.; Zacchetti, B.; Sakarika, M.; Delvigne, F.; Boon, N. Raman Spectroscopy-Based Measurements of Single-Cell Phenotypic Diversity in Microbial Populations. *mSphere* **2020**, *5*, e00806-20. [CrossRef]
26. Downes, A.; Mouras, R.; Bagnaninchi, P.; Elfick, A. Raman Spectroscopy and CARS Microscopy of Stem Cells and Their Derivatives. *J. Raman Spectrosc.* **2011**, *42*, 1864–1870. [CrossRef]
27. Bai, H.; Chen, P.; Fang, H.; Lin, L.; Tang, G.Q.; Mu, G.G.; Gong, W.; Liu, Z.P.; Wu, H.; Zhao, H.; et al. Detecting Viability Transitions of Umbilical Cord Mesenchymal Stem Cells by Raman Micro-Spectroscopy. *Laser Phys. Lett.* **2010**, *8*, 78. [CrossRef]
28. Azrad, E.; Zahor, D.; Vago, R.; Nevo, Z.; Doron, R.; Robinson, D.; Gheber, L.A.; Rosenwaks, S.; Bar, I. Probing the Effect of an Extract of Elk Velvet Antler Powder on Mesenchymal Stem Cells Using Raman Microspectroscopy: Enhanced Differentiation toward Osteogenic Fate. *J. Raman Spectrosc.* **2006**, *37*, 480–486. [CrossRef]
29. Molony, C.; McIntyre, J.; Maguire, A.; Hakimjavadi, R.; Burtenshaw, D.; Casey, G.; di Luca, M.; Hennelly, B.; Byrne, H.J.; Cahill, P.A. Label-Free Discrimination Analysis of de-Differentiated Vascular Smooth Muscle Cells, Mesenchymal Stem Cells and Their Vascular and Osteogenic Progeny Using Vibrational Spectroscopy. *Biochim. Biophys. Acta Mol. Cell Res.* **2018**, *1865*, 343–353. [CrossRef]
30. Butler, H.J.; Ashton, L.; Bird, B.; Cinque, G.; Curtis, K.; Dorney, J.; Esmonde-White, K.; Fullwood, N.J.; Gardner, B.; Martin-Hirsch, P.L.; et al. Using Raman Spectroscopy to Characterize Biological Materials. *Nat. Protoc.* **2016**, *11*, 664–687. [CrossRef]
31. Rangan, S.; Schulze, H.G.; Vardaki, M.Z.; Blades, M.W.; Piret, J.M.; Turner, R.F.B. Applications of Raman Spectroscopy in the Development of Cell Therapies: State of the Art and Future Perspectives. *Analyst* **2020**, *145*, 2070–2105. [CrossRef]
32. Geng, J.; Zhang, W.; Chen, C.; Zhang, H.; Zhou, A.; Huang, Y. Tracking the Differentiation Status of Human Neural Stem Cells through Label-Free Raman Spectroscopy and Machine Learning-Based Analysis. *Anal. Chem.* **2021**, *93*, 10453–10461. [CrossRef]
33. Wang, J.; Qi, G.; Qu, X.; Ling, X.; Zhang, Z.; Jin, Y. Molecular Profiling of Dental Pulp Stem Cells during Cell Differentiation by Surface Enhanced Raman Spectroscopy. *Anal. Chem.* **2020**, *92*, 3735–3741. [CrossRef]
34. Hsu, C.-C.; Xu, J.; Brinkhof, B.; Wang, H.; Cui, Z.; Huang, W.E.; Ye, H. A Single-Cell Raman-Based Platform to Identify Developmental Stages of Human Pluripotent Stem Cell-Derived Neurons. *Proc. Natl. Acad. Sci. USA* **2020**, *117*, 18412–18423. [CrossRef]
35. Lazarević, J.J.; Kukolj, T.; Bugarski, D.; Lazarević, N.; Bugarski, B.; Popović, Z.V. Probing Primary Mesenchymal Stem Cells Differentiation Status by Micro-Raman Spectroscopy. *Spectrochim. Acta. A Mol. Biomol. Spectrosc.* **2019**, *213*, 384–390. [CrossRef]
36. Notingher, I.; Bisson, I.; Bishop, A.E.; Randle, W.L.; Polak, J.M.P.; Hench, L.L. In Situ Spectral Monitoring of MRNA Translation in Embryonic Stem Cells during Differentiation In Vitro. *Anal. Chem.* **2004**, *76*, 3185–3193. [CrossRef]
37. Ghita, A.; Pascut, F.C.; Sottile, V.; Denning, C.; Notingher, I. Applications of Raman Micro-Spectroscopy to Stem Cell Technology: Label-Free Molecular Discrimination and Monitoring Cell Differentiation. *EPJ Tech. Instrum.* **2015**, *2*, 6. [CrossRef]
38. Ravera, F.; Efeoglu, E.; Byrne, H.J. Vibrational Spectroscopy for In Vitro Monitoring Stem Cell Differentiation. *Mol. Basel Switz.* **2020**, *25*, 5554. [CrossRef]

39. Carvalho, M.S.; Silva, J.C.; Hoff, C.M.; Cabral, J.M.S.; Linhardt, R.J.; da Silva, C.L.; Vashishth, D. Loss and Rescue of Osteocalcin and Osteopontin Modulate Osteogenic and Angiogenic Features of Mesenchymal Stem/Stromal Cells. *J. Cell. Physiol.* **2020**, *235*, 7496–7515. [CrossRef]
40. Wiercigroch, E.; Szafraniec, E.; Czamara, K.; Pacia, M.Z.; Majzner, K.; Kochan, K.; Kaczor, A.; Baranska, M.; Malek, K. Raman and Infrared Spectroscopy of Carbohydrates: A Review. *Spectrochim. Acta. A Mol. Biomol. Spectrosc.* **2017**, *185*, 317–335. [CrossRef]
41. Clemens, G.; Hands, J.R.; Dorling, K.M.; Baker, M.J. Vibrational Spectroscopic Methods for Cytology and Cellular Research. *Analyst* **2014**, *139*, 4411–4444. [CrossRef]
42. Czamara, K.; Majzner, K.; Pacia, M.Z.; Kochan, K.; Kaczor, A.; Baranska, M. Raman Spectroscopy of Lipids: A Review. *J. Raman Spectrosc.* **2015**, *46*, 4–20. [CrossRef]
43. de Gelder, J.; de Gussem, K.; Vandenabeele, P.; Moens, L. Reference Database of Raman Spectra of Biological Molecules. *J. Raman Spectrosc.* **2007**, *38*, 1133–1147. [CrossRef]
44. Pezzotti, G.; Zhu, W.; Adachi, T.; Horiguchi, S.; Marin, E.; Boschetto, F.; Ogitani, E.; Mazda, O. Metabolic Machinery Encrypted in the Raman Spectrum of Influenza A Virus-Inoculated Mammalian Cells. *J. Cell. Physiol.* **2020**, *235*, 5146–5170. [CrossRef]
45. Baker, M.J.; Byrne, H.J.; Chalmers, J.; Gardner, P.; Goodacre, R.; Henderson, A.; Kazarian, S.G.; Martin, F.L.; Moger, J.; Stone, N.; et al. Clinical Applications of Infrared and Raman Spectroscopy: State of Play and Future Challenges. *Analyst* **2018**, *143*, 1735–1757. [CrossRef]
46. Tanwar, S.; Paidi, S.K.; Prasad, R.; Pandey, R.; Barman, I. Advancing Raman Spectroscopy from Research to Clinic: Translational Potential and Challenges. *Spectrochim. Acta. A Mol. Biomol. Spectrosc.* **2021**, *260*, 119957. [CrossRef]
47. Crow, P.; Barrass, B.; Kendall, C.; Hart-Prieto, M.; Wright, M.; Persad, R.; Stone, N. The Use of Raman Spectroscopy to Differentiate between Different Prostatic Adenocarcinoma Cell Lines. *Br. J. Cancer* **2005**, *92*, 2166–2170. [CrossRef]
48. Ilin, Y.; Kraft, M.L. Identifying the Lineages of Individual Cells in Cocultures by Multivariate Analysis of Raman Spectra. *Analyst* **2014**, *139*, 2177–2185. [CrossRef]
49. Surmacki, J.M.; Woodhams, B.J.; Haslehurst, A.; Ponder, B.A.J.; Bohndiek, S.E. Raman Micro-Spectroscopy for Accurate Identification of Primary Human Bronchial Epithelial Cells. *Sci. Rep.* **2018**, *8*, 12604. [CrossRef]
50. Pijanka, J.K.; Kumar, D.; Dale, T.; Yousef, I.; Parkes, G.; Untereiner, V.; Yang, Y.; Dumas, P.; Collins, D.; Manfait, M.; et al. Vibrational Spectroscopy Differentiates between Multipotent and Pluripotent Stem Cells. *Analyst* **2010**, *135*, 3126–3132. [CrossRef]
51. Pudlas, M.; Carvajal Berrio, D.; Linneweh, M.; Koch, S.; Thude, S.; Walles, H.; Schenke-Layland, K. Non-Contact Discrimination of Human Bone Marrow-Derived Mesenchymal Stem Cells and Fibroblasts Using Raman Spectroscopy. *Med. Laser Appl.* **2011**, *26*, 119–125. [CrossRef]
52. Simonović, J.; Toljić, B.; Rašković, B.; Jovanović, V.; Lazarević, M.; Milošević, M.; Nikolić, N.; Panajotović, R.; Milašin, J. Raman Microspectroscopy: Toward a Better Distinction and Profiling of Different Populations of Dental Stem Cells. *Croat. Med. J.* **2019**, *60*, 78–86. [CrossRef] [PubMed]
53. Baghaei, K.; Hashemi, S.M.; Tokhanbigli, S.; Asadi Rad, A.; Assadzadeh-Aghdaei, H.; Sharifian, A.; Zali, M.R. Isolation, Differentiation, and Characterization of Mesenchymal Stem Cells from Human Bone Marrow. *Gastroenterol. Hepatol. Bed Bench* **2017**, *10*, 208–213. [PubMed]
54. Mennan, C.; Garcia, J.; Roberts, S.; Hulme, C.; Wright, K. A Comprehensive Characterisation of Large-Scale Expanded Human Bone Marrow and Umbilical Cord Mesenchymal Stem Cells. *Stem Cell Res. Ther.* **2019**, *10*, 99. [CrossRef]
55. Bhat, S.; Viswanathan, P.; Chandanala, S.; Prasanna, S.J.; Seetharam, R.N. Expansion and Characterization of Bone Marrow Derived Human Mesenchymal Stromal Cells in Serum-Free Conditions. *Sci. Rep.* **2021**, *11*, 3403. [CrossRef]
56. Yang, Y.-H.K.; Ogando, C.R.; Wang See, C.; Chang, T.-Y.; Barabino, G.A. Changes in Phenotype and Differentiation Potential of Human Mesenchymal Stem Cells Aging in Vitro. *Stem Cell Res. Ther.* **2018**, *9*, 131. [CrossRef]
57. Song, Y.; Zhao, H.-Y.; Lyu, Z.-S.; Cao, X.-N.; Shi, M.-M.; Wen, Q.; Tang, F.-F.; Wang, Y.; Xu, L.-P.; Zhang, X.-H.; et al. Dysfunctional Bone Marrow Mesenchymal Stem Cells in Patients with Poor Graft Function after Allogeneic Hematopoietic Stem Cell Transplantation. *Biol. Blood Marrow Transplant.* **2018**, *24*, 1981–1989. [CrossRef]
58. Zhou, Y.; Chen, H.; Li, H.; Wu, Y. 3D Culture Increases Pluripotent Gene Expression in Mesenchymal Stem Cells through Relaxation of Cytoskeleton Tension. *J. Cell. Mol. Med.* **2017**, *21*, 1073–1084. [CrossRef]
59. Petrenko, Y.; Vackova, I.; Kekulova, K.; Chudickova, M.; Koci, Z.; Turnovcova, K.; Kupcova Skalnikova, H.; Vodicka, P.; Kubinova, S. A Comparative Analysis of Multipotent Mesenchymal Stromal Cells Derived from Different Sources, with a Focus on Neuroregenerative Potential. *Sci. Rep.* **2020**, *10*, 4290. [CrossRef]
60. Mareschi, K.; Ferrero, I.; Rustichelli, D.; Aschero, S.; Gammaitoni, L.; Aglietta, M.; Madon, E.; Fagioli, F. Expansion of Mesenchymal Stem Cells Isolated from Pediatric and Adult Donor Bone Marrow. *J. Cell. Biochem.* **2006**, *97*, 744–754. [CrossRef]
61. Kern, S.; Eichler, H.; Stoeve, J.; Klüter, H.; Bieback, K. Comparative Analysis of Mesenchymal Stem Cells from Bone Marrow, Umbilical Cord Blood, or Adipose Tissue. *Stem Cells Dayt. Ohio* **2006**, *24*, 1294–1301. [CrossRef] [PubMed]
62. Araújo, A.B.; Salton, G.D.; Furlan, J.M.; Schneider, N.; Angeli, M.H.; Laureano, Á.M.; Silla, L.; Passos, E.P.; Paz, A.H. Comparison of Human Mesenchymal Stromal Cells from Four Neonatal Tissues: Amniotic Membrane, Chorionic Membrane, Placental Decidua and Umbilical Cord. *Cytotherapy* **2017**, *19*, 577–585. [CrossRef]
63. Ghaneialvar, H.; Soltani, L.; Rahmani, H.R.; Lotfi, A.S.; Soleimani, M. Characterization and Classification of Mesenchymal Stem Cells in Several Species Using Surface Markers for Cell Therapy Purposes. *Indian J. Clin. Biochem.* **2018**, *33*, 46–52. [CrossRef]

64. Pittenger, M.F.; Mackay, A.M.; Beck, S.C.; Jaiswal, R.K.; Douglas, R.; Mosca, J.D.; Moorman, M.A.; Simonetti, D.W.; Craig, S.; Marshak, D.R. Multilineage Potential of Adult Human Mesenchymal Stem Cells. *Science* **1999**, *284*, 143–147. [CrossRef] [PubMed]
65. Meppelink, A.M.; Wang, X.-H.; Bradica, G.; Barron, K.; Hiltz, K.; Liu, X.-H.; Goldman, S.M.; Vacanti, J.P.; Keating, A.; Hoganson, D.M. Rapid Isolation of Bone Marrow Mesenchymal Stromal Cells Using Integrated Centrifuge-Based Technology. *Cytotherapy* **2016**, *18*, 729–739. [CrossRef] [PubMed]
66. Meuleman, N.; Tondreau, T.; Delforge, A.; Dejeneffe, M.; Massy, M.; Libertalis, M.; Bron, D.; Lagneaux, L. Human Marrow Mesenchymal Stem Cell Culture: Serum-Free Medium Allows Better Expansion than Classical Alpha-MEM Medium. *Eur. J. Haematol.* **2006**, *76*, 309–316. [CrossRef] [PubMed]
67. Dmitrieva, R.I.; Minullina, I.R.; Bilibina, A.A.; Tarasova, O.V.; Anisimov, S.V.; Zaritskey, A.Y. Bone Marrow- and Subcutaneous Adipose Tissue-Derived Mesenchymal Stem Cells: Differences and Similarities. *Cell Cycle Georget. Tex.* **2012**, *11*, 377–383. [CrossRef]
68. Vishnubalaji, R.; Al-Nbaheen, M.; Kadalmani, B.; Aldahmash, A.; Ramesh, T. Comparative Investigation of the Differentiation Capability of Bone-Marrow- and Adipose-Derived Mesenchymal Stem Cells by Qualitative and Quantitative Analysis. *Cell Tissue Res.* **2012**, *347*, 419–427. [CrossRef]
69. Alcayaga-Miranda, F.; Cuenca, J.; Luz-Crawford, P.; Aguila-Díaz, C.; Fernandez, A.; Figueroa, F.E.; Khoury, M. Characterization of Menstrual Stem Cells: Angiogenic Effect, Migration and Hematopoietic Stem Cell Support in Comparison with Bone Marrow Mesenchymal Stem Cells. *Stem Cell Res. Ther.* **2015**, *6*, 32. [CrossRef]
70. Kolf, C.M.; Cho, E.; Tuan, R.S. Mesenchymal Stromal Cells. Biology of Adult Mesenchymal Stem Cells: Regulation of Niche, Self-Renewal and Differentiation. *Arthritis Res. Ther.* **2007**, *9*, 204. [CrossRef]
71. Boyer, L.A.; Lee, T.I.; Cole, M.F.; Johnstone, S.E.; Levine, S.S.; Zucker, J.P.; Guenther, M.G.; Kumar, R.M.; Murray, H.L.; Jenner, R.G.; et al. Core Transcriptional Regulatory Circuitry in Human Embryonic Stem Cells. *Cell* **2005**, *122*, 947–956. [CrossRef] [PubMed]
72. Riekstina, U.; Cakstina, I.; Parfejevs, V.; Hoogduijn, M.; Jankovskis, G.; Muiznieks, I.; Muceniece, R.; Ancans, J. Embryonic Stem Cell Marker Expression Pattern in Human Mesenchymal Stem Cells Derived from Bone Marrow, Adipose Tissue, Heart and Dermis. *Stem Cell Rev. Rep.* **2009**, *5*, 378–386. [CrossRef] [PubMed]
73. Miletić, M.; Mojsilović, S.; Okić-Đorđević, I.; Kukolj, T.; Jauković, A.; Santibacez, J.F.; Jovčić, G.; Bugarski, D. Mesenchymal Stem Cells Isolated from Human Periodontal Ligament. *Arch. Biol. Sci.* **2014**, *66*, 261–271. [CrossRef]
74. Tantrawatpan, C.; Manochantr, S.; Kheolamai, P.; U-Pratya, Y.; Supokawej, A.; Issaragrisil, S. Pluripotent Gene Expression in Mesenchymal Stem Cells from Human Umbilical Cord Wharton's Jelly and Their Differentiation Potential to Neural-like Cells. *J. Med. Assoc. Thail. Chotmaihet Thangphaet* **2013**, *96*, 1208–1217.
75. Park, E.; Patel, A.N. Changes in the Expression Pattern of Mesenchymal and Pluripotent Markers in Human Adipose-Derived Stem Cells. *Cell Biol. Int.* **2010**, *34*, 979–984. [CrossRef]
76. Jaramillo-Ferrada, P.A.; Wolvetang, E.J.; Cooper-White, J.J. Differential Mesengenic Potential and Expression of Stem Cell-Fate Modulators in Mesenchymal Stromal Cells from Human-Term Placenta and Bone Marrow. *J. Cell. Physiol.* **2012**, *227*, 3234–3242. [CrossRef]
77. Gao, L.R.; Zhang, N.K.; Ding, Q.A.; Chen, H.Y.; Hu, X.; Jiang, S.; Li, T.C.; Chen, Y.; Wang, Z.G.; Ye, Y.; et al. Common Expression of Stemness Molecular Markers and Early Cardiac Transcription Factors in Human Wharton's Jelly-Derived Mesenchymal Stem Cells and Embryonic Stem Cells. *Cell Transplant.* **2013**, *22*, 1883–1900. [CrossRef]
78. Kukolj, T.; Trivanović, D.; Mojsilović, S.; Okić Djordjević, I.; Obradović, H.; Krstić, J.; Jauković, A.; Bugarski, D. IL-33 Guides Osteogenesis and Increases Proliferation and Pluripotency Marker Expression in Dental Stem Cells. *Cell Prolif.* **2019**, *52*, e12533. [CrossRef]
79. Jauković, A.; Kukolj, T.; Trivanović, D.; Okić-Đorđević, I.; Obradović, H.; Miletić, M.; Petrović, V.; Mojsilović, S.; Bugarski, D. Modulating Stemness of Mesenchymal Stem Cells from Exfoliated Deciduous and Permanent Teeth by IL-17 and BFGF. *J. Cell. Physiol.* **2021**, *236*, 7322–7341. [CrossRef]
80. Han, S.-M.; Han, S.-H.; Coh, Y.-R.; Jang, G.; Chan Ra, J.; Kang, S.-K.; Lee, H.-W.; Youn, H.-Y. Enhanced Proliferation and Differentiation of Oct4- and Sox2-Overexpressing Human Adipose Tissue Mesenchymal Stem Cells. *Exp. Mol. Med.* **2014**, *46*, e101. [CrossRef]
81. Piccinato, C.A.; Sertie, A.L.; Torres, N.; Ferretti, M.; Antonioli, E. High OCT4 and Low P16(INK4A) Expressions Determine In Vitro Lifespan of Mesenchymal Stem Cells. *Stem Cells Int.* **2015**, *2015*, 369828. [CrossRef] [PubMed]
82. Pitrone, M.; Pizzolanti, G.; Tomasello, L.; Coppola, A.; Morini, L.; Pantuso, G.; Ficarella, R.; Guarnotta, V.; Perrini, S.; Giorgino, F.; et al. NANOG Plays a Hierarchical Role in the Transcription Network Regulating the Pluripotency and Plasticity of Adipose Tissue-Derived Stem Cells. *Int. J. Mol. Sci.* **2017**, *18*, 1107. [CrossRef] [PubMed]
83. Lu, Y.; Qu, H.; Qi, D.; Xu, W.; Liu, S.; Jin, X.; Song, P.; Guo, Y.; Jia, Y.; Wang, X.; et al. OCT4 Maintains Self-Renewal and Reverses Senescence in Human Hair Follicle Mesenchymal Stem Cells through the Downregulation of P21 by DNA Methyltransferases. *Stem Cell Res. Ther.* **2019**, *10*, 28. [CrossRef] [PubMed]
84. Li, X.; Bai, J.; Ji, X.; Li, R.; Xuan, Y.; Wang, Y. Comprehensive Characterization of Four Different Populations of Human Mesenchymal Stem Cells as Regards Their Immune Properties, Proliferation and Differentiation. *Int. J. Mol. Med.* **2014**, *34*, 695–704. [CrossRef] [PubMed]

85. Kundrotas, G.; Gasperskaja, E.; Slapsyte, G.; Gudleviciene, Z.; Krasko, J.; Stumbryte, A.; Liudkeviciene, R. Identity, Proliferation Capacity, Genomic Stability and Novel Senescence Markers of Mesenchymal Stem Cells Isolated from Low Volume of Human Bone Marrow. *Oncotarget* **2016**, *7*, 10788–10802. [CrossRef] [PubMed]
86. Nawrocka, D.; Kornicka, K.; Szydlarska, J.; Marycz, K. Basic Fibroblast Growth Factor Inhibits Apoptosis and Promotes Proliferation of Adipose-Derived Mesenchymal Stromal Cells Isolated from Patients with Type 2 Diabetes by Reducing Cellular Oxidative Stress. *Oxid. Med. Cell. Longev.* **2017**, *2017*, 3027109. [CrossRef]
87. Remnant, L.; Kochanova, N.Y.; Reid, C.; Cisneros-Soberanis, F.; Earnshaw, W.C. The Intrinsically Disorderly Story of Ki-67. *Open Biol.* **2021**, *11*, 210120. [CrossRef]
88. Sun, X.; Kaufman, P.D. Ki-67: More than a Proliferation Marker. *Chromosoma* **2018**, *127*, 175–186. [CrossRef]
89. Sales Gil, R.; Vagnarelli, P. Ki-67: More Hidden behind a "Classic Proliferation Marker". *Trends Biochem. Sci.* **2018**, *43*, 747–748. [CrossRef]
90. Chierico, L.; Rizzello, L.; Guan, L.; Joseph, A.S.; Lewis, A.; Battaglia, G. The Role of the Two Splice Variants and Extranuclear Pathway on Ki-67 Regulation in Non-Cancer and Cancer Cells. *PLoS ONE* **2017**, *12*, e0171815. [CrossRef]
91. Hafner, A.; Bulyk, M.L.; Jambhekar, A.; Lahav, G. The Multiple Mechanisms That Regulate P53 Activity and Cell Fate. *Nat. Rev. Mol. Cell Biol.* **2019**, *20*, 199–210. [CrossRef] [PubMed]
92. Xia, C.; Jiang, T.; Wang, Y.; Chen, X.; Hu, Y.; Gao, Y. The P53/MiR-145a Axis Promotes Cellular Senescence and Inhibits Osteogenic Differentiation by Targeting Cbfb in Mesenchymal Stem Cells. *Front. Endocrinol.* **2020**, *11*, 609186. [CrossRef] [PubMed]
93. Velletri, T.; Xie, N.; Wang, Y.; Huang, Y.; Yang, Q.; Chen, X.; Chen, Q.; Shou, P.; Gan, Y.; Cao, G.; et al. P53 Functional Abnormality in Mesenchymal Stem Cells Promotes Osteosarcoma Development. *Cell Death Dis.* **2016**, *7*, e2015. [CrossRef] [PubMed]
94. Boregowda, S.V.; Krishnappa, V.; Strivelli, J.; Haga, C.L.; Booker, C.N.; Phinney, D.G. Basal P53 Expression Is Indispensable for Mesenchymal Stem Cell Integrity. *Cell Death Differ.* **2018**, *25*, 679–692. [CrossRef] [PubMed]
95. O'Brate, A.; Giannakakou, P. The Importance of P53 Location: Nuclear or Cytoplasmic Zip Code? *Drug Resist. Updat. Rev. Comment. Antimicrob. Anticancer Chemother.* **2003**, *6*, 313–322. [CrossRef] [PubMed]
96. Gu, Z.; Jiang, J.; Tan, W.; Xia, Y.; Cao, H.; Meng, Y.; Da, Z.; Liu, H.; Cheng, C. P53/P21 Pathway Involved in Mediating Cellular Senescence of Bone Marrow-Derived Mesenchymal Stem Cells from Systemic Lupus Erythematosus Patients. *Clin. Dev. Immunol.* **2013**, *2013*, 134243. [CrossRef]
97. Solozobova, V.; Blattner, C. P53 in Stem Cells. *World J. Biol. Chem.* **2011**, *2*, 202–214. [CrossRef]
98. Solozobova, V.; Rolletschek, A.; Blattner, C. Nuclear Accumulation and Activation of P53 in Embryonic Stem Cells after DNA Damage. *BMC Cell Biol.* **2009**, *10*, 46. [CrossRef]
99. Ferretti, C.; Lucarini, G.; Andreoni, C.; Salvolini, E.; Bianchi, N.; Vozzi, G.; Gigante, A.; Mattioli-Belmonte, M. Human Periosteal Derived Stem Cell Potential: The Impact of Age. *Stem Cell Rev. Rep.* **2015**, *11*, 487–500. [CrossRef]
100. Sullivan, K.D.; Galbraith, M.D.; Andrysik, Z.; Espinosa, J.M. Mechanisms of Transcriptional Regulation by P53. *Cell Death Differ.* **2018**, *25*, 133–143. [CrossRef]
101. Aksoy, C.; Severcan, F. Role of Vibrational Spectroscopy in Stem Cell Research. *Spectrosc. Int. J.* **2012**, *27*, 167–184. [CrossRef]
102. Matthews, Q.; Jirasek, A.; Lum, J.; Duan, X.; Brolo, A.G. Variability in Raman Spectra of Single Human Tumor Cells Cultured in Vitro: Correlation with Cell Cycle and Culture Confluency. *Appl. Spectrosc.* **2010**, *64*, 871–887. [CrossRef] [PubMed]
103. Movasaghi, Z.; Rehman, S.; Rehman, I.U. Raman Spectroscopy of Biological Tissues. *Appl. Spectrosc. Rev.* **2007**, *42*, 493–541. [CrossRef]
104. Brauchle, E.; Noor, S.; Holtorf, E.; Garbe, C.; Schenke-Layland, K.; Busch, C. Raman Spectroscopy as an Analytical Tool for Melanoma Research. *Clin. Exp. Dermatol.* **2014**, *39*, 636–645. [CrossRef] [PubMed]
105. Hoppe, A. What MRNA Abundances Can Tell Us about Metabolism. *Metabolites* **2012**, *2*, 614–631. [CrossRef] [PubMed]
106. Verrier, S.; Notingher, I.; Polak, J.M.; Hench, L.L. In Situ Monitoring of Cell Death Using Raman Microspectroscopy. *Biopolymers* **2004**, *74*, 157–162. [CrossRef]
107. Parrotta, E.; De Angelis, M.T.; Scalise, S.; Candeloro, P.; Santamaria, G.; Paonessa, M.; Coluccio, M.L.; Perozziello, G.; De Vitis, S.; Sgura, A.; et al. Two Sides of the Same Coin? Unraveling Subtle Differences between Human Embryonic and Induced Pluripotent Stem Cells by Raman Spectroscopy. *Stem Cell Res. Ther.* **2017**, *8*, 271. [CrossRef]
108. Bogdan, P.; Deasy, B.M.; Gharaibeh, B.; Roehrs, T.; Marculescu, R. Heterogeneous Structure of Stem Cells Dynamics: Statistical Models and Quantitative Predictions. *Sci. Rep.* **2014**, *4*, 4826. [CrossRef]
109. McLeod, C.M.; Mauck, R.L. On the Origin and Impact of Mesenchymal Stem Cell Heterogeneity: New Insights and Emerging Tools for Single Cell Analysis. *Eur. Cell. Mater.* **2017**, *34*, 217–231. [CrossRef]
110. Tan, Y.; Konorov, S.O.; Schulze, H.G.; Piret, J.M.; Blades, M.W.; Turner, R.F.B. Comparative Study Using Raman Microspectroscopy Reveals Spectral Signatures of Human Induced Pluripotent Cells More Closely Resemble Those from Human Embryonic Stem Cells than Those from Differentiated Cells. *Analyst* **2012**, *137*, 4509–4515. [CrossRef]
111. Germond, A.; Panina, Y.; Shiga, M.; Niioka, H.; Watanabe, T.M. Following Embryonic Stem Cells, Their Differentiated Progeny, and Cell-State Changes During IPS Reprogramming by Raman Spectroscopy. *Anal. Chem.* **2020**, *92*, 14915–14923. [CrossRef] [PubMed]
112. Wang, L.; Zhang, T.; Wang, L.; Cai, Y.; Zhong, X.; He, X.; Hu, L.; Tian, S.; Wu, M.; Hui, L.; et al. Fatty Acid Synthesis Is Critical for Stem Cell Pluripotency via Promoting Mitochondrial Fission. *EMBO J.* **2017**, *36*, 1330–1347. [CrossRef] [PubMed]

113. Ow, Y.-L.P.; Green, D.R.; Hao, Z.; Mak, T.W. Cytochrome c: Functions beyond Respiration. *Nat. Rev. Mol. Cell Biol.* **2008**, *9*, 532–542. [CrossRef] [PubMed]
114. Zaidi, S.; Hassan, M.I.; Islam, A.; Ahmad, F. The Role of Key Residues in Structure, Function, and Stability of Cytochrome-c. *Cell. Mol. Life Sci.* **2014**, *71*, 229–255. [CrossRef] [PubMed]
115. Kühlbrandt, W. Structure and Function of Mitochondrial Membrane Protein Complexes. *BMC Biol.* **2015**, *13*, 89. [CrossRef] [PubMed]
116. Eleftheriadis, T.; Pissas, G.; Liakopoulos, V.; Stefanidis, I. Cytochrome c as a Potentially Clinical Useful Marker of Mitochondrial and Cellular Damage. *Front. Immunol.* **2016**, *7*, 279. [CrossRef]
117. Cai, J.; Yang, J.; Jones, D.P. Mitochondrial Control of Apoptosis: The Role of Cytochrome c. *Biochim. Biophys. Acta* **1998**, *1366*, 139–149. [CrossRef]
118. Martínez-Fábregas, J.; Díaz-Moreno, I.; González-Arzola, K.; Díaz-Quintana, A.; De la Rosa, M.A. A Common Signalosome for Programmed Cell Death in Humans and Plants. *Cell Death Dis.* **2014**, *5*, e1314. [CrossRef]
119. Okada, M.; Smith, N.I.; Palonpon, A.F.; Endo, H.; Kawata, S.; Sodeoka, M.; Fujita, K. Label-Free Raman Observation of Cytochrome c Dynamics during Apoptosis. *Proc. Natl. Acad. Sci. USA* **2012**, *109*, 28–32. [CrossRef]
120. Salehi, H.; Middendorp, E.; Panayotov, I.; Collart Dutilleul, P.-Y.; Dutilleul, P.-Y.C.; Vegh, A.-G.; Ramakrishnan, S.; Gergely, C.; Cuisinier, F. Confocal Raman Data Analysis Enables Identifying Apoptosis of MCF-7 Cells Caused by Anticancer Drug Paclitaxel. *J. Biomed. Opt.* **2013**, *18*, 56010. [CrossRef]
121. Ichimura, T.; Chiu, L.; Fujita, K.; Kawata, S.; Watanabe, T.M.; Yanagida, T.; Fujita, H. Visualizing Cell State Transition Using Raman Spectroscopy. *PLoS ONE* **2014**, *9*, e84478. [CrossRef] [PubMed]

Received: 9 February 2022 | Revised: 17 June 2022 | Accepted: 5 July 2022
DOI: 10.1002/jrs.6423

RESEARCH ARTICLE

Journal of RAMAN SPECTROSCOPY WILEY

Modification of Keggin anion structure with ion beams—A new spectroscopic insights into the effects of keV- and MeV-ion beam irradiation on 12-tungstophosphoric acid

Željko Mravik[1] | **Danica Bajuk-Bogdanović**[2] | **Sonja Jovanović**[1] | **Jelena Rmuš**[1] | **Andrzej Olejniczak**[3,4] | **Ana Mraković**[5] | **Jasmina Lazarević**[6] | **Snežana Uskoković-Marković**[7] | **Nenad Lazarević**[6] | **Vladimir Skuratov**[3,8,9] | **Zoran Jovanović**[1]

[1]Center of Excellence for Hydrogen and Renewable Energy (CONVINCE), Laboratory of Physics, "Vinča" Institute of Nuclear Sciences - National Institute of the Republic of Serbia, University of Belgrade, Belgrade, Serbia

[2]Faculty of Physical Chemistry, University of Belgrade, Belgrade, Serbia

[3]Flerov Laboratory of Nuclear Reactions, Joint Institute for Nuclear Research, Dubna, Russia

[4]Faculty of Chemistry, Nicolaus Copernicus University, Toruń, Poland

[5]Laboratory of Atomic Physics, "Vinča" Institute of Nuclear Sciences - National Institute of the Republic of Serbia, University of Belgrade, Belgrade, Serbia

[6]Center for Solid State Physics and New Materials, Institute of Physics Belgrade, University of Belgrade, Belgrade, Serbia

[7]Faculty of Pharmacy, University of Belgrade, Belgrade, Serbia

[8]National Research Nuclear University MEPhI, Moscow, Russia

[9]Dubna State University, Dubna, Russia

Correspondence
Zoran Jovanović and Željko Mravik, Center of Excellence for Hydrogen and Renewable Energy (CONVINCE), Laboratory of Physics, "Vinča" Institute of Nuclear Sciences - National Institute of the Republic of Serbia, University of Belgrade, P.O. Box 522, Belgrade 11001, Serbia.
Email: zjovanovic@vinca.rs and mravik@vinca.rs

Funding information
Ministry of Education, Science and Technological Development of the Republic of Serbia

Abstract

Ion beam irradiation is a versatile tool for structural modification and engineering of new materials. In this study, 12-tungstophosphoric acid (WPA) films of different thickness were spin-coated on platinized silicon substrate and irradiated with low energy hydrogen ions (10 keV) and swift heavy ions (Bi, Xe, and V) with energies up to 710 MeV. The different energy/fluence combinations allowed controllable structural changes that were investigated in detail using Raman and Infrared spectroscopy. For 120-nm-thick WPA samples, the irradiation led to the decrease of intensity of the skeletal and W-O_c-W bands of Keggin anion in order: Bi < V < Xe (for their applied energy/fluence combination). Also, symmetry change of Keggin anion similar to the one observed in the case of Keggin anions interacting with the supports was observed. For the selected ion beam irradiation parameters, xenon ion beam induced transformation of WPA to polytungstate. For 20-μm-thick WPA samples, the irradiation with hydrogen ion beam induced changes of skeletal vibrations and increased individualistic behavior of Keggin anions. As the fluence increased, the amount of the Keggin anions partially transformed to bronze also increased. Irradiation with vanadium also caused transformation to bronze-like structure but with higher ratio of terminal W=O_d bonds. The overall results show clear correlation between degree of structural modification of WPA and the calculated displacement per atom value. These results open possibilities for engineering new catalytically active structures of polyoxometalates with the help of ion beams.

KEYWORDS
ion beam irradiation, polyoxometalates, polytungstates, spectroscopic study, structure

1 | INTRODUCTION

Heteropolyacids (HPAs) are commonly used as a homogenous or heterogeneous catalysts due to their high oxidizing ability, high acidity, and good thermal stability. In this regard, the structural modification of planar Keggin and Wells–Dawson acid type to their lacunar form yields different but usually extraordinary catalytic properties.[1] Because of this, the structural modification can be beneficial for the applicability of HPAs because even the overall assembly of anions in a bulk phase (particle size, pore structure, uniformity of composition) plays an important role in the applicability of these materials in catalysis.[2] Polyoxometalates (POMs) are also used for controlling of self-assembled nanoparticles where negative charge of POMs and their capability for irreversible adsorption on different materials plays an important role. Self-assembly of different alkylamines into three-dimensional nanoflowers was achieved by introduction of Weakley-type POMs where self-assembly occurs mainly though the hydrogen bond and electrostatic interaction between EuW_{10} POM and alkylamines. This is principally derived from amine groups of tetraethylenepentamine and oxygen atoms originating from EuW_{10}.[3] Well-dispersed self-assembled carbon nanotubes (CNTs) were prepared based on the spontaneous and strong chemisorption of POMs on the CNT surface thanks to the negatively charged POM monolayer.[4] These examples show that structure of POMs is crucial for obtaining properties that are preferable for different type of assembly.[5]

Transition from Keggin via Wells–Dawson to the lacunary form of HPAs is commonly achieved by modifying the solution pH.[6] Structural modification of HPAs is also carried out via incorporation of different transition metal atoms. Vanadium atoms are usually incorporated by different chemical processes yielding higher acidity[7] and higher proton conductivity.[8] The Raman spectroscopy investigation showed that intact Keggin anions are not crucial for the catalytic activity of HPAs but their structurally reorganized intermediates.[9] Thermal treatment can also be outlined as a simple and efficient method for structural modification of HPAs, where the increase of temperature initiates a dehydration process of Keggin anion yielding a "denuded" Keggin anion, solid–solid recrystallization to monophosphate bronze, and transformation to cubic bronze, at temperatures of 1150°C.[10] In our recent work, thermal treatment of 12-tungstophosphoric acid (WPA) and the effect of the interaction with the graphene oxide support were proven beneficial for the charge storage capacity of the nanocomposite.[11] Therein, the thermal treatment up to 500°C caused structural modification of Keggin anion, which was observed by splitting of characteristic infrared (IR) bands in WPA spectrum. Although these methods produce structurally modified HPAs, the appearance of interesting properties can be expected from the unique structures, which justifies the applications of novel methods for their structural modification.

Utilization of ion beams for structural modification of POMs is not widely available in the literature. In fact, as far we are aware, our recent work is the only one in this area.[12] Ion beam irradiation is commonly used for the modification of different crystals,[13,14] 2D materials,[15] steels,[16] glassy carbons,[17] and so on. At lower ion beam energies, the energy of incident ion is lost in collision cascades between nuclei where atomic displacement occurs as the main effect. At higher energies, electron–electron interactions cause the energy to be dissipated between electronic clouds causing local overheating (thermal spike) and fast formation of the ion tracks in the samples. Overall structural modification with ion beams represents the synergy of these effects. Also, the energy of ion beams dictates the modification range in the material where keV ions modify a few hundred nm of the sample, while MeV ions can penetrate through several tens of μm, which is why in this study, we used films of corresponding thicknesses.

Our recent work showed that fluence plays an important role in the modification of the Keggin structure, where the gradual transformation of HPA from partially modified to bronze-like structure was observed.[12] It is known in literature that different processes can cause hydration/dehydration modification of the structure of HPAs.[18] X-ray diffraction (XRD) analysis performed in our previous work showed that overnight exposure to vacuum did not change the structure of thin layers of

WPA (trihydrate form). In order to better correlate the relationship between parameters of ion beam irradiation and degree and type of structural modification of HPAs, in the present work, the influence of ion beam irradiation of different ion types, energies, and fluences on the individual bonds of Keggin anion as well as Keggin anion cage as a whole was investigated. Hence, the structure of pristine and irradiated WPA samples was monitored by observing changes of characteristic Raman bands, whereas changes in Keggin anion cage were observed through skeletal vibration bands. The Raman results were also accompanied by attenuated total reflectance-Fourier transform infrared (ATR-FTIR) spectroscopy, which also elucidated the type of modification caused by different ions. A clear correlation was found between damage calculated in Stopping and Range of Ions in Matter (SRIM) and spectroscopic results.

The presented results provide novel insights into structural transformations of POMs by ion beams, which may open new perspectives for the advanced application of this class of materials. Exact correlation between structure of POMs and the parameters of ion beam irradiation is of essence for obtaining the preferable structure with active cites for different catalytic reactions or for designing POMs with charge-structure properties that might be beneficial for control of nanoparticles self-assembly.

2 | MATERIALS AND METHODS

Thin films of WPA on a platinized silicon substrate (Si/Pt, 200-nm-thick Pt (111) layer on Si (001), resistivity of 1–10 Ω/cm) were obtained by the procedure as described in Mravik et al.[12] Si/Pt substrate was chosen because it did not show any overlapping Raman bands with WPA. Also, the Pt layer prevented spontaneous reduction of WPA on Si/SiO_2 to heteropolyblue. For 120-nm-thick samples, ethanol solution of WPA (50 mg/ml) was spin-coated onto the substrate up to desired thickness; 20-μm-thick samples were obtained by the drop-casting method from the same WPA ethanol solution.

The low energy irradiation (10 keV H^+) of WPA samples was performed at the Facility for Modification and Analysis of Materials with ion beams (FAMA) in the Laboratory of Physics at the Vinča Institute of Nuclear Sciences, Belgrade, Serbia.[19] A constant current of about 10 $\mu A/cm^2$ was used, and the samples were irradiated by scanning the 2-mm ion beam with 1 kHz. The ion beam current was measured in the proximity of the samples, thus providing accurate information about the fluence. The applied fluence was 5×10^{16} ions/cm^2 and 1×10^{17} ions/cm^2, marked through-out the text as hydrogen I and hydrogen II, respectively. The high energy irradiation (V 61 MeV, 1×10^{12} ions/cm^2 for 120-nm-thick WPA and 6×10^{12} ions/cm^2 for 20-μm-thick WPA; Xe 167 MeV, 3×10^{13} ions/cm^2; Bi 710 MeV, 1×10^{11} ions/cm^2) was performed at room temperature at the IC-100 and U-400 cyclotrons in the Flerov Laboratory of Nuclear Reactions of the Joint Institute for Nuclear Research, Dubna, Russia.

For the Raman scattering experiment, TriVista 557 spectrometer was utilized in the backscattering micro-Raman configuration with an 1800/1800/2400 grooves/mm diffraction grating combination. As an excitation source, coherent Ar^+/Kr^+ ion gas laser with a 514.5-nm line was used. Laser beam focusing was achieved through the microscope objective (Olympus) with 50× magnification. All spectra shown are corrected for the Bose factor $n(\Omega,T) = [\exp(\hbar\Omega/k_BT) - 1]^{-1}$.[20] The resolution of the spectrometer was around 1 cm^{-1}. In order to avoid the thermal effect of laser irradiation, the intensity of the laser was lowered (1 mW) during the measurement with prolonged exposure times (300 s per spectral region). The spectra were presented with relative axis for clarity, having in mind that it is very difficult to compare absolute values of spectral intensities measured at different samples due to the possibly high impact of the surface quality and/or nonideal focusing, in particular in micro setup.

ATR-FTIR spectra of pristine and irradiated samples were recorded at ambient conditions in the mid-IR region (450–3500 cm^{-1}) using a Nicolet IS 50 FT-IR Spectrometer operating in the ATR mode using a monolithic diamond crystal and a measuring resolution of 4 cm^{-1} with 32 scans.

Software package SRIM was used in order to obtain the disorder profile, depth distribution of ions, and displacement per atom for each sample-ion combination.[21] In detailed calculation with full damage cascades, different ions were implanted in 120-nm-thick/20-μm-thick WPA target with density 5.18 g/cm^3. Displacement energies that were assigned automatically by SRIM code to each atom are 10, 25, 25, and 28 eV for hydrogen, phosphorus, tungsten, and oxygen atoms, respectively.

3 | RESULTS

3.1 | Raman spectroscopy

Raman spectroscopy is a commonly used tool for monitoring structural changes in POMs caused by interactions with the support,[11] thermal treatment,[10] or decomposition in solutions.[22] The ability of precise structural probing comes from a fact that there is a direct impact of any

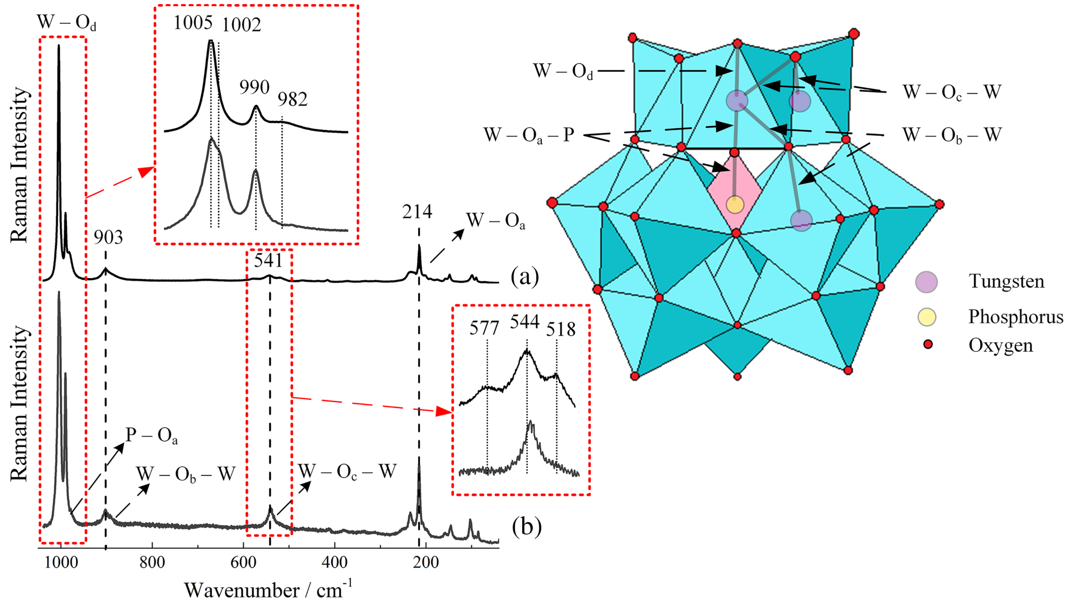

FIGURE 1 Raman spectrum of pristine 12-tungstophosphoric acid (WPA): (a) 20-μm-thick and (b) 120-nm-thick. Raman intensity of 120-nm-thick WPA spectrum was increased 10 times for clarity. On the right, a Keggin anion with characteristic bonds is presented. [Colour figure can be viewed at wileyonlinelibrary.com]

symmetry change on Raman spectra. In the structure of WPA, the specific interconnection of 12 WO_6 octahedrons around one central PO_4 tetrahedron yields four different types of oxygen (Figure 1). Central O_a oxygen serves as a bridge between P and W, O_b and O_c serve as a bridge between two W atoms in two different octahedrons, and O_d is terminal oxygen. The bands that are characteristic for Keggin anion can be observed in Raman spectrum of 20-μm-thick WPA shown in Figure 1a. The assignation of bands is quite straight-forward: 1005 and 990 cm^{-1} are assigned to symmetric and asymmetric W=O_d vibration, respectively, 982 cm^{-1} to stretching P-O_a vibration, 903 cm^{-1} to asymmetric stretching W-O_b-W vibration, 544 cm^{-1} to symmetric stretching W-O_c-W vibration, and the Raman band at 214 cm^{-1} is assigned to stretching W-O_a vibration.[11]

Closer inspection revealed that the interaction with the support influences these bands, which can be observed in Raman spectrum of 120-nm-thick WPA (Figure 1b). The inset part of Figure 1a shows in greater detail these changes: intensity ratio of symmetric and asymmetric W=O_d bands changes with decreasing thickness, whereas symmetric W=O_d band appears as a doublet with an additional shoulder at 1002 cm^{-1}. It is known that interactions of HPAs with the platinum[23] and zeolite[11] through terminal W=O_d bond change the position of its symmetric vibration. In the latter case, red shift of W=O_d bond indicates possible hydrogen bonding between terminal (O_d) oxygen of Keggin anion and hydrogen atoms of the support.[24] Higher loading of HPA resulted in unchanged W=O_d band thus suggesting the presence of two types of Keggin anions: ones strongly interacting with the support and with modified W=O_d vibration band and the others in bulk-like form interacting only with each other.[24,25] Most likely, this is the reason for the observed difference between Raman spectrum of 120-nm-thick and 20-μm-thick WPA presented here. The preservation of the Keggin structure for 20-μm-thick and 120-nm-thick films is indicated by the absence of shift of P-O_a, W-O_b-W, and W-O_a bands (Figure 1a,b). On the other hand, the W-O_c-W band at 541 cm^{-1} appears as a triplet in the spectrum of 20-μm-thick WPA, whereas this splitting is not evident at lower thickness (inset of Figure 1b). The difference in the W-O_c-W band between bulk and low thickness samples suggests that interactions between individual Keggin anions and also hydronium ions in bulk-like material have stronger influence on the modification of the Keggin anion cage. In the case of 120-nm-thick WPA sample, the degree of interconnection between individual Keggin anions is significantly reduced, and the interaction with the support is carried via the W=O_d bond, which is why there is no observable shift in the bridging W-O-W bonds in its spectrum (Figure 1b).

In order to better comprehend the effects of the ion beam irradiation on Keggin anion structure, the Raman spectra were analyzed region by region, and the impact on each Raman band is discussed. Regions are defined by the position of characteristic bands of Keggin anion, as well as by the position of Raman bands modified by ion beams and are as follows: region I from 0 to 400 cm^{-1}, region II from 400 to 600 cm^{-1}, region III from 600 to 1000 cm^{-1} (only for 20-μm-thick WPA), and region IV from 960 to 1030 cm^{-1}. Additionally, Raman spectra of irradiated samples were compared with the spectra of 20-μm-thick WPA thermally treated at 600°C to better understand the mechanism of structural modification, because the effects of thermal treatment on POMs structure are thoroughly investigated in literature.

Figure 2 shows region I of irradiated 120-nm-thick (left) and 20-μm-thick WPA (right) as well as 20-μm-thick WPA thermally treated at 600°C for comparison. As previously stated, in this region, band at 217 cm^{-1} is commonly assigned to stretching W-O$_a$ vibration, but the assignation of other bands remains scarce. Low wavenumber of these bands, as well as the theoretical approach in the work of Bridgeman,[26] suggests that these bands represent skeletal vibrations of Keggin anion cage.

After irradiation of 120-nm-thick WPA, a decrease of intensity of all the bands in region I can be observed (Figure 2, left). The lowest decrease is observed for 710-MeV bismuth ions, followed by 61-MeV vanadium ions, whereas for 167-MeV xenon, the complete disappearance of bands is observed. As these bands are assigned to skeletal vibrations of the entire Keggin anion, it can be concluded that for the 120-nm-thick samples, the influence on structural modification goes in the order Bi < V < Xe (for their applied energy/fluence combination).

Spectra of irradiated 20-μm-thick WPA show not only the decrease of intensity of Keggin anion skeletal vibrations but also the appearance of new wide bands (Figure 2, right). In the case of hydrogen irradiated samples, Keggin anion bands are preserved but with lower intensity. Also, a change in intensity ratio and line-shape of bands at 235 and 214 cm^{-1} can be observed. Additionally, bands at 100 and 90 cm^{-1} are further apart at 103 and 85 cm^{-1}, indicating modification of Keggin anion cage. If we compare the line-shapes and wavenumbers of Keggin anion preserved bands (235, 214, 103, and 85 cm^{-1}) in the spectrum of hydrogen irradiated 20-μm-thick WPA with the same bands in the spectrum of unirradiated 120-nm-thick WPA, some similarities can be observed (the intensity ratio between 214 and 235 cm^{-1} band is similar to the 120-nm-thick sample) suggesting that the irradiation cased reduction of intermolecular interactions of the same origin as those in thin film. The sample irradiated with hydrogen ions at 1×10^{17} ions/cm^2 (hydrogen II) and the sample irradiated with vanadium ions (Figure 2, right) show two wide bands from 400 to 150 cm^{-1} and from 150 to 50 cm^{-1}. These bands are comparable with those observed in Raman spectrum of 20-μm-thick WPA thermally treated at 600°C, which will be discussed later together with SRIM results.

Figure 3 shows region II of irradiated 120-nm-thick (left) and 20-μm-thick WPA (right), as well as 20-μm-thick WPA thermally treated at 600°C for comparison. In this region, W-O$_c$-W vibration is observed as a single band in the spectrum of 120-nm-thick WPA and as a triplet in the spectrum of 20-μm-thick WPA. Two additional bands are observed in the spectrum of 20-μm-thick WPA (471 and 416 cm^{-1}) and one low intensity band in the spectrum of 120-nm-thick WPA (412 cm^{-1}) that can likely be assigned to the coupling between different W-O-W vibrations.[26]

After irradiation of 120-nm-thick WPA (Figure 3, left), the intensity of W-O$_c$-W band decreases in the same order as for the skeletal vibrations in region I (Figure 2). This implies that ion beam irradiation causes structural changes on the entire Keggin anion cage leading to changes in bands of individual W-O-W bonds.

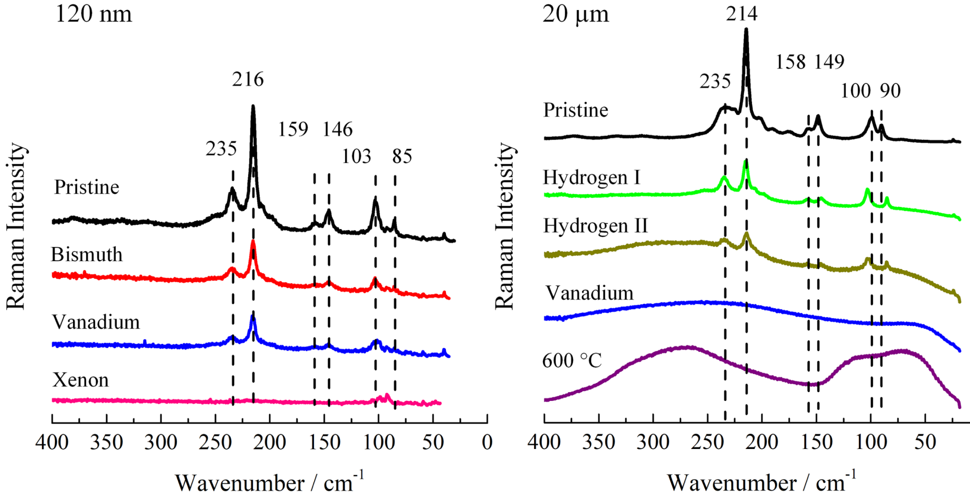

FIGURE 2 Region I of pristine and irradiated 120-nm-thick 12-tungstophosphoric acid (WPA) (left), pristine and irradiated 20-μm-thick WPA (right), and as well 20-μm-thick WPA thermally treated at 600°C [Colour figure can be viewed at wileyonlinelibrary.com]

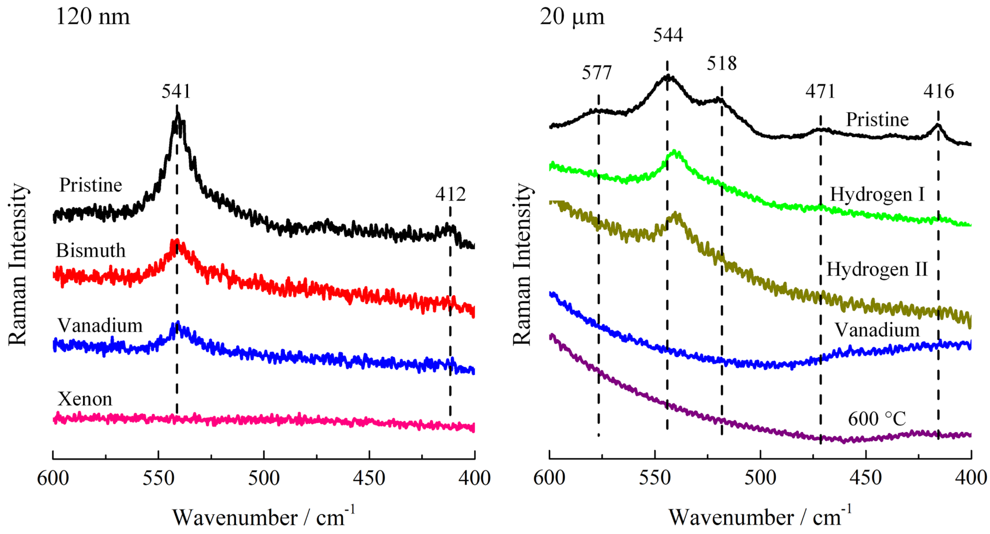

FIGURE 3 Region II of pristine and irradiated 120-nm-thick 12-tungstophosphoric acid (WPA) (left), pristine and irradiated 20-µm-thick WPA (right), and 20-µm-thick WPA thermally treated at 600°C [Colour figure can be viewed at wileyonlinelibrary.com]

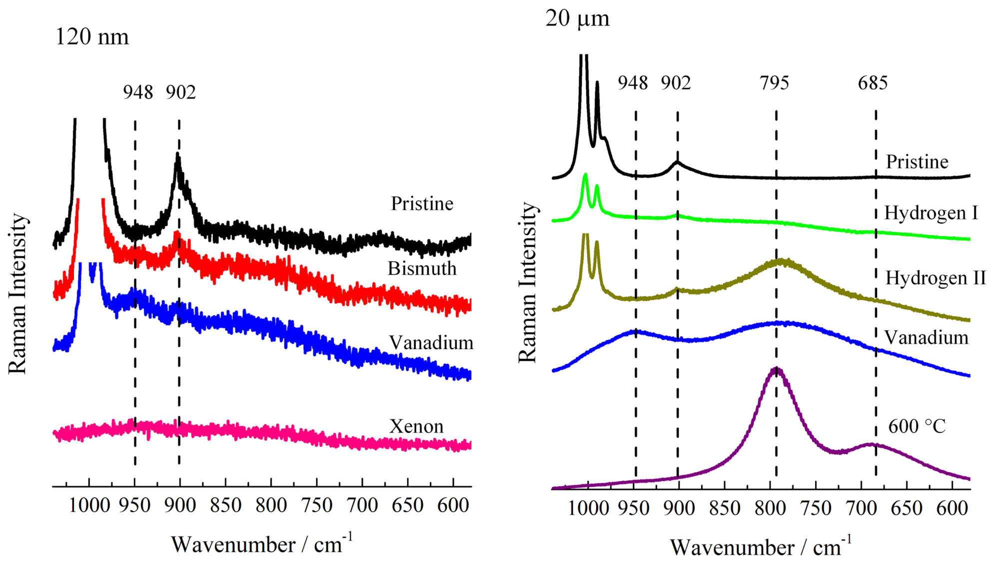

FIGURE 4 Region III of pristine and irradiated 120-nm-thick 12-tungstophosphoric acid (WPA) (left), pristine and irradiated 20-µm-thick WPA (right), and 20-µm-thick WPA thermally treated at 600°C [Colour figure can be viewed at wileyonlinelibrary.com]

Irradiation has even stronger influence on 20-µm-thick WPA films. In the case of samples irradiated with hydrogen ions (Figure 3, right), the triplet form of W-O_c-W vibration is lost, while the main component is shifted to 540 cm^{-1}. This change again demonstrates the modification of Keggin anion cage with irradiation. Furthermore, the similarities of the bands of hydrogen irradiated 20-µm-thick WPA (Figure 3, right) with the band of 120-nm-thick WPA (Figure 3, left) could suggest there is a decrease in interactions between individual Keggin anions, which is why they are acting independently from their surrounding as in thin films. Based on these results, it can be established that the components of the triplet band at 577 and 518 cm^{-1} of 20-µm-thick WPA probably originate from the different forms of interactions between Keggin anions and hydronium ions in the bulk state of WPA, that is, from the secondary structure interactions that, to some extent, modify Keggin anion cage. Additionally, bands at 471 and 416 cm^{-1} observed in spectrum of 20-µm-thick WPA (Figure 3, right) disappear after irradiation. This spectral region of the sample irradiated with hydrogen ions at 1×10^{17} ions/cm^2 (hydrogen II) as well as sample irradiated with vanadium ions also shows similarities with the bands of 20 µm-thick WPA thermally treated at 600°C.

Figure 4 shows region IV of Raman spectra of irradiated 120-nm-thick (left) and 20-µm-thick WPA (right), as well as 20-µm-thick WPA thermally treated at 600°C for comparison. In this part of spectra, W-O_b-W vibration at around 902 cm^{-1} is present in spectra of pristine 120-nm- and 20-µm-thick WPA. After irradiation of 120-nm-thick samples, the intensity of this band decreases while also an additional band can be noticed at 948 cm^{-1}. In the samples of 20-µm-thick WPA irradiated with hydrogen ions, the band of Keggin anion at 902 cm^{-1} can be noticed but with decreased Raman intensity. As opposed to the W-

O_c-W vibration (Figure 3, right), the W-O_b-W vibration remains at the same position after irradiation with no significant change in line-shape. This can be explained by the position of these bonds in Keggin anion where the W-O_b-W bond connects two octahedrons that are part of the sphere and are attached by each other only with one oxygen atom, while the W-O_c-W bond connects the two octahedrons that are part of the "cap" of Keggin anion and share two oxygen atoms (Figure 1). For that reason, the W-O_c-W bond is probably more exposed to the influence of the interaction in bulk state and with the environment and consequently more susceptible to the change.

In Raman spectrum of the sample irradiated with hydrogen ions at 1×10^{17} ions/cm^2 (hydrogen II), as well as the sample irradiated with vanadium ions, new wide bands are observed with higher intensity and certain differences (Figure 4, right). Samples irradiated with hydrogen ions show a band at 795 cm^{-1} and a lower intensity band at 695 cm^{-1} corresponding to the bands of 20-μm-thick WPA thermally treated at 600°C. These bands and those observed in Region I and II (Figures 2 and 3) are characteristic of phosphate tungsten bronzes commonly synthesized by thermal treatment of HPAs at higher temperatures, which yield structures of interconnected WO_6 octahedrons and PO_4 tetrahedrons.[10,27] Alternatively, the bands at 695 and 795 cm^{-1} can be attributed to poorly crystallized tetragonal WO_3 or WO_3 $1/3H_2O$.[28]

Raman spectrum of vanadium irradiated 20-μm-thick WPA shows a band at 795 cm^{-1} and a new band at 948 cm^{-1}, whereas the band at 695 cm^{-1} cannot be observed (Figure 4, right). The new band at 948 cm^{-1} is at a position where W=O_d vibration commonly resides, indicating that with vanadium irradiation, besides interconnection of bonds (evidenced by the band of phosphate tungsten bronze at 795 cm^{-1}), there are still certain number of the terminal W=O_d bonds that are not connected with other tungsten atoms. This is also noticed with 120-nm-thick sample irradiated with bismuth and vanadium but with band at 948 cm^{-1} of much lower intensity. The results show that hydrogen irradiation is more capable of transformation of Keggin structure into the bronze structure than vanadium irradiation at given experimental conditions.

Figure 5 shows region IV of irradiated 120-nm-thick (left) and 20-μm-thick WPA (right) as well as 20-μm-thick WPA thermally treated at 600°C for comparison. Symmetric and asymmetric vibrations of W=O_d are observed in this region, while the shoulder at 982 cm^{-1} assigned to P-O_a vibration is only observed in the spectrum of 20 μm-thick WPA. Raman spectra of 120-nm-thick WPA irradiated with bismuth, vanadium, and xenon ions show bands of W=O_d vibration with decreasing intensity in previously observed order (Bi < V < Xe, for their applied energy/fluence combination) (Figure 5, left). Additionally, band splitting originating from the symmetry change that is usual for the interaction with the support is more pronounced in irradiated samples with the wavenumbers of 1006 and 1001 cm^{-1} as opposite to the 1004 and 1002 cm^{-1} for pristine sample.

Region IV of Raman spectrum of hydrogen irradiated 20-μm-thick WPA shows W=O_d vibration with reduced Raman intensity (Figure 5, right). A symmetric vibration band at 1005 cm^{-1} has also shifted to 1002 cm^{-1}, which is comparable with the part of the doublet band of 120-nm-thick WPA, once again demonstrating the changed symmetry of the Keggin anions after irradiation. No bands of Keggin anion were found in this region of spectrum of vanadium irradiated sample.

3.2 | ATR-FTIR spectroscopy

In order to furthermore elucidate the influence of ion beam irradiation on the structure of WPA, the ATR-FTIR

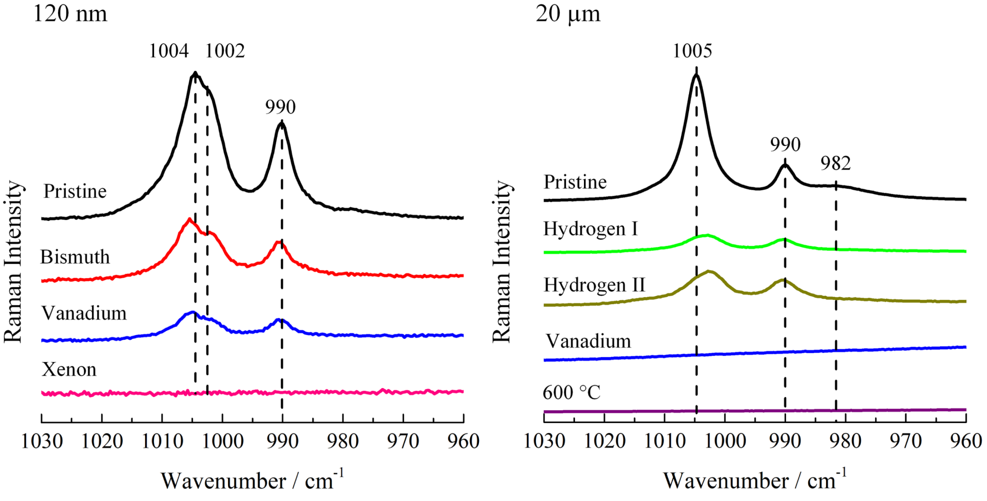

FIGURE 5 Region IV of pristine and irradiated 120-nm-thick 12-tungstophosphoric acid (WPA) (left), pristine and irradiated 20-μm-thick WPA (right), and as well 20-μm-thick WPA thermally treated at 600°C [Colour figure can be viewed at wileyonlinelibrary.com]

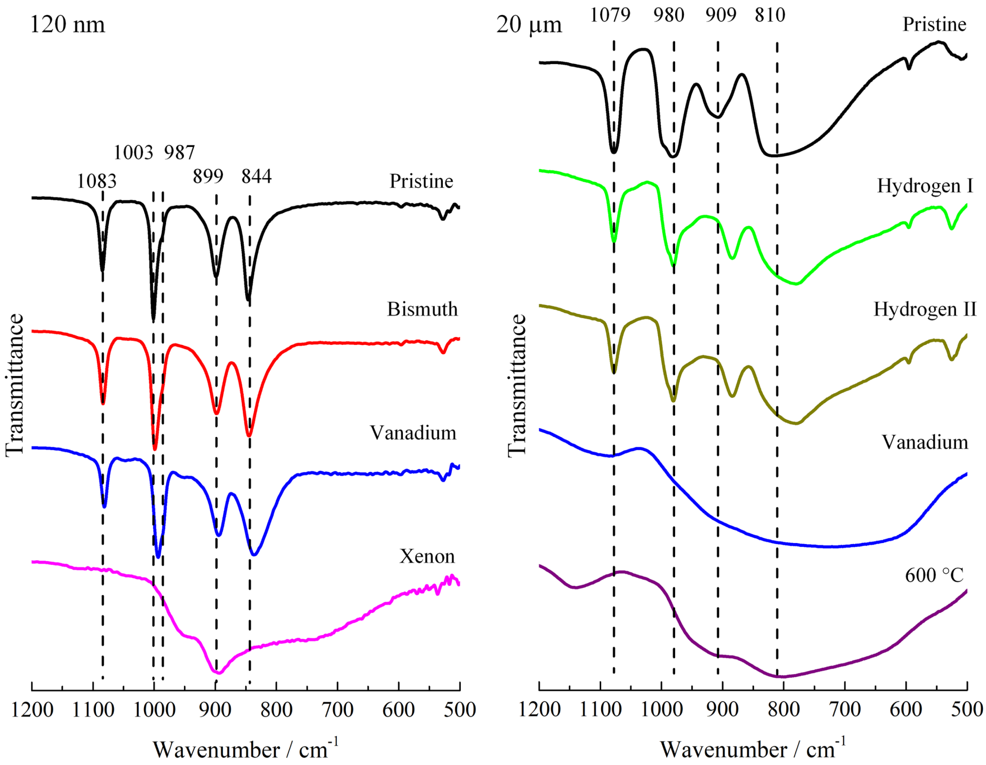

FIGURE 6 Attenuated total reflectance-Fourier transform infrared (ATR-FTIR) spectra of pristine and irradiated 120-nm-thick 12-tungstophosphoric acid (WPA) (left), pristine and irradiated 20-μm-thick WPA (right), and as well 20-μm-thick WPA thermally treated at 600°C [Colour figure can be viewed at wileyonlinelibrary.com]

spectra of pristine and irradiated samples were recorded (Figure 6). In IR spectra, the Keggin anion also exhibits characteristic bands that are in the case of 120-nm-thick WPA assigned as follows: Band at 1083 cm^{-1} is assigned to asymmetric P-O$_a$ vibration, band at 1003 with the shoulder at 987 cm^{-1} is assigned to asymmetric W=O$_d$ vibration, band at 899 cm^{-1} to asymmetric W-O$_b$-W vibration, and band at 844 cm^{-1} is assigned to asymmetric W-O$_c$-W vibration.[11] These bands in ATR-FTIR spectra of 20-μm-thick WPA are also observed at 1079, 980, 909, and 810 cm^{-1}, respectively.

Same as for the Raman band of W=O$_d$ vibration, the IR band is also influenced by interaction with the support. Bajuk-Bogdanović et al. noticed splitting of the W=O$_d$ vibration band in WPA supported on zeolite, while in the Bielanski and Lubanska's work, the W=O$_d$ vibration band was shifted to higher wavenumbers due to the existence of O$_d$ atom included in hydrogen bond.[11,29] In our case for 120-nm-thick WPA, the splitting is even more pronounced, with the higher wavenumber component being more intensive, thus showing that the large portion of the Keggin anion in 120-nm-thick layer interacts with the support.

ATR-FTIR spectra of irradiated 120-nm-thick WPA (Figure 6, left) showed changes in IR bands of Keggin anion that are more subtle for samples irradiated with bismuth and vanadium ions but are drastic for xenon irradiated sample. It can be observed that the degree of the modification follows the same trend as observed in Raman spectra: Bi < V < Xe (for their applied energy/fluence combination). Even though Raman spectra suggested complete destruction of the structure in xenon irradiated 120-nm-thick WPA, ATR-FTIR spectra of this sample showed new wide bands that cannot be compared with bands of thermally treated WPA. The difference between Raman and FTIR results arises from higher sensitivity of Raman bands to symmetry change of Keggin anion, which is also observed in our previous work.[12] In the Davantès et al. work a density functional theory (DFT) study of polytungstate species, $W_7O_{24}{}^{6-}$, revealed a IR spectrum similar to the one of xenon irradiated 120 nm-thick WPA, from which it can be concluded that xenon irradiation causes partial interconnection of tungstate species.[30] The degree of tungstate interconnection in irradiated sample is lower than in the bronze structures, which is seen by the absence of the band at 1150 cm^{-1} that is observed in spectra of bronze and overall different shape of wide IR bands (Figure 6, right).

ATR-FTIR spectra of pristine 120-nm-thick WPA where proton species can be identified showed a band and shoulder at 3275 and 3209 cm^{-1}, respectively (Figure S1, left, Supporting Information). Both the band and the shoulder can be assigned to the stretching O-H vibration.[31] Noise from the ATR crystal can also be observed in the range from 2000 to 2500 cm^{-1}, 3500 to 4000 cm^{-1}, and around 2900 cm^{-1}. With irradiation, intensity of the main band at 3275 cm^{-1} decreases while the observed shoulder becomes dominant (Figure S1, left, Supporting Information) following the already observed trend: Bi < V < Xe (for their applied energy/fluence combination). This can be associated with partial dehydration of the samples after irradiation.[31]

ATR-FTIR spectra of irradiated 20-μm-thick WPA (Figure 6, right) also highlights structural modification of WPA with irradiation. Hydrogen irradiated samples showed subtle changes in IR spectra, which are reflected in widening of bands and slight band shift. Vanadium irradiated 20-μm-thick WPA, on the other hand, shows significant changes in ATR-FTIR spectra that reflect in the appearance of wide bands. The spectra resemble the one of thermally treated WPA; however, band positions are changed so it can be said that the structure of phosphate tungsten bronzes is not achieved with irradiation. Similar results were observed in our previous work where carbon ion irradiation caused formation of bronze-like structure where increased interconnection was observed with ultraviolet–visible (UV–vis) method.[12] Bands of O-H vibrations were noticed in the spectra of 20-μm-thick WPA at 3191 and shoulder at 3030 cm^{-1} (Figure S1, right, Supporting Information). In the case of keV-energy H-ion irradiation, it can be noticed that the shoulder is wider and more pronounced compared with pristine sample. In our opinion, this is due to composite ATR-FTIR signal containing information both from modified (hundreds of nm) and non-modified, that is, pristine sample. In the case of sample irradiated with vanadium ions, a modification of significant volume of the layer was achieved, and the obtained spectrum is similar to the one obtained after thermal treatment at 600°C. This is indication of complete dehydration, most likely beyond denuded Keggin anion and toward bronzes.[10,11] A much better information on the proton species could be obtained using the transmission technique in fluorolube.[32] However, it should be noted that in the present study, the nature of the samples limited investigation only to the ATR technique. Our future studies will try to address this aspect in more detail.

3.3 | SRIM calculations

In order to get insight into ion ranges, ionization power of the used ions, and to explain the experimentally observed changes, the SRIM calculations were performed. The results showed that all of the used ions have dominant electronic energy loss in the irradiated part of the samples. We have chosen the DPA values, because they are often used in the literature when comparison of different energy loss/dose combinations is necessary; however, one should not ignore the contribution of electronic energy loss to the structural modification. The most of the damage induced by swift heavy ions originates from the electronic energy loss. At the same time, the SRIM calculations show that for the hydrogen, the electronic energy loss is dominant, but most probably, the thermal effects caused by it are not sufficient to generate the observed structural changes; that is, nuclear energy loss is a key contributor. In the case of 120-nm-thick WPA, the damage is mainly due to the electronic energy loss, while both electronic and nuclear energy losses are contributing to damage formation in 20-μm-thick WPA. Because of this, it would be interesting to perform Raman depth profile analysis of thicker samples in the future experiments.

In the case of 120-nm-thick WPA, calculations show that ion ranges far exceed the thickness of the sample. The total number of displacements per atom (DPAs) calculated as total number of vacancies divided by total number of atoms in the irradiated layer was used to quantify the total damage induced by the irradiation of the samples (Table S1, Supporting information).[33] It can be concluded that bismuth ions, even though the most energetic, induced the least damage due to low fluence. If we look at DPA induced by bismuth irradiation, it is shown that only half of the atoms are affected. This is in line with the results of Raman spectroscopy that showed lower intensity of bands of Keggin anion after bismuth irradiation while also ATR-FTIR spectroscopy confirmed preservation of the structure.

In the case of vanadium irradiated 120-nm-thick WPA, calculations showed that the total number of affected atoms is almost the same as the total number of atoms in the irradiated layer. Raman spectra of this sample indeed showed higher degree of modification than for the bismuth irradiated samples. Even though all of the atoms should be displaced, some number of Keggin anions are preserved, probably due to the statistical nature of the irradiation process because some atoms could be displaced several times and some none. This is proven with xenon irradiated samples where Raman spectra showed complete amorphization of the samples, while also SRIM calculations showed that all of the atoms are displaced more than 100 times, resulting in the rearranging of the structure. Similarity of ATR-FTIR spectra of xenon irradiated sample (Figure 6) with spectra of polytungstate species confirms rearranging of the structure.[30]

Hydrogen and vanadium ions that are used for irradiation of 20-μm-thick WPA are also included in SRIM calculations. It is shown that the ion range of hydrogen ions does not exceed 300 nm, whereas the penetration depth of vanadium ions is around 12 μm (Figure S2, Supporting information).

Table S1 (Supporting information) also shows parameters for irradiation of 20-μm-thick WPA where it can be concluded that hydrogen ions cause large number of atom displacement in the irradiated part of the sample with 6600 and 13 200 times for lower and higher fluence, respectively. On the other hand, vanadium ions that irradiate a much thicker part of the sample cause 74 times more vacancies than the total number of atoms in the layer. This casts a new light on Raman results, where hydrogen irradiated 20-μm-thick WPA showed preservation of Keggin anions as well as very close resemblance to the spectrum of phosphate tungsten bronze (Figure 4). The sampling depth of the Raman method is a few μm, whereas the penetration depth of hydrogen ion is around 300 nm because of which part of Raman bands of Keggin anion originate from unirradiated part of the sample. A large number of atom rearrangement induced with hydrogen ions clearly cause reorganization of the structure into a bronze-like structure, but low penetration depth of ions (300 nm) caused that only small ratio of the sample is modified because of which changes observed for lower fluence of hydrogen irradiation are modest. On the other hand, smaller displacement induced with vanadium ions was not enough for structural reorganization, which is evident from Raman spectra of this sample that showed the presence of terminal $W{=}O_d$ bands and no bands of phosphate tungsten bronzes (Figure 4). Additionally, the absence of structural reorganization in this sample can originate from the difference of depth of the probed and irradiated part of the sample. If we look at the first 2 μm of the sample (the part that is analyzed with Raman spectroscopy), SRIM calculations show that DPA value is around 30. This is twice lower than the in initial calculations (Table S1) but still remains at the same ratio compared with other ions (less than in the case of xenon and hydrogen irradiation but still induces more damage than in other cases), proving once again the validity of the results.

4 | CONCLUSIONS

In this work, 120-nm-thick and 20-μm-thick WPA films were irradiated with ion beams of different energies and fluences in order to better comprehend the influence of ion beams on the Keggin anion structure. This is important due to the non-thermodynamic nature of ion beam interaction with matter where deposited energy can alter the material in different ways as opposed to the standard methods of modification (chemical treatment, thermal treatment, etc.). Raman spectra of pristine 20-μm-thick and 120-nm-thick WPA revealed different symmetry of Keggin anion due to its interactions in bulk and its interactions with the support. For irradiated 120-nm-thick WPA, Raman spectra showed structural modification in order Bi < V < Xe (for their applied energy/fluence combination). This was in line with DPA values obtained in SRIM calculations. ATR-FTIR spectra of 120-nm-thick samples revealed similarities of xenon irradiated samples with polytungstate species, which demonstrates there is partial recombination but insufficient to obtain stoichiometric phosphate tungsten bronze. For irradiated 20-μm-thick WPA samples, changes in Raman and ATR-FTIR spectra also follow predictions of SRIM calculations, where hydrogen irradiation caused high DPA values, which resulted in the appearance of bands that very much resemble bands of phosphate tungsten bronzes. The low intensity of these bands and preservation of bands of Keggin anion for these samples is explained by the low thickness of the irradiated layer compared with the sampling depth of Raman analysis. Modification of the 20-μm-thick WPA sample was also achieved with vanadium ions, but Raman analysis showed lower similarity of this sample with phosphate tungsten bronze, which is a consequence of lower DPA values.

Observed forms of structural modification and rearrangement of WPA structure can be beneficial for application of the material in catalysis where the engineered structures can produce additional active sites for different reactions. This work can serve as foundation for the future research where the relation between parameters of ion beams and the structural modification can be crucial for future experimental design. Application of versatile ion beams with different energies and penetration depths to large area targets is already being used in semi-industrial and industrial scale (for example, wafers up to 10 inches and more). We believe that similar approaches can be applied and further developed in the case of ion beam irradiation of POMs.

ACKNOWLEDGEMENT

The research was financially supported by the Ministry of Education, Science and Technological Development (MoESTD) of the Republic of Serbia, and part of it was realized in the framework of MoESTD–Joint Institute for Nuclear Research collaboration.

DATA AVAILABILITY STATEMENT

The data that support the findings of this study are available from the corresponding author upon reasonable request.

ORCID

Željko Mravik https://orcid.org/0000-0003-2327-5165
Danica Bajuk-Bogdanović https://orcid.org/0000-0003-2443-376X
Sonja Jovanović https://orcid.org/0000-0003-3577-5060
Ana Mraković https://orcid.org/0000-0003-4569-5857

Snežana Uskoković-Marković https://orcid.org/0000-0003-2750-325X
Vladimir Skuratov https://orcid.org/0000-0002-9016-8370
Zoran Jovanović https://orcid.org/0000-0003-1727-4852

REFERENCES

[1] M. A. Hanif, S. Nisar, U. Rashid, *Catal. Rev.: Sci. Eng.* **2017**, *59*, 165.
[2] C. Jahier, R. Touzani, S. el Kadiri, S. Nlate, *Inorg. Chim. Acta* **2016**, *450*, 81.
[3] C. Xia, Z. Wang, D. Sun, B. Jiang, X. Xin, *Langmuir* **2017**, *33*, 13242.
[4] X. Li, Q. Zhu, S. Tong, W. Wang, W. Song, *Sens. Actuators, B* **2009**, *136*, 444.
[5] Y. Gao, M. Choudhari, G. K. Such, C. Ritchie, *Chem. Sci.* **2022**, *13*, 2510.
[6] I. Holclajtner-Antunović, D. Bajuk-Bogdanović, M. Todorović, U. B. Mioč, J. Zakrzewska, S. Uskoković-Marković, *Can. J. Chem.* **2008**, *86*, 996.
[7] D.-J. Yuan, J. Yang, A. M. Hengne, Y.-T. Lin, C.-Y. Mou, K.-W. Huang, *J. Saudi Chem. Soc.* **2020**, *24*, 1.
[8] X. Wu, Q. Wu, *Mater. Lett.* **2021**, *302*, 130372.
[9] G. Mestl, T. Ilkenhans, D. Spielbauer, M. Dieterle, O. Timpe, J. Kröhnert, F. Jentoft, H. Knözinger, R. Schlögl, *Appl. Catal., A* **2001**, *210*, 13.
[10] U. Mioč, R. Z. Dimitrijevic, M. Davidovic, Z. P. Nedic, M. Mitrovic, P. Colomban, *J. Mater. Sci.* **1994**, *29*, 3705.
[11] Z. Jovanović, I. Holclajtner-Antunović, D. Bajuk-Bogdanović, S. Jovanović, Ž. Mravik, M. Vujković, *Electrochem. Commun.* **2017**, *83*, 36.
[12] Ž. Mravik, D. Bajuk-Bogdanović, A. Mraković, L. Vukosavljević, I. Trajić, J. Kovač, D. Peruško, N. Gavrilov, Z. Jovanović, *Radiat. Phys. Chem.* **2021**, *183*, 109422.
[13] F. X. Zhang, G. Velisa, H. Xue, N. Sellami, C. Trautmann, Y. Zhang, W. J. Weber, *J. Phys.: Condens. Matter* **2021**, *33*, 185402.
[14] M. Gloginjić, M. Erich, M. Kokkoris, E. Liarokapis, S. Fazinić, M. Karlušić, K. Tomić Luketić, S. Petrović, *J. Nucl. Mater.* **2021**, *555*, 153143.
[15] Z. Li, F. Chen, *Appl. Phys. Rev.* **2017**, *4*, 011103.
[16] X. Liu, Y. Miao, M. Li, M. A. Kirk, S. A. Maloy, J. F. Stubbins, *J. Nucl. Mater.* **2017**, *490*, 305.
[17] M. Y. A. Ismail, Z. A. Y. Abdalla, E. G. Njoroge, O. S. Odutemowo, T. T. Hlatshwayo, E. Wendler, V. A. Skuratov, J. B. Malherbe, *Nucl. Instrum. Methods Phys. Res., Sect. B* **2021**, *489*, 11.
[18] A. Kremenović, A. Spasojević-de Biré, R. Dimitrijević, P. Sciau, U. B. Mioč, P. Colomban, *Solid State Ionics* **2000**, *132*, 39.
[19] N. Nešković In Proceedings of the III Advanced Ceramics and Applications Conference; Springer: **2016**, p 59.
[20] N. Lazarević, R. Hackl, *J. Phys.: Condens. Matter* **2020**, *32*, 413001.
[21] J. F. Ziegler, M. D. Ziegler, J. P. Biersack, *Nucl. Instrum. Methods Phys. Res., Sect. B* **1818**, *2010*, 268.
[22] D. Bajuk-Bogdanović, S. Uskoković-Marković, R. Hercigonja, A. Popa, I. Holclajtner-Antunović, *Spectrochim. Acta, Part A* **2016**, *153*, 152.
[23] P. J. Kulesza, M. Chojak, K. Karnicka, K. Miecznikowski, B. Palys, A. Lewera, A. Wieckowski, *Chem. Mater.* **2004**, *16*, 4128.
[24] D. Bajuk-Bogdanović, A. Jović, B. Nedić Vasiljević, M. Milojević-Rakić, M. Kragović, D. Krajišnik, I. Holclajtner-Antunović, V. Dondur, *Mater. Sci. Eng., B* **2017**, *225*, 60.
[25] K. Pamin, A. Kubacka, Z. Olejniczak, J. Haber, B. Sulikowski, *Appl. Catal., A* **2000**, *194-195*, 137.
[26] A. J. Bridgeman, *Chem. Phys.* **2003**, *287*, 55.
[27] M. Greenblatt, *Acc. Chem. Res.* **1996**, *29*, 219.
[28] S. Loridant, C. Feche, N. Essayem, F. Figueras, *J. Phys. Chem. B* **2005**, *109*, 5631.
[29] A. Bielański, A. Lubańska, *J. Mol. Catal. A: Chem.* **2004**, *224*, 179.
[30] A. Davantès, D. Costa, G. Lefèvre, *J. Phys. Chem. C* **2015**, *119*, 12356.
[31] N. Essayem, A. Holmqvist, P. Y. Gayraud, J. C. Vedrine, Y. Ben Taarit, *J. Catal.* **2001**, *197*, 273.
[32] U. B. Mioč, M. R. Todorović, P. Colomban, Z. P. Nedić, S. M. Uskoković, I. D. Borčić, *Solid State Ionics* **1999**, *125*, 425.
[33] R. M. Hengstler-Eger, P. Baldo, L. Beck, J. Dorner, K. Ertl, P. B. Hoffmann, C. Hugenschmidt, M. A. Kirk, W. Petry, P. Pikart, A. Rempel, *J. Nucl. Mater.* **2012**, *423*, 170.

SUPPORTING INFORMATION

Additional supporting information can be found online in the Supporting Information section at the end of this article.

How to cite this article: Ž. Mravik, D. Bajuk-Bogdanović, S. Jovanović, J. Rmuš, A. Olejniczak, A. Mraković, J. Lazarević, S. Uskoković-Marković, N. Lazarević, V. Skuratov, Z. Jovanović, *J Raman Spectrosc* **2022**, *53*(11), 1974. https://doi.org/10.1002/jrs.6423

PHYSICAL CHEMISTRY 2024

17th International Conference on Fundamental and Applied Aspects of Physical Chemistry

Organized by

The Society of Physical Chemists of Serbia

in co-operation with

Institute of Catalysis, Bulgarian Academy of Sciences

and

Boreskov Institute of Catalysis, Siberian Branch of Russian Academy of Sciences

and

University of Belgrade, Serbia:

Faculty of Physical Chemistry
Institute of Chemistry, Technology and Metallurgy
Vinča Institute of Nuclear Sciences
Faculty of Pharmacy

and

Institute of General and Physical Chemistry, Belgrade, Serbia

International Organizing Committee

Chairman: S. Anić (Serbia)
Vice-chairman: Z. Petkova Cherkezova-Zheleva (Bulgaria)
Oleg N. Martyanov (Russia)
S. N. Blagojević (Serbia)
Members: N. Cvjetićanin (Serbia), S. M. Blagojević (Serbia), M. Daković (Serbia), J. Dimitrić-Marković (Serbia), T. Grozdić (Serbia), Lj. Ignjatović (Serbia), A. Ivanović-Šašić (Serbia), D. Jovanović (Serbia), N. Jović-Jovičić (Serbia), M. Kuzmanović (Serbia), S. Maćešić (Serbia), D. Marković (Serbia), B. Milosavljević (USA), M. Mojović (Serbia), N. Pejić (Serbia), M. Petković (Serbia), A. Popović Bijelić (Serbia), B. Simonović (Serbia), B. Šljukić (Serbia), G. Tasić (Serbia), S. Veličković (Serbia), N. Vukelić (Serbia)

International Scientific Committee

Chairman: Ž. Čupić (Serbia)
Vice-chairman: V. Bukhtiyarov (Russia)
S. Minkovska-Dodova (Bulgaria)
B. Adnađević (Serbia)
Members: S. Anić (Serbia), A. Antić-Jovanović (Serbia), A. Clayton (Australia), P. Banković (Serbia), M. Fronczak (Poland), Lj. Gavrilovic (Norway), M. Jeremić (Serbia), E. Kiš (Serbia), A.V. Knyazev (Russia), L.I. László (Hungary), G. Lente (Hungary), S. Macura (USA), Z. Marković (Serbia), K. Novaković (UK), V. Parmon (Russia), D. Peddis (Italy), M.B. Plavšić (Serbia), L. J. Prins (Italy), J. Savović (Serbia), G. Schmitz (Belgium), I. Schreiber (Czech), L. Schreiberova (Czech), D. Stanisavljev (Serbia), N. Stepanov (Russia), Z. Šaponjić (Serbia), S. Tosti (Italy) Á. Tóth (Hungary), N. Vasilyeva (Russia), V. Vukojević (Sweden), A. De Wit (Belgium), A. Yüksel (Türkiye), M. Žabić (Bosnia and Herzegovina)

Local Executive Committee

Chairman: S. N. Blagojević
Vice-chairman: A. Ivanović-Šašić
Members: M. Ajduković, S. Bulatović, J. Dostanić, J. Đuričić-Milanković, M. Jelić, S. Jovanović, Z. Jovanović, N. Jović-Jovičić, B. Marković, J. Maksimović, S. Maćešić, S. Marinović, D. Milenković, T. Mudrinić, N. Nedić, M. Pagnacco, B. Stanković, I. Stefanović, T. Tadić, J. Parlić, M. Pejčić, G. Stevanović, H. Šalipur

WETTABILITY OF LANGMUIR-BLODGETT FILMS FROM SIZE-SELECTED LIQUID PHASE EXFOLIATED GRAPHENE FLAKES

B. Bekić [1], J. Lazarević [1], M. Spasenović[2] and T. Tomašević-Ilić [1]

[1] *University of Belgrade, Institute of Physics, Pregrevica 118, 11080 Belgrade, Serbia.*
(barbara.bekic@gmail.com)
[2]*Center for Microelectronic Technologies, Institute of Chemistry, Technology and*
Metallurgy, University of Belgrade, Njegoševa 12, 11000, Belgrade, Serbia

DOI: https://doi.org/10.46793/Phys.Chem24I.377B

ABSTRACT

We investigated the wettability of Langmuir-Blodgett films from liquid phase exfoliated graphene. By applying cascade centrifugation, dispersions with size-selected flakes are obtained, and depending on the selected dispersion for film formation, films with different defect density are produced. We determined the wettability of our films by measuring the contact angle (CA). Films with the highest defect density, produced by the self-organization of smaller-sized and thinner graphene flakes, exhibited the highest wettability, with a CA of 77°. Conversely, films produced from dispersions with larger nanosheet dimensions demonstrated a hydrophobic nature, with a CA of 90°. This suggests that the wettability of our films can be adjusted by varying the size of the nanosheets used for film formation. Controlling the defect density and wettability of self-assembled graphene films allows the optimization of their properties for various application, particularly in wearable electronics.

INTRODUCTION

Liquid Phase Exfoliation (LPE) is a widely-used method in obtaining a high yield of two-dimensional nanosheets in solution. It can be applied on a broad range of layered materials, in various liquids, and it is suitable for large-scale production. Followed by iterative centrifugation different rates (cascade centrifugation), obtained particles can be separated, and dispersions with narrow nanosheets size and thickness distributions can be produced [1]. Langmuir-Blodgett (LB) deposition is a simple and versatile method based on the self-organization of nanostructures from solution. It is used to make large surfaces of highly transparent graphene films, with few-nanometer thickness [2]. Our previous works demonstrated the potential of LB graphene films for utilization in sensor technology [3, 4]. Due to the high defect density and an abundance of edges, these films exhibit high reactivity, especially to gases [5]. However, the wettability of these films, as one of the fundamental properties of a material surface, has never been reported. Several factors could affect the wettability of graphene. The contact angle of water droplets on a graphene surface may vary from 33° to 127° depending on thickness, substrate of films, defect type and density, surface roughness, present impurities, production method, etc. [6]. Understanding the wetting behavior of graphene would benefit a diverse array of graphene applications. Graphene with a hydrophobic nature can reduce liquid deposition and prevent contamination of devices, while a hydrophilic surface of graphene could be beneficial for applications in biomaterials and the production of supercapacitor electrodes.

In this work we report tunable wettability of Langmuir-Blodgett films from LPE exfoliated graphene achieved through surface manipulation of our films by varying the size of the graphene nanosheets used in the film formation process. Varying the size of the graphene nanosheets used for film formation contributes to the production of graphene films with different defect densities, and such to the different wetting behavior.

METHODS

All chemicals were purchased from Sigma Aldrich: graphite powder (product number 332461), sodium cholate (SC), isopropyl alcohol (IPA) and N-Methyl-2-pyrrolidone (product number 328634). Two types of graphene dispersions were prepared: one by LPE from a water-based solution of SC, and one by LPE in NMP, using previously established methodologies [7]. The initial concertation of graphite was 20 mg/ml in both solutions. Centrifugation at 0.7 kg was used to remove the unexfoliated material in NMP-based dispersions, and obtain a solution with broad lateral flake size and thickness distributions. To obtain graphene dispersions with size-selected flakes, cascade centrifugation of the water-based dispersion was applied. After removing unexfoliated material at 0.1 kg, the supernatant was collected and subjected to further centrifugation at 0.5 kg. The resulting sediment was collected in diluted solution of SC, while the supernatant was centrifuged at 1 kg. The process was repeated once more for the centrifugation rate of 5 kg. To aid the deposition at the water–air interface, the aqueous dispersion was transferred to NMP. To this end, the dispersion was centrifuged at 15 kg (99 min) to force the nanosheets to sediment. The aqueous supernatant was discarded, and the sediment was redispersed in IPA. The centrifugation was repeated, and the sediment was redispersed in NMP by 5 minutes of bath sonication. Graphene films were formed at the water-air interface and deposited with the Langmuir-Blodgett method on SiO_2/Si substrates following the previously reported procedure [8].

Raman characterization was performed with a Jobin Yvon T64000 Raman spectrometer using a 514 nm laser line at room temperature and an exposure time of 300 s. The contact angle measurement was performed using the Ossila Contact Angle Goniometer. The deionized water droplet (9 μl) was released on the sample at room temperature, and the recording included 20 frames per second.

RESULTS AND DISCUSSION

Dispersions with the largest and thickest flakes, obtained with centrifugation rates 0.1-0.5 kg (G1), dispersions with nonselected flakes (G2), and dispersions with the smallest and thinnest flakes, obtained with centrifugation rates 1-5 kg (G3) are chosen for film formation. Lateral dimensions, and flake thicknesses were previously established [7], with thickness shown to be approximately 5 and 10 layers, for G1 and G3 respectively.

Figure 1a depicts Raman spectra of graphene films produced from dispersions with different flake sizes: G1, G2, and G3. All spectra feature four pronounced bands: D at ~1355 cm^{-1}, G at ~1582 cm^{-1}, D' at ~1625 cm^{-1}, and the 2D band at ~2715 cm^{-1}, characteristic for Langmuir-Blodgett graphene films. Raman spectra show evident changes of the intensity of the D mode depending on the choice of dispersion, i.e. size of the flakes used for film formation. **Figure 1b** depicts the intensity ratio of the D peak to the G peak, and calculated distance between defects (L_D) for the used laser wavelength [8]. The D/G ratio increases, and the L_D decreases (from 27 to 7 nm), with centrifugation rate. The results indicate a strong dependence of the film defect density on the flake size in dispersion. We also observe that the ratio of the D-peak intensity to the D’-peak intensity in our films is nearly constant at a value of 5.5 ± 0.5 (**Figure1c**), indicating that regardless of the graphene flakes size, edges are the dominant defect type in all films, ruling out vacancies, substitutional impurities, and sp3 defects [9, 10]. These findings point out that the self-organization of nanosheets with a narrow size and thickness distribution at an air-water interface will results in films that are abundant in edge defects.

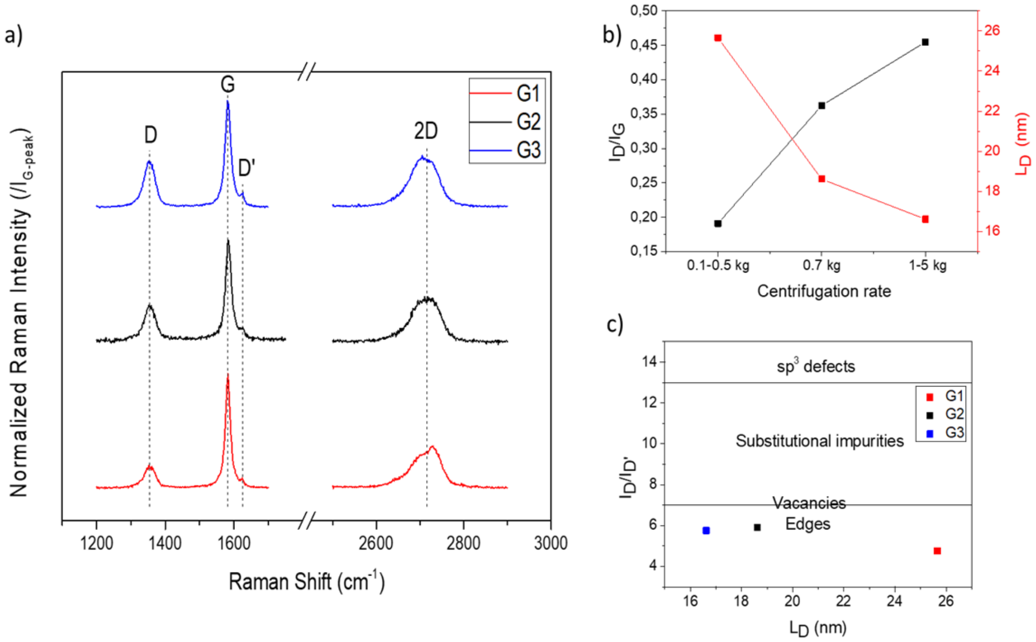

Figure 1. a) Representative Raman spectra of graphene films obtained from dispersion with: nanosheets isolated by centrifugation between 100-500 g (G1), broad lateral size and nanosheets thickness distribution (G2), and smallest nanosheets isolated by centrifugation between 1000-5000g (G3); b) The ratio of the intensities of the D and G modes (black) and distance between defects (red) of the samples; c) The D/D' intensity ratio as a function of the mean carrier path.

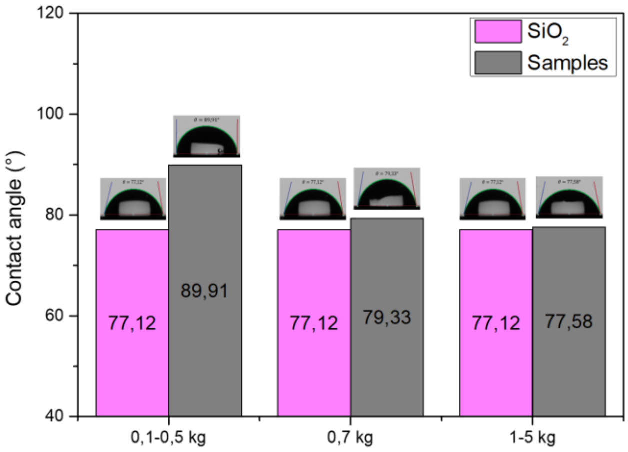

Figure 2. Contact angle measurements of LB graphene films deposited from dispersions with nanosheets isolated by centrifugation between 0.1-0.5 kg (G1), 1-5 kg (G2), and dispersion with dispersions with nonselected flakes (G3) on a SiO2/Si substrate.

Figure 2 depicts contact angle (CA) measurements for LB graphene films deposited from solution with different sizes and thicknesses. Films with the highest defect density, deposited from G3 dispersion, exhibited the highest wettability, with a CA of 77°. Films produced from G1 dispersions, with the lowest defect density, demonstrated a hydrophobic nature, with a CA of 90°. The CA value of 79° for films produced from the G2 dispersion was between values reported for films deposited from G1 and G3 dispersions. This outcome is anticipated since these films were made from a dispersion with a wide range of lateral flake sizes and thicknesses, encompassing nanosheets ranging from monolayers to multilayer graphene. The results are in agreement with previous studies on the wettability of vertically-oriented few-layer graphene, where graphene with a high density of defects shows a much better wettability, while surfaces with a low defect density show a hydrophobic nature [11]. Defects are favorable for the generation of C=O bonds when the graphene is in contact with water, imparting hydrophilic nature of the surface, and allowing water droplets to easily permeate between the nanosheets. Nevertheless, the wetting transparency of graphene must also be considered as a factor that affects the wetting behavior of our films, since the wettability of the SiO_2/Si substrate does not significantly differ from the wettability of the coated substrate with the thinner graphene nanosheets.

CONCLUSION

The wettability of Langmuir-Blodgett films from liquid-phase exfoliated graphene is reported for the first time. We show that by adjusting the size of the graphene nanosheets used in the film formation process, defect density on the graphene surface can be modulated. This surface manipulation enables the tuning of the wetting properties of self-assembled graphene films, ranging from hydrophilic to hydrophobic. Such control could be advantageous for numerous applications, particularly in the development of skin-interfaced sensors and devices.

Acknowledgment

This work was supported by the Institute of Physics Belgrade through the Grant by the Ministry of Science, Technological Development and Innovations. M. S. acknowledges the Ministry of Science, Technological Development, and Innovation of Republic of Serbia (Contract No: 451-03-66/2024-03/200026).

REFERENCES

[1] C. Backes et al., ACS Nano 10 (2016) 1589–1601.
[2] A. Matkovic et al., 2D Mater. 3 (2016) 015002.
[3] S. Andric et al., Nanotechnology 32 (2021) 025505
[4] S. Andric et al., Sens. Mater. 34 (2022) 3933-3947.
[5] M. Spasenović et al., 2021 IEEE 32nd International Conference on Microelectronics (MIEL), Nis, Serbia, 2021, pp. 25-28.
[6] J. Feng et al., Nanoscale Horiz. 4 (2019) 339-364.
[7] C. Backes et al., ACS Nano 13 (2019) 7050–7061.
[8] T. Tomasevic-Ilic et al., Appl. Surf. Sci. 458 (2018) 446–453.
[9] A. Eckmann et al., Nano Lett. 12 (2012) 3925–3930.
[10] A. Eckmann et al., Phys. Rev. B 88 (2013) 035426.
[11] J. L. Qi et al., Nanoscale 7 (2015) 3675–3682.

Materials Science Forum
ISSN: 1662-9752, Vol. 1145, pp 25-38
doi:10.4028/p-0N71lv

Submitted: 2024-07-11
Revised: 2024-09-30
Accepted: 2024-12-04
Online: 2025-03-13

Hydrogen Incorporation and Reduction of Oxidation States in WO_3 Thin Films Irradiated with Low-Energy H_2^+ Ions

Ivna Kavre Piltaver[1,2,a], Robert Peter[1,2b*], Krešimir Salamon[3,c],
Nenad Lazarević[4,d], Jasmina Lazarević[4,e], Maja Mičetić[3,f]
and Mladen Petravić[1,g]

[1]Faculty of Physic, University of Rijeka, Radmile Matejčić 2, 51000 Rijeka, Croatia

[2]Center for Micro- and Nanosciences and Technologies, University of Rijeka, Radmile Matejčić 2, 51000 Rijeka, Croatia

[3]Ruđer Bošković Institute, Bijenička cesta 54, 10000 Zagreb, Croatia

[3]Institute of Physics Belgrade, Pregrevica 118, 11080 Belgrade, Serbia

[a]ivna.kavre@uniri.hr, [b]rpeter@phy.uniri.hr, [c]Kresimir.Salamon@irb.hr, [d]nenadl@ipb.ac.rs, [e]jasminal@ipb.ac.rs, [f]maja.micetic@irb.hr, [g]mpetravic@phy.uniri.hr

Keywords: tungsten oxides, oxide reduction, hydrogen incorporation, hydrogen-tungsten bronze

Abstract. Tungsten trioxide (WO_3) is widely known for its technological importance in electrochromic sensors and catalytic devices. The incorporation of hydrogen into WO_3 can strongly influence the material's electrical, optical, and structural properties. This study investigates the evolution of different tungsten oxidation states and the mechanism of oxide reduction of polycrystalline WO_3 thin films induced by low-energy H_2^+ irradiation at room temperature. The reduction investigation was conducted *in situ* using X-ray photoelectron spectroscopy (XPS) measurements around W 4*f* and O 1*s* core levels. The hydrogen-implanted film, which was irradiated with 5 keV H_2^+ ions for 180 minutes, was subsequently characterized by scanning electron microscopy (SEM), X-ray diffraction (XRD), Raman spectroscopy and secondary ion mass spectrometry (SIMS).

During the initial phase of H_2^+ irradiation, the W^{6+} oxidation state in WO_3 is reduced to W^{5+} and W^{4+}, while the prolonged hydrogen bombardment leads to further reduction and the formation of W^{2+} and W^0 states. SEM reveals crystallinity loss in the irradiated WO_3 sample, while Raman and XRD indicate a phase transformation from monoclinic to tetragonal after hydrogen bombardment. Our analysis shows that WO_3 reduction is confined to the surface while hydrogen-tungsten bronze (H_xWO_3) is formed in the bulk of the material.

Introduction

Tungsten trioxide (WO_3), an n-type semiconductor, has recently attracted much attention due to its intriguing properties, such as wide band gap [1], good electronic mobility [2] and thermal and chemical stability [3]. Applications of WO_3 involve a range of different fields, such as catalysis [4], solar energy devices [5], and battery technology [6]. Its exceptional optical properties and its ability to change colour under different stimuli, such as light, temperature and voltage, make WO_3 an important material in many advanced technologies, such as "smart windows" for energy-efficient buildings [7], gas sensors [8], hydrogen detectors [9], UV sensors and electrochromic displays [10].
At ambient temperature, the WO_3 crystallographic structure is composed of corner-sharing [WO_6] octahedra with different degrees of distortion. The interplay between the lattice phonons and the electronic structure of WO_3 results in the occurrence of different phases, starting from the low-symmetry triclinic or monoclinic phases up to the tetragonal phase [11]. Various dopants can be incorporated into this structure, enabling rapid diffusion and migration within the material [12], [13]. By incorporating various electropositive elements, WO_3 forms compounds known as tungsten bronzes (M_xWO_3) [14], [15], including well-studied types such as Li_xWO_3 and Na_xWO_3 [16], [17]. Other bronzes containing alkaline earth metals, transition metals, rare earths or hydrogen [14], [15]

have also been studied in detail. These materials exhibit rich crystallographic chemistry and interesting electronic properties due to their metallic-like conductivity, which is based on high electron mobility.

Intercalation of hydrogen in the WO_3 matrix significantly influences the optical and electrical properties of WO_3 due to new hydrogen-related impurity states formed in the electronic structure of the material. These compounds are known as hydrogen-tungsten bronzes (H_xWO_3) [11], [15], [17], [18], [19]. Hydrogen atoms are unstable in the centre of the WO_6 octahedron and form chemical bonds with O atoms, forming hydroxyl groups in which the electron from the H atom is transferred to the neighbouring W atom, changing its state from W^{6+} to W^{5+}. During this process, newly occupied impurity states associated with the W^{5+} ions appear in the band gap just below the bottom of the CB or may even fuse with the CB [19]. This has a significant effect on the electrical conductivity and optical absorption of WO_3 and leads to various potential applications of hydrogenated WO_3, such as reversible electrical microcircuits [20], field-effect transistors [21], and memristive devices [22]. Furthermore, the known gasochromic and electrochromic properties of WO_3 are closely related to the insertion and subsequent extraction of hydrogen from the material. Gasochromic devices usually consist of a WO_3 film with a thin catalyst layer, such as Pt or Pd, on its surface. When the material is exposed to hydrogen gas, it changes colour, while air or oxygen bleaches the film. This phenomenon occurs due to the dissociation of H_2 molecules on the metallic catalyst into H atoms and their subsequent diffusion into the bulk of WO_3 (the so-called H-spillover effect), causing a change in optical absorption due to the formation of hydrogen-tungsten bronze [23], [24], [25]. Alternatively, H_xWO_3 can also be formed electrochemically by the double injection of an electron from a metallic electrode and an H^+ ion from an acidic electrolyte such as H_2SO_4 in WO_3. In this electrochemical system, the insertion and extraction of hydrogen into and from the WO_3 matrix can be controlled by altering the polarity of the voltage applied to the electrodes, leading to the electrochromic effect [25], [26]. The formation of hydrogen-tungsten bronzes from WO_3 by H-spillover and electrochemical H-intercalation reactions are still the most commonly used methods for the synthesis of H_xWO_3 [25]. Other methods include high-energy proton implantation of WO_3 [27], reactive mechanical alloying of WO_3 in hydrogen atmosphere [28], chemical reaction of WO_3 with gallium-based liquid metal in acidic solutions [19] or thermochemical reactions of WO_3 and poly(vinylidene fluoride) powders [11].

The incorporation of hydrogen usually reduces part of W^{6+} ions to W^{5+} [29], [30], [31], although some studies report on the additional formation of W^{4+} [19]. XPS studies show that different oxidation states of tungsten (from W^{+5} to W^{+2}) are present in WO_3 when exposed to hydrogen gas at high temperatures (623 K), while electron irradiation can even reduce part of the oxide layer to metallic tungsten [32], [33]. On the other hand, annealing WO_3 in a hydrogen atmosphere at temperatures above 1000 K can completely remove the oxygen and form metallic tungsten [34].

The irradiation of materials with energetic ions is a powerful technique for changing the composition and crystal structure of the material, which can significantly influence its various properties. For example, ion implantation is widely used in semiconductor technology as an efficient carrier doping method [35]. In the case of WO_3, low-energy Ar^+ ion bombardment (2-5 keV) can reduce W^{6+} to lower oxidation states or even metallic tungsten [36], [37], [38], while prolonged Ar^+ etching of WO_3 nanowires can lead to metallic tungsten cone assemblies [37]. On the other hand, it was found that high-energy Ar^+ and He^+ ion implantation (100-350 keV) changes the electrical conductivity and optical absorption of WO_3 [39], [40].

Although numerous studies have examined the formation of hydrogen-tungsten bronzes through various techniques ([11], [19], [23]-[28]), the effects of low-energy H_2^+ ion irradiation at room temperature have not yet been investigated. The primary objective of this study is, therefore, to explore the creation of hydrogen-tungsten bronze through low-energy H_2^+ ion irradiation at room temperature. Specifically, we aim to demonstrate that the oxide reduction is confined to the surface of the WO_3 thin films, while the hydrogen-tungsten bronze forms within the bulk of the material.

To achieve this, we investigated the chemical and compositional changes in polycrystalline WO_3 thin films bombarded with 5 keV H_2^+ ions. The reduction was studied *in situ* by X-ray photoelectron spectroscopy (XPS) around W 4*f* atomic levels. The hydrogen-implanted film, irradiated with 5 keV H_2^+ ions for 180 minutes, was then characterized by scanning electron microscopy (SEM) to determine the change in surface morphology, grazing incidence X-ray diffraction (GIXRD) and Raman spectroscopy, to determine the changes in the crystalline structure and the corresponding crystallographic phases of the irradiated WO_3 samples, and by secondary ion mass spectrometry (SIMS) to obtain the in-depth elemental composition of the bombarded WO_3 films.

Experimental Details

Samples were synthesized using the dc magnetron sputtering technique in an Elettrorava ER-SM500 system under ultrahigh vacuum (UHV), with a base pressure of around 10^{-8} Torr. Initially, metallic tungsten films were deposited onto Si (111) wafers at room temperature, with a target–substrate distance of 15 cm. The deposition parameters included a sputtering power of 120 W and an Ar pressure of 4 mTorr, resulting in a growth rate of approximately 4 nm/min. The average thickness of the WO_3 films was about 70 nm. To ensure uniformity, the substrate was rotated during the 1200-second deposition. XRD confirmed these films were amorphous tungsten. These films were subsequently annealed in air at 700 °C for 1 hour, forming polycrystalline WO_3 films, referred to as *grown samples*.

Hydrogen ion bombardment of WO_3 thin films was performed *in situ* at room temperature in the main chamber of the XPS instrument with a broad beam of 5 keV H_2^+ ions at a current density of about 10 μA/cm², with the ion beam at an angle of 45° to the sample surface. The implanted dose Φ (in H atoms/cm²) in our experiment is related to the bombardment time t (in seconds) as $\Phi = 6.25\times10^{13}\times t$. For the bombardment times used in the present study (15 seconds to 180 minutes), the corresponding implanted dose spans about 3 orders of magnitude, from 9.4×10^{14} to 6.8×10^{17} H atoms/cm².

The photoemission spectra were obtained with a SPECS XPS instrument equipped with the Phoibos MCD 100 hemispherical electron analyzer and a monochromatized source of Al Kα X-rays of 1486.74 eV. The measurements were performed under UHV conditions at a chamber pressure of about 10^{-7} Pa. XPS spectra around the W 4*f* core level were recorded with a pass energy of 10 eV, giving an energy resolution of about 800 meV. The photoemission spectra were simulated with several sets of mixed Gaussian-Lorentzian functions with Shirley background subtraction using the Unifit software [41].

Elemental depth profiling of the hydrogen-bombarded WO_3 samples was conducted using a Hiden SIMS workstation with a quadrupole mass analyzer. Depth profiles were obtained by irradiating samples with 5 keV Cs^+ primary ions and collecting negative secondary ions. The depth of SIMS craters was measured using a Dektak XT stylus profilometer.

The surface morphology was investigated in a Jeol JSM-7800F SEM instrument by collecting the secondary electrons with an electron beam acceleration voltage of 10 kV and a working distance of 3 mm. The thickness of the films and the changes in crystal morphology were determined in the same SEM instrument from the cross-sectional SEM images, taken at an accelerating voltage of 10 kV and a working distance of 2 mm.

The crystal structure of the samples was examined by GIXRD measurements in a Siemens D500 diffractometer equipped with a Cu anode, a Goebel mirror and a graphite monochromator. The GIXRD measurements were performed for two grazing incidence angles, $\alpha_i = 1^o$ (over the entire WO_3 film thickness) and $\alpha_i = 0.322^o$ (with minimum penetration depth, about 15 nm).

Raman analysis was performed using a Jobin Yvon T64000 spectrometer with an 1800/1800/2400 grooves/mm diffraction grating combination, in a backscattering configuration.-The 514.5 nm line of a Coherent Ar^+/Kr^+ ion laser was used as an excitation source. The direction of the incident (scattered) light was normal to the sample surface. A laser beam of 1 mW at the sample was focused through a microscope objective with 50× magnification. The spectrometer resolution is comparable to the Gaussian width of 1 cm^{-1}.

Results and Discussion

We start the examination of the reduction process of WO_3 with the analysis of photoemission spectra of samples exposed to H_2^+ ion bombardment. The ion induced-reduction eliminates the need for high temperatures typically required for the reduction processes. In this way, several thermally activated processes, such as adsorption, dissociation, place-exchange, diffusion or bond braking, can be bypassed by the interaction of energetic ions with the host matrix and the reduction process can occur even at room temperature [42].

The experimental conditions, particularly temperature and ion beam energy, can significantly influence the outcomes of the study on hydrogen-tungsten bronze formation in WO_3 thin films. We chose to conduct experiments at room temperature to preserve the crystallographic integrity of the WO_3 film. Elevated temperatures can induce phase transitions in WO_3, potentially altering its crystalline structure and electronic properties. Furthermore, higher temperatures might enhance thermal vibrations within the lattice, affecting the interaction dynamics between hydrogen ions and the WO_3 matrix. Therefore, maintaining a controlled room temperature environment was essential for isolating the effects of low-energy H_2^+ ion bombardment. The energy of the ion beam is another critical parameter influencing the reduction processes and structural modifications in the WO_3 films. In our study, we employed low-energy H_2^+ ions (5 keV) to minimize damage to the crystal lattice while allowing for effective hydrogen intercalation. Higher ion beam energies could lead to excessive lattice damage, creating defects that may cover the effects attributed to hydrogen incorporation. Consequently, the careful selection of ion beam energy is crucial to ensure that the observed phenomena are primarily due to the targeted ion interactions rather than artifacts of high-energy bombardment.

Turning to the reduction process of WO_3 through low-energy H_2^+ ion irradiation at room temperature, we can monitor it through the evolution of the W 4*f* peaks in the photoemission spectra of WO_3 following the different exposures of surface to H_2^+ irradiation. As an example, we show in Fig. 1 several W 4*f* spectra from the surface of the as-grown WO_3 thin film and from surfaces irradiated with 5 keV H_2^+ ions for different bombardment times ranging from 15s to 180 min (closed circles in Fig. 1). To identify the new chemical surroundings of W atoms in irradiated samples, we fit all experimental spectra with several sets of spin-orbit doublets, as illustrated in Fig. 1. The XPS spectra of the as-grown sample is characterized by a doublet with the W $4f_{7/2}$ component at a binding energy (BE) of 35.6 eV and an energy separation between the W $4f_{7/2}$ and W $4f_{5/2}$ peaks of 2.2 eV, which agrees well with the data for pure WO_3 (W^{6+} ionic state of tungsten) from the literature [31], [36], [37]. In addition, there is a small peak at a higher BE, shifted for about 5.6 eV from the W $4f_{7/2}$ peak, attributed to photoemission from the W $5p_{3/2}$ core-level [37], [43]. To obtain a good fit of the experimental results for the bombarded samples, we introduced four more doublets, assigned to the emissions from tungsten in the W^{5+} oxidation state (yellow doublet at BEs of 34.6 eV and 36.8 eV), W^{4+} state (green doublet at BEs of 33.5 eV and 35.7 eV), W^{2+} state (pink doublet at BEs of 32.2 eV and 34.4 eV) and finally, W^0 oxidation state (brown doublet at BEs of 31.1 eV and 33.3 eV).

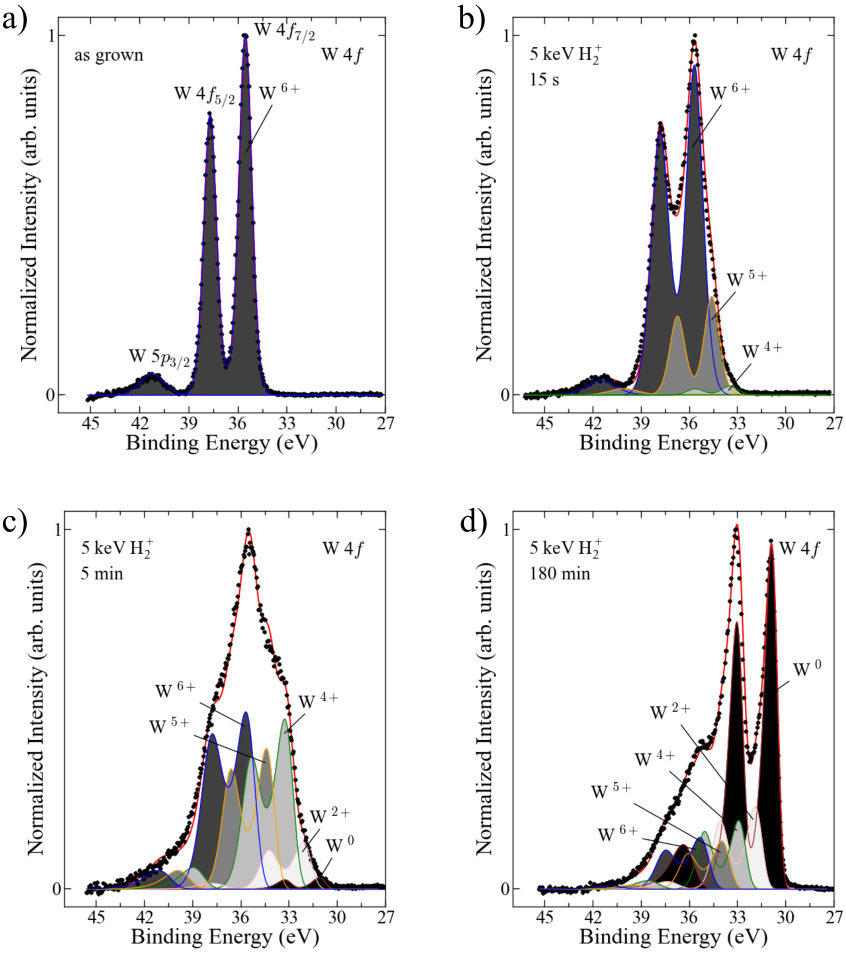

Fig. 1. W 4*f* core level photoemission spectra from an as-grown WO_3 surface (a) and surfaces bombarded with 5 keV H_2^+ for 15 s (b), 5 min (c) and 180 min (d). Closed circles represent experimental data and solid lines the fitting doublets of mixed G-L functions.

As demonstrated in Fig. 1, the relative contribution of different W oxidation states can be extracted from the deconvoluted W 4*f* photoemission curves. The relative concentration fraction of each oxidation state was determined from the area of the corresponding fitting curve, normalized to the total area of the W 4*f* doublet-structure. The results for all W 4*f* photoemission measurements are shown in Fig. 2. The W^{6+} signal decreases monotonically with the bombardment duration, while the W^{5+} and W^{4+} components appear at the beginning of the irradiation and increase sharply at short bombardment durations, only to decrease after 1 and 7.5 minutes of H_2^+ bombardment, respectively. On the other hand, signals related to photoemission of W^{2+} and W^0 states appear after 3.5 and 5 minutes of bombardment, respectively. The W^0 state gradually increases until it reaches the saturation value. After 180 minutes of bombardment, W^0 dominates the spectrum with a relative contribution of 54 %. About 14 % of the total W 4*f* signal is associated with W^{2+}, while the relative contributions of the W^{4+}, W^{5+} and W^{6+} components are in the range of 9 – 12%.

In this study, we employed XPS to investigate the effects of H_2^+ ion bombardment on the WO_3 thin films. Our findings indicate that this bombardment leads to significant reduction of the tungsten oxide surface. These results align qualitatively with previous data obtained from WO_3 samples bombarded with Ar^+ ions [36], [37]. However, the extent of surface reduction observed in the thin WO_3 films examined in the present work is quantitatively different due to the use of distinct ion types and ion energies.

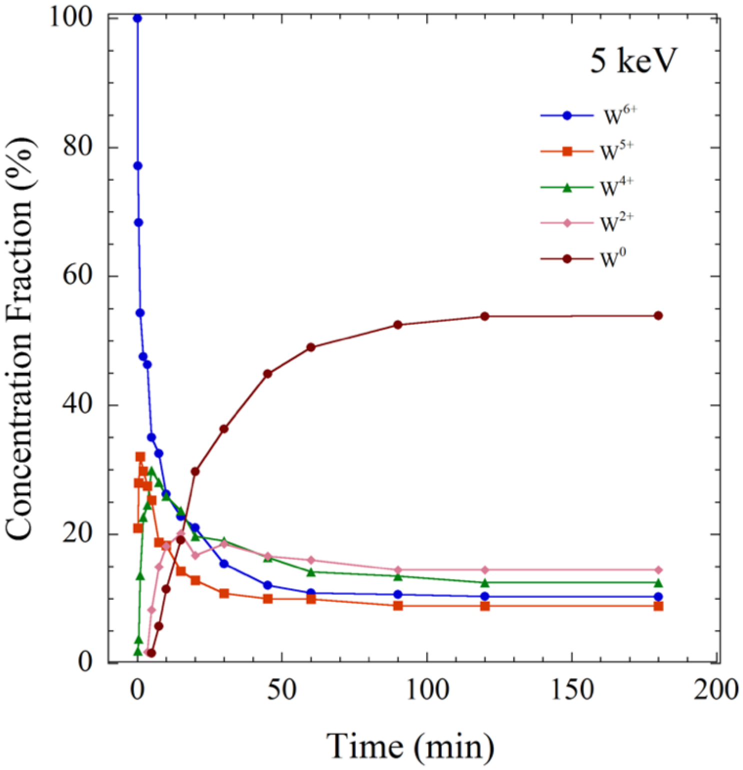

Fig. 2. Relative concentration fractions of different W oxidation states for sample irradiated with 5 keV H_2^+ as a function of bombardment time.

The reduction process of WO_3 under low-energy hydrogen ions was described in detail in our previous paper [42]. According to our model, the reduction process is controlled by the rapid diffusion of H atoms in the WO_3 matrix and the high chemical reactivity of the hydrogen. At the very beginning of hydrogen bombardment, W^{5+} oxidation state forms withn a thin surface layer due to the creation of O-H bonds and the electron transfer from H atom to W^{6+} ion. With increasing H implantation time, i.e. with increasing implanted hydrogen dose, the reduction progresses through the formation of H_2O gas molecules with O atoms extracted from the WO_3 matrix. Consequently, WO_3 reduces progressively to lower oxides and eventually to metallic W, which dominates on the surface after 180 minutes of bombardment time. The XPS spectra of hydrogen irradiated samples measured around O 1*s* core levels, shown in Fig. 3, fully support this reduction mechanism. All photoemission spectra around O 1*s* atomic levels are deconvoluted into three components: one at BE of 530.5 eV attributed to O atoms bonded with W in WO_3 matrix, and additional two related to O-H bonds (line at the BE of 531.2 eV) and H_2O (peak at the BE of 531.7 eV), respectively [29], [44]. The formation of W^{5+} for short bombardment times is accompanied by a significant increase of the peak related to O-H bonds in O 1*s* spectra, as seen for the sample irradiated for 15 s (Fig. 3b). With the prolonged bombardment times, leading to the creation of W^{4+}, W^{2+} and W^0 states, the H_2O-related contribution increases, as indicated in O 1*s* spectra of samples bombarded for 5 min (Fig. 3c).

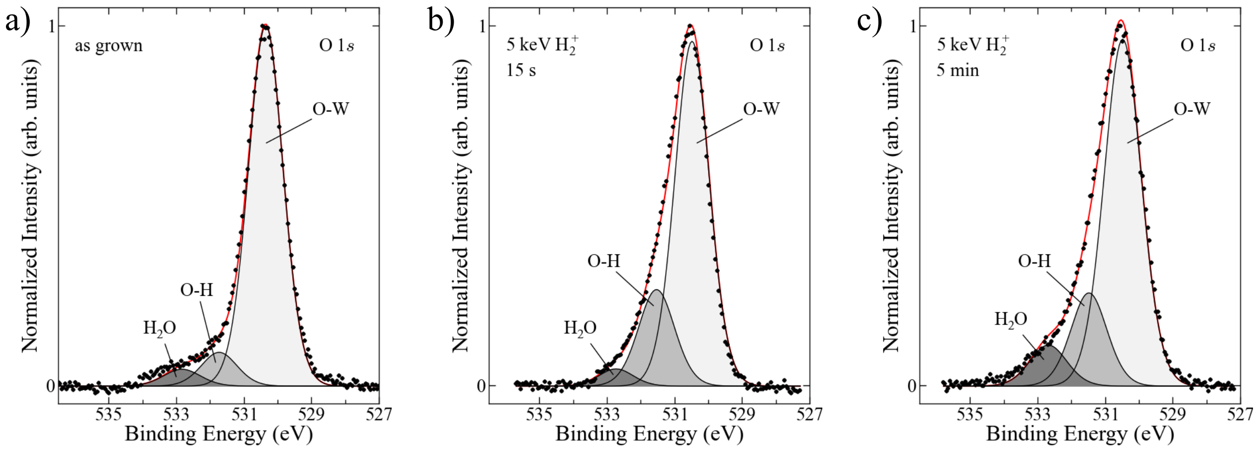

Fig. 3. Deconvoluted O 1*s* XPS spectra from an as-grown WO_3 sample (a) and samples bombarded with 5 keV H_2^+ for 15 s (b) and 5 min (c). Closed circles represent experimental data and solid lines the product of mixed G-L functions.

We note here that a signal associated with WO_3 was present in the corresponding W 4*f* photoemission spectra even after 180 minutes of bombardment (see Fig. 1). This indicates that the thickness of the layer reduced by hydrogen irradiation is less than the depth of the XPS sampling region. This is confirmed by the SIMS depth profile of the bombarded WO_3 film. Fig. 4a shows the SIMS profile of the as-grown sample, characterized by constant WO_3 and O signals throughout the film, with the expected substantial decrease at the WO_3/Si interface. In addition, a small amount of H is present in the film, due to the hydrogen impurities formed during the growth of the film. As shown in Fig. 4b, the WO_3 and O signals in the sample bombarded with 5 keV H_2^+ ions for 180 min remain stable, indicating that the hydrogen irradiation does not significantly affect the distribution of oxygen and WO_3 clusters in the bulk of the film. On the other hand, the intensity of the H signal is increased substantially compared to the as-grown sample and has a fairly constant value with only a slight decrease towards the interface between WO_3 and Si substrate.

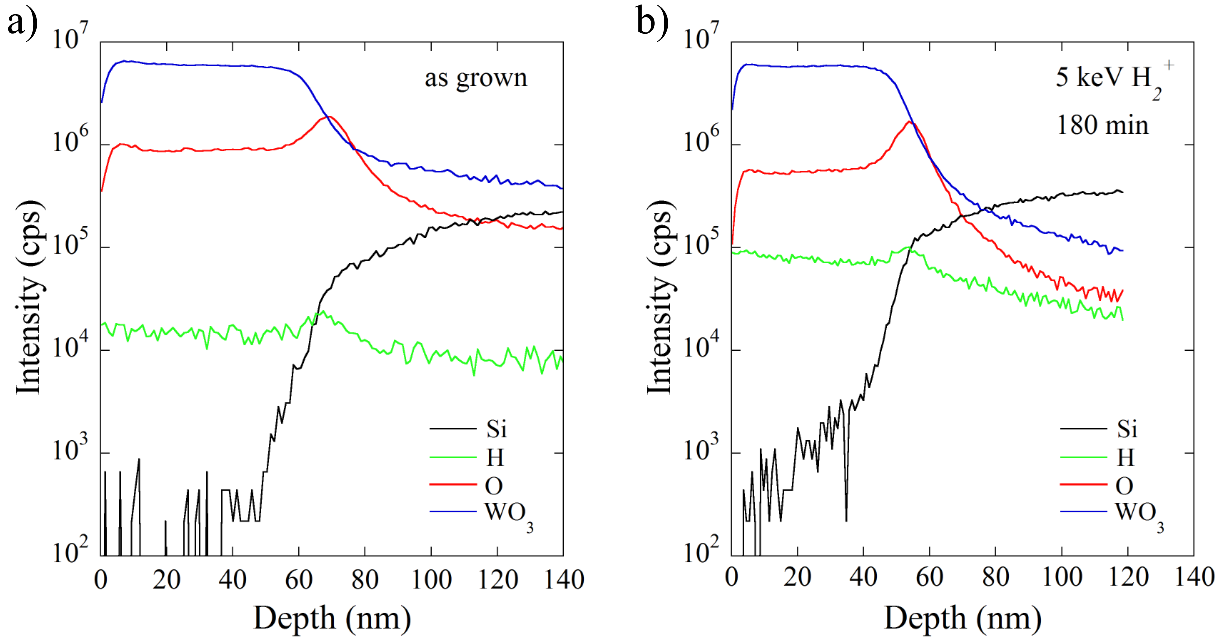

Fig.4. SIMS in-depth profiles of an as-grown sample (a), and WO_3 film bombarded for 180 min with 2 keV H_2^+ (b).

The initial penetration depth of the implanted hydrogen is determined by SRIM simulations [45]. For 5 keV H_2^+ bombardment (corresponding to 2.5 keV H atoms, as each 5 keV H_2^+ ion breaks into two 2.5 keV hydrogen atoms after collision with the surface), the ion range (R_p) of the hydrogen in WO_3 is 17.5 nm with a corresponding range straggling (ΔR_p) of 20.2 nm. Therefore, one would expect the concentration of implanted hydrogen to have Gaussian distribution within the sample with the maximum at about 18 nm below the surface. However hydrogen does not accumulate around the initial penetration depth of the implanted H atoms, but diffuses very rapidly into the WO_3 matrix, resulting in a uniform distribution of hydrogen throughout the film, in complete agreement with the SIMS measurements of Fig. 4. Similar results are reported in the literature for proton implantation of polycrystalline WO_3 thin films, where SIMS measurements revealed an almost homogeneous hydrogen distribution in the material after H^+ bombardment [27].

After examining the surface reduction and in-depth elemental distribution, we turn to the morphology of the analyzed samples. The crystallinity, the grain boundaries and the surface roughness depend critically on the irradiation process. These phenomena are illustrated in Fig. 5 using SEM images of the as-grown WO_3 thin film and the WO_3 thin film bombarded with 5 keV H_2^+ ions for 180 minutes. The SEM micrographs in Fig. 5a show the surface morphology with a granular structure that changes from densely packed crystal grains, characterized by visible grain boundaries with an average size between 25 and 100 nm in the as-grown film, to grains with less smooth and less distinct surfaces and boundaries after bombardment. It is clear from these images that the grain morphology and roughness change as a result of irradiation with 5 keV H_2^+ ions. The cross-sectional images in Fig. 5b show a reduction in the average film thickness from about 70 nm to 55 nm after bombardment, as well as a significant decrease in surface roughness. In addition, the SEM cross-sectional images reveal less pronounced grain boundaries after the bombardment process, which can also be seen in the SEM surface images in Fig. 5a. Both the surface and cross-sectional images of the bombarded WO_3 film show that the H_2^+ treatment caused no cracks.

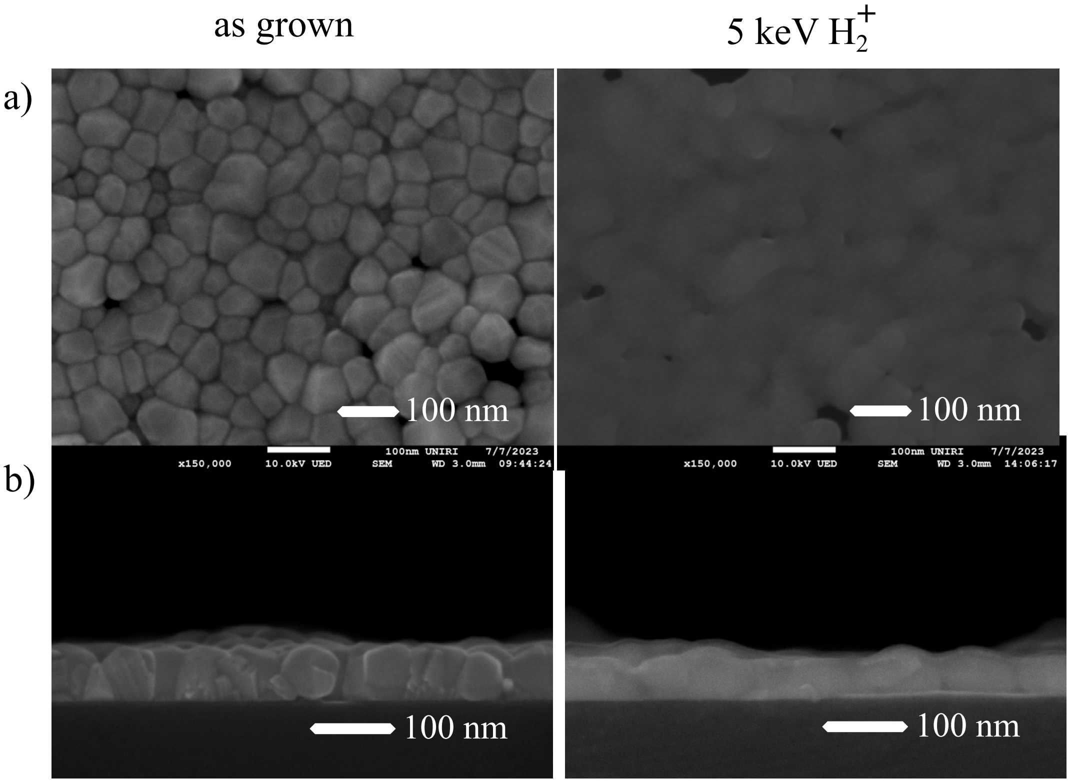

Fig. 5. Top-view FEG-SEM images of an as grown WO_3 film, and sample irradiated with 5 keV H_2^+ for 180 min (a) and the corresponding cross-section images (b).

SIMS measurements from Fig. 4 indicate an almost uniform distribution of hydrogen in WO_3 film after 180 minutes of H_2^+ exposure. It is known that the incorporation of H atoms induces structural changes in WO_3 and can transform the material into a hydrogen-tungsten bronze [19]. To investigate the influence of H_2^+ bombardment on the crystal structure of the material, we turn to Raman and XRD analysis of irradiated WO_3 films. The structural evolution of a WO_3 film exposed to H_2^+ ion bombardment for 180 minutes is shown in Fig. 6. To evaluate all phonon contributions within the considered factor-groups, Raman spectra were recorded in a parallel polarization configuration as shown in Fig. 6. In addition, the spectrum of the Si substrate used for the growth of the WO_3 film was recorded under identical conditions and is shown by the gray line. In addition to the peaks of the substrate, the as-grown WO_3 exhibits the characteristics of the monoclinic structure, such as the lines at 133, 270, 320, 714 and 803 cm^{-1} marked with green asterisks in Fig. 6 [46]. In WO_3 films irradiated with 5 keV H_2^+ ions, the structure stabilizes in the tetragonal phase, albeit with considerable crystalline disorder, as evidenced by the increase in the slope in the spectrum and the broadening of the peaks. Indeed, 714 cm^{-1} mode disappears after 5 keV H_2^+ bombardment for 180 minutes which is in full agreement with Ref. [47]. Moreover, the peak related to the ν(W-O) stretching mode at 803 cm^{-1} in the monoclinic as-grown sample shifts to a higher frequency (816 cm^{-1}). A similar shift was observed in hydrogenated WO_3 samples and was attributed to the formation of a H_xWO_3 structure with tetragonal symmetry [17]. A reasonable explanation of the existence of only one stretching mode in the tetragonal phase is the symmetrization of the W-O bonds in the *a-b* plane, while the bonds along the *c* axis remain different and Raman active.

The phase composition of WO_3 bombarded samples revealed by Raman spectroscopy agrees well with the XRD analysis displayed in Fig. 7. for the as-grown sample and the WO_3 film bombarded with 5 keV H_2^+ for 180 minutes. The spectra were recorded at the grazing incidence angles $\alpha_i = 1^o$ (Fig. 7a) and $\alpha_i = 0.322^o$ (Fig. 7b). The angle of incidence of 0.322^o is surface sensitive as it collects information from about 15 nm below the film surface. On the other hand, the spectra recorded with the angle of incidence of 1^o reflect the bulk structure of the samples, as in this case the X-rays penetrate through the entire film. For both X-ray incidence angles, the diffraction patterns obtained for the as-grown film are characteristic of the monoclinic phase, with the peaks at 28.9°, 33.6°, 35° and 41.7°, assigned to the reflections of the (112), (202), (122) and (222) lattice planes of monoclinic WO_3, respectively (JCPDS Card No. 83-0950). We restrict our analysis to the 2θ region in the 25-45° range because the XRD spectrum of WO_3 at higher diffraction angles has a complex structure and various diffraction features overlap, making it difficult to resolve individual peaks.

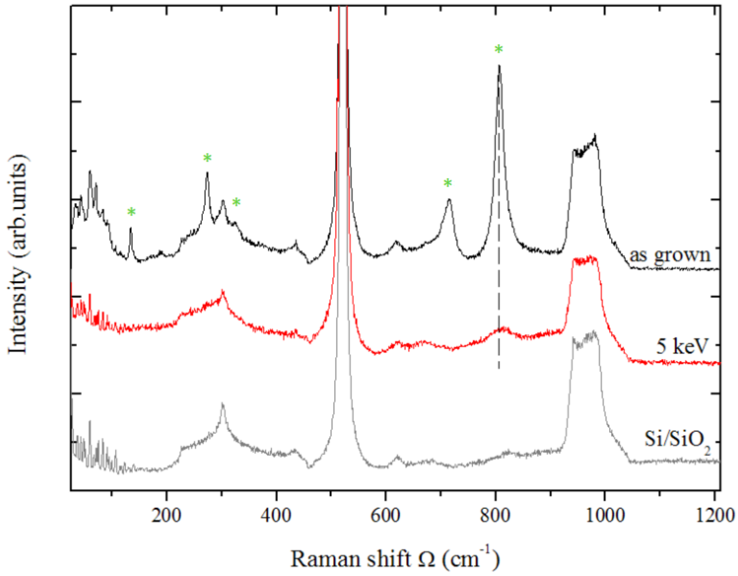

Fig. 6. Raman spectra of as-grown WO_3 and WO_3 bombarded with 5 keV H_2^+ ions. Gray line represents the spectrum of the substrate. Green asterisks show the characteristic peaks for the monoclinic phase.

In films bombarded with 5 keV H_2^+ ions for 180 minutes, the (112), (202) and (222) peaks are shifted to lower 2θ values, while the (122) reflection, which is present in the as grown sample, is absent. The diffraction patterns of the 5 keV bombarded samples are in good agreement with the XRD peaks of the tetragonal WO_3 phase (JCPDS Card No. 89-1287). The shift of the diffraction peaks to the lower diffraction angles indicates the distortion and expansion of the WO_3 lattice caused, in our case, by the hydrogen intercalation in the WO_3 matrix [48], [49]. Therefore, we attribute the observed tetragonal structure to the formation of H_xWO_3 in the bombarded films.

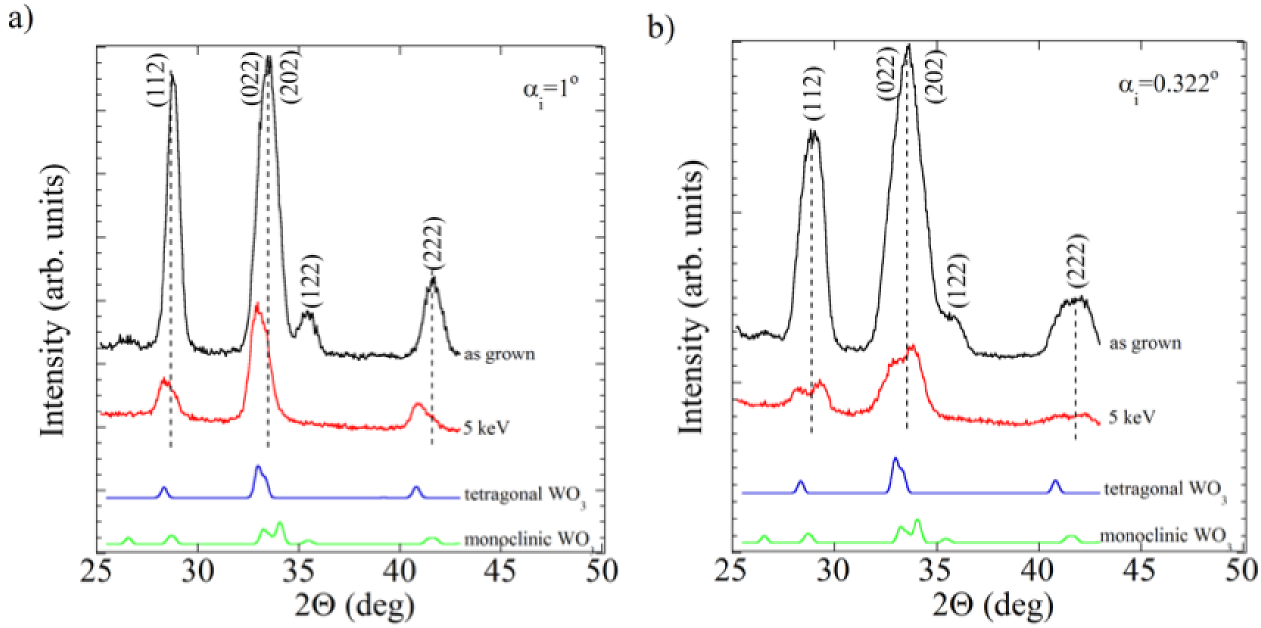

Fig. 7. GIXRD patterns of an as-grown WO3 sample and film irradiated with 5 keV H_2^+ for 180 min for grazing incidence angle a) $\alpha_i = 0.322^o$ and b) $\alpha_i = 1^o$.

When looking at the surface-sensitive XRD spectra shown in Fig. 7b, it is noticeable that the WO_3 samples bombarded with 5 keV H_2^+ show different diffraction patterns than the corresponding bulk spectra in Fig. 7a. The diffraction lines characteristic of the tetragonal phase are split, with each peak having an additional feature at a higher 2θ value. This indicates the formation of a new phase at the sample's surface, which has a smaller lattice constant compared to the tetragonal WO_3 phase [50]. The 5 keV H_2^+ions can cause a strong distortion of the crystal lattice and create many defects in the material, including vacancies. It is well known that the formation of oxygen vacancies in metal oxide compounds causes lattice contraction [51], [52]. Therefore, we assume that oxygen vacancies are formed as a result of ion bombardment, up to the ion range of the impinging ions (about 18 nm according to SRIM calculations). This leads to the formation of surface domains with a tetragonal structure with a reduced unit cell. This is in full agreement with our SEM and Raman analyses, which also show an evident degradation of the crystal structure for the 5 keV bombarded sample.

Both XRD and Raman spectra point at the structural transition from monoclinic to tetragonal phase in the bombarded sample. Indeed, the incorporation of hydrogen into WO_3 can cause the transformation into hydrogen-tungsten bronze (H_xWO_3), a non-stoichiometric compound that crysrallizes at room temperature in different structures: orthorhombic for $0.1<x<0.15$, tetragonal for $0.15<x<0.5$ or cubic for $x>0.5$ [11], [15], [17]. Since only the tetragonal phase was detected in the films irradiated with 5 keV, the hydrogen should be relatively homogeneously incorporated in these films. This fully agrees with our SIMS analysis showing an almost uniform distribution of H atoms in the bombarded film. Therefore, our XRD, Raman and SIMS analyses confirm that hydrogen atoms implanted in polycrystalline WO_3 films by H_2^+ bombardment do not accumulate around the penetration depth of the hydrogen atoms, but easily diffuse into the WO_3 matrix, filling the entire volume of the film and transforming the bulk of the material into hydrogen-tungsten bronze.

Conclusion

We have investigated the surface oxide reduction of polycrystalline WO_3 thin films under 5 keV H_2^+ bombardment and the structural changes in the bulk of the sample. Photoemission spectra around the W 4*f* core levels revealed the presence of several W oxidation states (W^{6+}, W^{5+}, W^{4+}, W^{2+} and W^0) in the bombarded samples. During the initial stage of H_2^+ irradiation, the W^{6+} oxidation state in WO_3 is reduced to W^{5+} and W^{4+}, while continued hydrogen bombardment leads to further reduction and the formation of W^{2+} and W^0 states. SEM analysis shows the loss of crystallinity of the WO_3 sample after 180 minutes of H_2^+ irradiation, compared to the as-grown polycrystalline film. On the other hand, Raman and XRD measurements show that the hydrogen-implanted WO_3 sample transforms from a monoclinic to a tetragonal phase. This indicates that the observed oxide reduction is limited to the surface of the WO_3 film, while hydrogen-tungsten bronze – a non-stoichiometric material with hydrogen atoms incorporated into the structure of WO_3 – forms in the bulk of the sample. This fully agrees with the SIMS measurements, which show a nearly uniform distribution of hydrogen in the WO_3 film after 180 minutes of H_2^+ exposure.

Building on these findings, future research could explore several promising directions. A particularly important area for further exploration is the study of the electrical conductivity of hydrogen-tungsten bronze samples. Considering the well-established influence of hydrogen intercalation on the electronic properties of WO_3, investigating conductivity could offer valuable insights into the material's behavior and potential for use in electronic devices. This research could open up new possibilities for developing advanced sensors, particularly for detecting hydrogen, where changes in electrical conductivity could serve as an indicator of hydrogen presence or concentration. Such research would be invaluable for applications in fields like environmental monitoring and industrial safety, where precise and responsive hydrogen detection is critical.

Acknowledgement

The research leading to these results has received funding from the core fundings NPOO.C3.2.R2-I1.06.0083 supported by the European Union NextGenerationEU and project numbers 23-190 and 23-4 supported by the University of Rijeka

References

[1] R. Vemuri, M. Engelhard, C. Ramana, Correlation Between Surface Chemistry, Density, and Band Gap in Nanocrystalline WO_3 Thin Films, ACS Appl. Mater. Interface 4 (2012) 1371-1377.

[2] W.C. Dautremont-Smith, M. Green, K. S. Kand, Optical and electrical properties of thin films of WO_3 electrochemically coloured, Electrochim. Acta 22 (1977) 751-759.

[3] F. Amano, D. Li, B. Ohtani, Tungsten (VI) Oxide Flake-Wall Film Electrodes for Photoelectrochemical Oxygen Evolution from Water, ECS Trans., 28 (2010) 127.

[4] C. Martín, G. Solana, P. Malet, V. Rives, V. Nb_2O_5-Supported WO_3: A Comparative Study with WO_3/Al_2O_3, Catal. Today 78 (2003) 365–376.

[5] T. Stubhan, N. Li, N. A. Luechinger, S. C. Halim, G. J. Matt, C. J. Brabec, High Fill Factor Polymer Solar Cell Incorporating a Low Temperature Solution Processed WO_3 Hole Extraction Layer, Adv. Energy Mater. 2 (2012) 1433-1438.

[6] W. Dang, W. Wang, Y. Yang, Y. Wang, J. Huanh, X. Fang, L. Wu, Z. Rong, X. Chen, X. Li, L. Huang, X. Tang, One-step hydrothermal synthesis of 2D WO_3 nanoplates@ graphene nanocomposites with superior anode performance for lithium ion battery, Electrochim. Acta 313 (2019) 99-108.

[7] S. Papaefthimiou, E. Syrrakou, P. Yianoulis, Energy performance assessment of an electrochromic window, Thin Solid Films 502 (2006) 257-264.

[8] S. Büyükköse, Highly selective and sensitive WO3 nanoflakes based ammonia sensor, Mater. Sci. Semicond. Process. 110 (2020) 104969.

[9] C.H. Chang, T.C. Chou, W.C. Chen, J.S. Niu, K.W. Lin, S.Y. Cheng, J.H. Tsai, W.C. Liu, Study of a WO_3 thin film based hydrogen gas sensor decorated with platinum nanoparticles, Sens. Actuators B Chem. 317 (2020) 128145.

[10] C.M. Lampert, Chromogenic smart materials, Mater. Today 7 (2004) 28-35.

[11] L. Jin, Q. Zhang, R. J. Cava, The hydrogen-containing bronzes $H_{0.23}WO_3$ and $H_{0.10}ReO_3$ synthesized via a polymer route, J. Solid State Chem. 297 (2021) 122059.

[12] Xie, Y.; Zhang, Q.; Cheng, H. Mechanism of hydrogen spillover on WO_3(001) and formation of H_xWO_3 (x=0.125, 0.25, 0.375 and 0.5). *J. Phys. Chem. C* 118 (2014) 494-501.

[13] Burkhardt, S.; Elm, M. T.; Lani-Wayda, B.; Klar, P. J. In situ monitoring of lateral hydrogen diffusion in amorphoous and polycrystalline WO_3 thin films. *Adv. Mater. Interfaces* 5 (2018) 1701587.

[14] S. Takai, N. Hoshimi, T. Esaka, Synthesis of Tungsten, Molybdenum and Vanadium Bronzes by Mechanochemical Method Milling with Liquid Hydrocarbons, Electrochem. 72 (2004) 876-879.

[15] G. Urretavizcaya, F. Tonus, E. Gaudin, J.-L. Bobet, F. J. Castro, Formation of tetragonal hydrogen tungsten bronze by reactive mechanical alloying, J. Solid State Chem. 180 (2007) 2785-2789.

[16] P. Hagenmuller, Comprehensive Inorganic Chemistry. Tungsten bronzes, Vanadium bronzes, and Related Compounds; vol. 4, Pergamon Press, Oxford, 1973, pp. 541–605 (Chapter 50)

[17] A. Hjelm, C.G. Granqvist, Electronic structure and optical properties of WO_3, $LiWO_3$, $NaWO_3$, and HWO_3. *Phys. Rev. B* 54 (1996) 2436-2445.

[18] F.J. Castro, F. Tonus, J.-L. Bobet G. Urretavizcaya, Synthesis of hydrogen tungsten bronzes $HxWO_3$ by reactive mechanical milling of hexagonal WO_3, J.Alloys Compd. 495(2010)537-540.

[19] Y. Cui, F. Liang, C. Ji, S. Xu, H. Wang, Z. Lin, J. Liu, Discoloration Effect and One-Step Synthesis of Hydrogen Tungsten and Molybdenum Bronze (H_xMO_3) using Liquid Metal at Room Temperature, ACS Omega 4 (2019) 7428-7435.

[20] C. Hu, X. Zhou, Y. Chen, L. Li, B. Li, H. Ren, S. Zhao, C. Zou, Selective hydrogenation of WO_3 for erasable conducting circuit, J. Appl. Phys. 129 (2021) 235702.

[21] M. Wang, S. Shen, J. Ni, N. Lu, Z. Li, H.-B. Li, S. Yang, T. Chen, J. Guo, Y. Wang, H. Xiang, P. Yu, Electric-Field-Controlled Phase Transformation in WO_3 Thin Films through Hydrogen Evolution, Adv. Mater. 29 (2017) 1703628.

[22] Y. Zhou, Y. Peng, Y. Yin, F. Zhou, C. Liu, J. Ling, L. Lei, W. Zhou, D. Tang, Modulating memristive performance of hexagonal WO_3 nanowires by water-oxidized hydrogen ion implantation, Sci. Rep. 6 (2016) 32712.

[23] C.C. Chan, W.C. Hsu, C.C. Chang, C.S. Hsu, Hydrogen incorporation in gasochromic coloration of sol-gel WO3 thin films, Sensors and Actuators B 157 (2011) 504-509.

[24] A. Inouye, S. Yamamoto, S. Nagata, M. Yoshikawa, T. Shikama, Hydrogen behavior in gasochromic tungsten oxide films investigated by elastic recoil detection analysis, Nucl Instrum Meth B 266 (2008) 301-307.

[25] E. V. Miu, J. R. McKone, Comparison of WO_3 reduction to H_xWO_3 under thermochemical and electrochemical control, J. Mater. Chem. A 7 (2019) 23756.

[26] A.G. Breuhaus-Alvarez, J. DiMeglio, J.J. Cooper, C. R. Lhermitte, B. Bartlett, Kinetics and Faradaic Efficiency of Oxygen Evolution on Reduced HWO Photoelectrodes, J. Phys. Chem. C 123 (2019) 1142-1150.

[27] M. Miyakawa, H. Hosono, H. Kawazoe, Formation of hydrogen tungsten bronze by proton implantantion, Materials Research Bulletin 34 (1999) 115-121.

[28] F. J. Castro, F. Tonus, J.-L. Bobet, G. Urretavizcaya, Synthesis of hydrogen tungsten bronzes H_xWO_3 by reactive mechanical milling of hexagonal WO_3, J. Alloy. Comp. 495 (2010) 537-540.

[29] X. Ren. M- Xia, B. Chong, X. Yan, N. Wells, G. Yang, Uniform NiPx nanospheres loaded onto defective H_xWO_{3-y} with three-dimensionally ordered microporous structure for photocatalytic nitrogen reduction, Appl. Catal. B 297 (2021) 120468.

[30] Y. F. Li, N. Soheilnia, M. Greiner, U. Ulmer, T. Wood, A. A. Jelle, Y. Dong, A. P. Y. Wong, J. Jia, G. A. Ozin, Pd@H_yWO_{3-x} Nanowires Efficiently Catalyze the CO_2 Heterogeneous Reduction Reaction with a Pronounced Light Effect, ACS Appl. Mater. Interfaces 11 (2018) 5610-5615.

[31] M. Vasilopoulou, I. Kostis, N. Vourdas, G. Papadimitropoilos, A. M. Douvas, N. Boukos, S. Kennou, D. Davazoglou, Influence of the Oxygen Sub-Stoichiometru and of the Hydrogen Incorporation on the Electronic Band Structure of Amorphous Tungsten Oxide Films, J. Phys. Chem. C 118 (2014) 12632-12641.

[32] A. Katrib, F. Hemming, P. Wehrer, L. Hilaire, G. Maire, The multi-surface structure and catalytic properties of partially reduced WO_3, WO_2 and WC+O_2 or W+O_2 as characterized by XPS, J Electro. Spectros. Relat. Phenomena 76 (1995) 195-200.

[33] J. Haber, J. Stoch, L. Ungier, Electron Spectroscopiec Studies of the Reduction of WO3, J. Solid State Chem. 19 (1976) 113-115.

[34] S. Keilholz, R. Paul, L. Y. Dorsch, H. Kohlmann, In Situ X-ray Diffraction Studies on the Reduction of V_2O_5 and WO_3 by using Hydrogen, Chem. Eur. J. 29 (2023) e202203932.

[35] J.S. Williams, J.M. Poate, Ion Implantation and Beam Processing, Academic Press, Sydney, Australia, 1984.

[36] N.V. Alov, XPS study of MoO3 and WO3 oxide surface modification by low-energy Ar^+ ion bombardment, Phys. Status Solidi C 12 (2015) 263-266.

[37] F. Y. Xie, L. Gong, X. Liu, Y. T. Tao, W. H. Zhang, S. H. Chen, H. Meng, J. Chen, XPS studies on surface reduction of tungsten oxide nanowire film by Ar^+ bombardment, J. Electron Spectros. Relat. Phenomena 185 (2012) 112-118.

[38] T. J. Driscoll, L. D. McCormick, W. C. Lederer, Altered layer formation and sputtering yields for 5 keV Ar^+ bombardment of MoO3 and WO3, Surf. Sci. 187 (1987) 539-558.

[39] B. Heinz, M. Merz, P. Widmayer, P. Ziemann, Tuning the hopping conductivity of WO_3 films by ion bombardment at different temperatures, J. Appl. Phys. 90 (2001) 4007.

[40] S. Keshri, A. Kumar, D. Kabiraj, Tailoring of optical and gas behaviors of WO_3 films by low energy Ar^+ ion implantation, Thin Solid Films, 526 (2012) 50-58.

[41] R. Hesse, T. Chassé, R. Szargan, Peak shape analysis of core level photoelectron spectra using UNIFIT for WINDOWS, Fresenius’ J. Anal. Chem. 365 (1999) 48-54.

[42] I. Kavre Piltaver, R. Peter, K. Salamon, M. Micetic. M. Petravic, In Situ X-ray Photoelectron Spectroscopy Study of Initial Stages of Tungsten Trioxide Reduction by Low-Energy Hydrogen Bombardment, J. Phys. Chem. C 128 (2024) 5345-5354.

[43] J. I. Jeong, J. H. Hong, J. H. Moon, J. S. Kang, Y. Fukuda, Xray photoemission studies of W 4f core levels of electrochromic H_xWO_3 films, J. Appl. Phys. 79 (1996) 9343.

[44] N. Tahmasebi, S. Sezari, P. Zaman, P. Fabrication and characterization of hydrogen-treated tungsten oxide nanofibers for cationic dyes removal from water. Solid State Sci. 100 (2020) 106073.

[45] J. F. Zigler, J. P. Biersack, U. Littmark, The Stopping and Range of Ions in Solids, Pergamon, New York, 1986.

[46] M. Boulova, G. Lucazeau, Crystallite Nanosize Effect on the Structural Transitions of WO_3 Studied by Raman Spectroscopy, J. Solid State Chem. 167 (2002) 425-434.

[47] E. Cazzanelli, C. Vinegoni, G. Mariotto, A. Kuzmin, J. Purans, Raman study of the phase transitions sequence in pure WO_3 at high temperature and in H_xWO_3 with variable hydrogen content, Solid State Ionics 123 (1999) 67-74.

[48] G. Liu, J. Han, X. Zhou, L. Huang, F. Zhang, X. Wang, C. Ding, X. Zheng, H. Han, C. Li, Enhancement of visible-light-driven O_2 evolution from water oxidation on WO_3 treated with hydrogen, J. Catal. 307 (2013) 148-152.

[49] H. Chen, N. Xu, S. Deng, D. Lu, Z. Li, J. Zhou, J. Chen, Gasochromic effect and relative mechanism of WO_3 nanowire films, Nanotechnology 18 (2007) 205701.

[50] E. T. Hoke, D. J. Slotcavage, E. R. Dohner, A. R. Bowring, H. I. Karunadasa, M. D. McGehee, Reversible photo-induced trap formation in mixed-halide hybrid perovskites for photovoltaics, Chem. Sci. 5 (2015) 613.

[51] D. Marrocchelli, S. R. Bishop, H. L. Tuller, B. Yildiz, Understanding Chemical Expansion in Non-Stoichiometric Oxides: Ceria and Zirconia Case Studies, Adv. Funct. Mater. 22 (2012) 1958-1965.

[52] J. Xi, H. Xu, Y. Zhang, W. J. Weber, Strain effects on oxygen vacancy energetics in $KTaO_3$, Phys. Chem. Chem. Phys. 19 (2017) 6264.

BOOK OF ABSTRACTS

ADVANCES
IN SOLID STATE PHYSICS
AND NEW MATERIALS

ДОСТИГНУЋА У ФИЗИЦИ ЧВРСТОГ СТАЊА И НОВИХ МАТЕРИЈАЛА

30 година Центра за физику чврстог стања и нове материјале
Института за физику у Београду

ADVANCES IN SOLID STATE PHYSICS AND NEW MATERIALS

30 years of the Center for Solid State Physics and New Materials at the
Institute of Physics Belgrade

19 - 23 May 2025
Belgrade, Serbia

Conference Chairs

Nenad Lazarević, *Institute of Physics Belgrade, Serbia*
Emil S. Božin, *Institute of Physics Belgrade, Serbia*
Rudi Hackl, *IFW Dresden, Germany*
Zoran V. Popović, *Serbian Academy of Sciences and Arts (SANU), Serbia* – honorary chair

Organizing Committee

Jelena Pešić - chair
Bojana Višić – chair

Ana Kanjevac
Ana Milosavljević
Andrijana Šolajić
Barbara Bekić
Bojan Stojadinović
Branka Hadžić
Ivana Milošević
Jasmina Lazarević
Jelena Mitrić
Jelena Trajković
Jovan Blagojević
Lenka Filipović
Marko Opačić
Milica Petrović
Nataša Tomić
Novica Paunović
Tea Belojica
Tijana Tomašević Ilić

Scientific Committee

Rudi Hackl, *IFW Dresden, Germany*
Nenad Lazarević, *Institute of Physics Belgrade, Serbia*
Emil S. Božin, *Institute of Physics Belgrade, Serbia*
Elena Gati, *Max Planck Institute for Chemical Physics of Solids, Germany*
John S. O. Evans, *Durham University, UK*
Zdeněk Sofer, *UCT Prague, Czech Republic*
Milorad Milošević, *University of Antwerp, Belgium*
Marija Drndić, *University of Pennsylvania, USA*
Simon J. L. Billinge, *Columbia University, USA*
Yann Gallais, *Université Paris Cité, France*

Advisory Committee

Bernd Büchner, *IFW Dresden, Germany*
Reshef Tenne, *Weizmann Institute of Science, Israel*
Zoran V. Popović, *Serbian Academy of Sciences and Arts (SANU), Serbia*
Dragana Popović, *Florida State University, USA*
Maja Remškar, *Jožef Stefan Institute, Slovenia*
Matthieu Le Tacon, *Karlsruhe Institute of Technology, Germany*
Wei Ku, *Tsung-Dao Lee Institute & Shanghai Jiao Tong University, China*

Exploring Structural Phase Transitions in Atorvastatin Calcium Trihydrate Through Variable-Temperature Raman Spectroscopy

Jasmina Lazarević[a], Snežana Uskoković-Marković[b], Jelena Mitrić[a] and Nenad Lazarević[a]

[a] *Center for Solid State Physics and New Materials, Institute of Physics Belgrade, University of Belgrade, Pregrevica 118, Belgrade, 11080, Serbia*
[b]*Faculty of Pharmacy, University of Belgrade, Vojvode Stepe 450, Belgrade, 11221, Serbia*

Abstract. A detailed Raman spectroscopic analysis of atorvastatin calcium trihydrate (Form I) was conducted across a broad temperature range (100 K to 460 K), with particular focus on the low-frequency vibrational region. This study reveals new insights into the structural evolution and thermal response of the compound.

Significant spectral changes were observed near 420 K, where the disappearance of external vibrational modes at ~34 cm^{-1}, 44 cm^{-1} and 140 cm^{-1} indicated a structural phase transition. At the same time, pronounced broadening of the 645 cm^{-1} and 1650 cm^{-1} modes indicated increased molecular fluctuations. A new Raman feature emerging around 75 cm^{-1} during this transition suggests the presence of a transient, ordered intermediate phase before complete loss of crystallinity at higher temperatures.

These findings offer the first in-depth view of temperature-driven structural changes in atorvastatin calcium trihydrate by means of inelastic light scattering, providing valuable information on its vibrational properties, phase behavior and implications for pharmaceutical stability.

BOOK OF ABSTRACTS

ADVANCES
IN SOLID STATE PHYSICS
AND NEW MATERIALS

ДОСТИГНУЋА У ФИЗИЦИ ЧВРСТОГ СТАЊА И НОВИХ МАТЕРИЈАЛА

30 година Центра за физику чврстог стања и нове материјале Института за физику у Београду

ADVANCES IN SOLID STATE PHYSICS AND NEW MATERIALS

30 years of the Center for Solid State Physics and New Materials at the Institute of Physics Belgrade

19 - 23 May 2025
Belgrade, Serbia

Conference Chairs

Nenad Lazarević, *Institute of Physics Belgrade, Serbia*
Emil S. Božin, *Institute of Physics Belgrade, Serbia*
Rudi Hackl, *IFW Dresden, Germany*
Zoran V. Popović, *Serbian Academy of Sciences and Arts (SANU), Serbia* – honorary chair

Organizing Committee

Jelena Pešić - chair
Bojana Višić – chair

Ana Kanjevac
Ana Milosavljević
Andrijana Šolajić
Barbara Bekić
Bojan Stojadinović
Branka Hadžić
Ivana Milošević
Jasmina Lazarević
Jelena Mitrić
Jelena Trajković
Jovan Blagojević
Lenka Filipović
Marko Opačić
Milica Petrović
Nataša Tomić
Novica Paunović
Tea Belojica
Tijana Tomašević Ilić

Scientific Committee

Rudi Hackl, *IFW Dresden, Germany*
Nenad Lazarević, *Institute of Physics Belgrade, Serbia*
Emil S. Božin, *Institute of Physics Belgrade, Serbia*
Elena Gati, *Max Planck Institute for Chemical Physics of Solids, Germany*
John S. O. Evans, *Durham University, UK*
Zdeněk Sofer, *UCT Prague, Czech Republic*
Milorad Milošević, *University of Antwerp, Belgium*
Marija Drndić, *University of Pennsylvania, USA*
Simon J. L. Billinge, *Columbia University, USA*
Yann Gallais, *Université Paris Cité, France*

Advisory Committee

Bernd Büchner, *IFW Dresden, Germany*
Reshef Tenne, *Weizmann Institute of Science, Israel*
Zoran V. Popović, *Serbian Academy of Sciences and Arts (SANU), Serbia*
Dragana Popović, *Florida State University, USA*
Maja Remškar, *Jožef Stefan Institute, Slovenia*
Matthieu Le Tacon, *Karlsruhe Institute of Technology, Germany*
Wei Ku, *Tsung-Dao Lee Institute & Shanghai Jiao Tong University, China*

Inorganic Nanotubes and Nanowires in Polymer Matrices: Potential for Sensing Applications

Andraž Rešetič[a], Luka Pirker[a, b], Anja Pogačnik Krajnc[a], Jasmina Lazarević[c], Maja Remškar[a], Bojana Višić[a,c]

[a] *Jozef Stefan Institute, Jamova cesta 39, Ljubljana, Slovenia*
[b] *J. Heyrovský Institute of Physical Chemistry, CAS, Dolejškova 2155/3, Prague 8, Czech Republic*
[c] *Center for Solid State Physics and New Materials, Institute of Physics Belgrade, University of Belgrade, Pregrevica 118, 11000 Belgrade, Serbia*

Abstract. The increasing need to move away from intrinsically rigid to flexible and wearable sensors requires finding a sensing material that responds well to mechanical deformations through a change in the electrical signal. The best way to achieve flexibility is to combine nanomaterials with polymer matrices. While the carbon nanotubes have a good potential as fillers, they have a few setbacks as well. As they do not disperse well in most organic solvents, resulting in poor homogeneity when mixed with a polymer matrix, they have to be functionalized in order to enhance the interaction with the solvent. On the other hand, various inorganic TMDC NTs promise a wide spectrum of physical effects beyond the physics of CNTs [1]. They have a high aspect ratio, high specific surface area and excellent mechanical and vibrational/acoustic properties, making them suitable as composite nanofillers as only a small amount can be used for forming a conductive path [2]. Furthermore, MS_2 NTs disperse well in all commonly used solvents, simplifying the composite preparation [3]. Another family of nanomaterials that shows a great promise as a filler, is the family of metal oxides. Their substoichiometric MO_{3-x} ($0 \leq x \leq 1$) phases grow in different shapes, such as nanowires, flakes, needles and sheets. The optical, electrical and structural properties depend strongly on the degree of the reduction [4].
Overall, these materials possess a variety of properties desirable for fabrication of sensors for human health monitoring. Despite the advancements, thorough safety assessments are needed before large-scale production and clinical deployment of nanomaterials for health sensing applications [5].

REFERENCES

1. Višić, B. et al., *JACS* **139** 12865-78 (2017)
2. Evarestov, R. et al., *Materials Research Express* ***5*** 115028 (2018)
3. Yadgarov, L. et al., Physical Chemistry Chemical Physics **20** 20812-20 (2018)
4. Višić, B., et al., Nanotechnology **33** 275705 (2022)
5. Lazarević, J. and Višić, B., under review

BOOK OF ABSTRACTS

ADVANCES
IN SOLID STATE PHYSICS
AND NEW MATERIALS

ДОСТИГНУЋА У ФИЗИЦИ ЧВРСТОГ СТАЊА И НОВИХ МАТЕРИЈАЛА

30 година Центра за физику чврстог стања и нове материјале Института за физику у Београду

ADVANCES IN SOLID STATE PHYSICS AND NEW MATERIALS

30 years of the Center for Solid State Physics and New Materials at the Institute of Physics Belgrade

19 - 23 May 2025
Belgrade, Serbia

CSSPNM
CENTER FOR
SOLID STATE PHYSICS
AND NEW MATERIALS

HIP-2D-QM

IPB

CAHY

Conference Chairs

Nenad Lazarević, *Institute of Physics Belgrade, Serbia*
Emil S. Božin, *Institute of Physics Belgrade, Serbia*
Rudi Hackl, *IFW Dresden, Germany*
Zoran V. Popović, *Serbian Academy of Sciences and Arts (SANU), Serbia* – honorary chair

Organizing Committee

Jelena Pešić - chair
Bojana Višić – chair

Ana Kanjevac
Ana Milosavljević
Andrijana Šolajić
Barbara Bekić
Bojan Stojadinović
Branka Hadžić
Ivana Milošević
Jasmina Lazarević
Jelena Mitrić
Jelena Trajković
Jovan Blagojević
Lenka Filipović
Marko Opačić
Milica Petrović
Nataša Tomić
Novica Paunović
Tea Belojica
Tijana Tomašević Ilić

Scientific Committee

Rudi Hackl, *IFW Dresden, Germany*
Nenad Lazarević, *Institute of Physics Belgrade, Serbia*
Emil S. Božin, *Institute of Physics Belgrade, Serbia*
Elena Gati, *Max Planck Institute for Chemical Physics of Solids, Germany*
John S. O. Evans, *Durham University, UK*
Zdeněk Sofer, *UCT Prague, Czech Republic*
Milorad Milošević, *University of Antwerp, Belgium*
Marija Drndić, *University of Pennsylvania, USA*
Simon J. L. Billinge, *Columbia University, USA*
Yann Gallais, *Université Paris Cité, France*

Advisory Committee

Bernd Büchner, *IFW Dresden, Germany*
Reshef Tenne, *Weizmann Institute of Science, Israel*
Zoran V. Popović, *Serbian Academy of Sciences and Arts (SANU), Serbia*
Dragana Popović, *Florida State University, USA*
Maja Remškar, *Jožef Stefan Institute, Slovenia*
Matthieu Le Tacon, *Karlsruhe Institute of Technology, Germany*
Wei Ku, *Tsung-Dao Lee Institute & Shanghai Jiao Tong University, China*

Diversification of Primary Mesenchymal Stromal/Stem Cell Populations at the Single-Cell Level Using Raman Spectroscopy

Tamara Kukolj [a], Jasmina Lazarević [b], Ana Borojević [c], Uroš Ralević [b], Dragana Vujić [cd], Aleksandra Jauković [a], Nenad Lazarević [b] and Diana Bugarski[a]

[a] *Group for Hematology and Stem Cells, Institute for Medical Research, National Institute of Republic of Serbia, University of Belgrade, 11129 Belgrade, Serbia.*
[b] *Center for Solid State Physics and New Materials, Institute of Physics Belgrade, University of Belgrade, Pregrevica 118, 11080 Belgrade, Serbia.*
[c] *Mother and Child Health Care Institute of Serbia "Dr Vukan Čupić", 11000 Belgrade, Serbia.*
[d] *School of Medicine, University of Belgrade, 11000 Belgrade, Serbia.*

Abstract. As a promising optical technique for application in biomedicine, Raman spectroscopy has been used for stem cell analysis, whereby the largest number of studies was based on the examination of the differentiation status of mesenchymal stromal/stem cells (MSCs) [1,2]. Namely, MSCs represent a diverse population of multipotent precursors that reside in many tissues. They have been isolated from various tissues and organs including bone marrow, adipose tissue, teeth, amniotic fluid, umbilical cord, tendon, etc., and due to simple and non-invasive isolation procedures MSCs are considered a valuable alternative source for cell replacement therapies. The main features of these cells are the ability to self-renew and the differentiation into several types of mature cells such as osteoblasts, adipocytes, chondrocytes under in vitro conditions. However, there is no precise marker that can be used to isolate and characterize this cell population, which significantly hinders further progress in potential application of these cells for therapeutic purposes. Therefore, our goal was to investigate the use of Raman spectroscopy to characterize biochemical profile of MSCs at single-cell level. In this study primary human MSCs derived from bone marrow (BM-MSCs) of five healthy pediatric donors collected during allogenic transplantation were analyzed. By using standard biological tests related to the MSCs features such as adherence, phenotype, clonogenicity, proliferation rate, pluripotency and multilineage differentiation potential variations between these donors were not detected. Raman spectroscopy analysis of MSCs at the single-cell level revealed a similar biochemical background of the tested samples. However, following the extensive principal component analysis (PCA), a clustering of MSCs populations was detected, particularly when the samples were analyzed in pairs. Obtained results indicate that Raman spectroscopy technique could provide valuable information for MSCs diversification and contribute to MSCs characterization, consequently accelerating their application in cell therapy [3].

REFERENCES

1. Bautista-González, S., Carrillo, González, N.J., Campos-Ordoñez, T., Acosta, Elías, M.A., Pedroza-Montero, M.R., Beas-Zárate, C., Gudiño-Cabrera, G., "Raman spectroscopy to assess the

BOOK OF ABSTRACTS

ADVANCES
IN SOLID STATE PHYSICS
AND NEW MATERIALS

ДОСТИГНУЋА У ФИЗИЦИ ЧВРСТОГ СТАЊА И НОВИХ МАТЕРИЈАЛА

30 година Центра за физику чврстог стања и нове материјале Института за физику у Београду

ADVANCES IN SOLID STATE PHYSICS AND NEW MATERIALS

30 years of the Center for Solid State Physics and New Materials at the Institute of Physics Belgrade

19 - 23 May 2025
Belgrade, Serbia

Conference Chairs

Nenad Lazarević, *Institute of Physics Belgrade, Serbia*
Emil S. Božin, *Institute of Physics Belgrade, Serbia*
Rudi Hackl, *IFW Dresden, Germany*
Zoran V. Popović, *Serbian Academy of Sciences and Arts (SANU), Serbia* – honorary chair

Organizing Committee

Jelena Pešić - chair
Bojana Višić – chair

Ana Kanjevac
Ana Milosavljević
Andrijana Šolajić
Barbara Bekić
Bojan Stojadinović
Branka Hadžić
Ivana Milošević
Jasmina Lazarević
Jelena Mitrić
Jelena Trajković
Jovan Blagojević
Lenka Filipović
Marko Opačić
Milica Petrović
Nataša Tomić
Novica Paunović
Tea Belojica
Tijana Tomašević Ilić

Scientific Committee

Rudi Hackl, *IFW Dresden, Germany*
Nenad Lazarević, *Institute of Physics Belgrade, Serbia*
Emil S. Božin, *Institute of Physics Belgrade, Serbia*
Elena Gati, *Max Planck Institute for Chemical Physics of Solids, Germany*
John S. O. Evans, *Durham University, UK*
Zdeněk Sofer, *UCT Prague, Czech Republic*
Milorad Milošević, *University of Antwerp, Belgium*
Marija Drndić, *University of Pennsylvania, USA*
Simon J. L. Billinge, *Columbia University, USA*
Yann Gallais, *Université Paris Cité, France*

Advisory Committee

Bernd Büchner, *IFW Dresden, Germany*
Reshef Tenne, *Weizmann Institute of Science, Israel*
Zoran V. Popović, *Serbian Academy of Sciences and Arts (SANU), Serbia*
Dragana Popović, *Florida State University, USA*
Maja Remškar, *Jožef Stefan Institute, Slovenia*
Matthieu Le Tacon, *Karlsruhe Institute of Technology, Germany*
Wei Ku, *Tsung-Dao Lee Institute & Shanghai Jiao Tong University, China*

Symmetry-Resolved Raman Study of Temperature-Induced Phonon Anomalies in $ZrTe_5$

Ana Kanjevac[a], Ana Milosavljević[a], Emil Božin[a,b], Jasmina Lazarević[a],
Jovan Blagojević[a], Qiang Li[c,d] and Nenad Lazarević[a]

[a]*Institute of Physics Belgrade, University of Belgrade, Pregrevica 118, 11080 Belgrade, Serbia*
[b]*Computational Science Initiative, Brookhaven National Laboratory, Upton, NY 11973, USA*
[c]*Condensed Matter Physics and Materials Science Department, Brookhaven National Laboratory, Upton, NY, USA*
[d]*Department of Physics and Astronomy, Stony Brook University, Stony Brook, NY, USA*

Abstract. Zirconium pentatelluride ($ZrTe_5$) has attracted considerable attention in the condensed matter community due to its temperature-dependent band gap variations. Additionally, it has been proposed that $ZrTe_5$ lies near a phase boundary between strong (STI) and weak topological insulator (WTI) phases, as well as undergoing an electronic topological (Lifshitz) transition. Depending on the sample and synthesis conditions, the Lifshitz transition temperature varies between 50 and 150 K [1–3]. In this study, we performed Raman spectroscopic analysis of $ZrTe_5$ single crystals over a temperature range of 76 to 300 K. The measurements were carried out in symmetry-resolved scattering geometries using parallel and cross polarization configurations along the principal crystallographic directions. In this setup, only phonon modes of A_g and B_{2g} symmetries are allowed in the respective configurations. The results reveal pronounced temperature-dependent behavior, including variations in phonon linewidths and peak positions. Notably, at lower temperatures, certain phonon modes exhibit asymmetric line shapes that are well described by the Fano profile. As the temperature increases, these features gradually evolve into symmetric peaks. This behavior indicates a strong coupling between lattice vibrations and electronic excitations in $ZrTe_5$. Our Raman scattering results provide valuable insight into the phonon dynamics and electron–phonon coupling in $ZrTe_5$, contributing to a deeper understanding of its fundamental properties.

REFERENCES

1. Zhang, J., Wang, C., Wang, J., et al. “Signatures of a Lifshitz Transition in the Mixed Dirac-Weyl Semimetal $ZrTe_5$,” Phys. Rev. B 108, L041202 (2023).
2. Lozano, P. M., et al. “Anomalous Hall Effect at the Lifshitz Transition in $ZrTe_5$,” Phys. Rev. B 106, L081124 (2022).
3. Zhang, Y., Xu, C., Song, Y., et al. “Electronic Evidence of Temperature-Induced Lifshitz Transition and Topological Nature in $ZrTe_5$” Nat. Commun. 8, 15512 (2017).

*This research was supported by the Science Fund of the Republic of Serbia, 10925, Dynamics of CDW transition in strained quasi-1D systems - DYNAMIQS

BOOK OF ABSTRACTS

ADVANCES
IN SOLID STATE PHYSICS
AND NEW MATERIALS

ДОСТИГНУЋА У ФИЗИЦИ ЧВРСТОГ СТАЊА И НОВИХ МАТЕРИЈАЛА

30 година Центра за физику чврстог стања и нове материјале Института за физику у Београду

ADVANCES IN SOLID STATE PHYSICS AND NEW MATERIALS

30 years of the Center for Solid State Physics and New Materials at the Institute of Physics Belgrade

19 - 23 May 2025
Belgrade, Serbia

Conference Chairs

Nenad Lazarević, *Institute of Physics Belgrade, Serbia*
Emil S. Božin, *Institute of Physics Belgrade, Serbia*
Rudi Hackl, *IFW Dresden, Germany*
Zoran V. Popović, *Serbian Academy of Sciences and Arts (SANU), Serbia* – honorary chair

Organizing Committee

Jelena Pešić - chair
Bojana Višić – chair

Ana Kanjevac
Ana Milosavljević
Andrijana Šolajić
Barbara Bekić
Bojan Stojadinović
Branka Hadžić
Ivana Milošević
Jasmina Lazarević
Jelena Mitrić
Jelena Trajković
Jovan Blagojević
Lenka Filipović
Marko Opačić
Milica Petrović
Nataša Tomić
Novica Paunović
Tea Belojica
Tijana Tomašević Ilić

Scientific Committee

Rudi Hackl, *IFW Dresden, Germany*
Nenad Lazarević, *Institute of Physics Belgrade, Serbia*
Emil S. Božin, *Institute of Physics Belgrade, Serbia*
Elena Gati, *Max Planck Institute for Chemical Physics of Solids, Germany*
John S. O. Evans, *Durham University, UK*
Zdeněk Sofer, *UCT Prague, Czech Republic*
Milorad Milošević, *University of Antwerp, Belgium*
Marija Drndić, *University of Pennsylvania, USA*
Simon J. L. Billinge, *Columbia University, USA*
Yann Gallais, *Université Paris Cité, France*

Advisory Committee

Bernd Büchner, *IFW Dresden, Germany*
Reshef Tenne, *Weizmann Institute of Science, Israel*
Zoran V. Popović, *Serbian Academy of Sciences and Arts (SANU), Serbia*
Dragana Popović, *Florida State University, USA*
Maja Remškar, *Jožef Stefan Institute, Slovenia*
Matthieu Le Tacon, *Karlsruhe Institute of Technology, Germany*
Wei Ku, *Tsung-Dao Lee Institute & Shanghai Jiao Tong University, China*

Theoretical Prediction and Experimental Validation of Temperature-Dependent Raman Spectra of Doxorubicin

Sylwia Orzechowska[a*], Ena Todorović[b*], Milan Milovanović[b], Jelena Pešić[c], Malgorzata Baranska[a], Jasmina Lazarević[c] and Nenad Lazarević[c]

[a] *Faculty of Chemistry, Jagiellonian University, 3 Ingarden Str., Krakow, Poland*
[b]*Faculty of Physical Chemistry, University of Belgrade*
[c] *Center for Solid State Physics and New Materials, Institute of Physics Belgrade, Pregrevica 118, Belgrade, Serbia*

[*]*The authors contributed equally*

Abstract Temperature-dependent Raman spectra of doxorubicin revealed a pronounced evolution of spectral features, with a notable crossover in peak intensities occurring between 100 K and 300 K. Theoretical Raman spectra of a single doxorubicin molecule were calculated using the ORCA program. The GOAT algorithm was used to identify isomers of neutral doxorubicin, doxorubicin hydrochloride, and its cationic form. The most stable structures were optimized, and harmonic vibrational frequencies and Raman activities were computed at the R2SCAN/def2-TZVP level of theory with D3 dispersion. Spectra for a doxorubicin dimer were also simulated. The observed temperature-dependent spectral features were successfully explained by resonant Raman calculations, which included spectral broadening, anharmonic scaling, and Duschinsky rotation effects. Theoretical predictions were compared with experimental data using the Python-based SARA program, showing excellent agreement across the studied temperature range.

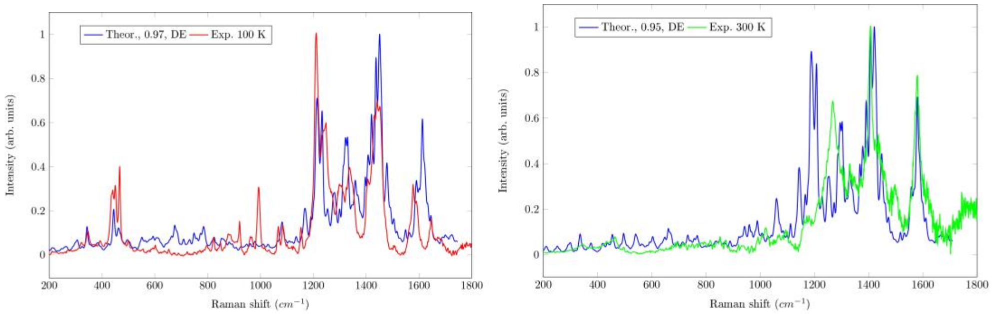

FIGURE 1. Experimental Raman and theoretical resonant Raman spectra of doxorubicin at 100K (left) and 300K (right).

Committees

Organising Committee

Antonio Correia	Phantoms Foundation (Spain) - **Chairperson**
Francesco Bonaccorso	Bedimensional (Italy)
Jean-Christophe Charlier	Universite Catholique de Louvain (Belgium)
Ricardo Diez Muiño	DIPC & Ikerbasque (Spain)
Vladimir Falko	The University of Manchester / NGI (UK)
Xinliang Feng	Technische Universitaet Dresden (Germany)
Max Lemme	AMO GmbH / RWTH Aachen (Germany)
Stephan Roche	ICREA/ICN2 (Spain)

Local Organizing Committee

Aran Garcia-Lekue	DIPC - EHU/UPV (Spain)
Amaia Zurutuza	Graphenea (Spain)

International Scientific Committee (ISC)

Vladimir Falko	The University of Manchester / NGI (UK) - **Chairperson**
Hiroki Ago	Kyushu University (Japan)
Jong-Hyun Ahn	Yonsei University (South Korea)
Leni Bascones	ICMM/CSIC (Spain)
Blanca Biel	University of Granada (Spain)
Peter Boggild	DTU (Denmark)
Lapo Bogani	Università degli Studi di Firenze (Italy)
Cinzia Casiraghi	University of Manchester (UK)
Hyeonsik Cheong	Sogang University (South Korea)
Camilla Coletti	IIT (Italy)
Alessandro Cresti	CNRS (France)
Costas Galiotis	FORTH/ ICE-HT and University of Patras (Greece)
Antti-Pekka Jauho	DTU (Denmark)
Ado Jorio	Universidade Federal de Minas Gerais (Brazil)
Jeanie Lau	Ohio State University (USA)
Vittorio Morandi	IMM-CNR (Italy)
Aitor Mugarza	ICN2 (Spain)
Shu Nakaharai	NIMS (Japan)
Iwona Pasternak	Warsaw University of Technology (Poland)
Rebeca Ribeiro	Université Paris-Saclay (France)
Yarjan Abdul Samad	Khalifa University (UAE)
Daniel Sanchez Portal	CFM/CSIC - UPV/EHU & DIPC (Spain)
Andrey Turchanin	Friedrich Schiller University Jena (Germany)
Christophe Voisin	ENS Paris (France)

Industrial International Committee (I2C)

Luigi Colombo	The University of Texas at Dallas (USA) - **Chairperson**
Max Lemme	AMO GmbH (Germany) - **Co-chairperson**
Francesco Bonaccorso	Bedimensional (Italy)
Yunqiao Fu	BGI (China)
Kari Hjelt	Chalmers Industriteknik (Sweden)

Technical Committee

Concepción Narros	Phantoms Foundation, Spain
Joaquin Ramón-Laca Maderal	Phantoms Foundation, Spain
Jose Luis Roldan	Phantoms Foundation, Spain

Phonon Signatures of Instabilities in van der Waals material $InSiTe_3$

Jasmina Lazarević[1]
Ana Milosavljević[1], Sanja Djurdjić Mijin[1,2], Tea Belojica[1], Jovan Blagojević[1], Andrijana Šolajić[1], Jelena Pešić[1], Bojana Višić[1], Vladimir Damljanović[1], Michael O. Ogunbunmi[3], Svilen Bobev[3,4], Yu Liu[4], Cedomir Petrovic[4,5,6], Zoran V. Popović[7], and Nenad Lazarević[1]

[1] Institute of Physics Belgrade, University of Belgrade, Pregrevica 118, 11080 Belgrade, Serbia
[2] Departamento de Fisica de Materiales, Facultad de Ciencias, Universidad Autnoma de Madrid, 28049 Madrid, Spain
[3] Department of Chemistry and Biochemistry, University of Delaware, Newark, Delaware 19716, U.S.A.
[4] Condensed Matter Physics and Materials Science Department, Brookhaven National Laboratory, Upton, NY 11973-5000, USA
[5] Shanghai Advanced Research in Physical Sciences (SHARPS), Shanghai 201203, China
[6] Department of Nuclear and Plasma Physics, Vinca Institute of Nuclear Sciences, University of Belgrade, Belgrade 11001, Serbia
[7] Serbian Academy of Sciences and Arts, Knez Mihailova 35, 11000 Belgrade, Serbia
jasmina.lazarevic@ipb.ac.rs

Although van der Waals materials are widely studied for their unique properties and applications, $InSiTe_3$ remains relatively neglected despite being synthesized over 30 years ago, especially when compared to the extensive research on related compounds like $CrSiTe_3$ and $CrGeTe_3$. Here, we present a detailed experimental and theoretical investigation of this van der Waals material. Single-crystal X-ray diffraction reveals the rhombohedral crystal symmetry of InSiTe3, described with the $P\bar{3}$ space group. Polarization-dependent inelastic light scattering experiments further validate the symmetry and reveal pronounced anharmonicity in $InSiTe_3$. Namely, in addition to the symmetry predicted Raman active modes, which show excellent agreement with DFT calculations, the spectra exhibit unexpected features; tripling of a localized high-energy A_g mode at approximately 500 cm^{-1}. For E_g modes the extracted phonon-phonon coupling constants indicate moderate anharmonicity. However, for A_g modes, the coupling strength increases dramatically, reaching values up to ten times higher than those of the doubly degenerate modes. The intensities of the analysed A_g modes display anomalous behaviour with increasing the temperature, particularly around 200 K. Notably, at this same temperature, higher-order overtone excitations emerge within the gap of the calculated phonon density of states. Having in mind that phonons couple to various degrees of freedom, these interactions leave a distinct fingerprint on their behaviour. While our findings highlight these instabilities, its origin lies beyond the scope of this research.

*This research was supported by the Science Fund of the Republic of Serbia, 10925, Dynamics of CDW transition in strained quasi-1D systems - DYNAMIQS

Aim of the Conference

Main aim of the conference is to enable young researchers (post-graduate, master or doctoral student, or a PhD holder younger than 35) working in the field of materials science and engineering, to meet their colleagues and exchange experiences about their research.

Topics

Biomaterials
Environmental science
Materials for high-technology applications
Materials for new generation solar cells
Nanostructured materials
New synthesis and processing methods
Theoretical modelling of materials

Scientific and Organizing Committee

Committee President

Smilja Marković	Institute of Technical Sciences of SASA, Belgrade, Serbia

Vice-presidents

Ivana Dinić	Institute of Technical Sciences of SASA, Belgrade, Serbia
Sonja Jovanović	Institute of Nuclear Sciences “Vinča”, Belgrade, Serbia
Đorđe Veljović	Faculty of Technology and Metallurgy, Belgrade, Serbia

Members

Katarina Cvetanović	Institute of Chemistry, Technology and Metallurgy, Belgrade, Serbia
Tatiana Demina	Enikolopov Institute of Synthetic Polymeric Materials, Russian Academy of Sciences
Xuesen Du	Chongqing University, Chongqing, China
Nenad Filipović	Institute of Technical Sciences of SASA, Belgrade, Serbia
Dragana Jugović	Institute of Technical Sciences of SASA, Belgrade, Serbia
Marijana Kraljić Roković	Faculty of Chemical Engineering and Technology, Zagreb, Croatia
Snežana Lazić	Universidad Autónoma de Madrid, Spain
Lidija Mančić	Institute of Technical Sciences of SASA, Belgrade, Serbia
Bojan Marinković	Pontifical Catholic University of Rio de Janeiro, Rio de Janeiro, Brazil
Marija Milanović	Faculty of Technology, Novi Sad, Serbia
Jelena Mitrić	Institute of Physics, Belgrade, Serbia
Nebojša Mitrović	Faculty of Technical Sciences, Čačak, Serbia
Anđela Mitrović Rajić	Institute of Technical Sciences of SASA, Belgrade, Serbia
Irena Nikolić	Faculty of Metallurgy and Technology, Podgorica, Montenegro
Marko Opačić	Institute of Physics, Belgrade, Serbia
Alexander Osmolovskiy	Lomonosov Moscow State University, Moscow, Russia
Vuk Radmilović	Faculty of Technology and Metallurgy, Belgrade, Serbia

Milan Radovanović	Technical Faculty in Bor, Serbia
Vladimir Rajić	Institute of Nuclear Sciences “Vinča”, Belgrade, Serbia
Julietta Rau	Institute of the Structure of Matter of the Italian National Research Council (ISM-CNR), Rome, Italy
Ana Stanković	Institute of Technical Sciences of SASA, Belgrade, Serbia
Boban Stojanović	Faculty of Sciences, Kragujevac, Serbia
Ivana Stojković Simatović	Faculty of Physical Chemistry, Belgrade, Serbia
Srečo Škapin	Institute Jožef Stefan, Ljubljana, Slovenia
Konrad Terpiłowski	Department of Interfacial Phenomena, Institute of Chemical Sciences, Faculty of Chemistry, Maria Curie-Skłodowska University in Lublin, Poland
Nina Tomić	Institute of Technical Sciences of SASA, Belgrade, Serbia
Vuk Uskoković	TardigradeNano, Irvine, CA, USA
Rastko Vasilić	Faculty of Physics, Belgrade, Serbia
Ljiljana Veselinović	Institute of Technical Sciences of SASA, Belgrade, Serbia

Conference Secretary

Aleksandra Stojičić	Institute of Technical Sciences of SASA, Belgrade, Serbia

Conference Technical Committee

Teodora Jakovljević, Željko Mravik, Sofija Petković, Miljana Piljević, Barbara Ramadani, Nina Tomić, Marina Vuković.

Results of the Conference

Beside printed «Program and the Book of Abstracts», which is disseminated to all conference participants, selected and awarded peer-reviewed papers will be published in journal “Tehnika – Novi Materijali”. The best presented papers, suggested by Session Chairpersons and selected by Awards Committee, will be proclaimed at the Closing Ceremony. Part of the award is free-of-charge conference fee at YUCOMAT 2026.

Sponsors

TEVUS
lab science

SUPERLAB®
Your Lab – Our Passion

Acknowledgement

The editor and the publisher of the Book of abstracts are grateful to the Ministry of Science, Technological Development and Innovation of the Republic of Serbia for its financial support of this book and The Twenty-Third Young Researchers’ Conference - Materials Sciences and Engineering, held in Belgrade, Serbia.

7-3

Evidence of temperature-induced lifshitz transition in topological material $ZrTe_5$

Ana Kanjevac[1], Ana Milosavljević[1], Jasmina Lazarević[1], Jovan Blagojević[1], Qiang Li [2,3]
Emil S Božin[1,2], Nenad Lazarević[1]

[1]*Center for Solid State Physics and New Materials, Institute of Physics Belgrade, University of Belgrade, Pregrevica 118, 11080 Belgrade, Serbia*
[2]*Condensed Matter Physics and Materials Science Department, Brookhaven National Laboratory, Upton, New York 11973-5000, USA*
[3]*Department of Physics and Astronomy, Stony Brook University, Stony Brook, New York, USA*

Topological Dirac semimetal $ZrTe_5$ has been the subject of extensive experimental and theoretical investigation, as it lies near the boundary between strong and weak topological insulator phases and hosts a Dirac semimetal state at the electronic (Lifshitz) transition. The reported Lifshitz transition temperature in $ZrTe_5$ varies between 50 and 150 K, depending on sample quality and synthesis conditions. In this study, we performed Raman spectroscopic analysis of $ZrTe_5$ single crystals over a temperature range from 40 to 300 K. The measurements were carried out in symmetry-resolved scattering geometries using parallel and cross polarization configurations along the principal crystallographic directions, within the *ac* plane, allowing observation of six A_g and two B_{2g} phonon modes. Our results reveal that all A_g modes exhibit changes in energies and linewidths within the temperature range of the proposed topological transition. In the parallel polarization configuration, peak asymmetry is observed for four of the six A_g modes, while in the crossed polarisation configuration, only the first B_{2g} mode exhibits a similar feature. These asymmetric line shapes are well described by the Fano profile, suggesting a significant electron–phonon interaction. Our Raman scattering results provide insight into the coupling between lattice vibrations and electronic structure and its temperature-driven topological behavior.

Acknowledgements: This research is financed by HIP-2D-QM Project. This project received funding from the European Union's Horizon Europe research and innovation programme under grant agreement NO 101185375. This research was supported by the Science Fund of the Republic of Serbia, 10925, Dynamics of CDW transition in strained quasi-1D systems – DYNAMIQS. The authors acknowledge funding provided by the Institute of Physics Belgrade, through the grant by the Ministry of Science, Technological Development and Innovation of the Republic of Serbia.

Aim of the Conference

Main aim of the conference is to enable young researchers (post-graduate, master or doctoral student, or a PhD holder younger than 35) working in the field of materials science and engineering, to meet their colleagues and exchange experiences about their research.

Topics

Biomaterials
Environmental science
Materials for high-technology applications
Materials for new generation solar cells
Nanostructured materials
New synthesis and processing methods
Theoretical modelling of materials

Scientific and Organizing Committee

Committee President

Smilja Marković	Institute of Technical Sciences of SASA, Belgrade, Serbia

Vice-presidents

Ivana Dinić	Institute of Technical Sciences of SASA, Belgrade, Serbia
Sonja Jovanović	Institute of Nuclear Sciences "Vinča", Belgrade, Serbia
Đorđe Veljović	Faculty of Technology and Metallurgy, Belgrade, Serbia

Members

Katarina Cvetanović	Institute of Chemistry, Technology and Metallurgy, Belgrade, Serbia
Tatiana Demina	Enikolopov Institute of Synthetic Polymeric Materials, Russian Academy of Sciences
Xuesen Du	Chongqing University, Chongqing, China
Nenad Filipović	Institute of Technical Sciences of SASA, Belgrade, Serbia
Dragana Jugović	Institute of Technical Sciences of SASA, Belgrade, Serbia
Marijana Kraljić Roković	Faculty of Chemical Engineering and Technology, Zagreb, Croatia
Snežana Lazić	Universidad Autónoma de Madrid, Spain
Lidija Mančić	Institute of Technical Sciences of SASA, Belgrade, Serbia
Bojan Marinković	Pontifical Catholic University of Rio de Janeiro, Rio de Janeiro, Brazil
Marija Milanović	Faculty of Technology, Novi Sad, Serbia
Jelena Mitrić	Institute of Physics, Belgrade, Serbia
Nebojša Mitrović	Faculty of Technical Sciences, Čačak, Serbia
Anđela Mitrović Rajić	Institute of Technical Sciences of SASA, Belgrade, Serbia
Irena Nikolić	Faculty of Metallurgy and Technology, Podgorica, Montenegro
Marko Opačić	Institute of Physics, Belgrade, Serbia
Alexander Osmolovskiy	Lomonosov Moscow State University, Moscow, Russia
Vuk Radmilović	Faculty of Technology and Metallurgy, Belgrade, Serbia

Milan Radovanović	Technical Faculty in Bor, Serbia
Vladimir Rajić	Institute of Nuclear Sciences “Vinča”, Belgrade, Serbia
Julietta Rau	Institute of the Structure of Matter of the Italian National Research Council (ISM-CNR), Rome, Italy
Ana Stanković	Institute of Technical Sciences of SASA, Belgrade, Serbia
Boban Stojanović	Faculty of Sciences, Kragujevac, Serbia
Ivana Stojković Simatović	Faculty of Physical Chemistry, Belgrade, Serbia
Srečo Škapin	Institute Jožef Stefan, Ljubljana, Slovenia
Konrad Terpiłowski	Department of Interfacial Phenomena, Institute of Chemical Sciences, Faculty of Chemistry, Maria Curie-Skłodowska University in Lublin, Poland
Nina Tomić	Institute of Technical Sciences of SASA, Belgrade, Serbia
Vuk Uskoković	TardigradeNano, Irvine, CA, USA
Rastko Vasilić	Faculty of Physics, Belgrade, Serbia
Ljiljana Veselinović	Institute of Technical Sciences of SASA, Belgrade, Serbia

Conference Secretary

Aleksandra Stojičić	Institute of Technical Sciences of SASA, Belgrade, Serbia

Conference Technical Committee

Teodora Jakovljević, Željko Mravik, Sofija Petković, Miljana Piljević, Barbara Ramadani, Nina Tomić, Marina Vuković.

Results of the Conference

Beside printed «Program and the Book of Abstracts», which is disseminated to all conference participants, selected and awarded peer-reviewed papers will be published in journal “Tehnika – Novi Materijali”. The best presented papers, suggested by Session Chairpersons and selected by Awards Committee, will be proclaimed at the Closing Ceremony. Part of the award is free-of-charge conference fee at YUCOMAT 2026.

Sponsors

TEVUS lab science

SUPERLAB® Your Lab – Our Passion

Acknowledgement

The editor and the publisher of the Book of abstracts are grateful to the Ministry of Science, Technological Development and Innovation of the Republic of Serbia for its financial support of this book and The Twenty-Third Young Researchers’ Conference - Materials Sciences and Engineering, held in Belgrade, Serbia.

9-1

Theoretical prediction and experimental validation of temperature-dependent raman spectra of doxorubicin

Ena Todorović[1], Sylwia Orzechowska[2], Milan Milovanović[1], Jelena Pešić[3], Malgorzata Baranska[2], Jasmina Lazarević[3], Nenad Lazarević[3]

[1]Faculty of Physical Chemistry, University of Belgrade, Studentski trg 12-16, PAC 105305, Belgrade, Serbia
[2]Faculty of Chemistry, Jagiellonian University, Krakow, Poland
[3]Center for Solid State Physics and New Materials, Institute of Physics Belgrade, Pregrevica 118, Belgrade, Serbia

Temperature-dependent Raman spectra of doxorubicin (DOX) show pronounced changes in band intensities between 100 and 300 K. Detailed analysis and comparison with simulated resonance Raman spectra indicate that these variations arise primarily from temperature-dependent resonance effects. The GOAT algorithm, implemented through the ORCA program, was employed to identify isomers of neutral DOX, DOX-HCl, and DOX-H^+. The most stable structures were optimized, and harmonic vibrational frequencies and Raman activities were computed at the R2SCAN/def2-TZVP level of theory with D3 dispersion corrections. The observed temperature-dependent spectral features were successfully reproduced by resonance Raman calculations that included spectral broadening, anharmonic scaling, and Duschinsky rotation effects. Quantitative comparison using the SARA algorithm yielded 91–94% agreement between theory and experiment across all temperatures. Increasing temperature was found to weaken hydrogen-bonding modes while enhancing collective ring vibrations, consistent with reduced hydrogen-bond strength and increased vibrational delocalization.

PHYSICAL CHEMISTRY 2024

17th International Conference on Fundamental and Applied Aspects of Physical Chemistry

Organized by

The Society of Physical Chemists of
Serbia

in co-operation with

Institute of Catalysis, Bulgarian Academy of Sciences

and

Boreskov Institute of Catalysis, Siberian Branch of
Russian Academy of Sciences

and

University of Belgrade, Serbia:

Faculty of Physical Chemistry
Institute of Chemistry, Technology and Metallurgy
Vinča Institute of Nuclear Sciences
Faculty of Pharmacy

and

Institute of General and Physical Chemistry, Belgrade, Serbia

International Organizing Committee

Chairman: S. Anić (Serbia)
Vice-chairman: Z. Petkova Cherkezova-Zheleva (Bulgaria)
Oleg N. Martyanov (Russia)
S. N. Blagojević (Serbia)
Members: N. Cvjetićanin (Serbia), S. M. Blagojević (Serbia), M. Daković (Serbia), J. Dimitrić-Marković (Serbia), T. Grozdić (Serbia), Lj. Ignjatović (Serbia), A. Ivanović-Šašić (Serbia), D. Jovanović (Serbia), N. Jović-Jovičić (Serbia), M. Kuzmanović (Serbia), S. Maćešić (Serbia), D. Marković (Serbia), B. Milosavljević (USA), M. Mojović (Serbia), N. Pejić (Serbia), M. Petković (Serbia), A. Popović Bijelić (Serbia), B. Simonović (Serbia), B. Šljukić (Serbia), G. Tasić (Serbia), S. Veličković (Serbia), N. Vukelić (Serbia)

International Scientific Committee

Chairman: Ž. Čupić (Serbia)
Vice-chairman: V. Bukhtiyarov (Russia)
S. Minkovska-Dodova (Bulgaria)
B. Adnađević (Serbia)
Members: S. Anić (Serbia), A. Antić-Jovanović (Serbia), A. Clayton (Australia), P. Banković (Serbia), M. Fronczak (Poland), Lj. Gavrilovic (Norway), M. Jeremić (Serbia), E. Kiš (Serbia), A.V. Knyazev (Russia), L.I. László (Hungary), G. Lente (Hungary), S. Macura (USA), Z. Marković (Serbia), K. Novaković (UK), V. Parmon (Russia), D. Peddis (Italy), M.B. Plavšić (Serbia), L. J. Prins (Italy), J. Savović (Serbia), G. Schmitz (Belgium), I. Schreiber (Czech), L. Schreiberova (Czech), D. Stanisavljev (Serbia), N. Stepanov (Russia), Z. Šaponjić (Serbia), S. Tosti (Italy) Á. Tóth (Hungary), N. Vasilyeva (Russia), V. Vukojević (Sweden), A. De Wit (Belgium), A. Yüksel (Türkiye), M. Žabić (Bosnia and Herzegovina)

Local Executive Committee

Chairman: S. N. Blagojević
Vice-chairman: A. Ivanović-Šašić
Members: M. Ajduković, S. Bulatović, J. Dostanić, J. Đuričić-Milanković, M. Jelić, S. Jovanović, Z. Jovanović, N. Jović-Jovičić, B. Marković, J. Maksimović, S. Maćešić, S. Marinović, D. Milenković, T. Mudrinić, N. Nedić, M. Pagnacco, B. Stanković, I. Stefanović, T. Tadić, J. Parlić, M. Pejčić, G. Stevanović, H. Šalipur

INVESTIGATING TEMPERATURE-INDUCED PHASE TRANSITIONS IN ATORVASTATIN USING RAMAN SPECTROSCOPY

J.J. Lazarević, S. Usković-Marković, J. Mitrić and N. Lazarević

Center for Solid State Physics and New Materials, Institute of Physics Belgrade, University of Belgrade, Pregrevica 118, 11080 Belgrade, Serbia (jasminal@ipb.ac.rs)
[2] Faculty of Pharmacy, University of Belgrade, 11221 Belgrade, Serbia
.

DOI: https://doi.org/10.46793/Phys.Chem24II.595L

ABSTRACT

The Raman spectra of atorvastatin calcium trihydrate (ATC) were systematically investigated across a temperature range from 100 K to 460 K, revealing intricate vibrational and structural dynamics. Key observations included temperature-induced changes in spectral features, with significant transformations at 420 K, where intermolecular vibrations were strongly suppressed, indicating a collapse in crystal structure and potential formation of a liquid crystalline phase. This phase transition was evidenced by the disappearance of well-defined peaks and the appearance of broad hump-like structures, suggesting residual order before complete isotropic melting at 460 K. The study focused on both intramolecular and intermolecular vibrations, with the latter being prominent below 175 cm^{-1}. Temperature variations affected Raman modes, notably around 420 cm^{-1}, 490 cm^{-1}, and 635 cm^{-1}, reflecting structural and electronic changes. The investigation highlighted the stepwise dehydration of ATC, especially between 320 K and 380 K, supporting prior findings. These raveled changes provide extremely usable insights into the thermal adaptability and structural responsiveness of ATC, offering implications for its stability and performance in pharmaceutical applications.

IBSC

International Bioscience Conference and the
8th International PSU – UNS Bioscience Conference

Towards the SDG Challenges

ONLINE

25-26 November 2021, Novi Sad, Serbia

BOOK OF ABSTRACTS

IBCS2021 is organized jointly by:

University Prince of Songkla, Thailand
FACULTY OF SCIENCE

University of Novi Sad, Faculty of Sciences, Serbia

CIP - Каталогизација у публикацији
Библиотеке Матице српске, Нови Сад

631(082)(048.3)
602(082)(048.3)
502/504(082)(048.3)

THE International Bioscience Conference (2021 ; Novi Sad)
[Book of abstracts] / The International Bioscience Conference and the 8th International PSU - UNS Bioscience Conference IBSC 2021, 25-26 November, 2021 ; [editors Neda Mimica-Dukić, Slobodanka Pajević, Anamarija Mandić]. - Novi Sad : Prirodno-matematički fakultet, 2021. - 261 str. : ilustr. ; 30 cm

Način pristupa (URL): https://ibsc2021.pmf.uns.ac.rs/ebook-of-abstracts/. - Registar.

ISBN 978-86-7031-541-9

1. Joint international PSU-UNS Bioscience Conference (6 ; 2021 ; Novi Sad)
а) Пољопривреда -- Зборници -- Апстракти б) Биотехнологија -- Зборници -- Апстракти в) Животна средина -- Заштита -- Зборници -- Апстракти

COBISS.SR-ID 53483017

International Bioscience Conference (IBSC 2021) was supported by Ministry of Education, Science and Technological Development of the Republic of Serbia

Content

ABSTRACTS

Committee

Organizing Committee

1. Slobodanka Pajević, President, University of Novi Sad, Faculty of Sciences, Serbia
2. Anamarija Mandić, Vice president, University of Novi Sad, Institute of Food Technology, Serbia
3. Srđan Rončević, University of Novi Sad, Faculty of Sciences, Serbia
4. Gordana Vlahović, University of Novi Sad, Faculty of Sciences, Serbia
5. Ivana Pejović, University of Novi Sad, Faculty of Sciences, Serbia
6. Živana Komlenov Mudrinski, University of Novi Sad, Faculty of Sciences, Serbia
7. Saša Rakić, University of Novi Sad, Faculty of Sciences, Serbia
8. Branislava Lalić, University of Novi Sad, Faculty of Agriculture, Serbia
9. Vesna Mijatović Jovin, University of Novi Sad, Faculty of Medicine, Serbia
10. Biljana Božin, University of Novi Sad, Faculty of Medicine, Serbia
11. Nataša Simin, University of Novi Sad, Faculty of Sciences, Serbia
12. Milan Borišev, University of Novi Sad, Faculty of Sciences, Serbia
13. Dejan Orčić, University of Novi Sad, Faculty of Sciences, Serbia
14. Emilija Svirčev, University of Novi Sad, Faculty of Sciences, Serbia
15. Danijela Arsenov, University of Novi Sad, Faculty of Sciences, Serbia
16. Milan Županski, University of Novi Sad, Faculty of Sciences, Serbia
17. Aleksandra Tubić, University of Novi Sad, Faculty of Sciences, Serbia
18. Vidak Raičević, University of Novi Sad, Faculty of Sciences, Serbia
19. Jovana Grahovac, University of Novi Sad, Faculty of Technology, Serbia
20. Jaroslava Švarc-Gajić, University of Novi Sad, Faculty of Technology, Serbia
21. Neda Lakić, University of Novi Sad, Faculty of Medicine, Serbia
22. Mladen Horvatović, University of Novi Sad, Faculty of Sciences, Serbia
23. Oskar Marko, University of Novi Sad, BioSense Institute, Serbia
24. Miloš Ilić, University of Novi Sad, Faculty of Sciences, Serbia
25. Milana Rošul, University of Novi Sad, Institute of Food Technology, Serbia
26. Nataša Đerić, University of Novi Sad, Institute of Food Technology, Serbia
27. Nemanja Teslić, University of Novi Sad, Institute of Food Technology, Serbia
28. Dejan Ćaćić, University of Novi Sad, Faculty of Sciences, Serbia

Scientific Committee

1. Neda Mimica Dukić, President, University of Novi Sad, Faculty of Sciences, Serbia
2. Anchana Prathep, Prince of Songkla University (PSU), Thailand
3. Pimonsri Mittraparp-Arthorn, Prince of Songkla University (PSU), Thailand
4. Sara Bumrungsri, Prince of Songkla University (PSU), Thailand
5. Wipawadee Sianglum, Prince of Songkla University (PSU), Thailand
6. Chongdee Buranachai, Prince of Songkla University (PSU), Thailand
7. Pissared Muangnil, Prince of Songkla University (PSU), Thailand
8. Jaruwan Mayakul, Prince of Songkla University (PSU), Thailand
9. Komwit Surachat, Prince of Songkla University (PSU), Thailand
10. Patamarerk Engsontia, Prince of Songkla University (PSU), Thailand

11. Viktor Nedović, Ministry of Education, Science and Technological Development of the Republic of Serbia, University of Belgrade, Faculty of Agriculture, Serbia
12. Snežana Đorđević, University Colleague London (UCL), UK
13. Rudolf Bauer, University of Graz, Faculty of Pharmacy, Austria
14. Sari Kontunen-Soppela, University of Eastern Finland (UEF), Joensuu, Finland
15. Carmen Arena, University of Naples Federico II, Italy
16. Sílvia Rocha, University of Aveiro, Portugal
17. Declan Troy, The Agriculture and Food Development Authority (TEAGASC), Ireland
18. Brijesh Tiwary The Agriculture and Food Development Authority (TEAGASC), Ireland
19. Valerija Dunkić, University of Split, Croatia
20. Darko Modun, University of Split, Croatia
21. Olga Tzakou, University of Athens, Greece
22. Maria Couladis, University of Athens, Greece
23. Svetlana Kulevanova, University of Skopje, Macedonia
24. Rossella Russo, University of Calabria, Italy
25. Guido Jurgenliemk, University of Regensburg, Germany
26. Saša Orlović, University of Novi Sad, Institute of Lowland Forestry and Environment, Faculty of Agriculture, Serbia
27. Dragana Miladinović, Institute of Field and Vegetable Crops, Novi Sad, Serbia
28. Branko Ćupina, University of Novi Sad, Faculty of Agriculture, Serbia
29. Diana Bugarski, University of Belgrade, Institute for Medical Research, Serbia
30. Nada Kovačević, University of Belgrade, Faculty of Pharmacy, Serbia
31. Niko Radulović, University of Niš, Faculty of Sciences, Serbia
32. Jasmina Agbaba, University of Novi Sad, Faculty of Sciences, Serbia
33. Jadranka Luković, University of Novi Sad, Faculty of Sciences, Serbia
34. Snežana Radenković, University of Novi Sad, Faculty of Sciences, Serbia
35. Marijana Ačanski, University of Novi Sad, Faculty of Technology, Serbia
36. Jelena Pejin, University of Novi Sad, Faculty of Technology, Serbia
37. Aleksandar Fišteš, University of Novi Sad, Faculty of Technology, Serbia
38. Isidora Samojlik, University of Novi Sad, Faculty of Medicine, Serbia
39. Biljana Basarin, University of Novi Sad, Faculty of Sciences, Serbia
40. Ivana Beara, University of Novi Sad, Faculty of Sciences, Serbia
41. Nataša Nikolić, University of Novi Sad, Faculty of Sciences, Serbia
42. Aleksandra Mišan, University of Novi Sad, Institute of Food Technology, Serbia
43. Jaroslava Švarc-Gajić, University of Novi Sad, Faculty of Technology, Serbia
44. Jovan Matović, University of Novi Sad, BioSense Institute, Serbia
45. Milica Pojić, University of Novi Sad, Institute of Food Technology, Serbiaa
46. Suzana Jovanović-Šanta, University of Novi Sad, Faculty of Sciences, Serbia
47. Mihajla Đan, University of Novi Sad, Faculty of Science, Serbia
48. Silvana Andrić, University of Novi Sad, Faculty of Sciences, Serbia
49. Jelica Simeunović, University of Novi Sad, Faculty of Sciences, Serbia

source of novel antimicrobial drugs due to the increase in multiple resistance to antibiotics in current clinical use. Lupinifolin is important bioactive compound isolated from stem of *Albizia myriophylla* Benth. The compound showed high antibacterial activity against Gram-positive bacteria including *Enterococcus*. However, the mechanisms of its antibacterial action are still poorly understood.

OBJECTIVES:

The aim of this study was to reveal the effect of lupinifolin against *E. faecium* HTY0256 strain using proteomic analysis.

METHOD / DESIGN:

Antibacterial activity of lupinifolin against the enterococci was conducted using broth microdilution method and time-killing assay. Proteome analysis of the bacteria after exposure to 2 MIC (minimal inhibitory concentration) of lupinifolin was performed to identify the protein expression changes compared to untreated control cultures by LC-MS/MS.

RESULTS:

MIC and MBC (minimal bactericidal concentration) of lupinifolin against enterococci were ranged from 4 to 8 μg/ml. Proteomic analysis of VRE in the presence of lupinifolin revealed different expression of proteins between the control and treatment groups. Proteins associated with stress response, acid phosphatase, virulence factor, ribosome, and carbohydrate metabolism, and also some virulence factors were down-regulated. The significant induction after treatment was noticed in proteins associated with cell membrane integrity, cell division, peptidoglycan biosynthesis, ABC transport, phosphotransferase system (PTS), aminoacyl-tRNA biosynthesis, acid-resistance of membrane and DNA recombination.

Interestingly, biological processes responsible for cell wall modification and cell shape were disrupted. The results demonstrated that lupinifolin expresses antibacterial activity mainly by effecting on cell membrane of the bacteria and that certain proteins may be responsible for the specific response of VRE to lupinifolin.

CONCLUSIONS:

These findings provide further evidence to support therapeutic efficiency of lupinifolin which could lead to the development of a new effective drug for treatment of multidrug resistant infections.

T3-P-23 Bone marrow derived mesenchymal stem cells from five donors perceived by Raman spectroscopy at a single cell level

Tamara Kukolj[78], Jasmina Lazarević[79], Ana Borojević[80], Uroš Ralević[79], Dragana Vujić3[81], Slavko Mojsilović[78],
Aleksandra Jauković[78], Diana Bugarski[78]

KEYWORDS: Mesenchymal stem cells; Raman spectroscopy; Biochemical characterization

INTRODUCTION:

Although mesenchymal stem cells (MSCs), as adult stem cells, hold great promise in the field of regenerative medicine, signif-

---

[78] Laboratory for Experimental Hematology and Stem Cells, Institute for Medical Research, University of Belgrade, Serbia.

Corresponding author: tamara.kukolj@imi.bg.ac.rs

[79] Center for Solid State Physics and New Materials, Institute of Physics Belgrade, University of Belgrade

[80] Serbia Mother and Child Health Care Institute of Serbia Dr Vukan Cupic, Belgrade, Serbia

[81] School of Medicine, University of Belgrade, Serbia

icant obstacle for their clinical application is the lack of standardized markers for their isolation and characterization. Raman spectroscopy is fast, non-invasive optical technique based on an inelastic scattering of the visible light on a probed material, providing a unique (bio)chemical information. Therefore, it is considered that the Raman spectrum is a unique imprint of the analyte, implying that Raman spectroscopy could be the method of choice for the analysis of MSCs properties on a single cell level.

OBJECTIVES:

Objective of this study was to isolate and characterize bone marrow MSCs (BMMSCs) from five donors using standard biological procedures and to detect their biochemical profile using micro-Raman spectroscopy with the goal to investigate the possibility to employ micro-Raman system to distinguish individual features of BMMSCs populations.

METHOD / DESIGN:

BMMSCs were isolated from samples (2 ml) aspirated from iliac bone during collection of bone marrow for allogenic transplantation. Five healthy donors (age 2-12 years) were analyzed in this study. All experiments were performed using BMMSCs of the 5th passage. To assess immunophenotype of isolated, adherent cells expression of positive mesenchymal cell surface markers (CD90, CD44, CD73, CD105) and negative markers (CD34, CD45 and HLA-DR), a flow cytometry was used. Multilineage differentiation capacity was investigated based on corresponding histochemical staining: alkaline phosphatase and alizarin red staining were used to detect early and late osteogenesis; chondrogenesis was detected based on Safranin O staining of proteoglycans, while Oil red was used to visualize lipid drops of differentiated adipocytes. Following these standard procedures, Raman spectroscopy was performed on methanol-fixed BMMSCs. Excitation was realized by Ar^+/Kr^+ ion laser at 514.5 nm. The beam was focused through the x50 long range microscope objective, NA=0.5 in the backscattering configuration setup. Thermal damage was prevented by keeping low power density absorbed by the sample. Acquisition time was 300 s per spectrum and every cell was probed on several randomly chosen positions. For every donor, 50 to 100 cells were analyzed.

RESULTS:

In accordance with the minimal criteria for defining MSCs of International Society for Cellular Therapy (ISCT) we successfully isolated bone marrow MSCs showing typical adherent, fibroblast-like morphology. All donors exhibit high expression of positive mesenchymal cell surface markers (CD90, CD44, CD73, CD105) without expression of negative markers (CD34, CD45 and HLA-DR), along with the multilineage differentiation capacity toward osteogenesis, chondrogenesis, and adipogenesis. Based on these standard biological tests, no differences between donors were detected. However, Raman spectroscopy coupled with multivariate statistical method – Principal component analysis – showed distinct clustering between donors, based on specific spectral features, implying that Raman spectroscopy could be a step forward in routine analyzes of BMMSCs.

CONCLUSIONS:

As Raman spectroscopy still paves a way towards wider application in biological/biomedical field, our results once more contribute to the achievement of that goal. This technique allows the collection of a large number of data on the biochemical composition at a single cell level in a short time interval, thus providing prompt and unambiguous interpretation of cell populations' features, which is not possible by performing available methods in cell biology. Although the significance of standard techniques should not be neglected, a comprehensive analysis can only be achieved by their association with Raman spectroscopy.

Bone Marrow Derived Mesenchymal Stem Cells from Five Donors Perceived by Raman Spectroscopy at a Single Cell Level

T.Kukolj [1], J. J. Lazarević [2], A. Borojević [3], U. Ralević [2], S. Mojsilović [1], D. Vujić [3,4], A. Jauković [1], and D. Bugarski [1]

[1] Laboratory for Experimental Hematology and Stem Cells, Institute for Medical Research, University of Belgrade, Belgrade 11000, Serbia
[2] Center for Solid State Physics and New Materials, Institute of Physics Belgrade, University of Belgrade, Pregrevica 118, 11080 Belgrade, Serbia
[3] Mother and Child Health Care Institute of Serbia Dr. Vukan Cupic, Belgrade, Serbia
[4] School of Medicine, University of Belgrade, Serbia

Introduction

- **Mesenchymal stem cells (MSCs)**, as adult stem cells, hold great promise in the field of regenerative medicine. However, significant obstacle for their clinical application is the lack of standardized markers for their isolation and characterization.
- **Raman spectroscopy** is fast, non-invasive optical technique based on an inelastic scattering of the visible light on a probed material, providing a unique (bio)chemical information. Therefore, it is considered that the Raman spectrum is a unique imprint of the analyte, implying that Raman spectroscopy could be the method of choice for the analysis of MSCs properties on a **single cell level**.

OBJECTIVES:

- to **isolate and characterize** bone marrow MSCs (BMMSCs) from **five donors** using **standard biological procedures** and to detect their **biochemical profile using micro-Raman spectroscopy** with the goal to investigate the possibility to employ micro-Raman system **to distinguish individual features** of BMMSCs populations.

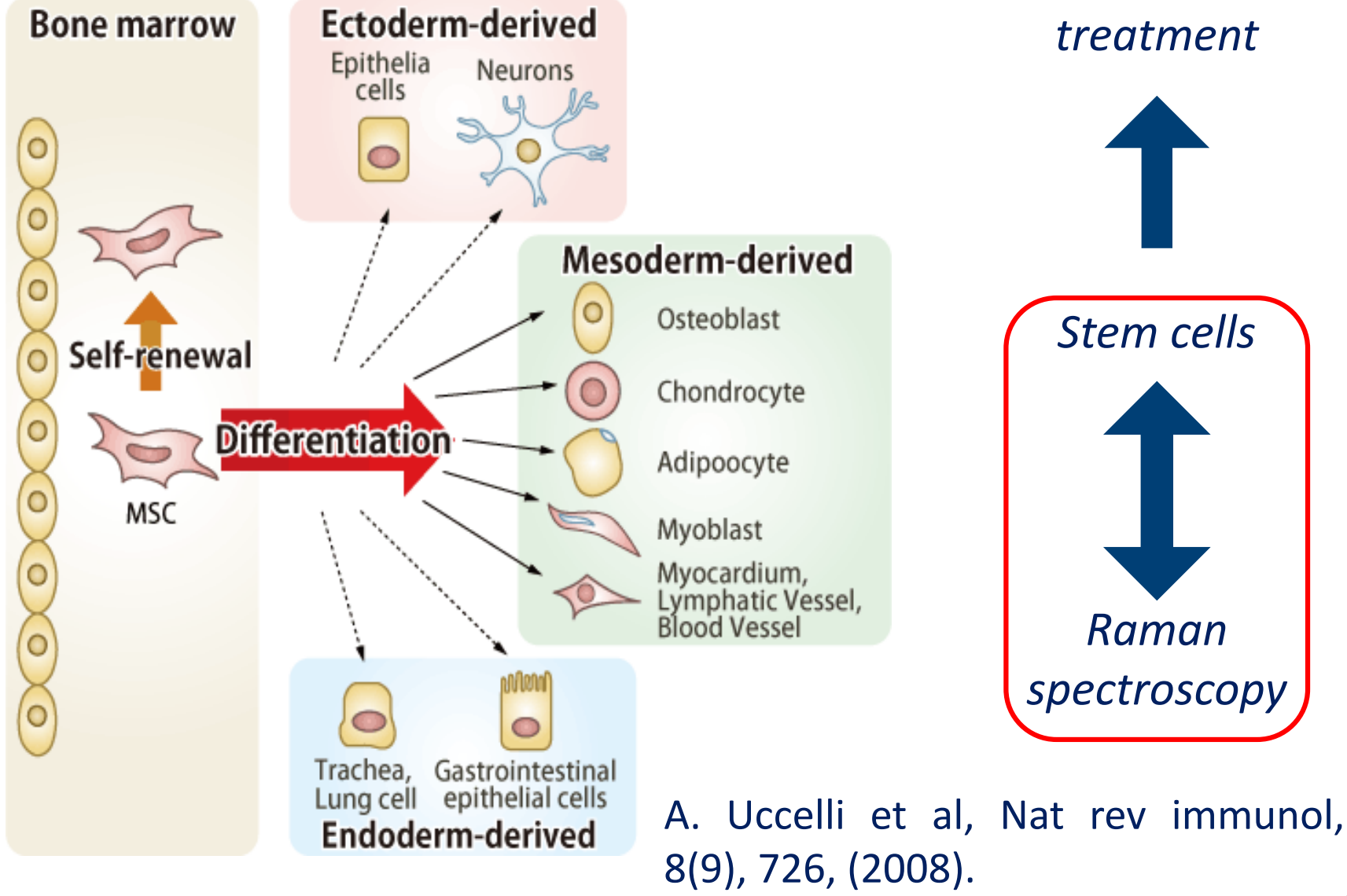

A. Uccelli et al, Nat rev immunol, 8(9), 726, (2008).

Method/Design

1. Isolation and Cultivation of Bone Marrow Derived Mesenchymal Stem Cells **(BMMSCs):**
   - Isolated from samples (2ml) aspirated from iliac bone during collection of bone marrow for allogenic transplantation from five healthy donors (age 2-12 years), grown in standard cultivation conditions; cells from 5th passages were used.
   - Confirmed immunophenotype by flow cytometry: expression of positive mesenchymal cell surface markers (CD90, CD44, CD73, CD105) and negative markers (CD34, CD45 and HLA-DR).
   - Multilineage differentiation capacity was investigated based on corresponding histochemical staining: alkaline phosphatase and alizarin red staining were used to detect early and late osteogenesis; chondrogenesis was detected based on Safranin O staining of proteoglycans, while Oil red was used to visualize lipid drops of differentiated adipocytes.
2. Sample preparation
   - BMMSCs were seeded on rounded CaF_2 Raman grade slides in 24-well plate (5 x 10^3 cells per slide) and cultivated in standard conditions during 24 h.
   - Following the adhesion, cells were washed with saline buffer and fixed with methanol for 10 min at the room temperature.
   - Right before Raman spectroscopy was performed, the samples were washed with distilled water.
3. Raman spectroscopy:
   - TriVista 557 Raman system,
   - backscattering configuration,
   - Coherent Ar^+/ Kr^+ ion gas laser, 514.5 nm,
   - x 50 microscope objective, NA=0.50,
   - laser spot diameter ≈ 20 µm,
   - laser power at the sample plain ≈ 5 mW,
   - acquisition time/spectrum 300s,
   - 50-100 cells per each cell population (D1-D5) were analyzed.

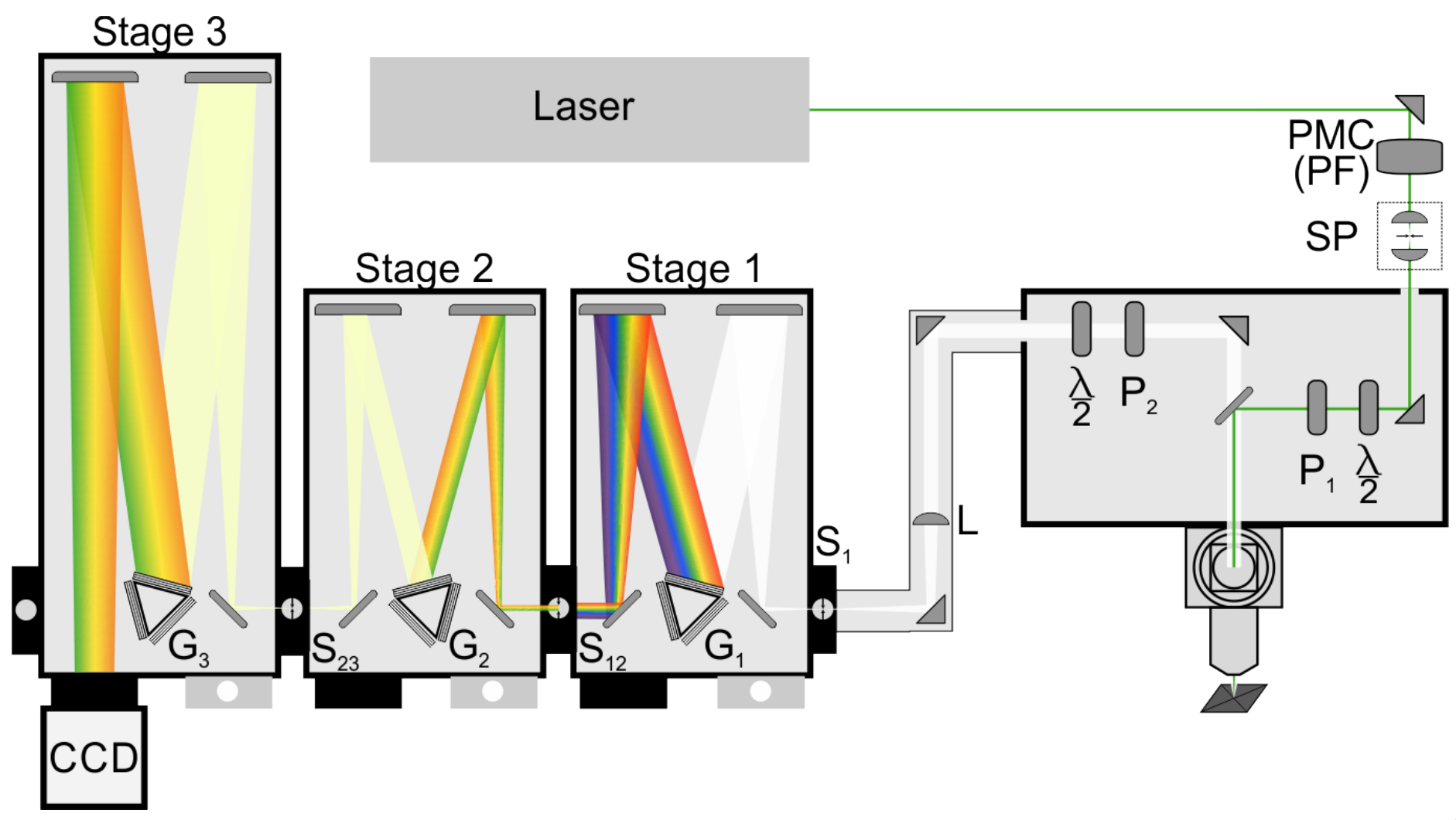

Results: Biological Assays

In accordance with the minimal criteria for defining MSCs of International Society for Cellular Therapy (ISCT), we successfully isolated BMMSCs, showing typical adherent, fibroblast-like morphology (**Figure 1A**). All donors (D1-D5) exhibit high expression of positive mesenchymal cell surface markers (CD90, CD44, CD73, CD105) without the expression of negative markers (CD34, CD45 and HLA-DR) (**Figure 1B).**

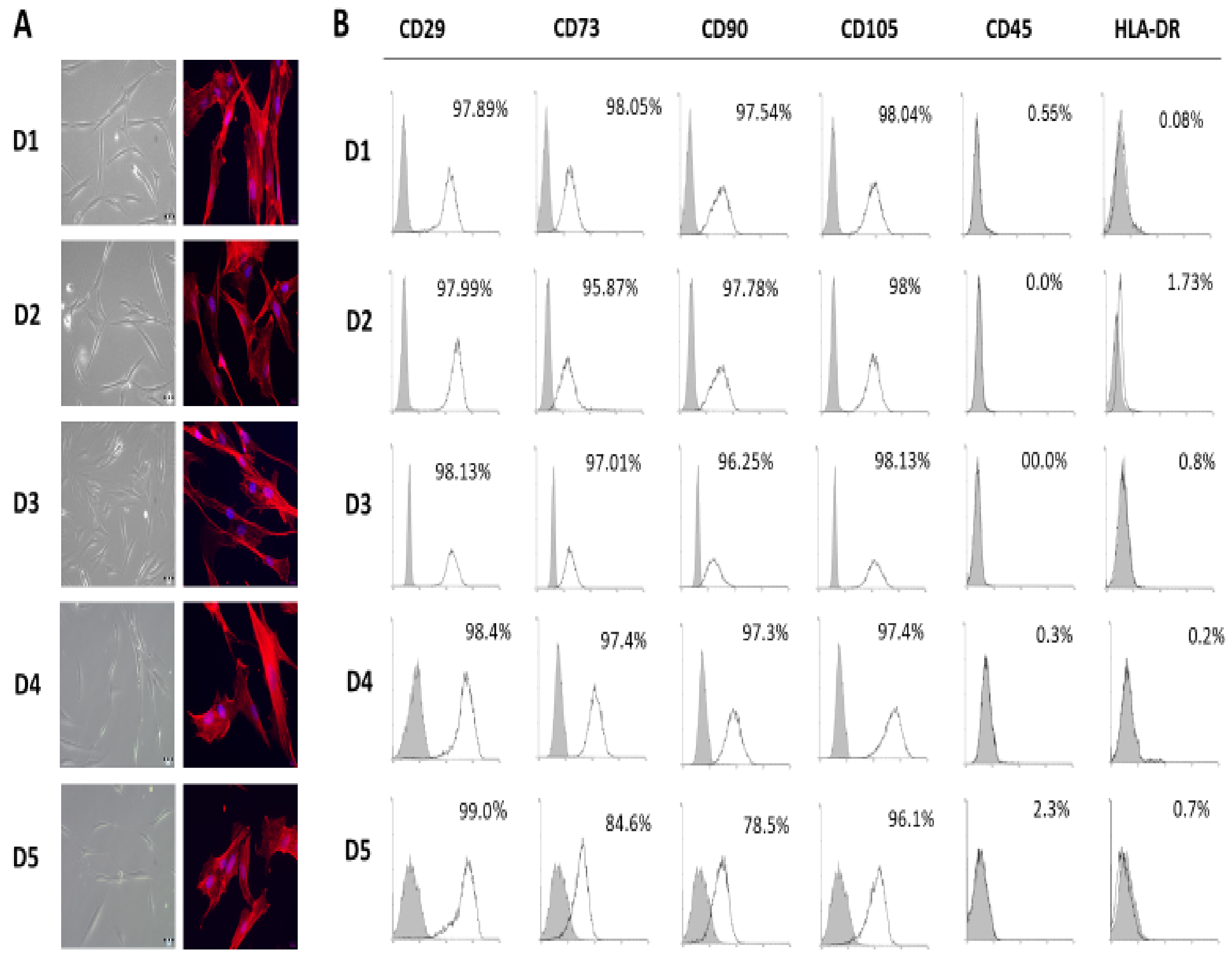

Figure 1. Morphology and immunophenotype of BMMSCs. A) Fibroblaste-like shape of isolated BMMSCs. Cells were grown in GM (Scale bars: 50 µm); TRITC-conjugated phalloidin labeled F-actin (red)/DAPI nuclear staining (blue) merged (Scale bars: 20 µm). **B)** Immunophenotype of cells determined by flow cytometry. Representative flow cytometry histograms are shown. Empty histograms indicate the percentages of positive cells based on the isotype controls (shaded histograms).

Results: Biological Assays

- The multilineage differentiation capacity toward osteogenesis, chondrogenesis, and adipogenesis was confirmed (**Figure 2**) .

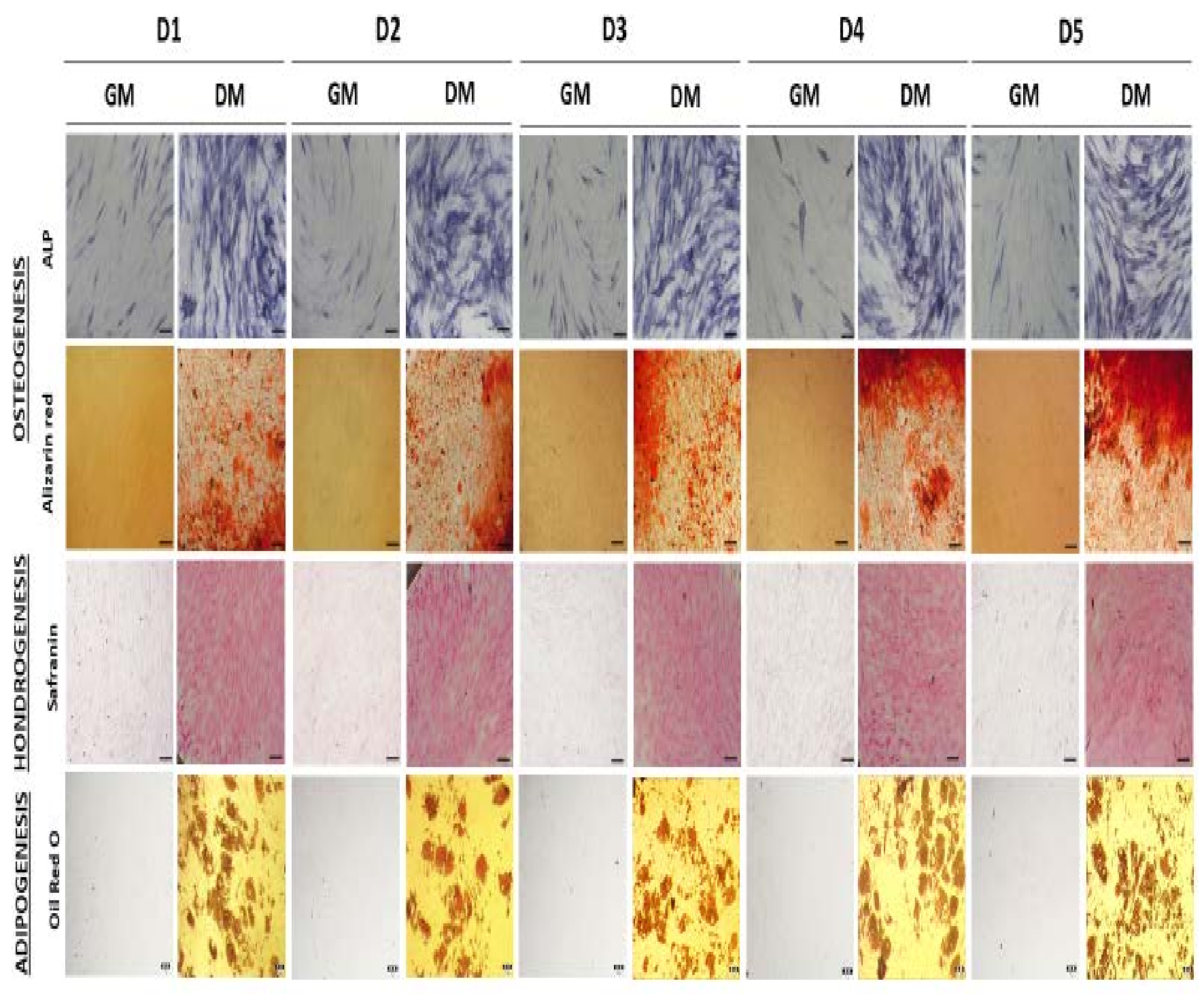

Figure 2. Multilineage differentiation potential of BMMSCs. Cells were cultivated in GM or differentiation medium (DM). Representative photos of osteogenesis determined by ALP and Alizarin staining (Scale bars: 50 µm), chondrogenesis determined by Safranin (Scale bars: 50 µm) and adipogenesis determined by Oil red (Scale bars: 20 µm) are shown.

Results: Raman Spectroscopy

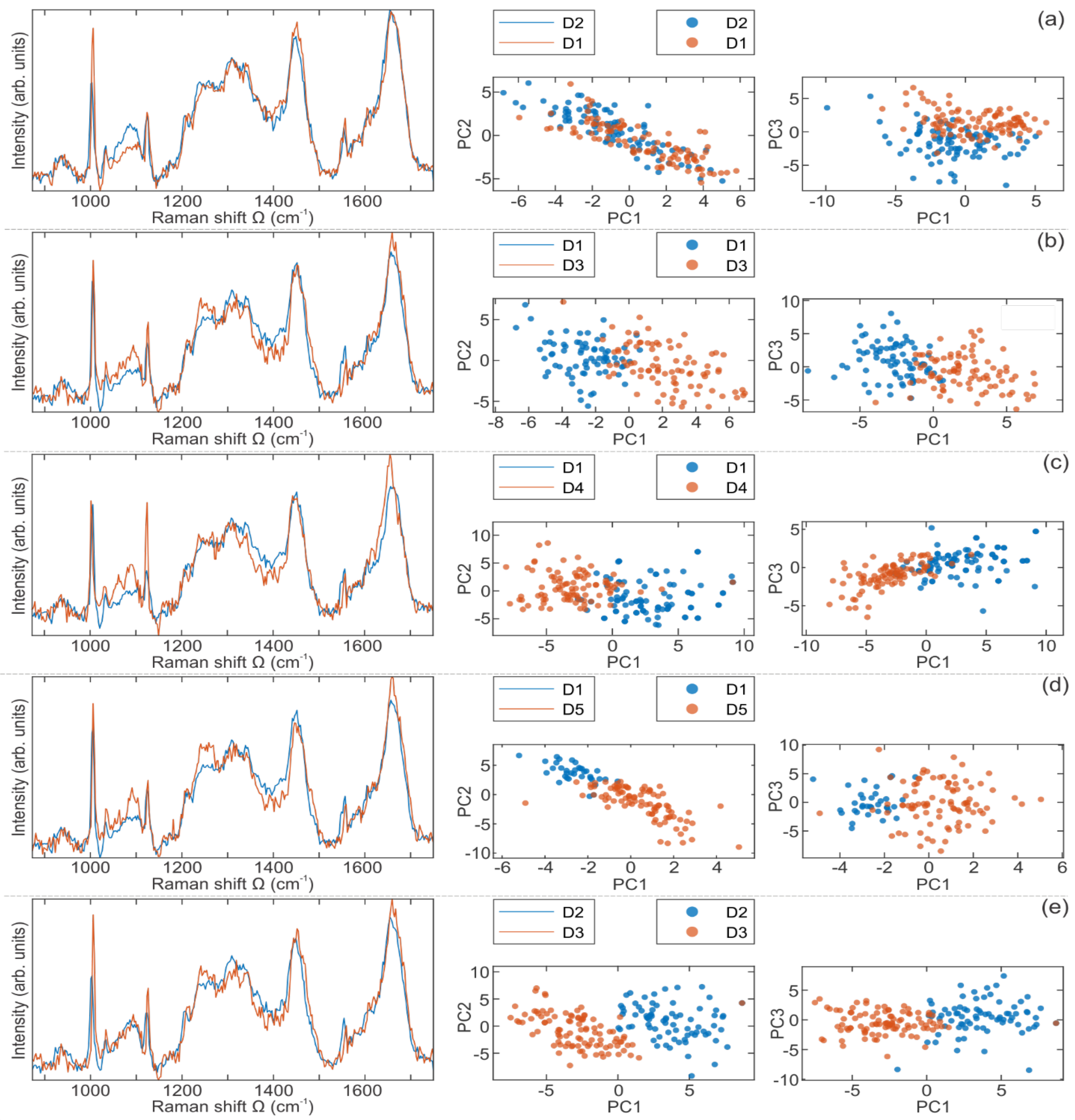

Figure 3. A comparative display of the averaged Raman spectra (red and blue lines), per cell populations: a) D1-D2, b) D1-D3, c) D1-D4, d) D1-D5, e) D2-D3. Principal Component Analysis (PCA) score plots are represented with red and blue dots.

Results: Raman Spectroscopy

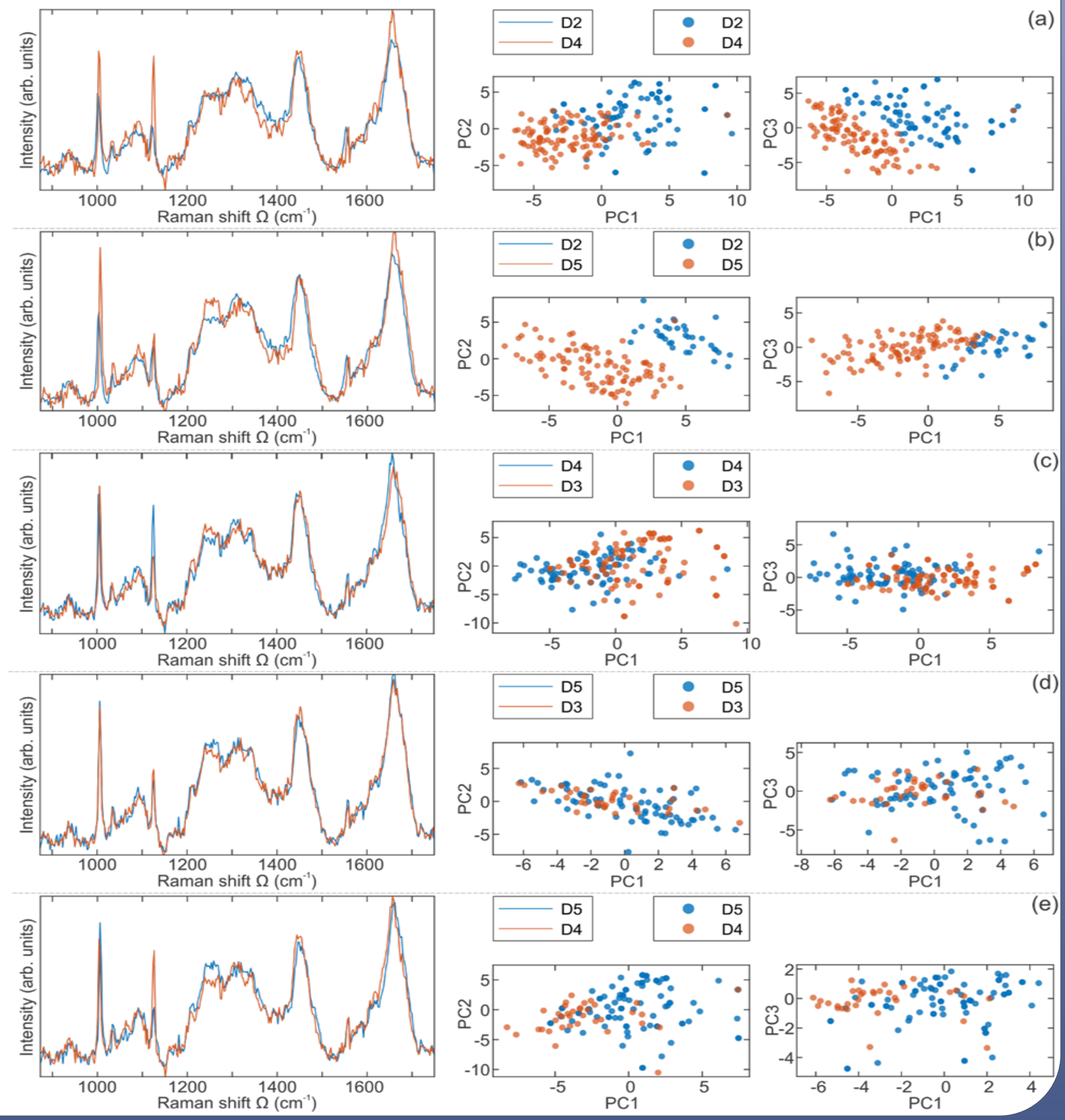

Figure 4. A comparative display of the averaged Raman spectra (red and blue lines), per cell populations: a) D2-D4, b) D2-D5, c) D3-D4, d) D3-D5, e) D4-D5. PCA score plots are represented with red and blue dots.

Conclusions

- Based on *standard biological tests*, **no differences between the donors were detected**.
- *Raman spectroscopy* coupled with multivariate statistical method – **Principal Component Analysis, showed distinct clustering**, based on specific spectral features, **between the donors**, implying that Raman spectroscopy could be a step forward in routine analyzes of BMMSCs (**Figure 3 and 4**).
- Although the significance of standard techniques should not be neglected, a comprehensive analysis can only be achieved by their association with Raman spectroscopy.

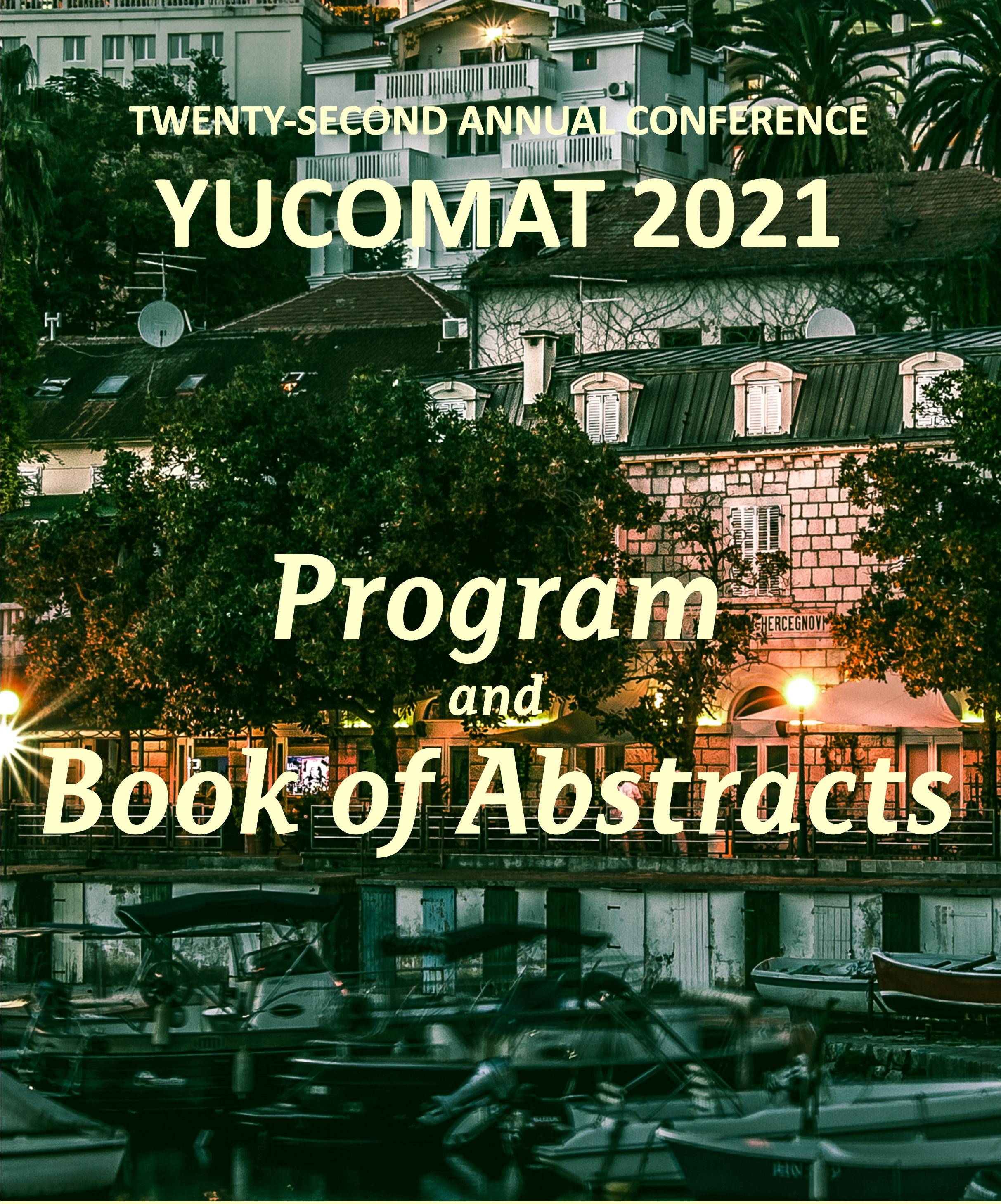

TWENTY-SECOND ANNUAL CONFERENCE

YUCOMAT 2021

Program
and
Book of Abstracts

endorsed by

FEMS

FEDERATION OF EUROPEAN
MATERIALS SOCIETIES

SERBIA MRS Materials Research
Society of Serbia

TWENTY-SECOND ANNUAL CONFERENCE

YUCOMAT 2021

Hunguest Hotel Sun Resort, Herceg Novi, Montenegro
August 30 - September 3, 2021
http://www.mrs-serbia.org.rs

Program
and
Book of Abstracts

Organised by:
Materials Research Society of Serbia

Endorsed by:
Federation of European Material Societies

CIP - Каталогизацијаупубликацији
НароднабиблиотекаСрбије, Београд

66.017/.018(048)

DRUŠTVO za istraživanje materijala Srbije (Beograd). Godišnja konferencija (22 ; 2021 ; Herceg Novi)
Programme ; and the Book of abstracts / Twenty-second Annual Conference YUCOMAT 2021 Herceg Novi, Montenegro, August 30 - September 3, 2021 ; organised by Materials Research Society of Serbia ; [editor Dragan P. Uskoković]. - Belgrade : Materials Research Society of Serbia, 2021 (Herceg Novi : Biro Konto). - XXXIII, 146 str. : ilustr. ; 23 cm

Tiraž 150. - Bibliografija uz pojedine apstrakte. - Registar.

ISBN 978-86-919111-6-4

а) Наука оматеријалима-- Апстрактиб) Техничкиматеријали—Апстракти

COBISS.SR-ID 44447497

Title: THE TWENTY-SECOND ANNUAL CONFERENCE
YUCOMAT 2021
Program and Book of Abstracts

Publisher: Materials Research Society of Serbia
Knez Mihailova 35/IV, P.O. Box 433, 11000 Belgrade, Serbia
Phone: +381 11 2185-437; hhttp://www.mrs-serbia.org.rs

Editor: Prof. Dr. Dragan P. Uskoković

Technical editor: Jasmina R. Jevtić

Typesetting
and prepress: Dr. Aleksandar Dekanski
Cover page: Nenad Ignjatović
Covers: Images on front & back covers are the property of MRS Serbia

ISBN 978-86-919111-6-4

MRSS is member of the
Federation of European Materials Societies

FEMS

Printed in: Biro Konto
Sutorina bb, Igalo – Herceg Novi, Montenegro
Phones: +382-31-670123, 670025, E-mail: bkonto@t-com.me
Circulation: 150 copies. The end of printing: August 2021

CONTENTS

ABSTRACTS

MRS-Serbia

President of the Council: Slobodan Milonjić
President: Dragan Uskoković
Vice-presidents: Velimir Radmilović, Dejan Raković, Smilja Marković
General Secretary: Nenad Ignjatović
Members: Gordana Ćirić-Marjanović, Vera Dondur, Djordje Janaćković, Dragana Jugović, Đuro Koruga, Slavko Mentus, Bojana Obradović, Zoran Petrović, Milenko Plavšić, Zoran Popović, Vladimir Srdić, Jovan Šetrajčić, Petar Uskoković, Miodrag Zlatanović.

International Advisory Board
Chair: Robert Sinclair (USA)
Members: Fritz Aldinger (Germany), Rostislav A. Andrievski† (Russia), Aline Auroux (France), Xavier Batlle (Spain), Serena Best (UK), Ivan Božović (USA), Philippe Colomban (France), Uli Dahmen (USA), Miha Drofenik (Slovenia), Rafal Dunin-Borkowski (Germany), Mauro Ferrari (USA), László Forró (Switzerland), Yury Gogotsi (USA), Horst Hahn (Germany), Paul Harrison (UK), Felix T. Hong (USA), Robert Hull (USA), Wolfgang Jaeger (Germany), Josè M. Kenny (Italy), Alexander H. King (USA), Feng-Huei Lin (Taiwan), Toshiaki Makabe (Japan), Amelia Montone (Italy), Eva Olsson (Sweden), Eiji Osawa (Japan), Davor Pavuna (Switzerland), Doug Perovic (Canada), Zoran S. Petrović (USA), Robert Ritchie (USA), Peter Franz Rogl (Austria), Frances Ross (USA), Richard W. Siegel (USA), Mamoru Senna (Japan), Valeriy V. Skorohod† (Ukraine), Danilo Suvorov (Slovenia), Enrico Traversa (Italy), Vuk Uskoković (USA), Gordana Vunjak Novaković (USA), Jackie Ying (Singapore)

P.S.III.2.

Ion beam irradiation of 12-tungstophosphoric acid – influence of energy of accelerated ions on structural properties

Željko Mravik[1], Danica Bajuk-Bogdanović[2], Andrzej Olejniczak[3,4], Milica Pejčić[2], Jasmina Lazarević[5], Nenad Lazarević[5], Zoran Jovanović[1]
[1]Center of excellence for hydrogen and renewable energy (CONVINCE), Department of Physics, "Vinča" Institute of Nuclear Sciences - National Institute of the Republic of Serbia, University of Belgrade, P.O. Box 522, 11001 Belgrade, Serbia, [2]Faculty of Physical Chemistry, University of Belgrade, P.O. Box 47, 11158 Belgrade, Serbia, [3]Flerov Laboratory of Nuclear Reactions, Joint Institute for Nuclear Research, 141980 Dubna, Moscow region, Russia, [4]Faculty of Chemistry, Nicolaus Copernicus University, Toruń, Poland, [5]Center for Solid State Physics and New Materials, Institute of Physics Belgrade, University of Belgrade, Pregrevica 118, Belgrade 11080, Serbia

Ion beam irradiation is a versatile tool for structural modification and engineering of new materials, where the energy of ions determines the nature of interactions between accelerated ions and the target. In this study, 12-tungstophosphoric acid (WPA) films of different thickness were spin-coated on platinized silicon substrate and irradiated with: low energy hydrogen ions (10 keV) and swift heavy ions (Bi, Xe and V) with energies up to 710 MeV. Raman spectroscopy and Fourier-transform infrared spectroscopy (ATR-FTIR) were used for investigation of structural properties of irradiated WPA. Raman spectra of irradiated samples revealed new wide vibrational bands in regions from 100 to 500 and 600 to 1000 cm^{-1} which are comparable to the ones obtained for WPA thermally treated at 600 °C. Additionally, bands of remaining Keggin anion structure appeared modified with observed shifting and splitting of bands. In ATR-FTIR spectra of irradiated samples additional wide bands at around 800 and 1100 cm^{-1} also appeared and resemble the ones of thermally treated WPA. The degree of change of these bands compared to the bands of Keggin anion was justified by SRIM calculations. The most prominent changes were observed in those samples for which the number of induced vacancies was the highest. The results show that structure of WPA can be tuned by ion beam irradiation, by optimizing the fluence and the type and energy of ions.